Digital Photoelasticity in Biomedical Sensing

GURTEJ SINGH GREWAL

A thesis submitted in partial fulfilment of the requirements of Bournemouth University for the degree of Doctor of Philosophy

June 2007

Bournemouth University

Abstract

This research investigates on the use of digital photoelasticity in biomedical sensing applications with a particular emphasis on assessment of diabetic foot ulceration. One of the main causes of foot ulceration in diabetic patients is excessive pressure at the sole of the foot, which involves vertical as well as shear forces. Precise role of these forces in predisposing the foot to ulceration is not very well understood, however, a general consensus is that the combined effect of vertical and shear forces is much more harmful than the vertical force alone. Whilst the vertical force can be measured relatively easily, it is difficult to decouple the shear force from the combined force, which is considered to be of more clinical relevance in assessment of diabetic foot ulceration. The major impediment in achieving this objective is lack of suitable shear force measuring devices and limitation of the existing systems that can simulate the actual conditions of foot loading. In this research a photoelastic material has been used to develop a prototype-sensing device, which develops coloured fringes due to foot loading. Intelligent image processing techniques have been employed to analyse and obtain relevant load information from these fringes.

The research surveys the existing sensing devices that are commonly used in diabetic foot clinics. It highlights the need for a new sensor design that can be used for pressure-induced pathologies. To meet these requirements and develop a sensor based on the principle of photoelasticity, conventional techniques of RGB photoelasticity and Phase-shifting methods have been fully investigated. This led to identify suitable optical elements for the system design and applicability of these techniques for the intended application. This resulted in devising an experimental setup that can provide coloured image of foot *per se* actual conditions of foot loading. However, the conventional technique of stress analysis cannot be directly applied in the present case, since the photoelastic effect is induced due to the material deformation as opposed to the usual component loading in photoelastic experiments with coatings. Also, in the current application the applied load has to be estimated from the fringe patterns (i.e. inverse problem) under varying environmental conditions with different loading situations for each subject. As it is difficult to develop analytical models under these conditions and the related inverse might have infinite number of solutions, the use of neural networks has been proposed to overcome these complexities. The network has been trained with direct image data which provides input load information under controlled experimental conditions of vertical as well as shear forces. The prototype sensor also provides qualitative whole-field data of the actual foot loading, which can be used for quick differentiation of foot with or without callus. This may also find use in haptics, pattern recognition and other biomedical sensing applications such as pressure sore assessment for disabled subjects or patients with numbness. With further enhancement in image processing technique this can be developed into a clinically viable system capable of providing complete foot analysis from early stage detection to prevention of ulceration.

List of Publications resulting from the Thesis

1. Grewal, GS and Dubey, VN (2007). "Inverse problem of photoelastic fringe mapping using neural networks." Measurement Science and Technology **18**: 1361-1366.

2. Grewal, GS, Dubey, VN and Claremont, DJ (2006). "Isochromatic demodulation by fringe scanning." Strain **42**: 1-9.

3. Grewal, GS, Bharara, M, Cobb, JE, Dubey, VN and Claremont, DJ (2006). "A Novel approach to thermochromic liquid crystal calibration using neural networks." Measurement Science and Technology **17**: 1918-1924.

4. Dubey, VN, Grewal, GS and Claremont, DJ (2006). "Extraction of load information from photoelastic images using neural networks." Experimental Mechanics **47**: 263-270.

5. Dubey, VN, Grewal, GS and Claremont, DJ (2006). Extraction of load information from photoelastic images using neural networks. ASME International Design Engineering Technical Conference, Philadelphia, Pennsylvania (USA), Sep 10-13.

6. Grewal, GS, Dubey, VN and Claremont, DJ (2006). Diabetic foot ulceration: a predictor-instrument for the pandemic. Britain's Top Younger Scientists, Engineers and Technologists at the House of Commons, London (UK), House of Commons.

7. Grewal, GS, Dubey, VN and Claremont, DJ (2005). Shear force sensor for detection of diabetic foot ulceration. Life Sciences Interfaces Conference, Southampton (UK), Southampton University.

8. Bharara, M, Grewal, GS, Claremont, DJ and Hadley, G (2006). Association of plantar foot temperatures and sensory loss in diabetic foot disease. 10th European Congress of Medical Thermology, Zakopane (Poland).

9. Grewal, GS, Dubey, VN and Claremont, DJ (2005). Shear force sensor for an early detection of diabetic neuropathy. 5th Academic Biomedical Engineering Research Group workshop, Bournemouth University (UK).

10. Bharara, M, Grewal, GS, Cobb, JE and Claremont, DJ (2006). "Association of plantar foot temperatures and sensory loss in diabetic foot disease." Thermology International **16**(3): 101-102.

LIST OF CONTENTS

List of Figures

List of Tables

Acknowledgement

This research would not have reached a successful completion without the help, support and encouragement of many individuals, to whom I am forever indebted.

First of all, I thank God, who gave me the strength and knowledge to execute this work and then my family and friends who supported me all the way through years.

I am grateful to my supervisor Dr. Venketesh N Dubey for all his help and guidance during the course of my research. I would also like to thank Professor Denzil Claremont for his supervision. My sincere thanks to Dr. Tom Teng for his suggestions, encouragement and criticism that helped me work more diligently.

I would like to thank my friends and colleagues Mr. Manish Bharara and Bright Osei Twumasi for their support and encouragement.

My sincere thanks to technicians Mr. Gary Toms and Mr. Kevin Smith for their help in fabrication of many of the setup required during the course of this PhD.

Finally, I am grateful to Bournemouth University for funding this research, thereby giving me the opportunity to pursue a Doctorate.

Chapter 1 Introduction

1.1 Background

Pressure induced tissue anomaly is of crucial clinical importance in many pathological investigations. This includes pressure sore identification in older and disabled subjects with neuropathic impairment; such as numbness in the case of patients with leprosy or diabetic patients at the risk of developing foot ulceration. Whilst simple pressure sore identification at the contact interface is relatively easy, measurement and visualisation of the causation forces are of vital clinical importance. As walking involves tissue shearing it has been argued that the shear forces may have more damaging effect than the vertical force alone in the growth of foot ulceration in diabetic patients. However, measurement of the shear force at the plantar surface is considered to be a major impediment in understating its precise role due to the limitations of current measurement technologies. Commercially available pressure pads just provide foot pressure and some research based shear sensors which are in fact displacement sensors providing only discrete measurements and ignore the effect of the vertical loading. Therefore, there is a need to develop a sensor that can sense the actual condition of foot loading by providing the whole field visualisation and quantification of the loading conditions. This research aims at developing a prototype sensor based on photoelasticity for measurement of shear force and early detection of diabetic foot ulceration. Historically, photoelasticity has been used for experimental stress analysis, however, due to special characteristics of the photoelastic materials to provide whole field visualisation of the stress field led to consider the use of this material for biomedical sensing application in this research. This chapter starts with the role of plantar pressure in foot ulceration and is followed by problems in measuring interface forces. The chapter also reviews the existing sensors, their limitations and outlines the need for developing a whole field sensor for stress visualisation. Finally, the aims and objectives of the research are discussed. The research implements digital photoelasticity as a sensing technique for early detection of foot ulceration. A 'principle demonstrator' using photoelasticity in clinical sensing applications was built and coupled with artificial intelligence to measure the vertical and shear force under a controlled environment and provide qualitative loading condition of the foot.

1.2 Role of Plantar Pressure in Foot Ulceration

The foot experiences mechanical stresses during the normal gait due to combined vertical and shear forces ranging from 250-270 kPa and 70-80 kPa respectively (Hosein and Lord 2000a; 2000b). Both vertical and shear loading have an adverse affect on diabetic feet and are considered as important factors in foot ulceration besides neuropathy and ischaemia. The literature in Appendix-I provides detail on diabetes and its complications. The vertical load acts normal to skin surface thus physiologically and anatomically stressing the heavily loaded regions such as those overlying bony prominences. The shear force acts tangential to the foot surface causing bunching and stretching of tissues but its effect has not been well studied; mainly due to limitations of existing technology. Periodic exposure to high stresses on the foot together with callus, tissue damage and loss of sensitivity leads to traumatic complications. Shear is found to increase the stresses in the area ahead of the direction of shear forces. Model analysis of the effect of such forces on skin and soft tissue revealed changes in stress distribution in the superficial layer of tissues (Zhang et al. 1994). It is important to develop measurement systems of high accuracy in order to understand the role of vertical and shear forces and help support systems reducing the chances of ulcer development by pressure redistribution and blood flow control (Bader et al. 2005). The heterogeneous nature of the body can affect clinical measurements not only between different subjects but even within a given subject. For instance, in the context of foot pressure; measurements can vary if the subject's posture is changed as it would redistribute the pressure to different regions under the foot. The tissue properties and variation in thickness under different bony prominences account for variance in pressure measurement between different subjects. Thus, the reliability of measurement systems and parameters measured like pressure and peak pressure points are affected by a number of hard to control-for factors.

1.2.1 Vertical Loading at Plantar Interface and Its Measurement

Vertical loads are prominent under areas of previous ulceration, bony prominences and callus zones and are regarded as major risk factors leading to ulceration. The vertical load affects the blood flow, plantar tissue thickness and deteriorates properties of soft tissues under plantar area. Stresses induced by vertical load are higher in barefoot gait than shod gait as shoes provide a cushioning effect. Peak pressures points have been reported mostly under bony structures of the first or second metatarsal heads. Hosein and Lord (2000a, 2000b) recorded maximum pressure of 273 kPa under the second metatarsal in a neuropathic group and 228 kPa under the second and third metatarsal for normals, using the F-Scan measurement system (Section 1.2.1.3). In addition to body weight and tissue properties, speed of walking is also considered to alter pressure values. It increases pressure under the heel and shifts the load medially under the forefoot (Rosenblaum et al. 1994). Perry et al (2002) have reported maximum pressure at the first and second metatarsal heads with value of (189±64) kPa and minimum at toe area with (80±36) kPa in a group of 12 neuropathic subjects. Maximum pressure to be present under the lateral foot of (279±102) kPa and (230±81.9) kPa under the first metatarsal head has also been reported in 50 diabetic subjects (Payne et al. 2001). In a study to evaluate critical level of plantar pressure for identifying the risk to ulceration, peak pressure was found to be (831±247) kPa (Armstrong et al. 1998). Authors also concluded there is no optimal cut-off because higher the peak pressure, higher is the commensurate risk. The assigned value of 700 kPa as cut off gave a balanced sensitivity and specificity in a study of 219 patients with and without neuropathy.

Vertical load measuring devices have been developed extensively and can be categorised as in-shoe or external sensors and can be further categorised as footprint or cumulative output sensors.

1.2.1.1 Pedobarograph Based Sensor

A pedobargraph based sensor is an external barefoot measurement device based on the principle of change in refractive index of glass due to pressure loading, which alters the critical angle of internal reflection and leads to scattering of light. The system has mostly been used for research studies and for comparison with other systems like EMED, F-Scan (Quaney et al. 1995; Kumar et al. 2005). It comprises of a thin mat of deformable material with fine patterns avoiding any local pressure redistribution that might occur when using foam sheets. A glass plate is edge lit and a mirror is used to project image onto the camera. The pressure from the mat is converted to light intensity patterns from the scattered light and calibrated to the applied load. The system requires calibration using weights and the results show that a cell of 100 mm^2 can gives an average pressure which is nearly 60-70% of the peak value. The averaging depends not only on the cell size but also on swing of the peak and sharpness of the peak. Results for this technique can be as good as 93% of true peak (Lord 1997).

1.2.1.2 EMED Pedar System

The EMED Pedar is a commercial in-shoe capacitance based sensor. The sensor is based on the principle that there is change in capacitance due to change in the distance between two conducting wires separated by a dielectric material. The measurement of capacitance change is correlated to the applied force. The Pedar insoles are 2 mm thick and consist of 99 transducers with capability of measuring up to frequencies of 1000 Hz, Figure 1.1 shows the actual system and the pressure patterns generated. These systems are found to exhibit a good linearity and low errors especially under high loads. Another advantage is accessible calibration of individual sensor, making it useful for clinical applications by establishing a baseline for measurements (Finch 1999). The sensor is reported prone to damage under higher loads. Pedar systems have been used in various clinical trials for evaluation of repeatability of the total contact casts (Harstell et al. 2001) and effect of different prosthetic foot designs on the patterns of the plantar pressure (Hayden et al. 2000).

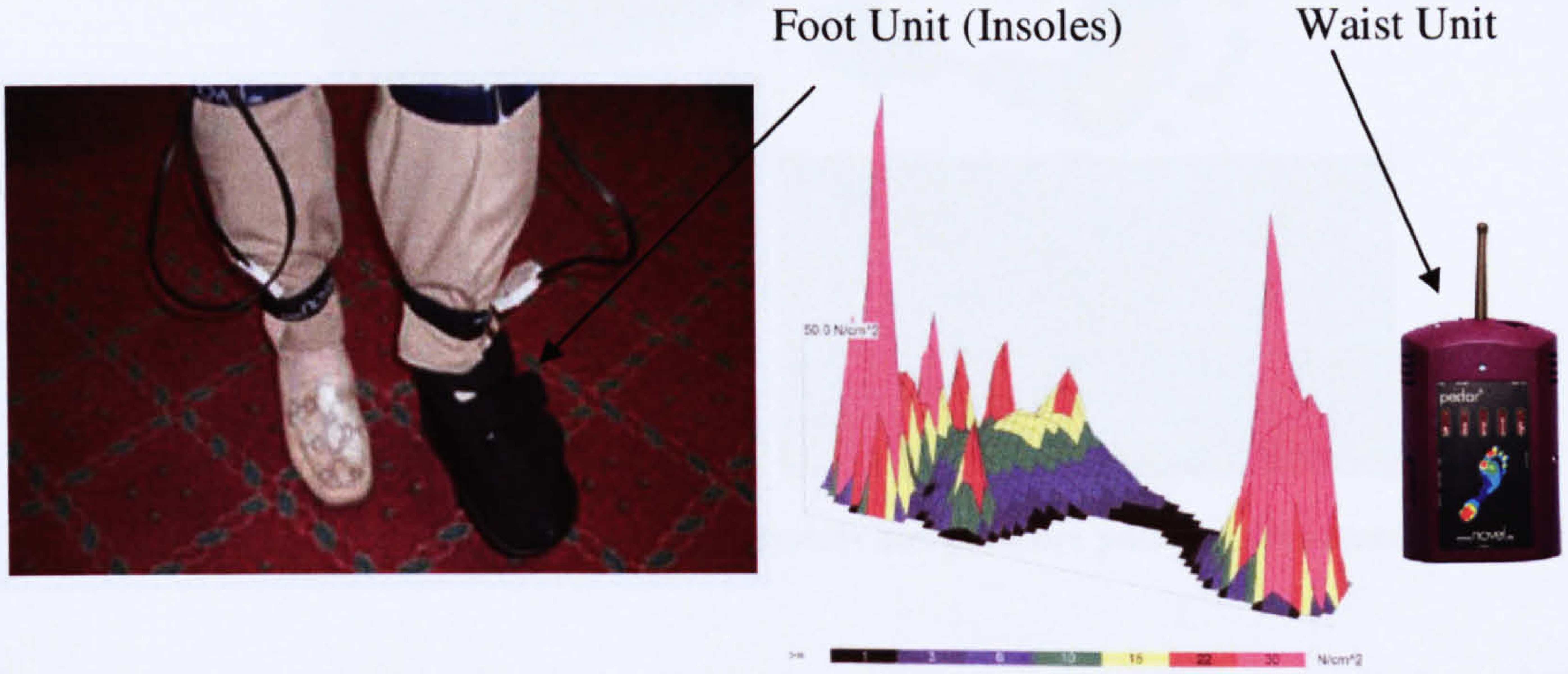

Figure 1-1: EMED Pedar (Finch 1999) a capacitance based system

1.2.1.3 F-Scan

The F-Scan system is another in-shoe measurement device that has been used in numerous research and clinical based studies for pressure evaluation and efficiency of insoles. The system has been implemented in dynamic monitoring of plantar pressure with respect to time. It is composed of ultra thin pressure sensitive, resistive based links embedded in Mylar coating insole (Randolph et al. 2000), Figure 1.2. The sensor utilises force-sensitive resistive film in form of matrix as sensor element. The base unit comprises of 960 cells with insole thickness of 0.18 mm. Non-linearity claimed by manufacturers is of 5% with sensitivity of ±4 kPa but higher non-linearity has been reported with hysterisis of 10% (Nicolopoulos et al. 2000). The system requires easy calibration process of loading individual sensor insole with complete bodyweight. An incompressible base for accommodating insole in shoe is obtained by using semi-rigid plastazote inset into flexible Poron. The sensor is reported to require 60-90 sec of conditioning prior to measurement, due to viscoelastic recovery from the period of rest (Hosein and Lord 2000a).

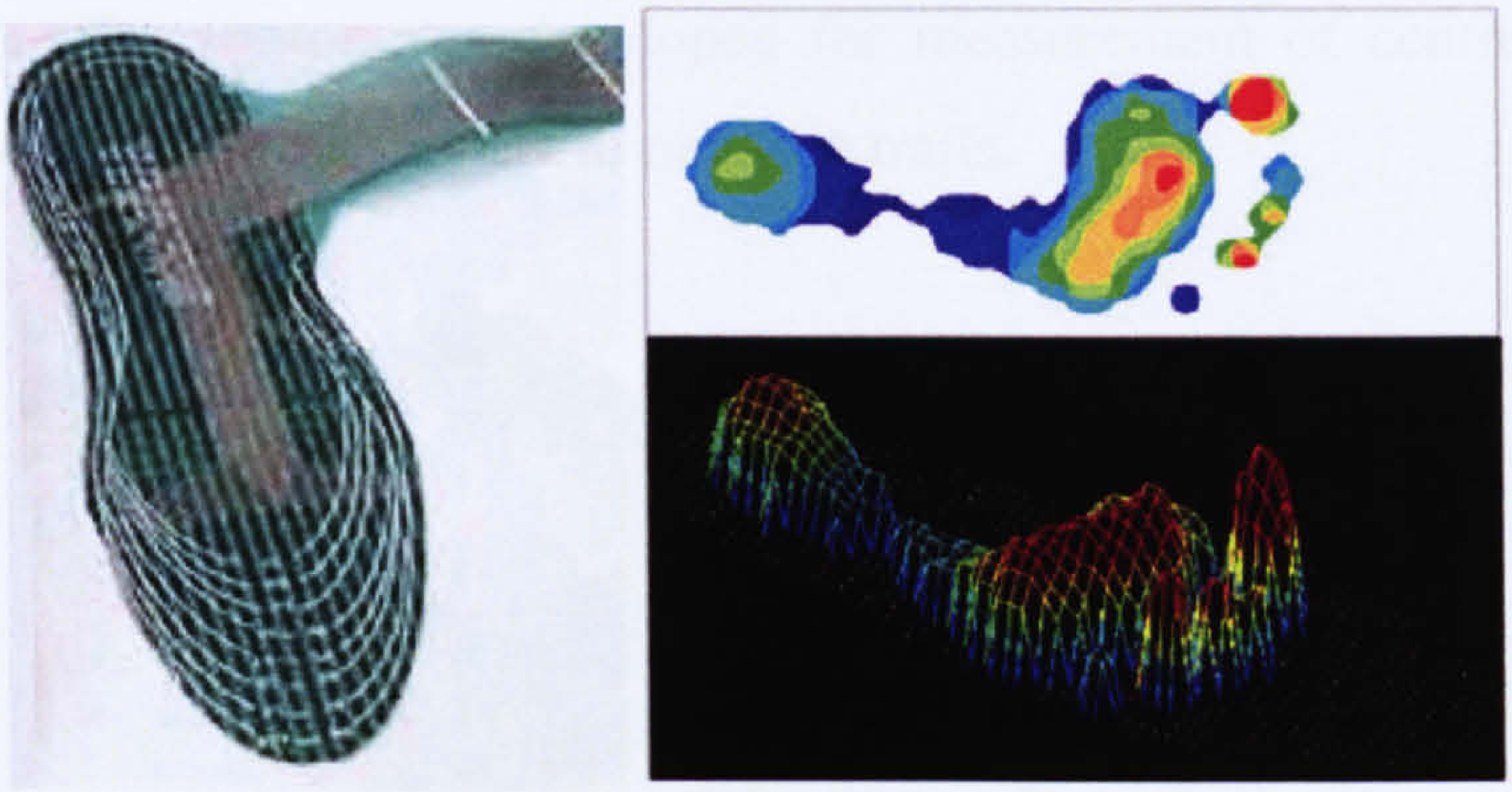

Figure 1-2: F-Scan measurement system and pressure patterns (Tekscan®)

Errors in measurement of pressure have been reported from 7% to as high as 24% at higher loads (Nicolopoulos et al. 2000). The sensor has been evaluated under different calibration techniques and reported to be sensitive to the method of calibration. Tests for hysterisis showed preconditioning effect making static calibration difficult, thus requiring dynamic calibration of system at 0.5 Hz. Maximum hysterisis was 18.3% at 1000 N attributed to viscoelastic property of Poron backing rather than the sensor itself. High repeatability was shown with small error of 0.3% but output to input error of 44% was shown. The sensor was also found to be prone to bending as evaluated by analysing a single cell element. Randolph et al (2000) reported sensor to be reliable in management of patient for prevention of ulceration. Overall the sensor has been reported to be efficient and reliable if calibrated with some standard reference like force plate.

1.2.1.4 Parotec System

The Parotec system is an in-shoe pressure measurement device designed to measure pressure due to both vertical and shear component (Chesnin et al. 2000). The sensor comprises of 3 mm insoles with 24 sensor areas. The design consists of micro-sensor under constrained hydrocell with an incompressible fluid sealed in a polyurethane packet, Figure 1.3. The fluid packet deflects only at top and bottom surfaces. The micro-sensor has a balanced bridges circuit etched on silicone membrane that deflects into an evacuated chamber on application of load. The system has a sensitivity of 2.5 kPa with load limit of 625 kPa, repeatability of ±0.4%, accuracy of ±2% with maximum measuring frequency 300 Hz. The sensor was developed for measurement of centre of pressure during gait and proved to be efficient with multiple trails.

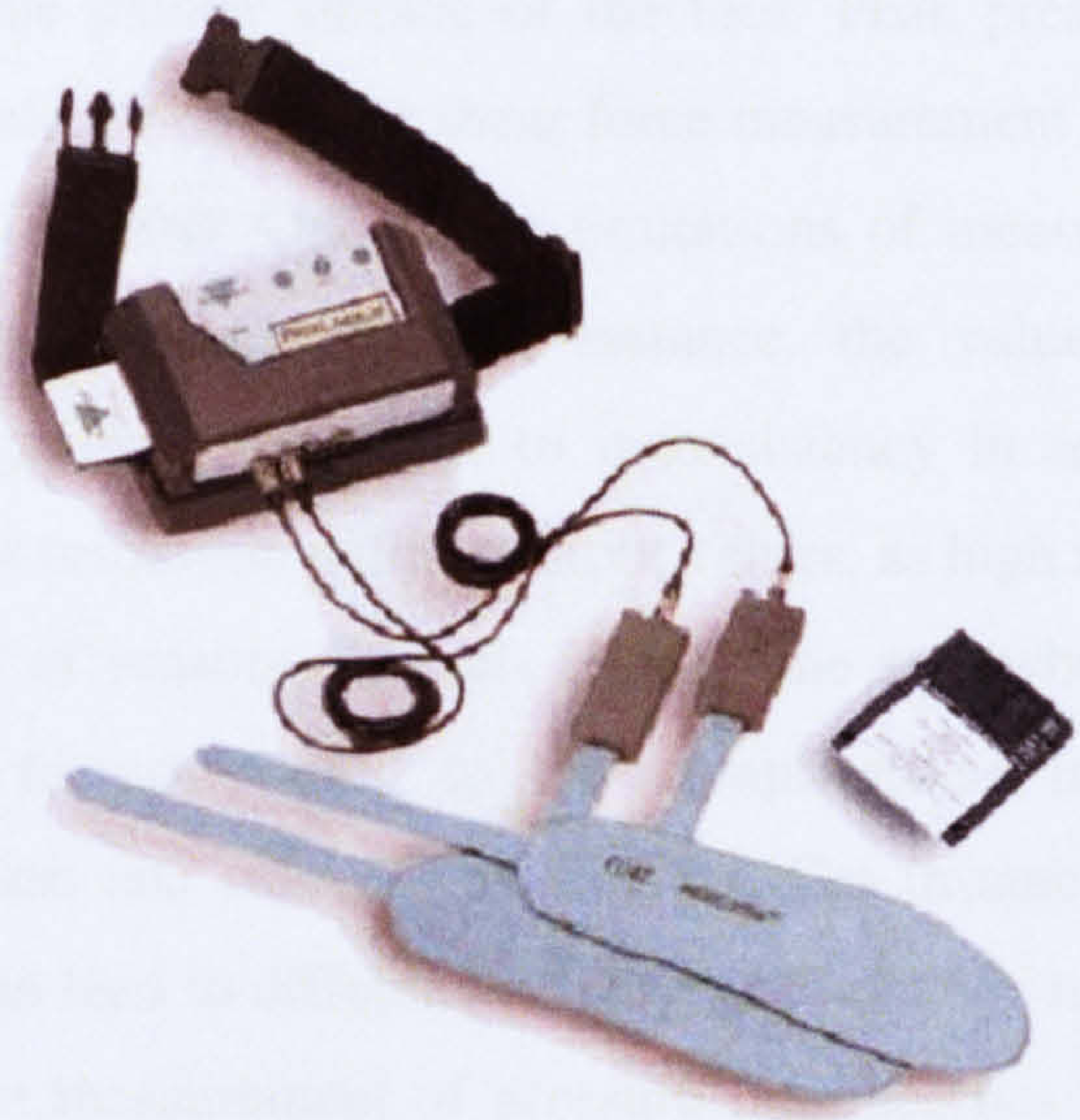

Figure 1-3: Parotec system (Metitur® 2004), an in-shoe measurement device

1.2.1.5 Interferometer based Sensor

Interferometry is a well established high resolution technique for measurement of surface deformation by analysing patterns generated by superimposition of two light beams. A sensor was developed based on the above principle where a laser beam is directed through an optically clear material and interferogram is generated between reflected beams from top and bottom surface of plate (Hughes et al. 2000). Any change in interferogram due to deformation of one of the surface is analysed. The analysis was carried out using Fourier Transform for interpretation of fringes.

Selection of the optical plate is critical and for the selected material no more than 4 wavelengths of laser (He-Ne) interfere should occur at maximum load. Hughes et al (2000) used perspex and best results were achieved after sampling the material 1000 times. The pressure range of sensor is 1-1000 kPa with low hysterisis. Collimated beam of laser of 145 mm diameter from 0.5mm was produced using specific lens arrangement.

1.2.2 Limitations of Pressure Measuring Devices

The evaluation of vertical loading is important in determination of pressure distribution and peak pressures over the plantar surface of the foot. Peak pressure points help in determination of exact points for mounting shear force measurement sensors and support systems for pressure redistribution. One of the limitations of measuring devices is the lack of standardisation in measurement. For instance, the value and the point of maximum peak pressure generally vary due to inconsistency in selection of the area under consideration. Sensor resolution defines output values, as high resolution is capable of triggering more number of sensors elements under same area when compared to low resolution sensor. Other factors adding to the complications in measurement are heterogeneous nature of skin and anatomy of the foot. For instance, the repeated foot loading by same subject can lead to different results due to change in posture. The effect of individual's anatomy on measurement of pressure interface has been reported to be subtle (Bader et al. 2005). The heterogeneous structure of body determines amount of loading under particular body part depending upon the amount of subcutaneous tissue and weight supported there. The above factors also limit the shear measuring devices in the same way.

1.2.3 Shear Loading at Plantar Interface and Its Measurement

The forces acting in the plane of the foot are referred to as shear forces. The internal compression experienced by the soft tissues causing damage is the resultant of both vertical and shear forces. The application of shear further increases the stress in direction of force due to compression of tissues. It has been argued that shear forces may have a crucial role in the causation of foot ulceration, however, measurement of the shear forces has been an elusive goal (Cavanagh et al. 2000) The direction of shear is another important factor to be considered. As per the law of friction, shear forces can act potentially at the regions of high plantar pressure.

The maximum shear in walking adults is reported to be up to 45% of the maximum vertical at the same site. Patients with prior ulceration history were found with maximum shear force of 72.7 kPa under the first metatarsal using a magneto resistive transducer (Hosein and Lord 2000b). Use of nylon sock was found to reduce the frictional force and thus lowered the maximum shear to 57.6 kPa. Maximum shear in Normals with and without nylon hose was recorded under third metatarsal as 86.5 kPa and 70.4 kPa. From the recordings of shear and pressure under foot, shear is known to be distributed more laterally than pressure. Another study reported maximum shear to be under lateral metatarsals i.e third and fourth of about (33 ± 9) kPa (Perry et al. 2002). They also reported a higher degree of stretching of adjacent tissues than bunching due to shear. The values of shear reported were comparable to those reported earlier at the average of 33 kPa without socks (Tappin and Robertson 1991). On the contrary another study showed consistent increase in shear with socks (45 kPa) when compared to without socks (33.75 kPa) (Hosein et al. 1992). In a study conducted to determine the shear modulus of tissues using MR elastography, it was reported that shear modulus changed from 8 kPa to 12 kPa from a load of 100 N to 200 N (Weaver et al. 2005) under the heel pads. It is of vital importance to understand the mechanical properties of tissue and distribution of forces under the foot to help alleviate high pressures that leads to foot ulceration.

As discussed earlier shear sensing is an important consideration in assessment of diabetic foot ulceration, however only a few sensors have been reported for shear measurement. The following section describes a few well known shear sensors.

1.2.3.1 Magneto Resistive Shear Transducer

A magneto resistive transducer is based on principle of change in resistance under the influence of magnetic field (Tappin et al. 1980). It consists of a semi-conductor coil mounted on a stainless steel disc as shown in Figure 1.4. The disc couples to another steel disc (with a small magnet mounted on it) through a groove. The purpose of the groove is to provide a sliding guide for uni-directional mechanism. A layer of silicone is sandwiched between the two plates and the displacement of semi-conductor in the magnetic field causes change in resistance proportional to the applied force. The sensor was later modified to bi-axial for measuring shear in orthogonal directions. The resultant shear was calculated from vector addition of the longitudinal and transverse vectors.

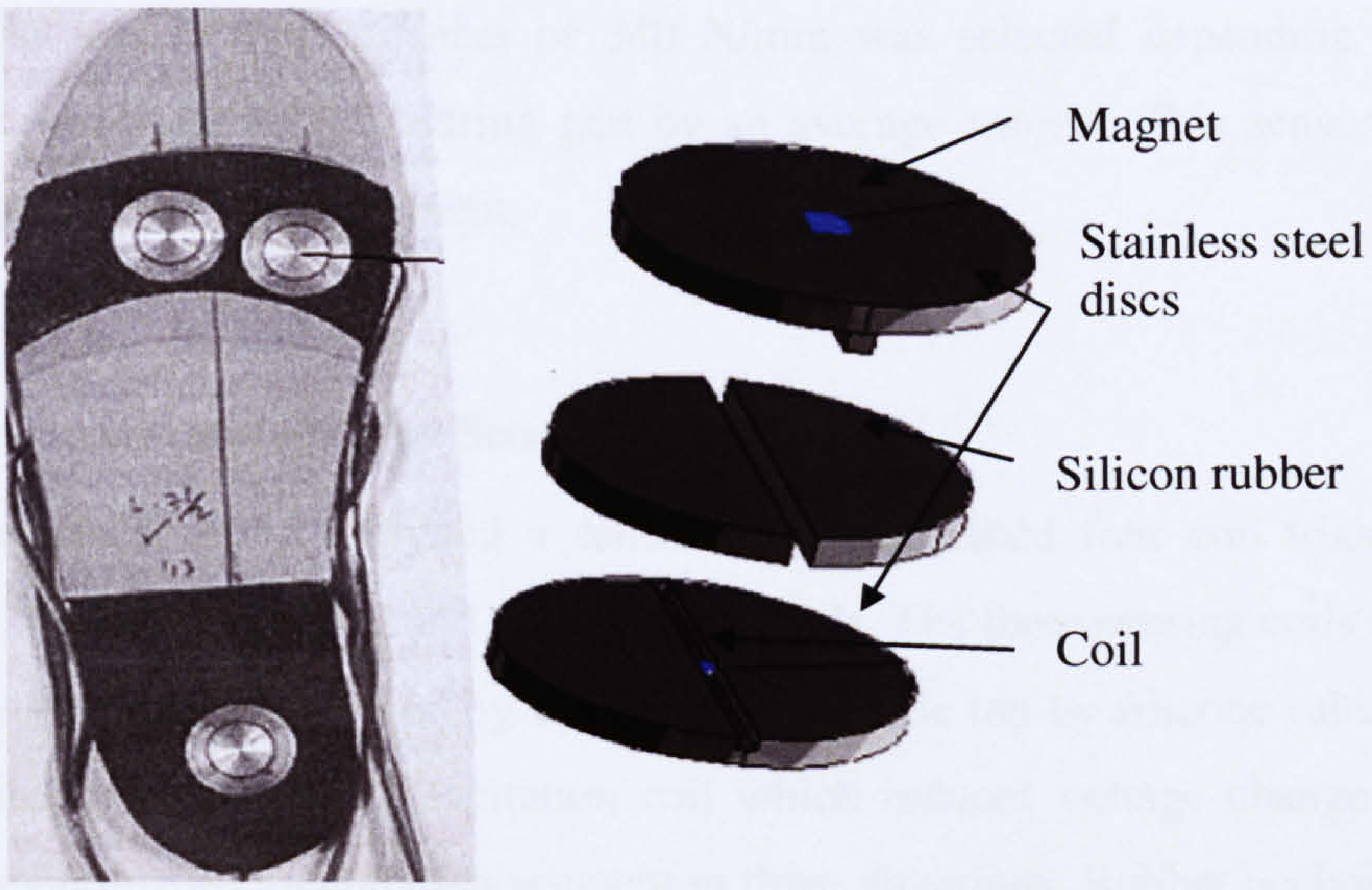

Figure 1-4: Magneto resistive based bi-axial shear transducer, (b) schematic diagram of placement of steel discs and silicon rubber

The full scale deflection range is ±0.6 mm with a design range of ±50 N, which corresponds to 250 kPa of shear per 200 mm. Quasi-static calibration at 0.1 Hz is required with ±30 N sinusoidal shear input (Hosein et al. 1992). From the working principle it appears that sensor measures displacement rather than shear.

1.2.3.2 Opto-electronic Shear Transducer

A prototype miniature shear sensing transducer was developed using photodiodes and laser capable of measuring shear force uni-directionally (Lebar et al. 1996). The sensor was based on the principle that the current increases linearly with the optical power of the incoming light source, as the photodiode produces a current proportional to the spectral intensity of the light received. Electro-optical light source of 660 nm and photodiode solar cell were used for fast response, easy adaptability and low cost. The amount of light received by photodiode was controlled by displacement of a wedge shaped mount. The displacement is the response of applied shear force which is mechanically resisted by spring mechanism shown. Sensor displacement is limited to 0.5 mm to provide relatively stiff sensor and yet allowing adequate light control. This requires matching of wedge shape and spring stiffness; wedge controls amount of light being transmitted and sufficient spring stiffness allows shear measurement within specified displacement of 0.5 mm. Rectangular flat spring with stiffness of 340 N/mm was selected depending on maximum load that would be applied during gait by an average subject. This sensor is again based on the principle of displacement.

1.2.3.3 Three Dimensional Displacement Sensor

Warren-Forward and their group designed a sensor in 1992, named four coil triaxial sensor (Urry 1999), one excitation coil and three sensing coils. The three sensing coils are arranged in circular layout and separated by excitation coil at the top by silicone rubber. Application of load alters position of excitation coil which induces voltage change in sensing coils corresponding to oriental displacement in three directions. Rubber is chosen for its specific elastic and mechanical characteristics but has the disadvantage of introducing non-linearity to the sensor. Also the sensor has many electro-mechanical components that make it prone to failure.

1.2.4 Limitations of Shear Measuring Devices

Besides the anatomical factors discussed in section 2.2.2, the shear force measurements are limited due to complexity of the force itself when compared to vertical force. The major disadvantage of the shear force sensors is that they all are displacement based sensors thus the calibrated output is related solely to the displacement; actual condition of loading (vertical as well as shear) is ignored by these devices. For instance in a magneto resistive transducers, for two different vertical loads two different shear forces would be required to induce the same displacement. But since the sensor is based on amount of displacement induced the shear output will be same. The same fact holds true for other displacement based shear transducers. Thus, there is a need for developing a system that can not only consider vertical load during shear measurement but also present the whole field view of stress patterns at foot the interface.

1.3 Need for a New Technology

The sensors described in the preceding section have had the merits of being efficient, easy to use and have a moderate measuring range. However, demerits include complexity in design and electronics, calibration requirement and no direct visual output. As far as shear measurement is concerned, prior knowledge of peak pressure points is required to install them at appropriate positions and most of them are displacement sensors ignoring the effect of vertical force to determine shear forces. With bi-axial transducers it is difficult to mount the sensor at sites of edges because area of high pressure being too close to edge of inlay. Also high pressure regions with close proximity would hinder mounting of more than one or two sensors, such as four metatarsals. Thus a sensor should be designed which can measure the actual condition of foot loading with the possibility that forces could be separated and visualised under different loading conditions. This research is aimed at developing a photoelasticity based sensor to overcome the above mentioned limitations of the existing technology and finally be used to develop a system for early detection of foot ulceration from the fringe patterns induced under foot loading.

Photoelastic materials when loaded with internal or external forces, exhibits fringe patterns representing the stress. This phenomenon of photoelastic materials can be exploited in developing sensors suitable for different applications. The low cost and dynamic response from photoelastic material can be extended to any sensing applications if coupled with appropriate classifier algorithms. Intelligent techniques need to be devised to extract and analyse the photoelastic data that can be used to calibrate against any desired outputs. Previously sensors have been developed for specific industrial applications like torque and bending load determination (Chung 1998; Noroozi et al. 2003).

However, the attempts to use photoelastic effect for determining diabetic foot loading have been limited to vertical forces and discrete sensing in the foot regions (Acran and Brull 1976; Rhodes et al. 1988). In most cases research has been confined to greyscale photoelasticity with empirical relations between some statistical fringe parameter and the load. The use of sole statistical parameter limits the accuracy, repeatability and the tolerance of the system. This research takes photoelasticity a step further towards developing a system for diabetic foot measurements.

1.4 Aims and Objectives

Use of photoelasticity can be advantageous for sensing applications since it can exhibit actual conditions of loading in terms of providing pressure patterns, load evaluation and direction of shear force. When compared to the existing sensors photoelasticity based sensor can provide direct visual output of high pressure points. The discussions so far have underlined that both vertical and shear forces acting at plantar interface were detrimental and were the risk factors to foot ulceration. The presence of shear forces further damage deep tissues through compression and stretching. Determination of shear force and its direction are important to understand its effect on foot ulceration and this may also lead to better design of orthopaedic footwear.

The aim of the project is to develop a portable shear sensing device based on photoelasticity for biomedical applications. The final sensor would provide qualitative and quantitative load information. The objectives of this research are:

- to design a sensor with appropriately selected photoelastic material and components
- to develop a prototype shear sensor that can be used for determining shear force at the plantar interface in diabetic subjects
- to obtain qualitative information from the visual output of the sensor
- to develop a classifier methodology that can be used to predict foot ulceration at an early stage

1.5 Preview

The research presented in this thesis includes study of currently available technology in vertical and shear force measurement and exploring the use of digital photoelasticity for biomedical sensing. Appropriate selection of modulus of photoelastic material is very important. The amount of shear force applied combined with the modulus and optical properties of material determine the extent to which fringes will be generated. Chapter 2 presents the basic physics of photoelasticity and various elements included in the application. The available photoelastic stress analysis techniques were revisited and enhanced for force measurement. Chapter 3 provides a detailed design and description of experimental rigs used in the research. Chapter 4 is exclusively devoted to use of conventional photoelastic techniques of RGB (Red, Green & Blue) calibration and phase shifting methods as applied to unconventional loading scenarios. The drawbacks experienced in conventional photoelastic techniques in force measurement were overcome by incorporating neural networks for inverse analysis of photoelastic data in Chapter 5. The photoelasticity based sensor would aid to immediate recognition of area of higher stresses from visual inspection of fringes. Foot regions with callus and hard tissues will generate different fringe patterns when compared to soft areas. Chapter 6 presents implementation of neural networks for decoupling vertical as well as shear forces including the case study for qualitative whole field image analysis of foot loading. The research methodology involves digital image acquisition of photoelastic fringes using flatbed scanner and specifically designed experimental setups. The prototype sensor is based on an external platform for barefoot analysis using reflection photoelasticity. Finally Chapter 7 concludes with research achievements and future research directions and potentials.

Chapter 2 Literature Review

2.1 Introduction

The need for a new system based on photoelastic principle for shear measurement in diabetic foot was discussed in the first Chapter. This Chapter provides details on photoelasticity; its basics, definitions, optical elements, material properties, light sources and image acquisition systems. Later sections discuss the major photoelastic techniques followed by its applications in sensing for industrial and clinical environment.

2.2 Principle of Photoelasticity

Photoelasticity is an optical technique for experimental stress analysis for solving engineering problems. It is based on the principle of temporary birefringence i.e. double refractive index, possessed by some non-crystalline transparent materials. Under state of external or internal stress the material exhibits birefringence characteristics, which splits the incident light into two components travelling at different speed. At emergence the two beams are out of phase and the difference in phase is dependent on the value of stress at that point. The greater the stress, the higher is the birefringence and hence relative retardation between the two resulting light components. This retardation or the temporary state of double refraction of photoelastic materials is used for stress analysis. The technique can be implemented in either transmission or reflection mode depending upon the application requirement. This research implements photoelasticity in reflection mode due to the application requirement where transmission is not optional.

The incident light is polarised in nature and falls perpendicular to the optic axis of the material to induce the photoelastic effect. Figure 2.1 shows isochromatic fringe patterns generated in a section of a stressed model seen through a configured polariscope. The whole-field view of stress patterns is represented in form of coloured fringes under white light. The fringes are designated by a number *N*, called Fringe Order.

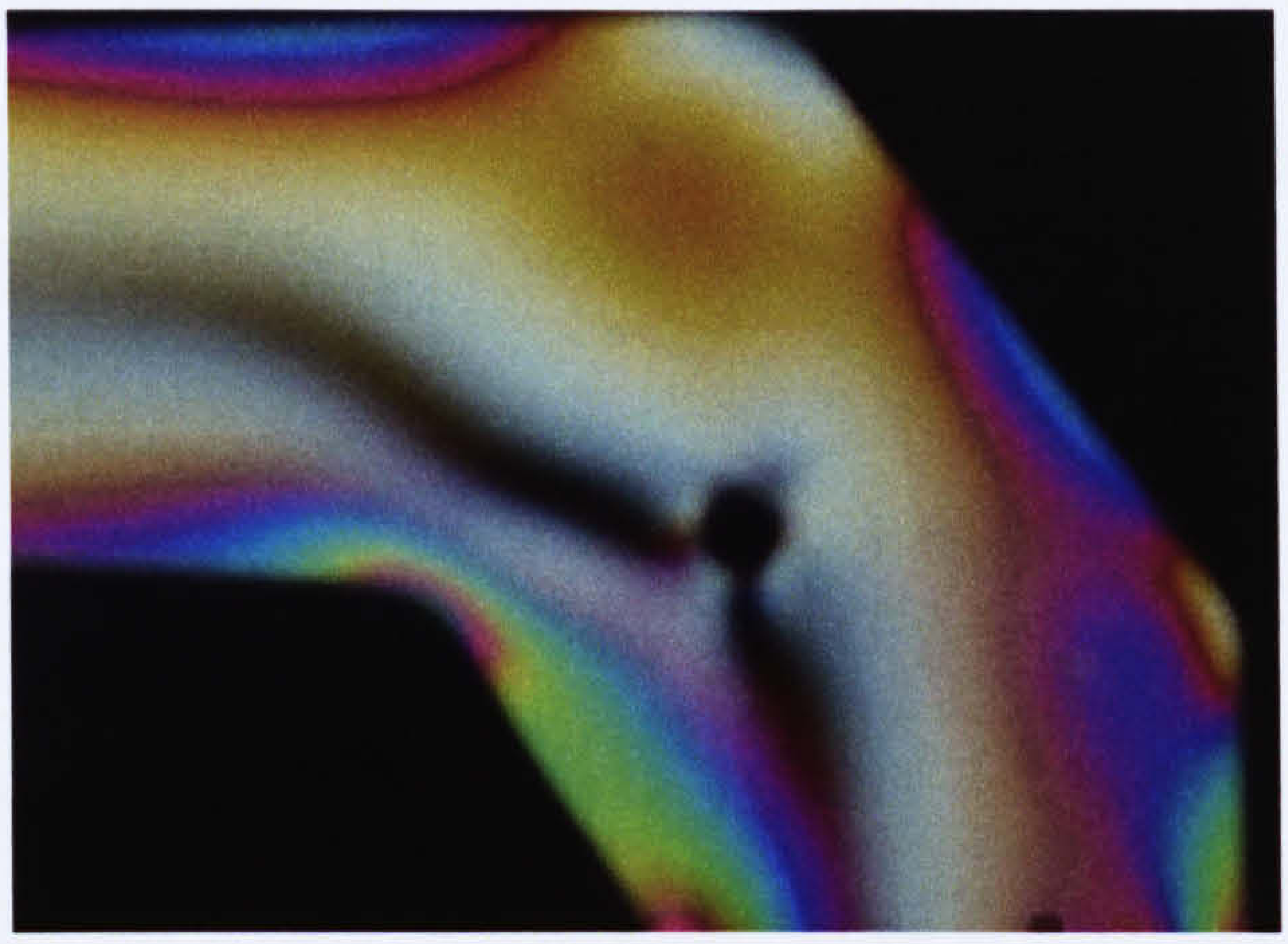

Figure 2-1: Photoelastic fringe patterns (isochromatics) generated in a section of a stressed model

The conventional photoelastic applications involve determining regions of high stress and value of stress-strain in different regions.

The analytical relation used to find the principal strain difference in reflection photoelasticity is given by Equation (2.1).

$$\varepsilon_1 - \varepsilon_2 = \frac{Nf}{2t} \tag{2.1}$$

Where, $\varepsilon_1 - \varepsilon_2$ is the principal strain difference, N is the fringe order, f is the fringe value, t is the thickness of the photoelastic material. The relation can be modified to represent principal stress difference as shown in Equation 2.2.

$$\sigma_1 - \sigma_2 = \frac{N\,f\,E}{2t(1+\nu)} \tag{2.2}$$

Where, E is the modulus of elasticity of the material and ν is the Poisson's ratio.

The sensitivity of a photoelastic material is represented by its strain optic coefficient, K and Equation (2.1) can be modified to include the K parameter as in Equation (2.3).

$$\varepsilon_1 - \varepsilon_2 = \frac{N\lambda}{2Kt} \tag{2.3}$$

Where, λ is the wavelength of the light source.

Whether the fringe patterns represent principal stress or strain difference depends on the mathematical relation used to determine the values. Henceforth, the term 'stress' will be used as the parameters under evaluation.

2.3 Photoelastic Fringes

The photoelastic fringes generated are designated either as isoclinics or isochromatics. As a model is loaded from zero stress condition, the fringes start to appear and propagate from the point of application of load. Depending on the configuration of polariscope, either both isoclinics and isochromatics can be seen or only isochromatics can be visualised. This section describes the type of fringes with their properties in accordance to the type of light source used.

2.3.1 Isoclinic Fringes

The isoclinics show the direction of principal stresses in a stressed model and always appear black irrespective of type of light source used as shown in Figure 2.2(a) with a monochromatic light and Figure 2.2(b) with a white light. It is important to note that the isoclinics in these figures show only those points on the model whose principal stress axes coincide with the axes of polariser and analyser. However, different optical orientation of polariser and analyser is required to generate a whole field view of isoclinics.

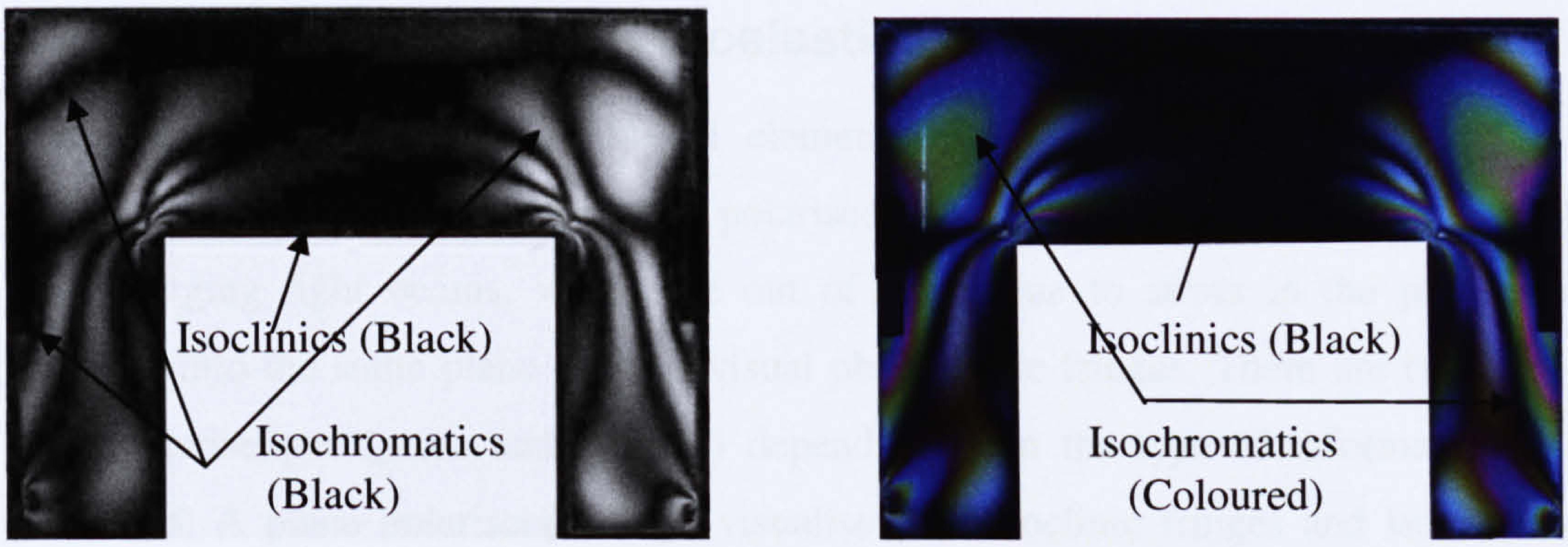

Figure 2-2: (a) A stressed C-shaped model under monochromatic light, (b) under white light for plane polariscope configuration

Isoclinic fringes do not propagate or move with increase in load unless a high deformation of material occurs. Isoclinics are dependent on the orientation of optical elements i.e. the polariser and the analyser.

2.3.2 Isochromatic Fringes

The principal stress difference is shown by isochromatic fringes. Isochromatic fringes would appear black when illuminated with a monochromatic light, Figure 2.2(a) and coloured with white light, Figure 2.2(b). Under monochromatic light source the isochromatics are designated by integral fringe orders only i.e. a black fringe will represent an integral fringe order (0 or 1 or 2 or 3 …). New isochromatic fringes appear with increase in load and thus in order to determine integral fringe order at a point under monochromatic light source, it would be required to count the number of fringes that passed the point of interest during increase of load. To determine fractional fringe orders advanced techniques are required like Tardy's Compensation as will be discussed later in this chapter. However, under white light the complete fringe order can be determined from the colour of the fringe.

2.4 Optical Elements in Photoelasticity

A configured arrangement of optical elements is required to visualise the fringes generated in a photoelastic material. A polariscope is an instrument required to bring the two emerging light beams, which are out of phase due to stress in the photoelastic material, into the same plane to form visual photoelastic fringes. There are two type of basic polariscopes (plane and circular) depending upon the type of information to be visualised. A plane polariscope helps visualise both isoclinic fringes and isochromatic fringes and a circular polariscope eliminates the isoclinics and thus revealing only stress information. A polariscope has two main elements as described below.

2.4.1 Linear Polariser

The basic component of a polariscope is a linear polariser. Light beams from a common light source such as light bulbs or sun vibrate in all possible directions; a linear polariser filters it into beams that vibrate only in the direction of the axis of polariser. Two linear polarisers can be coupled together to form a plane polariscope.

2.4.2 Quarter Wave Plate

A quarter-wave plate is a form of retarder of known thickness that splits the incident linearly polarised light into two beams. It provides the incident beam a quarter shift in wavelength on emergence, thus converts a linearly polarised light into a circularly polarised light. Quarter-wave plates have two axes, slow and fast, with different refractive indices that accomplishes the quarter shift (Edmund Optics 2004). Insertion of quarter-wave plates to a plane polariscope alters the configuration to a circular polariscope.

2.4.3 Plane Polariscope Configuration

A Plane polariscope arrangement is made by using two linear polarisers kept crossed to each other. Plane polariscope is the simplest configuration that shows the stress information. Figure 2.3(a) shows a schematic setup for a plane polariscope and Figure 2.3(b) shows the fringe patterns generated for a circular disc under diametral compression. Equation (2.4) represents the intensity relation for a plane polariscope configuration.

$$I_p = I_a \sin^2 2\theta \sin^2 \frac{\delta}{2} \tag{2.4}$$

Where, I_p is the output intensity, I_a is the input intensity, θ is the isoclinic angle and δ is the retardation at any point of interest.

Since the elements are kept crossed to each other the configuration is called dark-field setup. The photoelastic information generated has both isoclinic and isochromatic fringes as indicated in Figure 2.3(b). The fringe visualisation under monochromatic light is different from that under a white light (discussed in section 2.6.2).

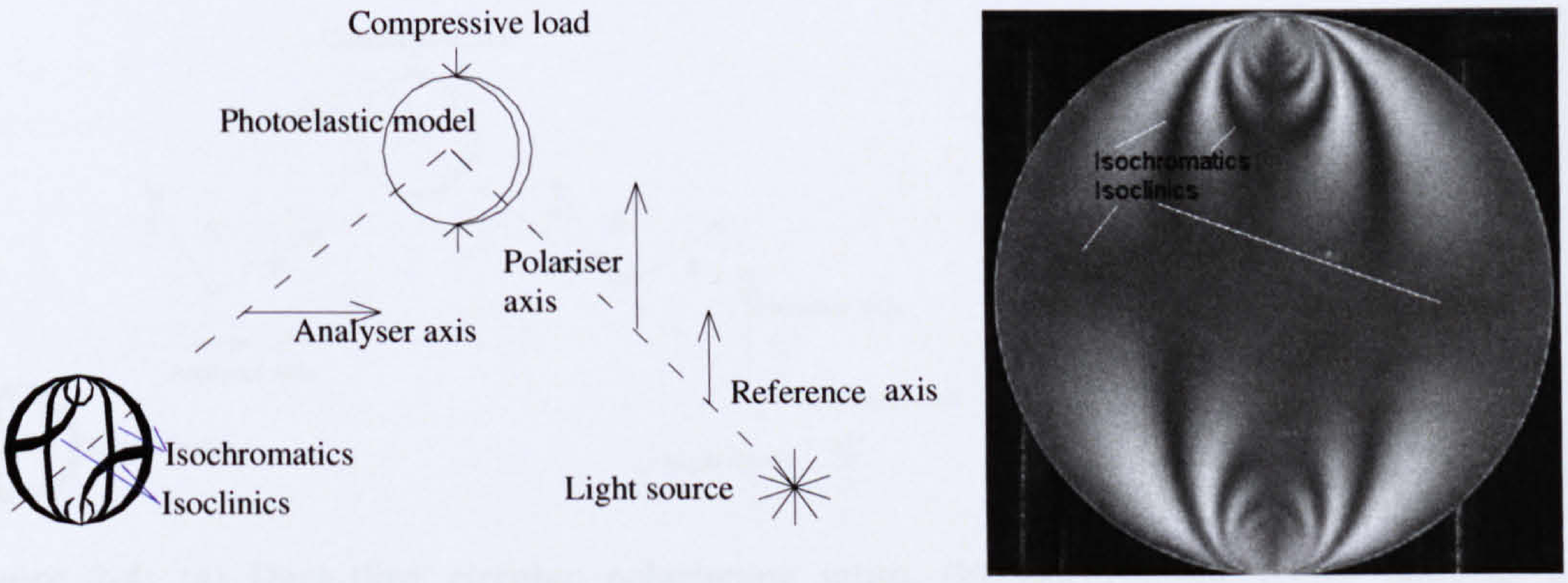

Figure 2-3: (a) Plane polariscope setup, (b) Fringe patterns generated with the setup under monochromatic light

2.4.4 Circular Polariscope Configuration

The fringe information from a plane polariscope has both isoclinic and isochromatic data overlapping each other. A Circular polariscope eliminates the isoclinic fringes using quarter wave plates and thus facilitates the stress analysis. There are different arrangements used for circular polariscope setup, the most commonly used has 1st quarter wave plates at 45^0 to the polariser and 2nd plate at 135^0 to reference polariser axis. The Equations (2.5) & (2.6) correspond to the intensity relation for a dark and a light field circular polariscope.

$$I_d = I_a \sin^2 \frac{\delta}{2} \tag{2.5}$$

$$I_l = I_a \cos^2 \frac{\delta}{2} \tag{2.6}$$

Where, I_d and I_l are the output intensities for a dark and light field configuration, I_a is the input intensity and δ is the retardation at the point of interest.

Figure 2.4(a) shows the schematic setup for a dark-field circular polariscope and Figure 2.4(b) shows the fringes generated from the corresponding circular polariscope setup with designated fringe orders.

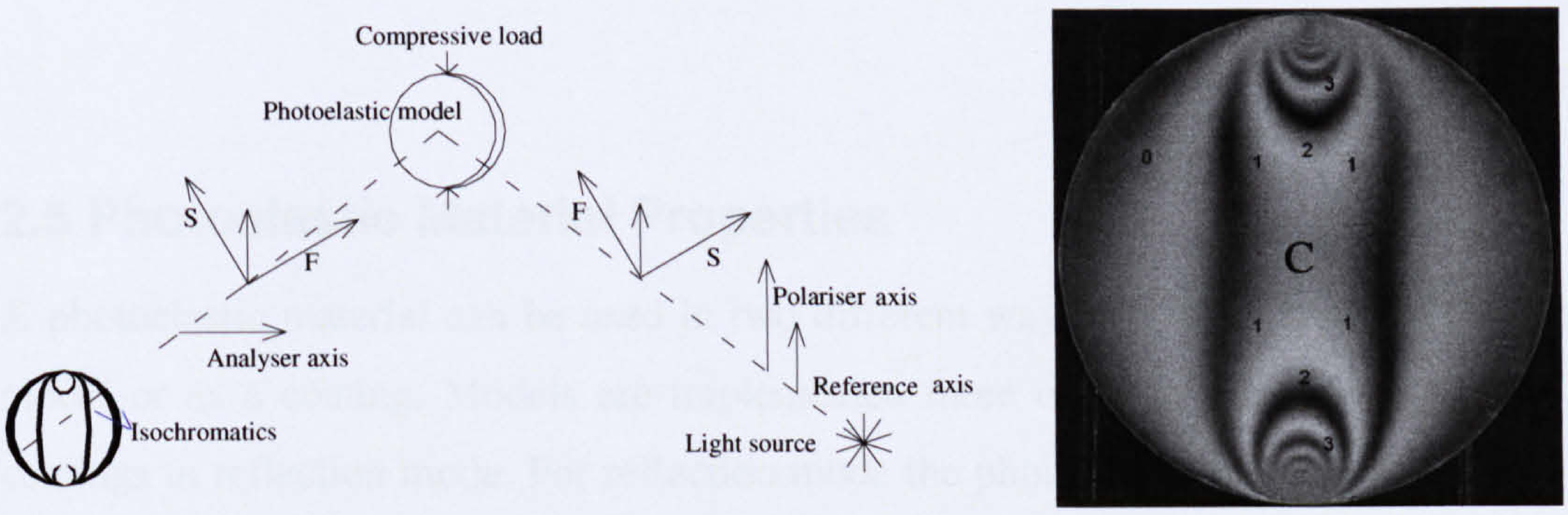

Figure 2-4: (a) Dark-filed circular polariscope setup, (b) Isochromatic fringe patterns under monochromatic light

2.4.5 Determining Complete Fringe Order

The basic configuration of a plane or circular polariscope only reveals integral fringe orders (0, 1, 2…) corresponding to points with direction of stress coinciding with the axes of polariser and analyser. In order to determine the complete fringe order at other points; several rotations of optical elements are required. Tardy's compensation is one of the techniques for determining the complete fringe order in point based analysis (Ramesh

2000). For instance, to determine complete fringe order at point ‘C’ in Figure 2.4(b), the first step would be to align the polariscope so that principle stress direction at the point of interest coincide with the axis of polariscope, for this a plane polariscope configuration is set and both polariser and analyser are rotated together until an isoclinic fringe passes through the point of interest. The second step involves the rotation of analyser alone to move an integral fringe order towards the point of interest and the direction of rotation determines whether a higher or a lower fringe order moves. Finally, by measuring the angle of rotation and its direction complete fringe order, *N* at the point of interest is calculated by using Equation 2.7.

$$N = n \pm r \tag{2.7}$$

Where, N is the fringe order at the point of interest, n is the moving integral fringe order, r is the fractional fringe order determined by the angle of rotation ($r = \alpha / 180$); α is the angle of rotation.

2.5 Photoelastic Material Properties

A photoelastic material can be used in two different ways for stress analysis either as a model or as a coating. Models are implemented more often in transmission mode and coatings in reflection mode. For reflection mode the photoelastic material is glued to the test part and the strain is transferred from the test part to the coating. A configured polariscope is used for visualisation and analysis. The type of coating material used is application dependent and some of the parameters that affect the selection of the coating are discussed below.

2.5.1 Strain Optic Co-efficient

Strain optic coefficient is an optical property of photoelastic materials and represents the sensitivity of the material to strain. It is designated by the letter K and is a dimensionless quantity. The value of K needs to be recalibrated for the type of photoelastic material used in a set of experiments (Chapter 3section 3.3.1). The strain optic coefficient is assumed to be independent of the wavelength of light source used. Higher the value of K, more sensitive the material is and thus less strain is required to induce fringe patterns.

2.5.2 Modulus of Elasticity

The sensitivity of photoelastic materials (K) to the applied strain is found directly proportional to its modulus of elasticity (E) i.e. as the sensitivity increases so does the modulus of elasticity. Thus materials with higher modulus of elasticity require less amount of strain to induce fringe patterns. However, for high modulus materials the amount of force required to induce the strain will also be high. The above factors may limit photoelastic applications, for instance, applications where a photoelastic material with low modulus and high sensitivity is required.

2.5.3 Thickness of Material

The thickness (t) of photoelastic material is another important parameter since increase in thickness increases the sensitivity of coating. On the other hand, when photoelastic material is used as a model, the fringe response is independent of the thickness. The thickness, however, will affect the sensitivity of photoelastic models that are used as sensing medium and load unconventionally.

2.6 Light Sources in Photoelasticity

The type of light source used in photoelastic experiments depends on the application and the accuracy required and can range from a monochromatic to a custom made RGB light source (Yoneyama et al. 1998; Umezaki and Kodama 2000). This section explains two commonly used light sources in digital photoelasticity.

2.6.1 Monochromatic Light Source

A Monochromatic light refers to the light specific to a particular wavelength. The fringe patterns generated always appears in greyscale under monochromatic light. The most commonly adopted monochromatic light source in photoelasticity is a low pressure sodium vapour lamp (also called SOX). An SOX emits a constant yellow light at a wavelength (λ) of 589 nm with a high intensity. This type of light source is used for both point based techniques as well as phase shifting for whole-field analysis. Figure 2.5(a) & 2.5(b) shows the images of a disc under diametral compression obtained using a custom made LED (yellow-589 nm) light source used in this research (Chapter 3 section 3.4).

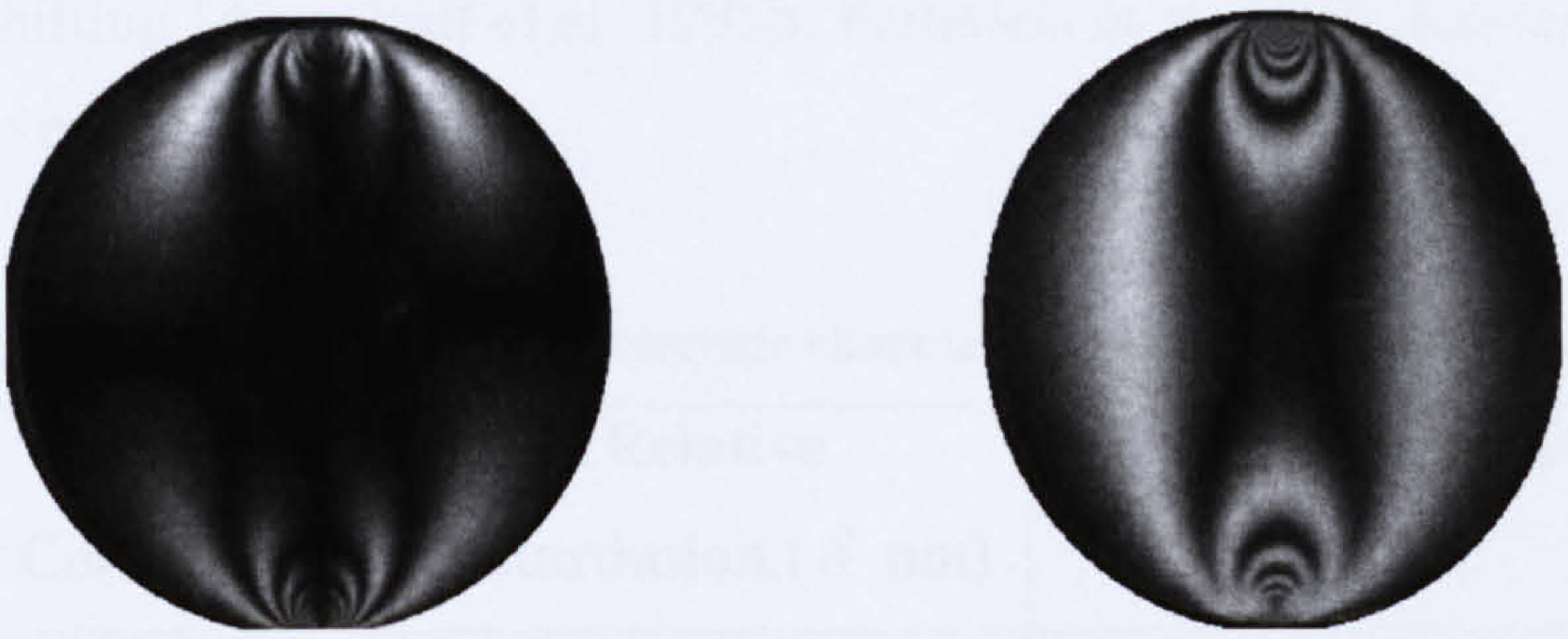

Figure 2-5: Disc under diametral compression (a) Plane, (b) Circular polariscope with specifically designed LED light source (λ=589)

Monochromatic light sources provided high quality images and are also ideal for comparison purposes as they serve as a reference light source. The cost of using a monochromatic light source like SOX is high and the setup tends to be bulky. With the advent of modern technology and better image acquisition systems, white light sources are widely used in photoelasticity due to the economical reasons and portability.

2.6.2 White Light Source

A White light source is the most inexpensive form of light source that can be used in photoelasticity. It has been used both in calibration based techniques (Ajovalasit et al 1995a; Ramesh 2000; Quiroga et al. 2002a) and phase-shifting (Patterson and Wang 1998; Ramesh 2000; Hobbs et al. 2003; Lesniak 2004).

While using white light the isochromatic fringe patterns will appear coloured except for the zero fringe order (no stress), which is black, this facilities quick manual analysis. The coloured representation of stress fields led to the advent of Look up Table (LUT) based photoelastic techniques like Three Fringe Photoelasticity. The Table 2-1 provides a part of isochromatic characteristic (colour code) till fringe order 2 under a white light (Zandman et al. 1997; Ramesh 2000). The visualisation of colours may vary with different white light sources but the basic sequence of colour remains the same under any white light. The use of white light in photoelastic research has extensively been reported (Gotoh et al. 1996; Quiroga and Botella 2001; Quiroga et al. 2002a) including techniques like three fringe photoelasticity (Ajovalasit et al. 1995a; Ramesh and Deshmukh 1996) and in phase shifting (Ajovalasit et al. 1995b; Patterson et al. 1996; Ramesh and Mangal 1997; Acquisto et al. 2002).

Table 2-1: Isochromatic characteristic chart using compact fluorescent light

Colour	Relative Retardation (δ nm)	Fringe order (N)
Black	0	0
Grey	160	0.28
White	260	0.45
Pale Yellow	350	0.60
Orange	460	0.79
Dull Red	520	0.90
Purple	577	1.0
Deep Blue	620	1.06
Blue Green	700	1.20
Green Yellow	800	1.38
Orange	940	1.62
Red	1050	1.81
Purple	1150	2

The fringe order values tabulated against the colour in Table 2-1 can be compared to the sequence of colours in the disc model in Figure 2.6, illuminated by a compact fluorescent tube. The optical elements (polarisers, quarter wave plates) were placed directly in front of light source and camera as experiment must be carried out using polarised light to visualise the fringes.

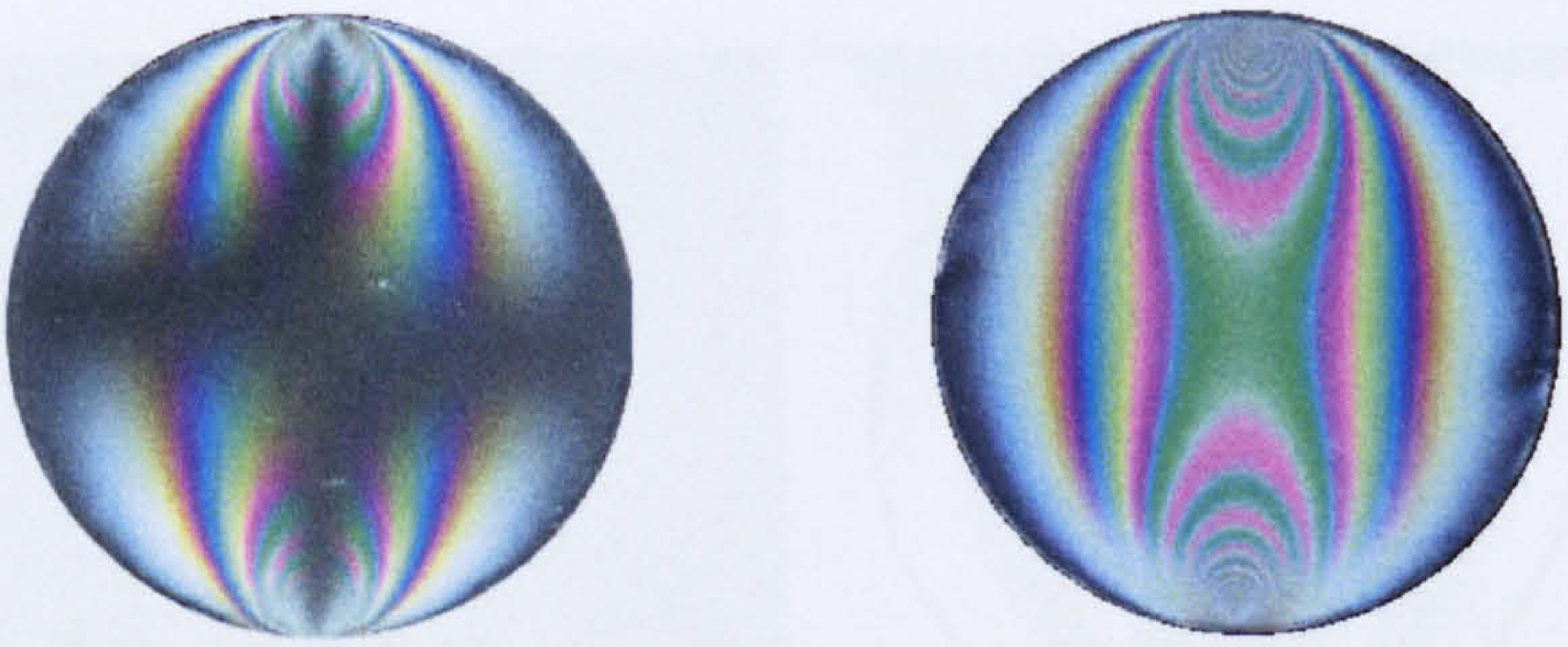

Figure 2-6: Disc under diametral compression (a) fringes with a plane polariscope, (b) fringes with a circular polariscope

White light sources with a high spectral response not only provide better LUTs but also high quality images for phase wrapping and unwrapping used in phase shifting (Ng et al. 2003).

2.7 Image Acquisition Systems

The image acquisition system is one of the main components of digital photoelasticity, as any analysis or computation can only be done after an image has been acquired. The imaging systems range from greyscale cameras to high end RGB cameras. This section describes some of the conventional imaging devices and their advantages and disadvantages.

2.7.1 Greyscale Imaging

The image acquired from a monochromatic light source provides integral fringe orders (0, 1, 2...) and can be used both for a point based analysis or phase shifting. Figure 2.7 shows an image acquired using a greyscale camera with the model illuminated using a polarised monochromatic light source.

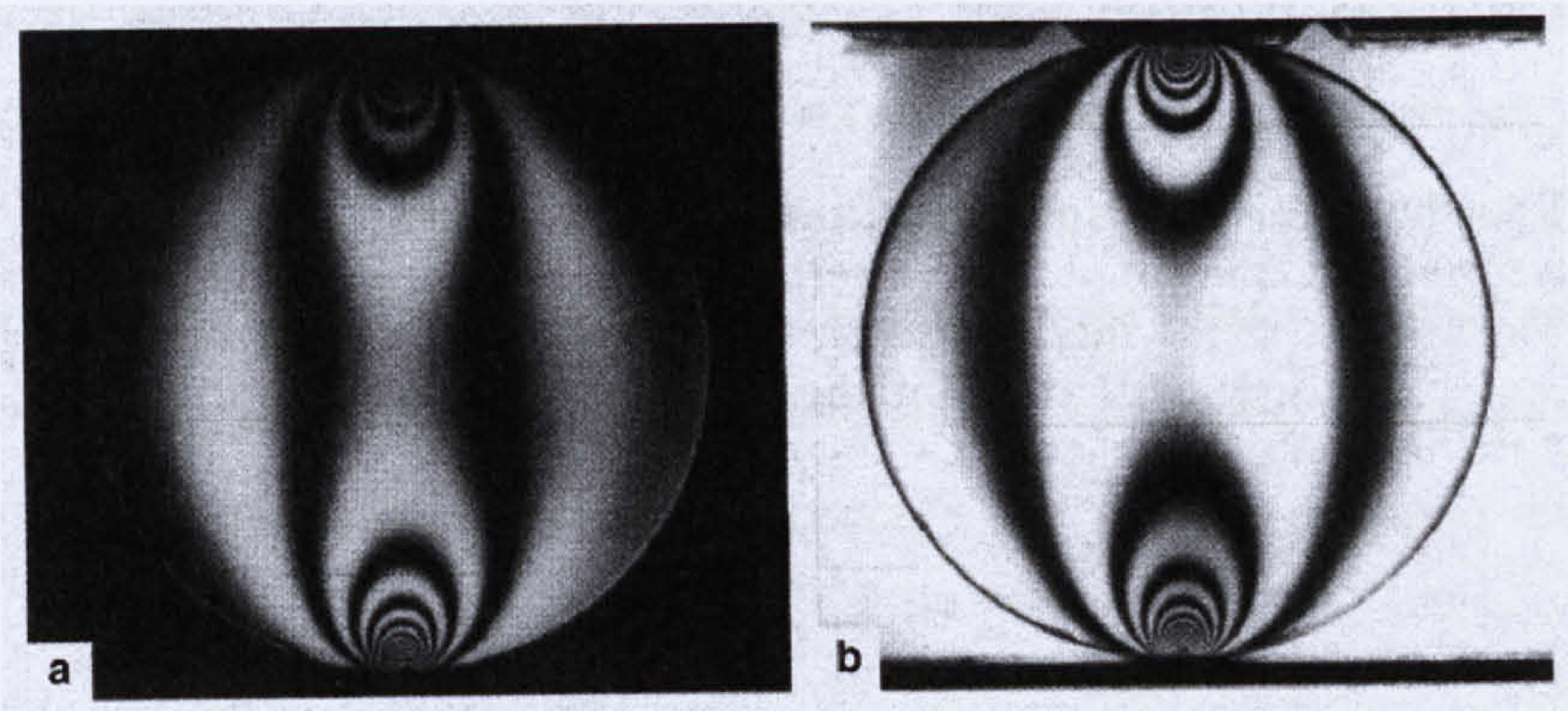

Figure 2-7: (a) Dark field and (b) Bright field images of disc under diametral compression acquired using greyscale camera under monochromatic light source (Ramesh 2000)

A greyscale camera needs to be coupled with a frame grabber to display the image for further analysis on a computer. The image from a monochromatic light and a greyscale camera cannot be used for colour coding (LUT) technique.

2.7.2 RGB Imaging

An RGB camera refers to a computer controlled CCD chip integrated camera with an RGB image output with in-built colour filters. The image resolution of a CCD chip can range from 1 to 11 Mega pixels or even higher as the technology develops thus providing a finer spatial resolution. However, higher the resolution more expensive is the camera. Low cost commercial camcorders can be an alternative to RGB cameras, as used in three fringe photoelasticity (Ramesh and Deshmukh 1996). Digital camcorders can provide up to 1M resolution with 30 frames per second. The images acquired in Figure 2.6 were acquired using a commercial digital camera (SP 500, Olympus). Use of commercial digital cameras and camcorders for look up table (LUT) based calibration in photoelasticity is limited due to the difficulty of maintaining camera settings (zoom, aperture, shutter speed) during calibration and analysis. However, by using a camera control package, full control over digital cameras can be achieved and thus overcome the above limitations with by product of higher resolution.

It is worth mentioning that the individual image planes of an image acquired using RGB camera can be approximated as filtered images from different monochromatic light sources (Ramesh 2000; Ng et al. 2003). However, most of the literature has emphasised on using only the Green plane image due to better contrast compared to Red or Blue plane. Figure 2.8 shows an RGB image with isolated image planes of R, G and B from a white light. The quality of individual planes is low compared to an image from a monochromatic light but at the cost of accuracy the system becomes efficient and portable.

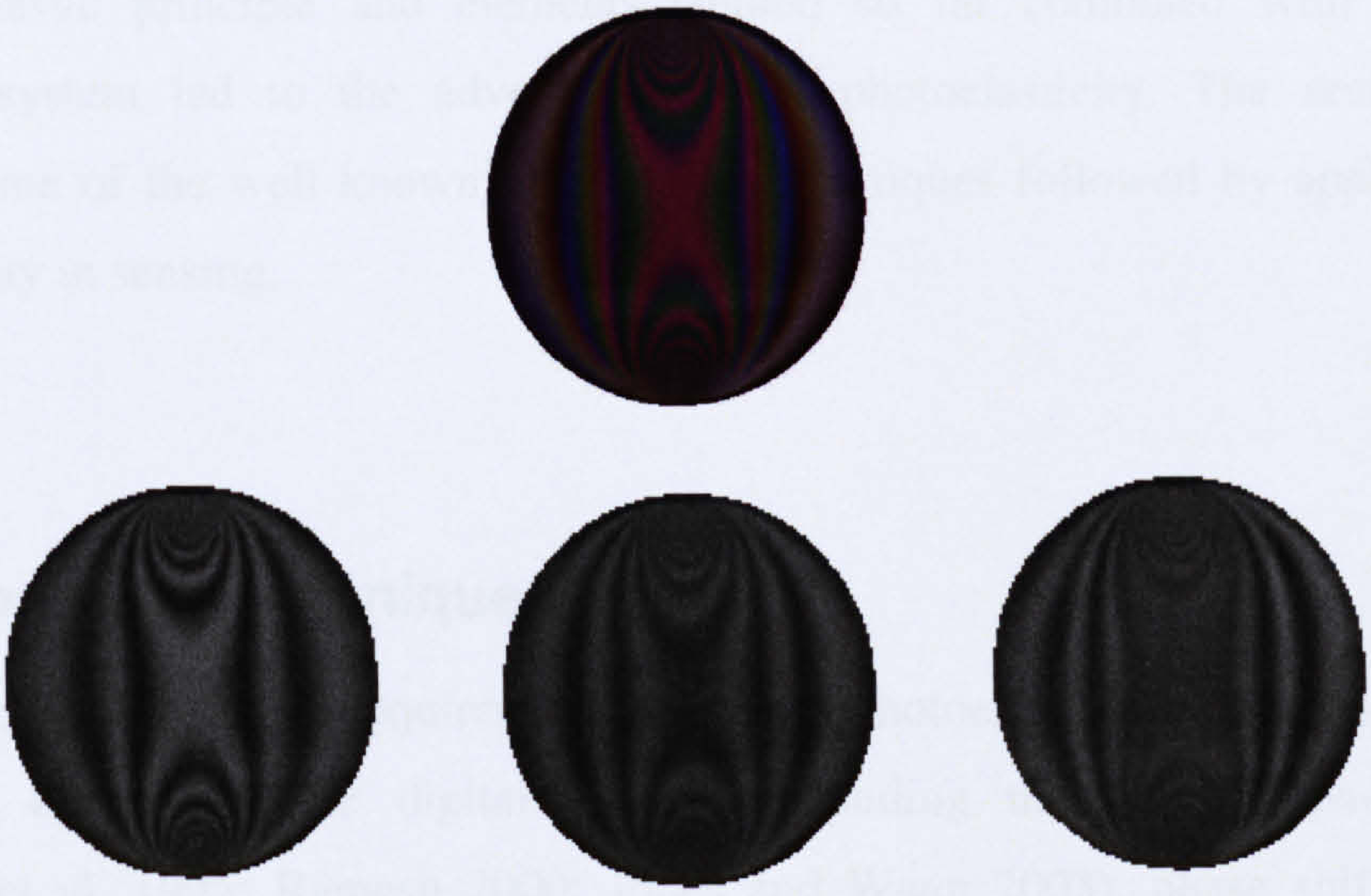

Figure 2-8: An RGB photoelastic image with isolated R, G and B planes for individual image plane comparison in terms of spectral response

The determined wavelength of Green plane (551.9 nm) was found to be closest to the ideal wavelength of green (546.1 nm) (Gonzalez and Woods 1993) which is another reason for using green plane image for analysis in phase shifting. The Red (598.1 nm against ideal 700 nm) and Blue (445.7 nm against ideal 435.8 nm) plane wavelengths

(Ramesh and Deshmukh 1997; Ramesh and Mangal 1997; Ramesh 2000) are relatively far from ideal. In evaluation of equivalent wavelength from R-G-B planes of the image, the type of CCD camera and the light source used play an important role, as colour response is dependent on the emitted light and camera filters.

In this research two different image acquisition systems were used; a commercial digital camera (SP500, Olympus) and a scanner based system, described in Chapter 3. In the imaging system based on a commercial digital camera, it was found that the Red plane image had a higher spectral response and thus would generate higher quality phasemap during phase shifting. And since spectral response of the light source is also responsible for the quality of individual image planes, Red plane wavelength was determined for this research experiments (Chapter 3 Section 3.3.2). The closest match to ideal wavelength should not matter as the determined wavelength of image plane is used for calculations.

The photoelastic principle and elements studied so far combined with the image acquisition system led to the advent of digital photoelasticity. The section below discusses some of the well known photoelastic techniques followed by applications of photoelasticity in sensing.

2.8 Photoelastic Techniques

Digital imaging is the basic requirement in modern photoelastic experiments and all the photoelastic techniques use digital imaging including three fringe photoelasticity (Ajovalasit et al. 1995; Ramesh 2000; Jones and Wang 2003), phase shifting, multi-wavelength techniques (Hu 1999; Chen et al. 2001). These techniques can be categorised by the number of images required for analysis.

Single image analysis technique use only one image and manipulates data from all the three image planes i.e. Red, Green and Blue. As this requires only one image, the processing is much faster and makes the analysis dynamic in nature. Some of the techniques using single image are discussed below.

2.8.1 Look Up Table Based Technique

The isochromatic characteristic table presented in section 2.6.2 is a way of qualitatively analysing coloured photoelastic fringes. In order to derive qualitative information (stress) from the colours it is important to record the colour information in detail. A systematic calibration is required in order to record the colour information against a unique fringe order to form a LUT. The technique was developed by Ajovalasit (1995a) and is also known as three fringe photoelasticity (TFP). The colours tend to merge beyond fringe order 3 with conventional white light, thus limiting the technique to a maximum of third fringe order. However, the technique is simple in providing isochromatic information of complete fringe order, N upto to 3. TFP exploits the fact of colour sequence to generate a LUT with colour information against fringe order. During analysis the RGB triplet value of a test point is compared to the LUT values and fringe order is determined to perform stress analysis using Equations 2.1 to 2.3.

A number of modification and improvements have been added to the technique (Ajovalasit et al. 1995a; Yoneyama and Takashi 1998; Ramesh 2000; Quiroga and Botella 2001) over the period of time. A detailed description of the techniques is presented here.

2.8.1.1 Calibration Procedure

The calibration procedure involves subjecting a beam of known dimensions to four point bending load. The four point bending load generates uniform stress patterns in the mid section of the beam along the x-axis and a linear variation of stress along the y-axis of the model. The model is illuminated with a white light and visualised under a circular polariscope configuration. Following the general colour code from Table 2-1, appropriate bending load can be applied to induce just the fringe order required (for instance 1, 2 or 3...). Since the stress distribution is known along different axes and induced fringe order is known, an RGB image is acquired. Images are acquired under different bending loads to incorporate different fringe orders and to account for the variation in fringe gradient (Ramesh 2000).

RGB triplet data is extracted along axis of linear variation in fringe order and the process is repeated for 30-40 lines to average the results and remove any noise. The fringe order at each pixel is calculated following the linear relation from Equation 2.8.

$$N_i = N\frac{i}{n} \qquad (2.8)$$

Where, N is the fringe order induced, N_i is the fringe order required at the pixel of interest, i is the pixel number and n is the total number of pixels in the selected line.

The extracted RGB triplet values and the determined fringe orders are coupled to form a database or LUT that has colour information against fringe order. This LUT can then later be used for analysis of test images with unknown stress fields. Generally more than one LUT is prepared to account for different fringe gradients; 0-1 for low, 0-2 for medium and 0-3 for high fringe gradient.

The above procedure may vary depending on the accuracy of results and the processing of images required, however, the basic procedure and the data extraction remains the same. The procedure followed in this research is explained in Chapter 4 section 4.2.1. However, there are two important factors that may affect the measurement accuracy for LUT based technique; the geometric and chromatic parameters (Quiroga and Botella 2001). The geometric parameters include the camera aperture and distance between the model and the camera. The camera aperture determines the amount of light falling on the CCD which can cause a variation in the colour information. The varying distance between the camera and the model affects the intensity of the light falling on the model. The chromatic parameters include the thickness of model, the RGB response of camera filters and the emission spectrum of light source. The chromatic parameters are hard to control as they are linked to the hardware, thus it is advised to focus on controlling the geometric parameters and compensate wherever possible.

2.8.1.2 Analysis of Test Images

The final LUT is prepared which can be used for analysing the test images. During the analysis, it is possible that the RGB triplet value of the point under consideration may not be available in the database. To account for this, a search is carried out to find the closest match of RGB triplet using the least square method using Equation 2.9.

$$e=(R_s-R_m)^2+(G_s-G_m)^2+(B_s-B_m)^2 \qquad (2.9)$$

Where, e is the error, $(RGB)_m$ are the measured RGB triplet values at the test point and $(RGB)_s$ are the stored RGB triplet values in the LUT.

The triplet value with minimum error is selected and corresponding fringe order is assigned, which can be used to find the stress difference. The technique has been implemented and modified by many researchers (Ajovalasit et al. 1995a; Ajovalasit et al. 1995b). The circular polariscope setup implemented in this technique uses quarter wave plates that are designed for a specific wavelength only. Such plates are efficient for stress analysis using monochromatic light source, but they introduce errors with white light. Since white light is composed of a wide range of wavelengths, use of conventional quarter wave plate is incapable of introducing a 'quarter shift' to all the wavelengths, thus introducing errors in calculations. Ajovalasit accounted for quarter plate error and suggested that calibration be carried out at isoclinics of 22.5^0 in dark field polariscope setup. Ramesh and Deshmukh (1996) accounted for fringe gradient by preparing 3 tables (0-1, 0-2 and 0-3 fringe order) instead of just one. In order to minimise the noise they used RGB triplet obtained from the difference of dark and light field in the image. Quiroga et al. (2002) modified the standard Euclidean cost function with an improved regularised algorithm, which had two terms one maintaining the minimum Euclidean distance and the other for piecewise continuity of isochromatics. The light source was replaced by a discrete fluorescent lamp giving an advantage of higher modulation of RGB signals over the conventional white light.

2.8.1.3 Factors Influencing the LUT

Besides the above mentioned issues there are some factors that influence the accuracy of a system based on the colour code calibration:

I. **Geometric Variations:** Research has shown that both the chromatic and geometric parameters influence the accuracy of technique (Quiroga and Botella 2001). The geometric parameters can, however, be controlled in the following way:

   a. *r,g,b:* Implementing *r,g,b* instead of *R,G,B* to account for the non-uniformity of the light illumination. The *r,g,b* are computed by normalising the RGB triplet values. Though they account for the geometric variations to some extent but generate erroneous results at low fringe orders due to noise amplification (Ajovalasit et al. 1995a; Ramesh 2000; Quiroga et al. 2002b).
   b. *Background subtraction:* The background subtraction can help in overcoming geometric variations of non-uniform illumination to some level. A base image under 'zero load' is subtracted from each image under analysis and also during the calibration procedure; although background subtraction may not be an ideal approach if the model deformation is high (Ramesh 2000).

II. **Resolution:** Since all the possible RGB triplet values against the fringe order cannot be obtained and stored in the database, the following points need to be considered during database creation:

   a. *Bit-depth:* Most digital cameras support only 8-bit (0-255) image acquisition per channel[1]. If the calibration database is built using a higher bit value like

---

[1] R, G and B channels

10-bits (0-1023) per image plane, the minimum error search can be improved as the resolution is much higher (Ramesh 2000).

b. *Image size:* Another approach is to calibrate at a higher pixel resolution (say 4 Mega pixel) and perform the analysis at a lower resolution (say 2 Mega pixel). Calibrating at 4 Mega pixels will include more values of RGB triplets and thus minimising the errors.

c. *Calibration database:* Building more than one calibration database will account for not only the resolution issue but also for the varying fringe gradient. It is also important to note that the calibration is performed on a linear fringe variation but in many cases the test specimen will have non-linear stress distribution and a different fringe gradient. Therefore, more than one calibration database is necessary.

d. *Dark and light field:* The calibration database can be built for both light field and dark field polariscope setup, thus further minimising the errors in the final results. But this approach makes the system less dynamic in nature as it requires two images with different optical orientation (Ramesh 2000).

e. *Light intensity:* Selecting the appropriate light intensity is important for the quality of image acquired, but care must be taken to avoid saturation of RGB planes with too high intensity, so that the colour information is not lost (Ramesh 2000).

It is important to account for the above factors in order to build a robust and accurate calibration database. Care must also be taken for the camera setting which includes appropriate zoom, focus and the aperture. The whole procedure is rather complex and needs a controlled environment. The technique is limited to a maximum of third fringe order with a conventional white light source due to low contrast at higher fringe orders (Ramesh 2000; Quiroga et al. 2002a; 2002b). The RGB signals tend to attenuate beyond the third fringe order, making it difficult to employ this technique but can be extended to higher fringe orders if a high spectral response light source is used and robust algorithms for fringe tracking (Quiroga et al. 2002a; 2002b) are implemented. A range of algorithms and techniques have been proposed and implemented to eliminate or reduce these errors;

normalised RGB values (Ajovalasit et al. 1998), subtraction of dark and bright field images (Ramesh and Deshmukh 1996; Ramesh 2000), B-spline curves for smoothing the results (Govindarajan 1997).

2.8.2 Tri-Colour Based Technique

The tricolour image techniques overcome the coloured based LUT drawbacks by implementing specifically designed light sources (Yoneyama et al. 1998; Umezaki and Kodama 2000). An approach was developed by Yoneyama et al. (1998) by treating all the three planes of coloured image as monochromatic images. A special light source was designed for this purpose by combining mercury light for blue and green and a halogen light for red. Interference filters and dichroic mirrors were used to achieve this and the intensity of each light source was controlled by using a neutral density filter depending upon the spectral response of the camera. Non-linear equations were developed for evaluation of isochromatic and isoclinic parameters and the validity of this technique was proven with the computer generated data and the experimental data. However, the technique failed to obtain isochromatic at points of isoclinic interactions and at points where R-G-B intensities tend to be equal. The setup was rather complex due to the involvement of two light sources, filters and the mirror arrangement.

2.8.3. Phase Shifting Technique

A large number of techniques use more than one image for higher accuracy and in order to extract both isochromatic and isoclinic data, hence are called *mulit-image techniques.* Even the colour code based calibration techniques have been reported to use two images, dark and bright field and combines the LUTs to achieve higher accuracy (Ramesh 2000). Phase shifting is the most promising multi-image technique providing both isoclinic and isochromatic information.

Phase-Shifting was introduced by Hecker and Morche in 1986 (Ramesh 2000) and is considered to be the most accurate technique for full field analysis. Patterson and others continued the work of Hecker and Morche and significantly contributed towards further development of this technique (Patterson and Wang 1991; Buckberry and Towers 1996; Patterson et al. 1996; Patterson and Wang 1998; Patterson 2002; Hobbs et al. 2003; Ajovalasit et al. 2007). Phase-shifting technique is based on acquisition of phase stepped images of photoelastic model at different orientation of the optical elements (Ramesh and Ganapathy 1996; Ramesh 2000). Figure 2.9 shows six phase stepped images obtained from a disc under diametral compression with 1st polariser and quarter wave plate at $\pi/4$ and $3\pi/4$ respectively and Table 2-2 listing the orientation of 2nd polariser and quarter wave plate. It is important to note that the configurations in the table show one of the many possible combinations of optical elements to obtain the phase stepped images.

Table 2-2: Optical arrangement for phase stepped images

Image	Second Quarter Wave Plate	Analyser
1	0	$\pi/4$
2	0	$3\pi/4$
3	0	0
4	$\pi/4$	$\pi/4$
5	$\pi/2$	$\pi/2$
6	$3\pi/4$	$3\pi/4$

Figure 2-9: Six phase stepped images for phase-shifting technique acquired in reflection mode for a disc under diametral compression

The intensity equations for these images are used for determination of isochromatics and isoclinics as given by Equations 2.10 and 2.11.

$$\theta = \frac{1}{2}\tan^{-1}\left(\frac{i_5 - i_3}{i_4 - i_6}\right) \tag{2.10}$$

$$\delta = \tan^{-1}\left(\frac{i_4 - i_6}{\cos 2\theta (i_1 - i_2)}\right) \tag{2.11}$$

Where, θ is the isoclinic value, δ is the retardation (isochromatic value) and i_n are the intensity representation of phase stepped images, n is an integer (1, 2… 6)

The results obtained from the Equations 2.10 and 2.11 have retardation in the range of $-\pi$ to π radians and the isoclinic in the range $-\pi/4$ to $\pi/4$ radians. For the results to be represented in form of an image, the value of isoclinics and isochromatics needs to be converted from radians to digital form (0-255) and also the ambiguity of +/- sign needs to be removed for the isochromatics. Figure 2.10 shows the isoclinics and isochromatics represented in form of an image.

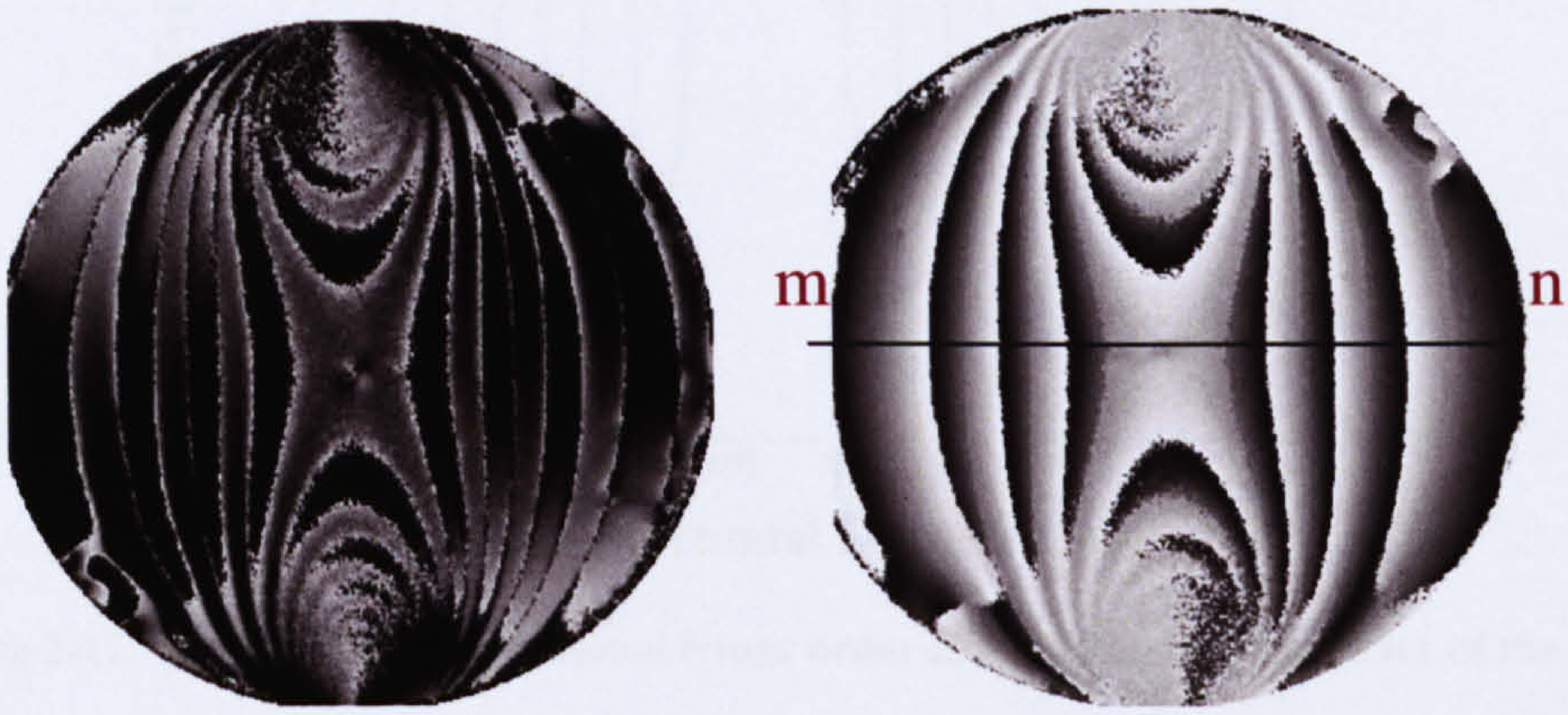

Figure 2-10: Phasemap (a) Isoclinics between $-\pi/4$ to $\pi/4$, (b) Isochromatic phasemap between 0 - π

Further algorithms (Asundi and Sajan 1997; Su et al. 1997; Asundi 1998; Kihara 2003) are required for phase unwrapping of the isochromatic data obtained.

As seen in Figure 2.10 the errors are prominent at the point of loading and would be difficult to unwrap. These errors can be suppressed to some extent by a precise loading mechanism. Some of the errors are unavoidable due to isoclinic-isochromatic interactions as isoclinics are indeterminate at the points where retardation is a multiple of λ. Isoclinic values also act as noise at the points where the retardation values are very close to 0, π, 2π and are multiples of π (Ramesh 2000). However, a multi-wavelength light source or step loading can be used to determine isoclinic values in the erroneous zones (Ramesh and Tamrakar 2000; Villa et al. 2004).

Figure 2.11 plots the fractional fringe order along the horizontal diameter 'm-n' of the disc, the fractional fringe order can be unwrapped to achieve the complete fringe order *N*. Adding fractional fringes order in Figure 2.11, the mid-point 'P' of the disc gives *N* to be 3.7.

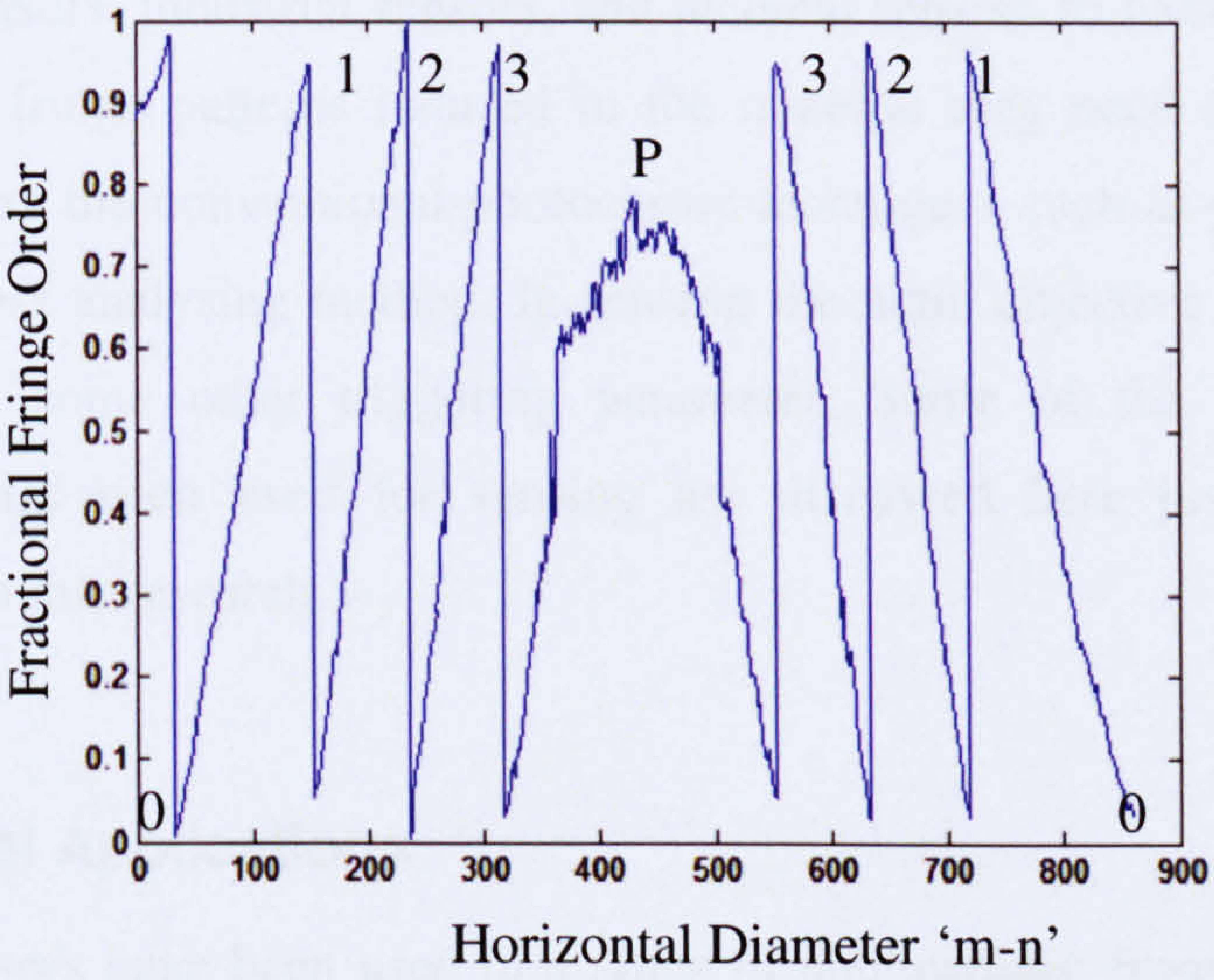

Figure 2-11: The determined fractional fringe order along horizontal diameter of the disc

The technique was initially limited to due static nature of the systems in collecting six images one by one, later a novel instrument was designed by Patterson and Wang (1998) for simultaneous acquisition of four phase-stepped images using four digital cameras. Using this setup dynamic operation of the whole process was possible, however, one major disadvantage was that the setup was bulky. A modification to this design was mde (Hobbs et al. 2003) using a beam-splitter to create four images on the same CCD chip.

Further improvements were made and a new instrument was developed which is commercially available as pelidoscope (Lesniak et al. 2004) that uses a simple convex lens split into four and glued back with a small gap between the four pieces. Thus each part of lens acted as a separate imaging element and different optical arrangement of polariser and quarter wave plate were set for each part. The instrument was capable of focusing four phase stepped images on a single CCD.

2.9 Application of Photoelasticity in Sensing

Perception of something and its translation into meaningful results is defined as sensing, since a photoelastic material when stressed causes an optical retardation, this property of material has been used in many sensing applications. Applications include robotic grippers, slip sensors, industrial sensors, and medical sensors to name a few. In sensing applications the fringe patterns induced in the material may need to be analysed in a different way than the conventional photoelastic techniques such as phase-shifting, TFP or any other stress analysing method. In sensing the main objective is determination of applied load or some other triggering parameter. Some of the applications where photoelasticity has been used for sensing are discussed here justifying the use of photoelasticity in this research.

2.9.1 Industrial Applications

Photoelastic sensors have been used in a range of applications, from robotic grippers to bending load and torque sensors (Hopkins et al. 1991; Saad et al. 1994; Chung 1998; Eghtedari and Morgan 1998; Noroozi et al. 2003). Some sensors based on photoelastic effect have been developed for robotic applications to complement the sensing deficit. Industrial robots require sensory information to undertake intelligent decisions regarding the manipulation of the objects in an industrial environment to be adaptable. This information is delivered by an array of sensors on the robot gripper providing information on slip, temperature, force or some other stimulating parameters. Due to the high resolution and quick response photoelastic materials have been used as slip sensing devices, although the techniques used may varied in terms of analysing the photoelastic outputs; visual (Eghtedari and Morgan 1998; Hopkins et al. 1991), signal (Dubey and Crowder 2006). The visual techniques used image subtraction algorithms between successive images and a threshold to detect slip. The value of threshold is important, if set too low, it may amplify the noise and if set too high, small slip may not be detected. The same principle of threshold is applied to manipulate the signals for slip and force detection. On a signal based sensors a wide range of techniques have been implemented to achieve discernable slip detection for preventive measures to avoid the slipping or falling of an object. However, due to the lack of analytical relationship between the force and the fringes and complications involved due to the slip causing shearing effect, most of the research has been limited to numerical analysis and signal processing techniques. Compared to other slip sensors, photoelasticity based sensors can provide both visual and signal output for slip and force, making it a more viable tool for robotic applications. Studies have also been conducted to investigate mechanical and optical properties of the material (Eghtedari et al. 1993; Cameron et al. 1998) for optimal design of the sensor.

2.9.2 Biomedical Applications

An early attempt to discover the potential of photoelastic materials for screening diabetic foot in force determination was by Arcan and Brull (1976) as shown in Figure 2.12. The proposed technique used independent hemispherical-end shaped plungers to load the photoelastic material through foot. The induced fringe patterns appeared as concentric circles in greyscale as working with monochromatic light source. Prior calibration was required for the diameter of fringe against the applied load. The range and sensitivity of the device was dependent on the material's optical and mechanical properties and plunger head diameter. Due to the setup and loading constraints, only vertical load could be determined.

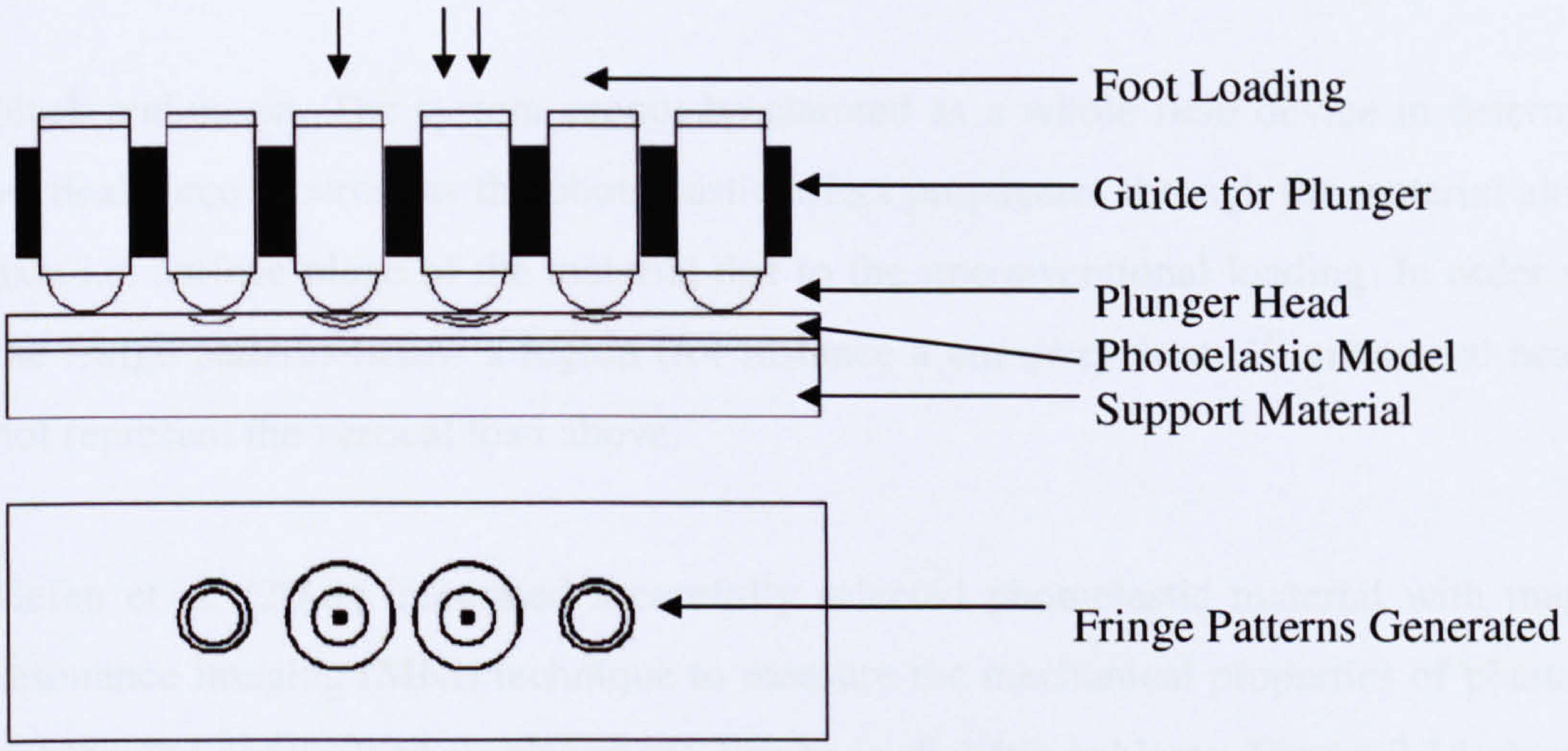

Figure 2-12: Photoelasticity based vertical load measurement technique by Arcan and Brull (1976)

An alternative was later developed by Rhodes et al. (1988) for whole field view of vertical force using 2.8 mm thick photoelastic material glued to a plexiglass, loaded by the foot through a grooved mat. The grooved mat provided an intervention to introduce discontinuities in x-y plane loading. Figure 2.13 shows the fringe patterns induced during the foot loading in the system. The system was calibrated with intensity against the load, black colour for zero load and white for maximum load. The system was limited to determination of vertical force and had a small dynamic range.

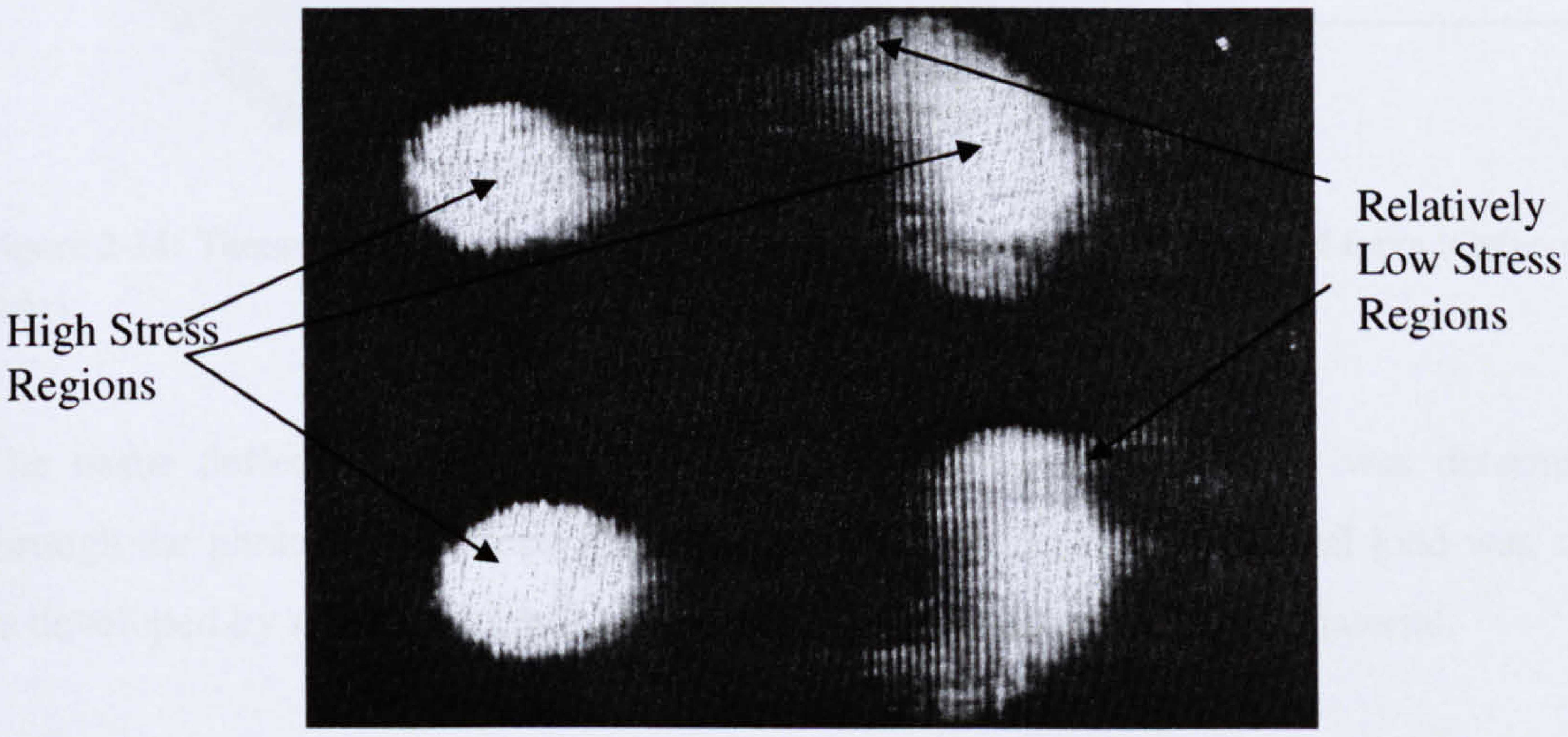

Figure 2-13: Photoelasticity based vertical load measurement technique by Rhodes et al. (1988)

However, only one cycle of colour gradient i.e. black-white can be used in this technique due to repetitive nature of fringes as colour swings from black to white and again back to black and so on. The system cannot be claimed as a whole field device in determining vertical force or stress as the photoelastic effect propagates through the material along x-axis i.e. surface plane of the material due to the unconventional loading. In order words the fringe patterns below a region (for instance a cm away from 1st metatarsal head) do not represent the vertical load above.

Gefen et al. (2001) integrated a carefully selected photoelastic material with magnetic resonance imaging (MRI) technique to measure the mechanical properties of plantar soft tissues and obtain load-displacement curves in diabetic subjects. Figure 2.14 shows the schematic representation of the implemented method. The measurements and foot loading was in supine state.

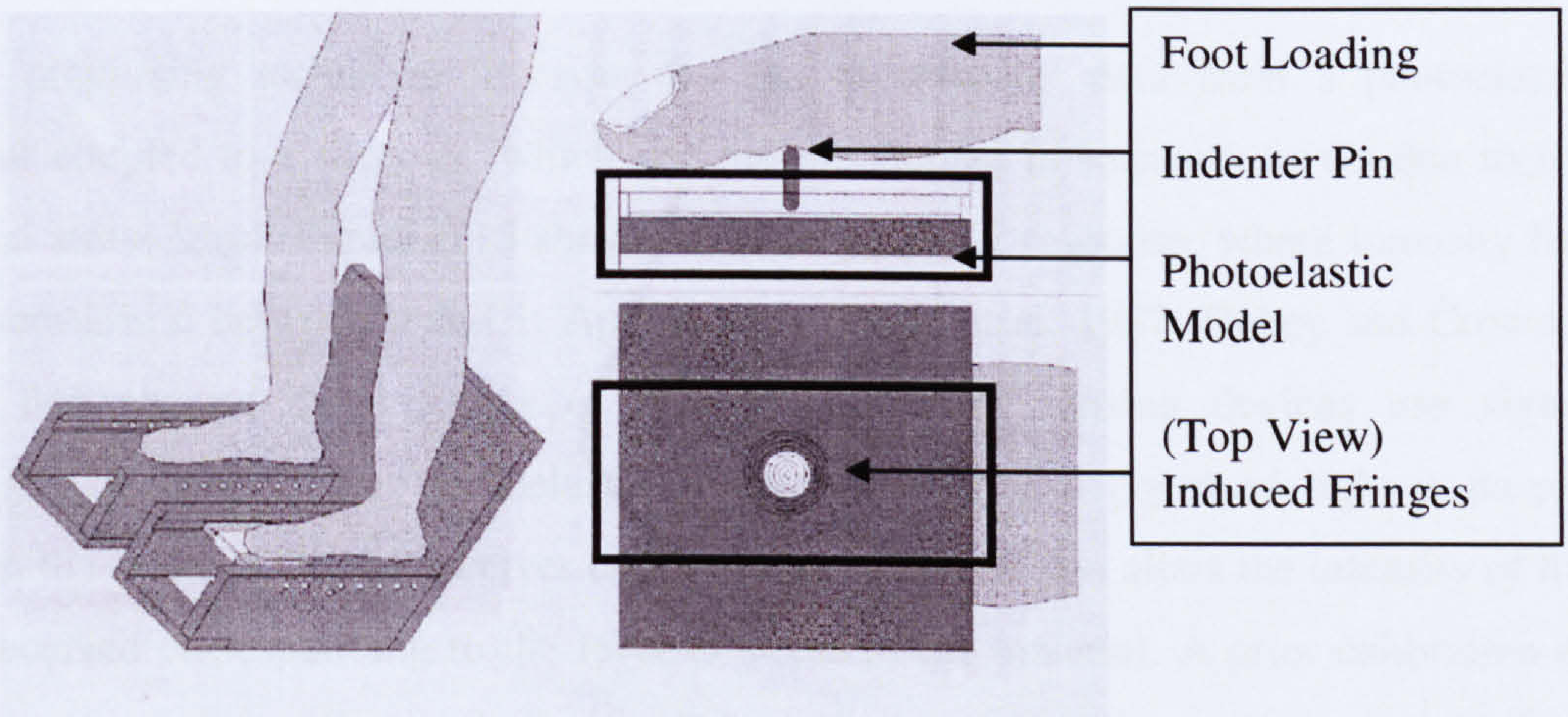

Figure 2-14: Tissue stiffness measurement integrated with photoelastic sensing of force (Gefen et al. 2001)

The tissue deflection was measured through MRI scan and the load was determined through the photoelastic effect. The principle for determining the vertical load was same as developed by Arcan and Brull (1976) through the indentation of the material.

Besides applications in the assessment of the diabetic foot, photoelastic materials have also been used for biomedical sensing including development of a fibre optic catheter-tip

(Dario et al. 1987). The following section describes the techniques employed to analyse photoelastic fringe information for the above applications.

2.9.3 Analysis of Photoelastic Information

For sensing applications the photoelastic fringes are analysed mostly through non-conventional photoelastic techniques to extract the relevant information. The technique used for analysis is application dependent. The following section describes the three most commonly employed techniques to analyse the photoelastic data with their relative advantages and disadvantages.

2.9.3.1 Signal Processing

Signal processing technique involves the use of intensity data from a photoelastic material coupled to a receiver, which records the change in intensity levels due to the material stress level. Figure 2.15 shows an ideal intensity response, where intensity has been normalised between 0 and 1. Applications (Dario et al. 1987; Dubey and Crowder 2006) that require development of low cost compact sensing devices use signal processing technique. The photoelastic model is loaded and polarised light is passed through the material. At the receiver end it has a phase shift that alters the intensity of the light received corresponding to the level of stress in the material. A prior calibration of change in intensity against a desired parameter (voltage) is used to determine the load value. The setup requirements are light source, receiver, model, polariser and signal filtering (amplification in some cases). In an attempt to achieve continuous signals during slip Dubey and Crowder (2006) found that placing a metallic strip on the front contact surface of the model induced vibrations between the two contacting surfaces. The sensors incorporating signal processing techniques are low cost but limited to a low dynamic range due to sinusoidal nature of the intensity curve (Figure 2.15).

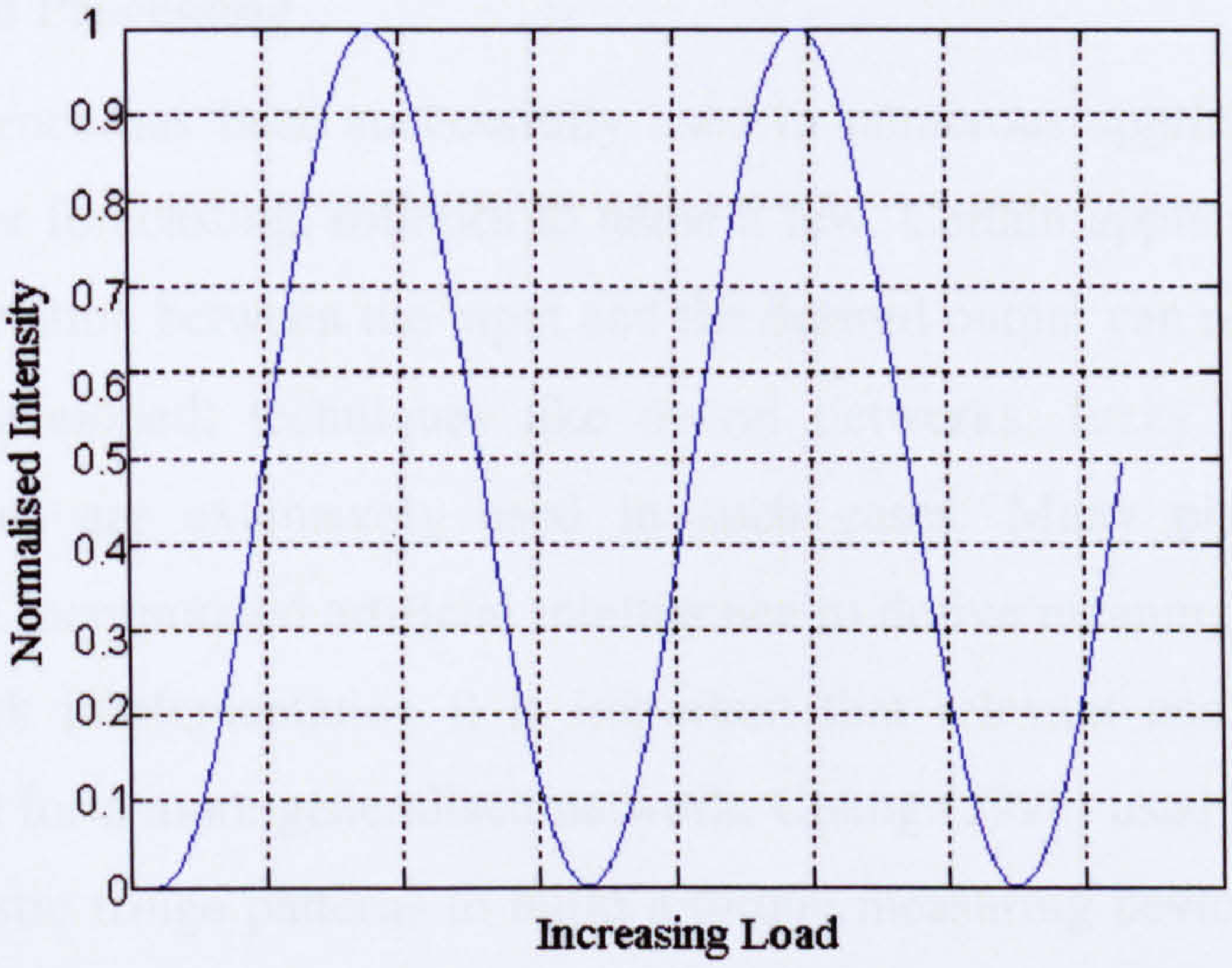

Figure 2-15: An ideal intensity variation in photoelastic model with increasing load

Gradual tracking of the sinusoidal curve is required from zero load onwards to increase the load measuring range of sensor. The technique is simple yet efficient and sensitivity can be controlled by choosing a photoelastic material with appropriate mechanical and optical properties.

2.9.3.2 Image Processing

Acquiring images of fringe patterns can reveal more information than mere one-dimensional signals. As in some applications signal information may not be adequate and visual patterns are required, for instance robot grippers (Eghtedari and Morgan 1998; Hopkins et al. 1991; Eghtedari et al. 1993) intending to determine the position and the slip of object, medical applications (Arcan and Brull 1976; Rhodes et al. 1988; Gefen et al. 2001) where pressure prints are useful. The measurable range of sensor will still be limited if only one gradient cycle of black-white intensity is used; for instance by Rhodes (1988). However, using coloured fringe patterns would increase the measurement range as sinusoidal nature of intensity curve is no longer an issue. The technique does require more computational power and analysing as the fringes can be complicated but using images could yield higher accuracy and wider range than greyscale analysis.

2.9.3.3 Intelligent Processing

Artificial intelligence has been successfully used in numerous applications of medical, industrial, weather forecasting, robotics to name a few. Certain applications where there is no analytical relation between the input and the desired output can require a non-linear relation to be developed; techniques like neural networks, fuzzy logic, neurofuzzy, genetic algorithms are extensively used in such cases. Many photoelastic sensing applications have incorporated artificial intelligence to derive meaningful results. In case of neural network implementation it is important that relevant and sufficient data is extracted and fed for a more generalised network. Chung (1998) used neural networks to analyse photoelastic fringe patterns to build a torque measuring device. An RGB image was acquired and intensity data from a section was used to train and test the neural network. Figure 2.16 shows the different intensity profiles (input) used to train the network. Since the data from fringe patterns can be significantly more than required, only a relevant section of image was used. The input dimensionality ranged from 32-96, which could have been avoided using Principal Component Analysis (PCA).

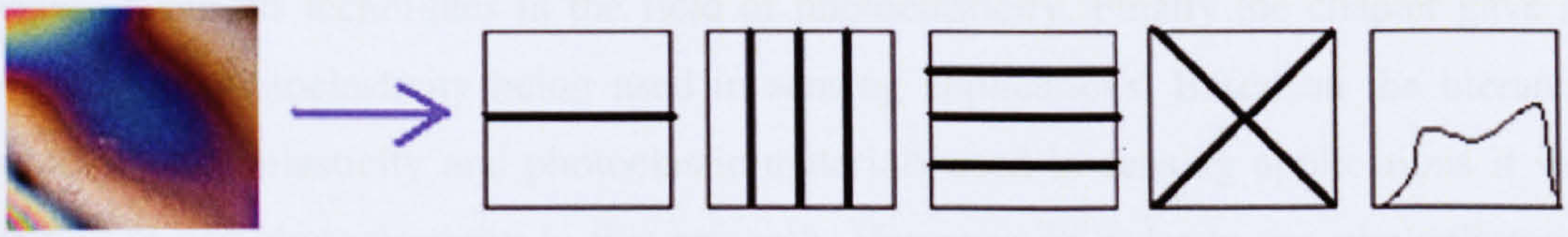

Figure 2-16: Different input parameters extracted from the fringe patterns for training of neural networks

On the same principle Noroozi et al. (2003) attempted inverse photoelastic analysis using neural networks to determine the bending load. A tensile testing machine was used to apply bending load on a photoelastic beam and the fringe order was determined at known points which would act as input parameters for the neural network. However, finite element analysis was integrated in the technique to generate training data, thus the system relied on input from theoretical calculations and did not use direct image data.

During analysis of fringe patterns under unknown loads, the fringe order at predefined points needs to be determined using photoelasticity to be fed as input to the neural network. The technique gave an error of 4% but required prior knowledge of photoelasticity to determine the fringe order at input points during actual implementation of the system.

The drawbacks of Chung (1998) and Noroozi et al. (2003) have been overcome in this research by directly feeding relevant image data to the neural network. Principal component analysis was performed to keep the input dimensionality low unlike Chung (1998). Low input dimensionality requires lesser training time and yields a more generalised network. Chapter 5 gives a detailed account of enhancements applied to implement the neural network for analysing photoelastic images for inverse analysis.

2.10 Summary

This chapter gave a detailed description of basic physics of photoelasticity, the definitions and terminology used in photoelasticity, the optical elements required and review of various techniques in the field of photoelasticity. Finally the chapter gave an overview of photoelasticity being used in sensing applications. Based on the literature review of photoelasticity and photoelastic materials used in sensing applications it was justified to use photoelasticity in this research. However, in order to use photoelasticity for sensing applications various elements of this technique would need to be identified and tailored to suit the application requirements. In the following chapter the selection of material and the design of experimental rigs is presented.

Chapter 3 Experimental Methods

3.1 Introduction

The previous chapter provided a detailed description on the basics of photoelasticity. The Chapter described two major photoelastic techniques; LUT based calibration and phase shifting. This chapter provides details on the suitability of the material properties as required for sensing applications, selection of appropriate material and calibration required for selected material. In order to use photoelasticity for sensing, appropriate elements of this technique needs to be identified and tailored to suit the requirement. Finally, the designs of various experimental setups used in this research are discussed.

3.2 Material Preparation for Sensing

In preparation for the sensing plate a photoelastic material was glued to a support surface (polycarbonate sheet) but was treated as a photoelastic model. During selection of the material it is treated as coating (due to the fact that change in thickness changes the behaviour of the material), however, during loading and analysis it is treated as a model because the stress-strain is not transferred from the glued surface (polycarbonate) rather the load is applied to the coating surface.

Due to the above facts it is required that a careful selection of the material properties is made to provide sufficient fringes under the controlled loading environment. Finally, a sensing plate is prepared from the selected material to form a part of final prototype sensor.

3.2.1 Load Direction

In conventional photoelastic analysis load is applied in the plane of photoelastic material, however, in this research the direction of applied load was perpendicular to the surface of the material. Due to the above fact, appropriate selection of material properties needs careful considerations. The photoelastic effect deteriorates under such conditions of loading especially with a low modulus material as required here, since the photoelastic effect is generated due to material deformation in z-plane. In this research the photoelastic effect is induced due to a vertical force on the surface of a photoelastic material added by a shear force, which means that the direct photoelastic relationship cannot be used.

3.2.2 Material Properties

The strain optic co-efficient, the modulus and the thickness of a photoelastic material must be carefully chosen for sensing applications as they contribute to the sensitivity of the material. Figure 3.1 shows a 3-dimensional plot illustrating the effect of thickness and strain optic coefficient on the sensitivity of material.

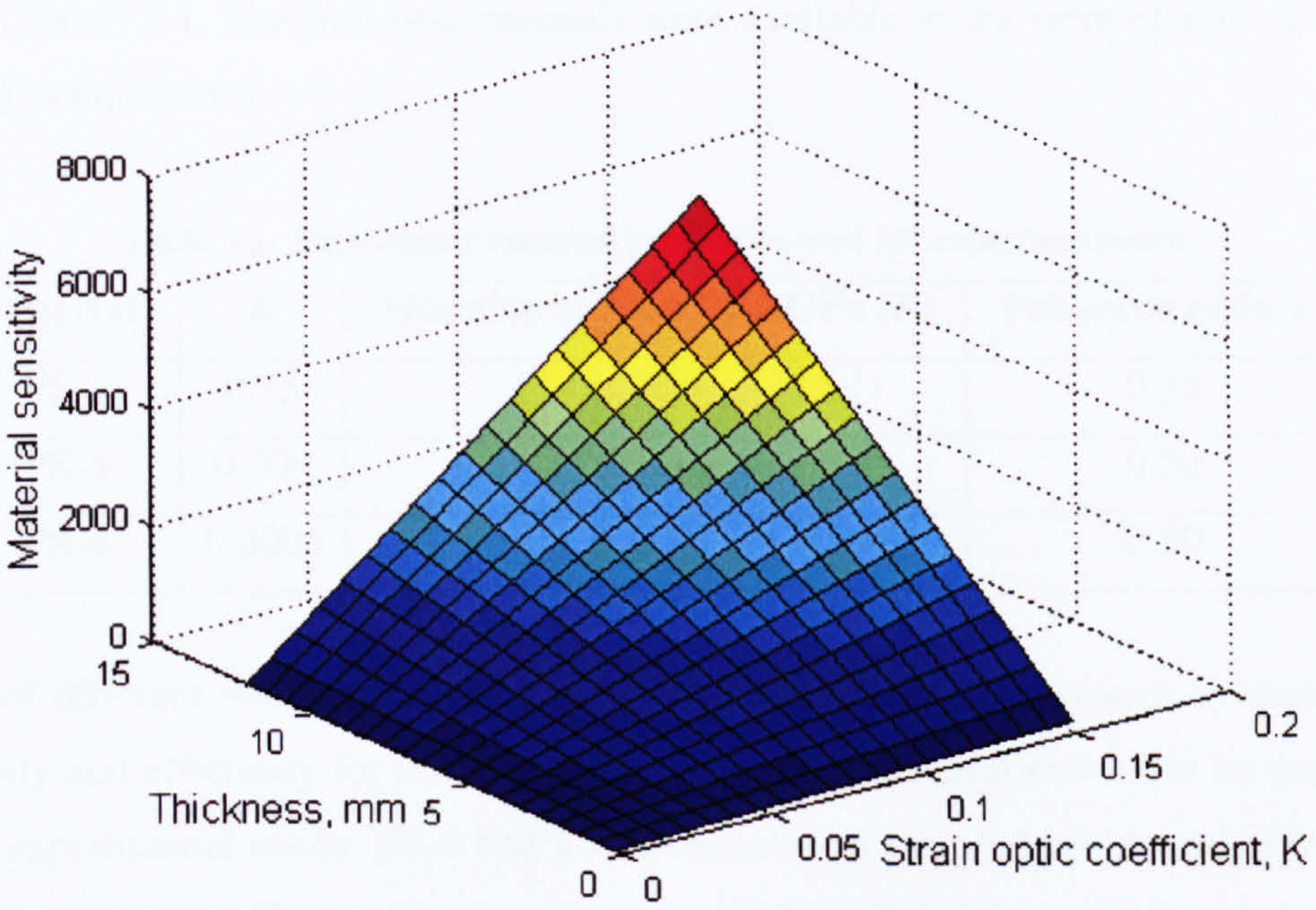

Figure 3-1: A three dimensional sensitivity plot for photoelastic materials

Thickness of material plays a vital role as increase in thickness increases the sensitivity of material. For major stress analysis applications selection of material is dependent on the modulus of the test object and the amount of stress-strain expected. For instance, if analysing a machine part with expected low stress-strain values, the photoelastic coating used should have a high modulus and high strain optic co-efficient. However, for this research the material was desired to have a high strain optic co-efficient with a low modulus of elasticity to facilitate foot loading.

3.2.3 Material Selection

The availability of photoelastic materials is described in terms of strain optic co-efficient of the materials. Higher the strain optic co-efficient higher is the sensitivity of material, as can be seen in Figure 3.1 a material with low thickness but high *K* could be more sensitivity than a material with thrice as much of thickness but lower *K*.

The experiments conducted in this research used three types of photoelastic materials[2] and narrowed down to one for the final sensor design. The properties of the materials are listed in Table 3-1. The first two materials were available in the form of flat sheets and the third in liquid form.

Table 3-1: Photoelastic material properties used for experimentation

Material[1]	*K*	**Modulus of Elasticity GPa (*E*)**	**Poisson's ratio v**
PS-1	0.15	2.5	0.38
PS-4	0.009	0.004	0.50
PS-6	0.0006	0.0007	0.50

Sheets of different thickness were casted from PS-6 during this research to evaluate its sensitivity and efficiency for the research; however the material proved to be unsuitable for the experimental needs. PS-6 had a low modulus as required but the sensitivity was too low to induce sufficient fringe patterns under the controlled vertical and shear load range in the experiments. Figure 1 in Appendix-II shows the casting setup and some of the casting prepared using liquid PS-6.

---

[2] Vishay Measurements Groups

PS-1 sheets on the other hand had high sensitivity but also high modulus of elasticity, thus unsuitable for the experimental loading required here. The available photoelastic materials exhibited a direct relation between the strain optic co-efficient and the modulus of elasticity, in order words the materials that had high sensitivity to strain also had high values of E and materials with low value of E had low sensitivity to strain thus not entirely ideal for the experimental needs of this research. A balance between K and E led to selection of PS-4, proving the best suitable material for building the sensing plate from the available list of materials. A PS-4 sheet with 3 mm thickness has low modulus of elasticity and sufficiently high sensitivity. The number of fringes induced increase with increase in thickness, however since the photoelastic effect travels through the entire thickness and also the loading was unconventional the fringes patterns tend to fade. This loss of colour information was less prominent with 3 mm thickness compared to any lower or higher thickness. Thus a PS-4 sheet with 3 mm thickness was considered the best suited for sensing plate. These different materials were used in the following set of experiments:

1. PS-1: A sheet of 3 mm thickness used to cut two models, a C-shaped and a Disc (Section 3.2.4). Implemented in the experiments for determining image plane wavelength (Section 3.3.2) and developing and testing of neural network based methodology (Chapter 5).
2. PS-4: Used for calibrating K value of the material and building the sensing plate for final experimentation in Chapter 6.

3.2.3 Sensing Plate

The selected PS-4 material was used to build a sensing plate, the arrangements of various components to design the sensing module are shown in Figure 3.2. A 3 mm thick PS-4 photoelastic sheet was glued to a 15 mm thick polycarbonate sheet using a clear adhesive of matching elasticity. The top surface was coated with a reflective paint with appropriate elastic properties to provide a reflective backing.

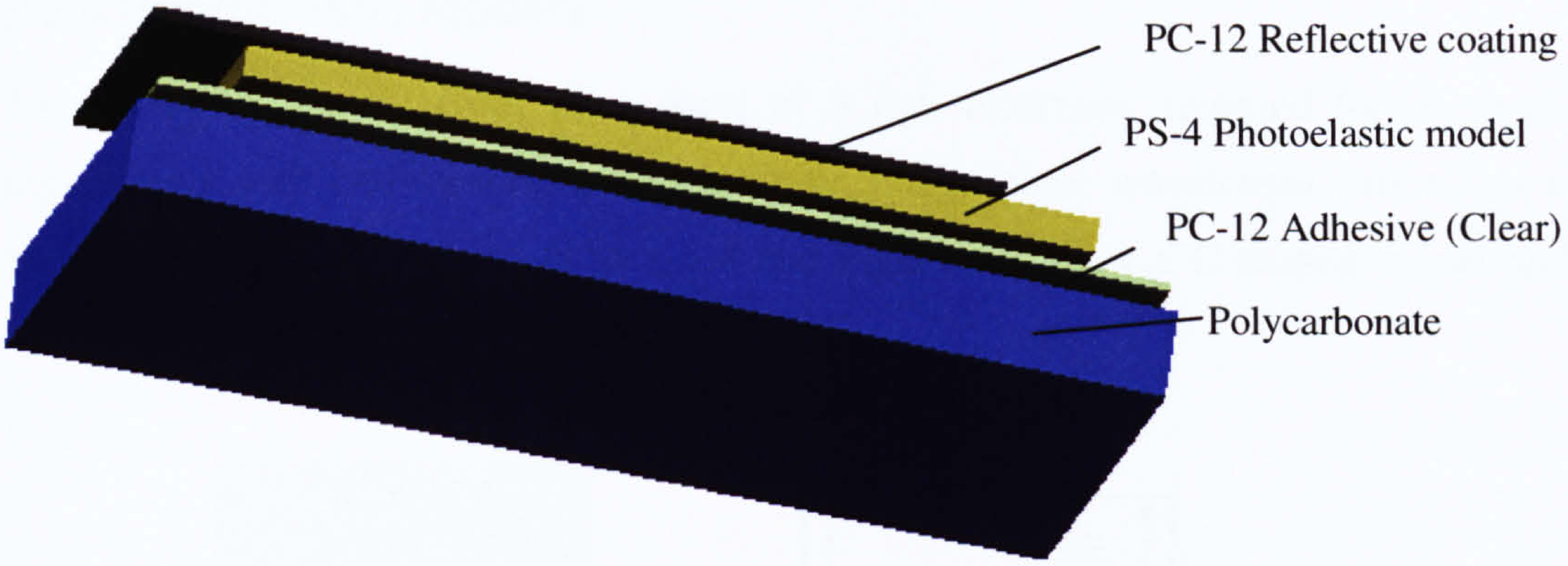

Figure 3-2: The components of the sensing module prepared from PS-4 photoelastic sheet

The polycarbonate sheet served as a strong support for the low modulus photoelastic sheet for loading. It is important to make sure that the polycarbonate support sheet is not birefringent in nature as that can lead to unwanted fringe patterns. Figure 3.3 shows the actual sensing plate with reflective coating on the top of photoelastic material glued to a 15 mm thick polycarbonate sheet.

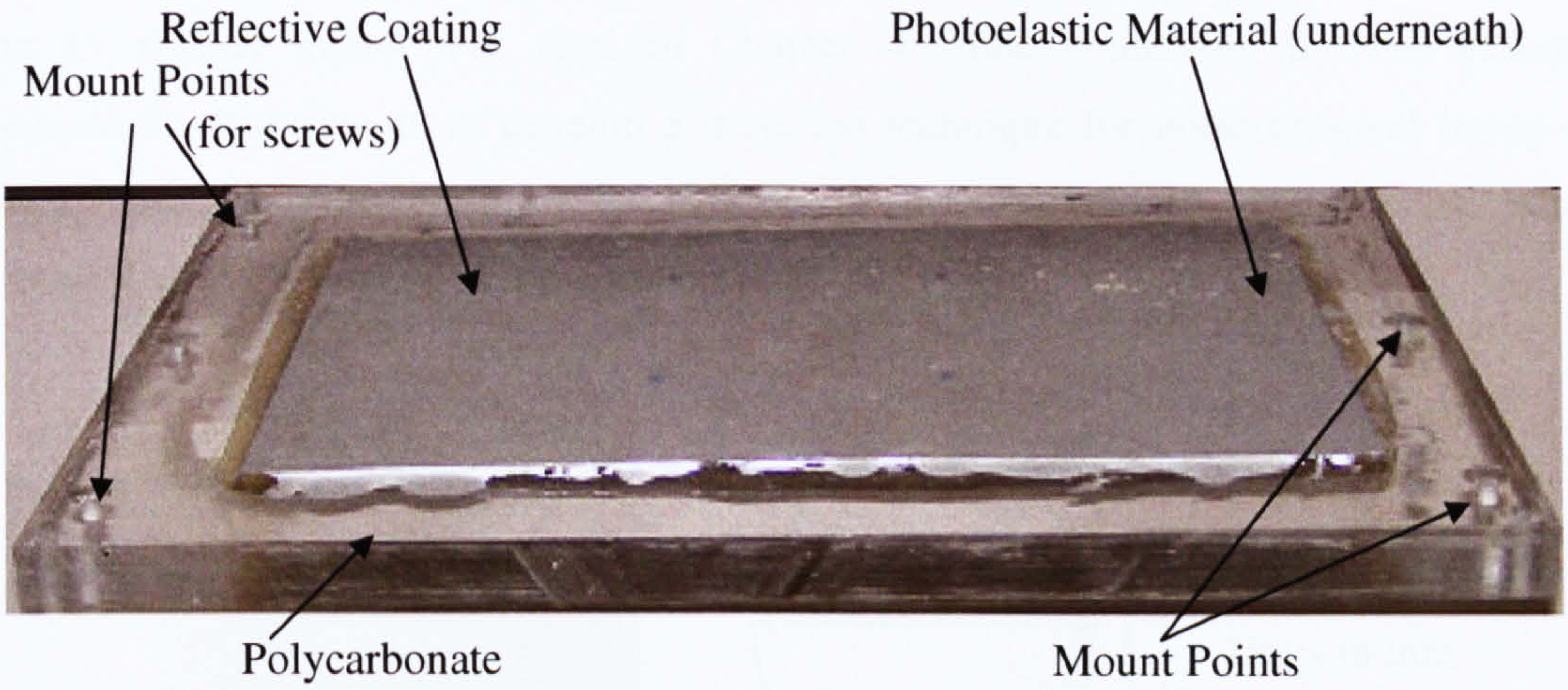

Figure 3-3: The final sensing plate prepared using PS-4 photoelastic material glued to a non-birefringent polycarbonate of 15 mm thickness as transparent support material

The polycarbonate sheet was finally mounted on the experimental rigs; design description provided later in this Chapter.

3.2.4 Photoelastic Models

Two models were cut from PS-1 sheet of 3 mm thickness, required for conducting experiments with conventional photoelasticity, image plane wavelength calibration and photoelastic inverse analysis. Figure 3.4 and Figure 3.5 show a C-shaped model and a disc with a dimensional sketch respectively.

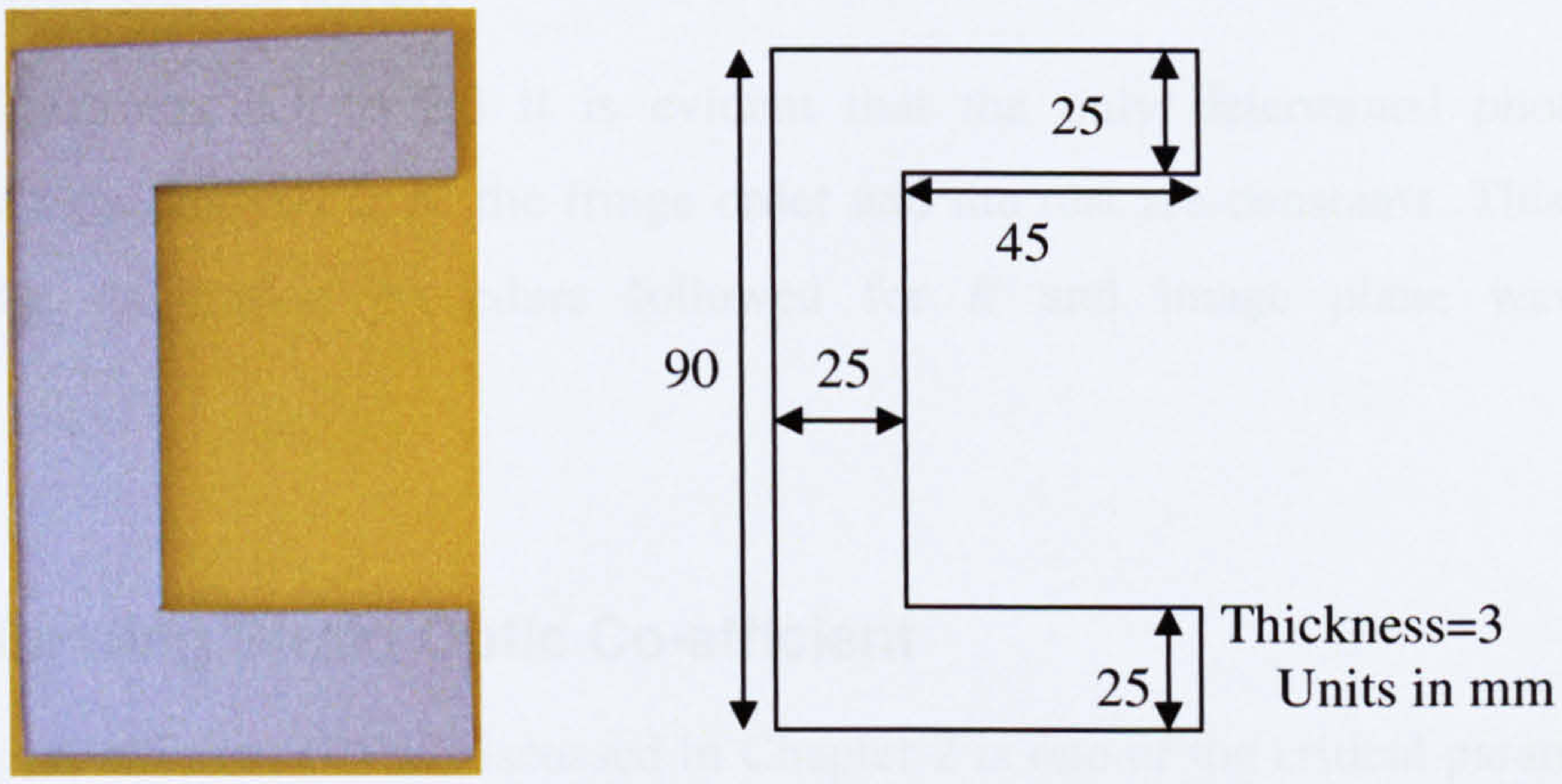

Figure 3-4: (a) A C-shaped model from PS-1 sheet, (b) the dimensional sketch of the model

The C- shaped model was used in Chapter 4 while evaluating the conventional photoelastic experiments to develop a modified technique for noise removal based on simple filtering. Also used in Chapter 5 for developing a neural network based methodology for photoelastic inverse analysis.

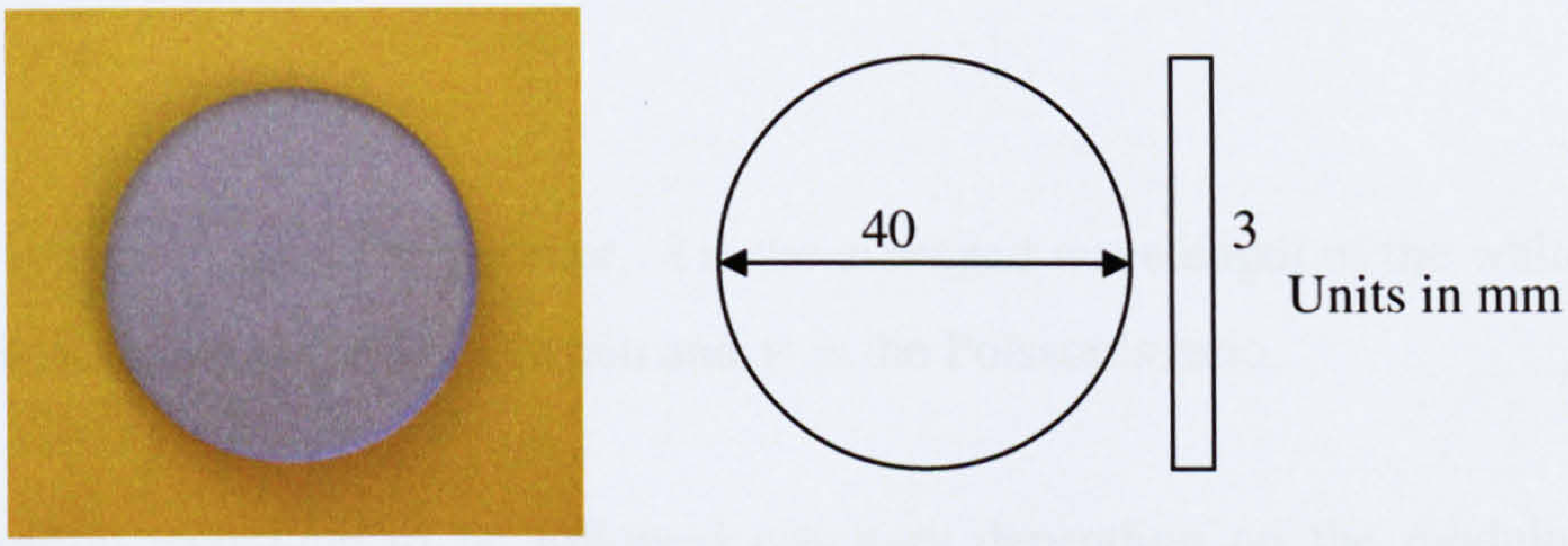

Figure 3-5: (a) A Disc model , (b) the schematic diagram with dimensions

The disc model was used in experiments for determining image plane wavelength for a commercial digital camera used in this research and the conventional photoelastic experiments conducted in Chapter 4.

3.3 Material Calibration

Recalling Equations 2.1 to 2.3 it is evident that the only determined photoelastic parameter during analysis is *N*, the fringe order and the rest are constants. This section describes the calibration procedure followed for *K* and image plane wavelength evaluation.

3.3.1 Calibrating Strain Optic Co-efficient

Strain optic co-efficient (*K*) as discussed in Chapter 2 is one of the critical parameters in photoelastic experiments. In fact, *K* is the only constant relating to the optical property of the material, thus crucial in stress calculations. The influence of *K* on the material selection i.e. the mathematical relation of *K* with strain is given by Equation 3.1. The value of *K* provided by the manufacturer is the nominal value and material recalibration is required to verify any change in the constant, as may occur over a period of time.

$$K = \frac{N\lambda}{2t(1+\nu)\varepsilon} \tag{3.1}$$

Where, N is the recorded fringe order, λ is the averaged wavelength of the white light, t is the material thickness, ε is the strain and ν is the Poisson's ratio.

The calibration technique to be followed can vary depending on the modulus of the photoelastic material, for instance high modulus materials (such as PS-1) are calibrated using cantilever beam under bending load (Zandman et al. 1997; Ramesh 2000; Measurement Group 2004). In the above case, PS-1 (high modulus material) is glued to a reflective aluminium beam and subjected to deflection with known strain value. Since expected value of K is high (~0 .15) for PS-1 material, a small value of strain is sufficient to induce measurable fringes thus deflection of beam required is in the range of 0.1~1 mm. On the other hand, for low modulus materials (PS-4) the conventional calibration technique of cantilever is not useful because the low sensitivity of material does not generate enough fringes even at higher deflection of 3~5 mm. Thus, to calibrate low modulus materials, imposed curvature method (Zandman et al. 1997) is used as shown in Figure 3.6.

The standard calibration procedure involves the following steps:

- Gluing a thin layer of photoelastic material with reflecting backing (designated by 1) to a material (designated by 2) with known mechanical properties (typically a medium modulus thick material).

- Bend the material (2) to a known curvature to induce strain, the strain then get transferred from material (2) to specimen (1). Calculate strain (ε) at the edge of the material using Equation 3.2

$$\varepsilon = \frac{h}{R} \tag{3.2}$$

- Record the fringe order (N) at pre-defined points on the specimen (1) to evaluate K from Equation 3.1.

Figure 3.6(a) shows a schematic diagram illustrating the technique and Figure 3.6(b) shows a section of the actual image with the induced fringes.

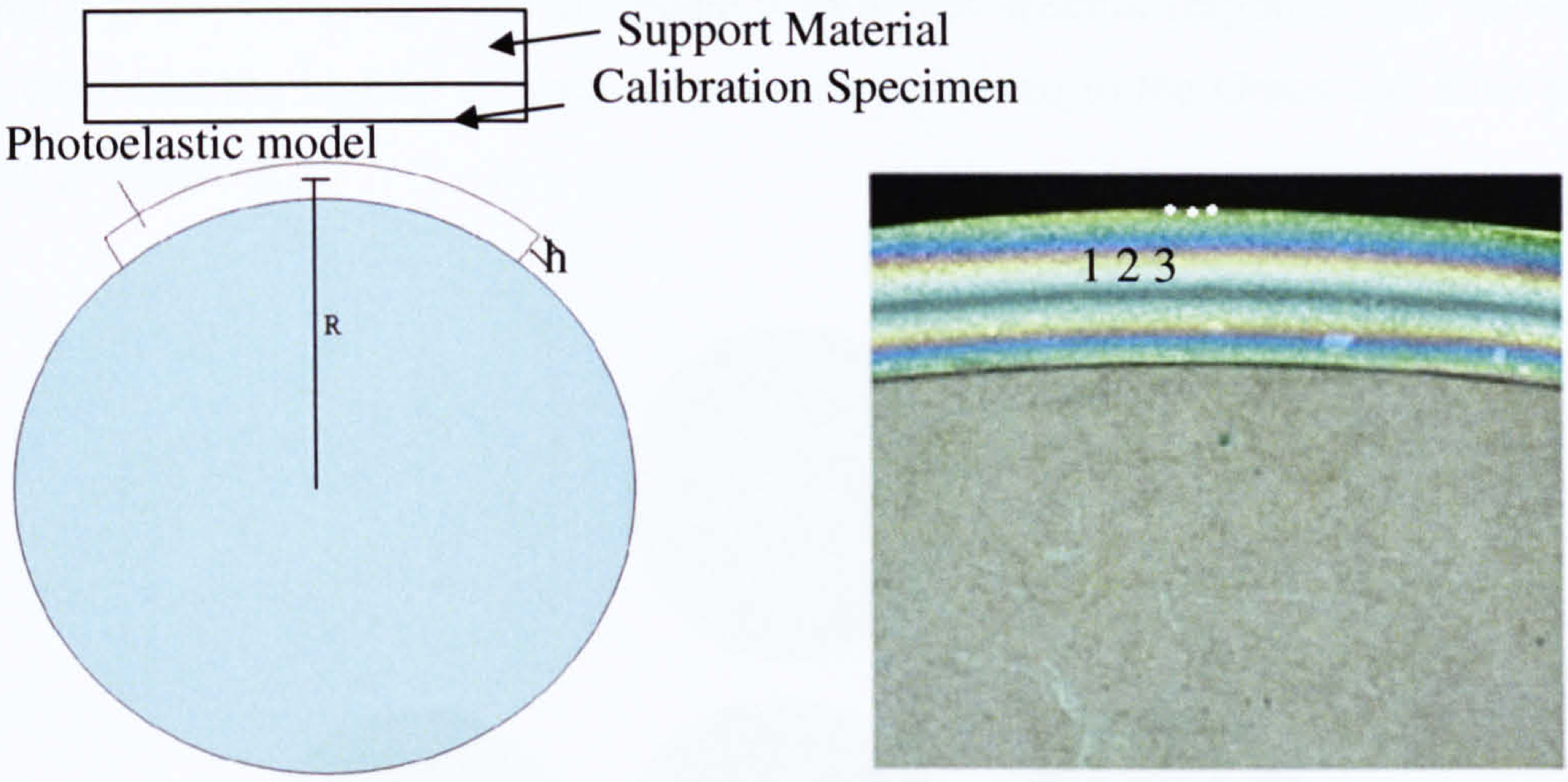

Figure 3-6: Calibration of PS-4 photoelastic material (a) the schematic diagram of imposed curvature technique, (b) section of the material with actual induced fringes

Following the calibration procedure and substituting the variables (h 4 mm and R 156.4 mm) the strain ε was calculated as 0.025575. The next step was recording fringe order at 3 different points (1,2,3) as shown in Figure 3.6(b).

The fringe order was found to be 1.5585 averaged from 30 experiments to minimise the error. Finally, with the evaluated strain and experimentally recorded fringe order N, K was determined to be 0.011679 using Equation 3.1. The determined K was different from the manufacturer's quoted value of (0.009) by 0.002679. This is significant from the accuracy point of view for photoelastic experiments. The above experimentation can also be performed with a monochromatic light source to determine fringe order at the point of interests but would require Tardy's compensation method (Zandman et al. 1997) as discussed in Chapter 2 Section 2.4.5.

3.3.2 Image Plane Wavelength

As discussed in Chapter 2 Section 2.8.3, while using white light for phase shifting an individual plane images from an RGB acquired image can be approximated to represent filtered images. Since a commercial digital camera (Olympus SP 500UZ) was used as image acquisition system (Section 3.5.4) for phase shifting it is mandatory to determine the image plane wavelength for this plane with higher spectral response. The Red image plane exhibited the highest spectral response as compared to the Green and Blue planes as seen in Figure 3.7.

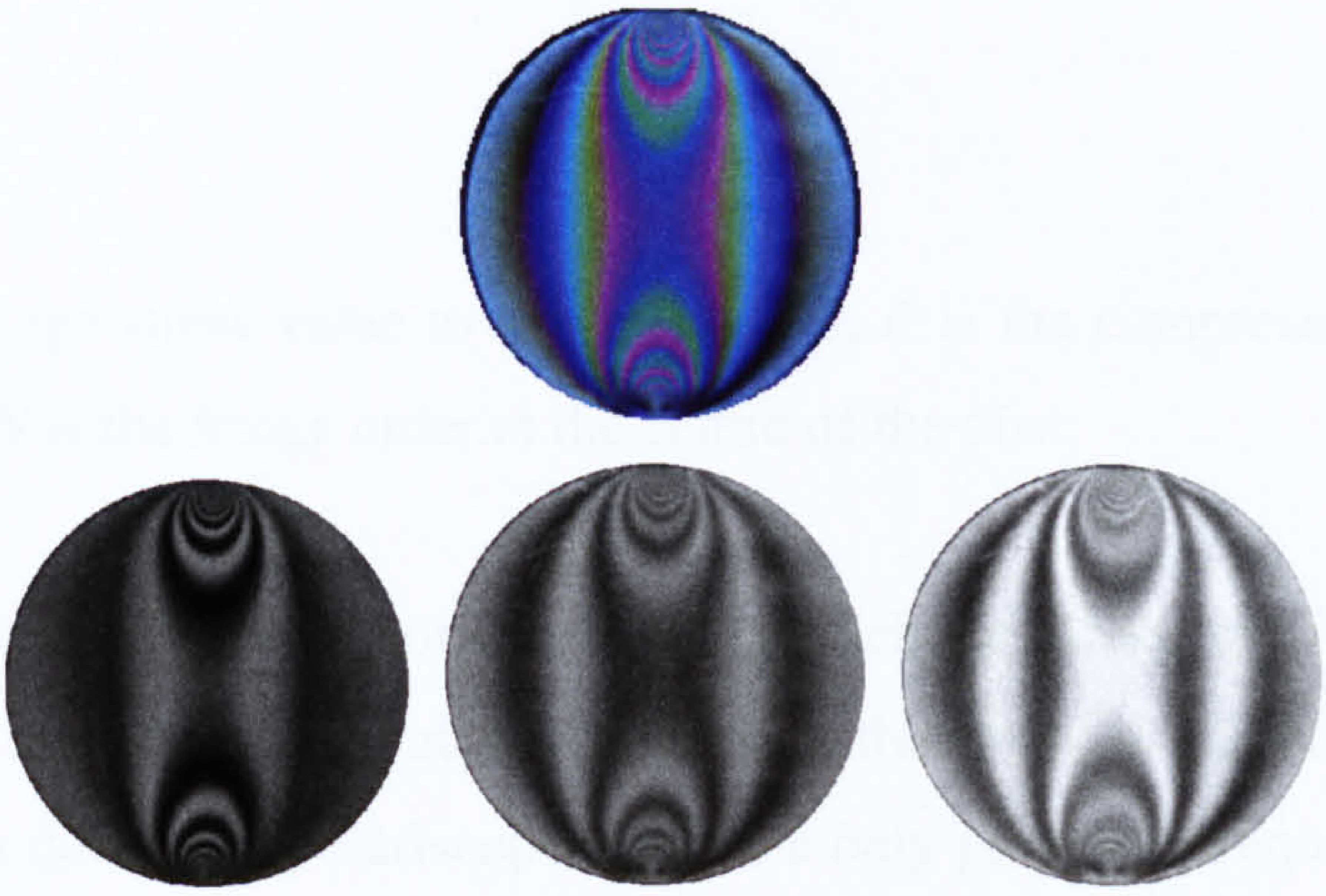

Figure 3-7: An RGB image with corresponding R, G and B planes respectively acquired by Olympus SP500

Equation 3.3 is used for determining the wavelength of an image plane from the RGB image with the prior knowledge of *f* (fringe stress value). The *f* however, must be known under both reference light source and the image plane with white light.

$$\lambda_i = \frac{f_i \lambda_r}{f_r} \tag{3.3}$$

where, λ_i is determined the wavelength of the image plane *i*, f_i is the fringe stress value from the image plane (R, G or B), f_r is the fringe stress value under the reference light source and λ_r is the wavelength of the reference light source (yellow 589 nm, custom designed in this research – Section 3.4). The next step is to determine *f* under the reference light source and for image plane from an RGB image, which is done in the following way:

To determine the fringe stress value (*f*) a relation between *f*, load *P* and *N* is required. Applying Bousinesque's solution to a disc under diametral compression through the centre of the disc, the relation to represent this is given by Equation 3.4 (Ramesh 2000).

$$f = \frac{8P}{\pi D N} \tag{3.4}$$

Where, f is the fringe stress value to be determined, P is the compressive load, D is the diameter of disc, N is the fringe order at the centre of the disc.

Due to the type of loading and geometry of the model, the direction of principal stresses is so aligned that the isoclinic are at zero degrees at the centre of the disc under the basic configuration of a dark-field polariscope. Thus the only parameter required is N which is determined using Tardy's compensation method (Zandman et al. 1997; Ramesh 2000). As the point of interest may not have an integral fringe order, the Tardy's compensation method is used to determine fringe order N at the point of interest by rotation of the polariscope elements.

Figure 3-8: Tardy's compensation (a) non-integral fringe order at 'Pni' (b) integral fringe order at 'Pi' after rotation of polariscope (circular polariscope configuration)

Figure 3.8(a) shows the fringe patterns for a disc under diametral compression and Figure 3.8(b) represents the fringes obtained from Tardy's compensation method when the analyser was rotated by an angle of 82.5 degrees to make pass an integral fringe order from point 'P_i'. The determined fringe order was found to be 2.458.

The same procedure was repeated with different loads and *N* was determined at the centre of disc for each load using Tardy's compensation method. Plotting *N* against *P* gives a line with the slope representing *f*. Figure 3.9 and 3.10 shows the graph plotted between *N* and *P* with monochromatic reference light source and R-plane image.

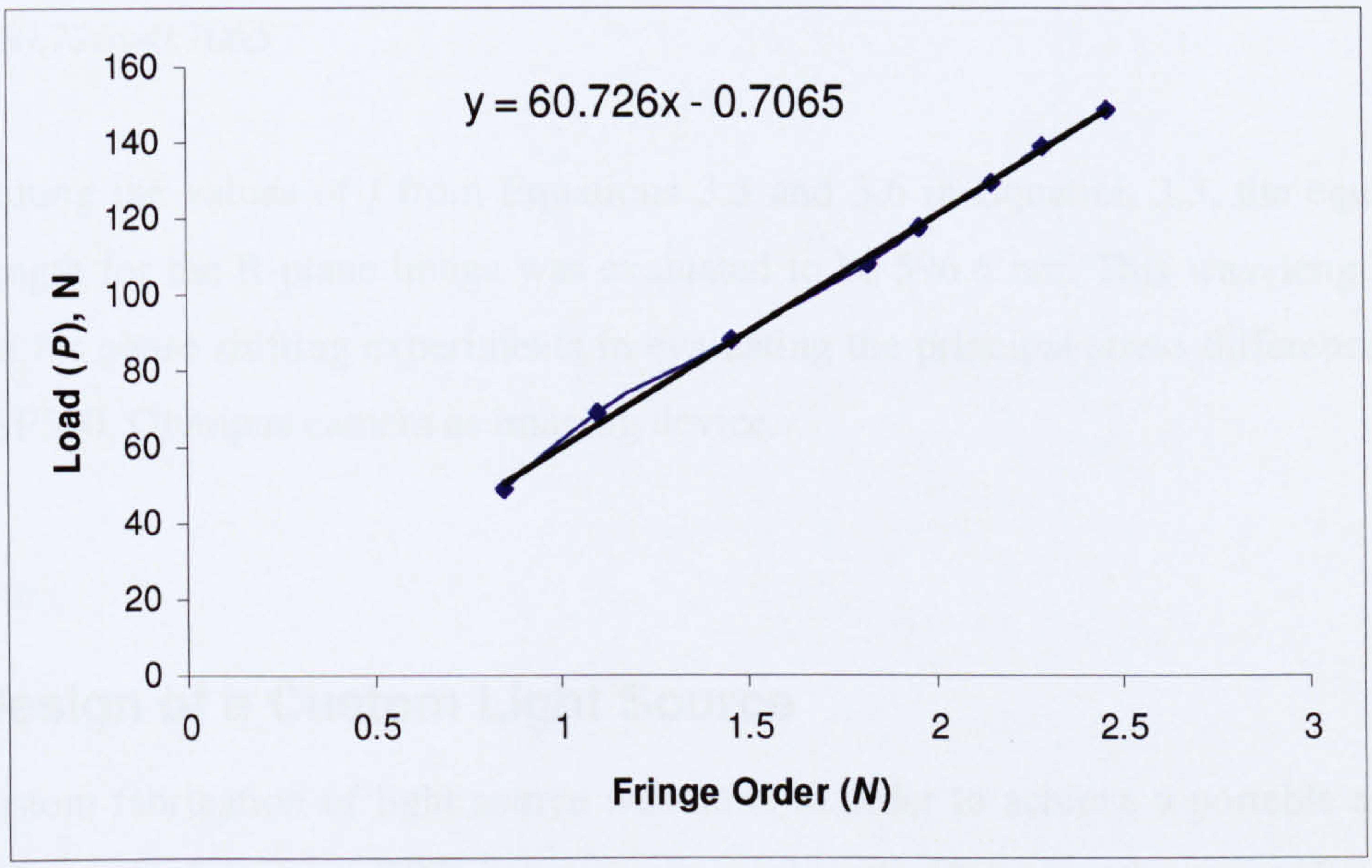

Figure 3-9: Fringe stress value plots with monochromatic light source

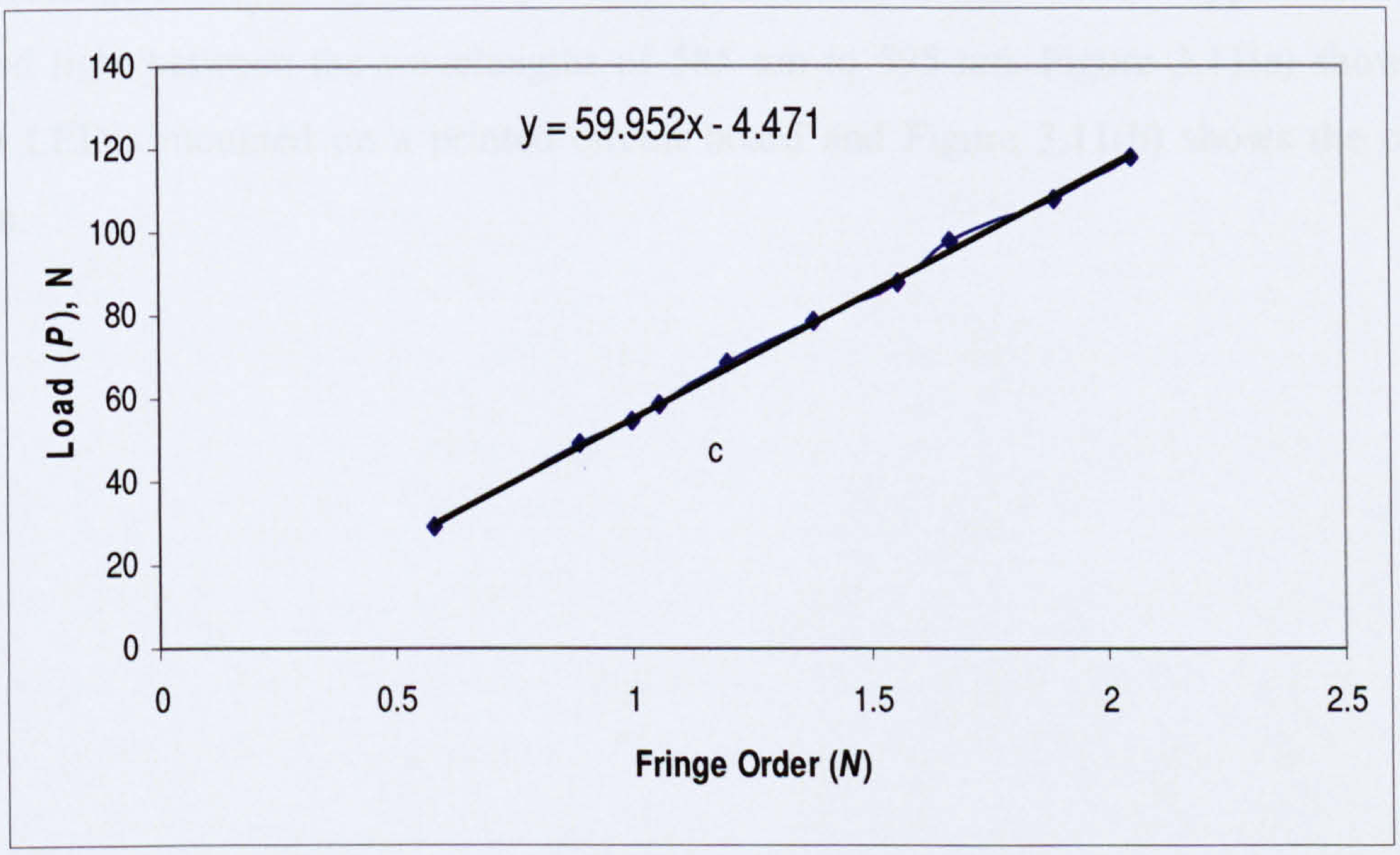

Figure 3-10: Fringe stress value plot for R-plane of RGB image (Olympus, SP500)

Equations 3.5 and 3.6 were derived using linear fits on the graphs plotted above and the corresponding fringe stress value with monochromatic (f_r) and R-plane (f_i) image were determined from the slope of the line to be 59.95 and 60.726 respectively.

$$f(x) = 59.952x - 4.471 \tag{3.5}$$

$$f(y) = 60.726y - 0.7065 \tag{3.6}$$

Substituting the values of f from Equations 3.5 and 3.6 in Equation 3.3, the equivalent wavelength for the R-plane image was evaluated to be 596.6 nm. This wavelength must be used for phase shifting experiments in evaluating the principal stress difference when using SP500, Olympus camera as imaging device.

3.4 Design of a Custom Light Source

The custom fabrication of light source was done in order to achieve a portable and low cost light equivalent to an SOX in terms of wavelength. However, the spectral response of a light source using LEDs would not be as sharp as that for SOX due to a wide range of wavelengths emitted by LEDs. From the data sheet provided by the supplier the LEDs emitted light between the wavelengths of 585 nm to 595 nm. Figure 3.11(a) shows the actual LED's mounted on a printed circuit board and Figure 3.11(b) shows the circuit design.

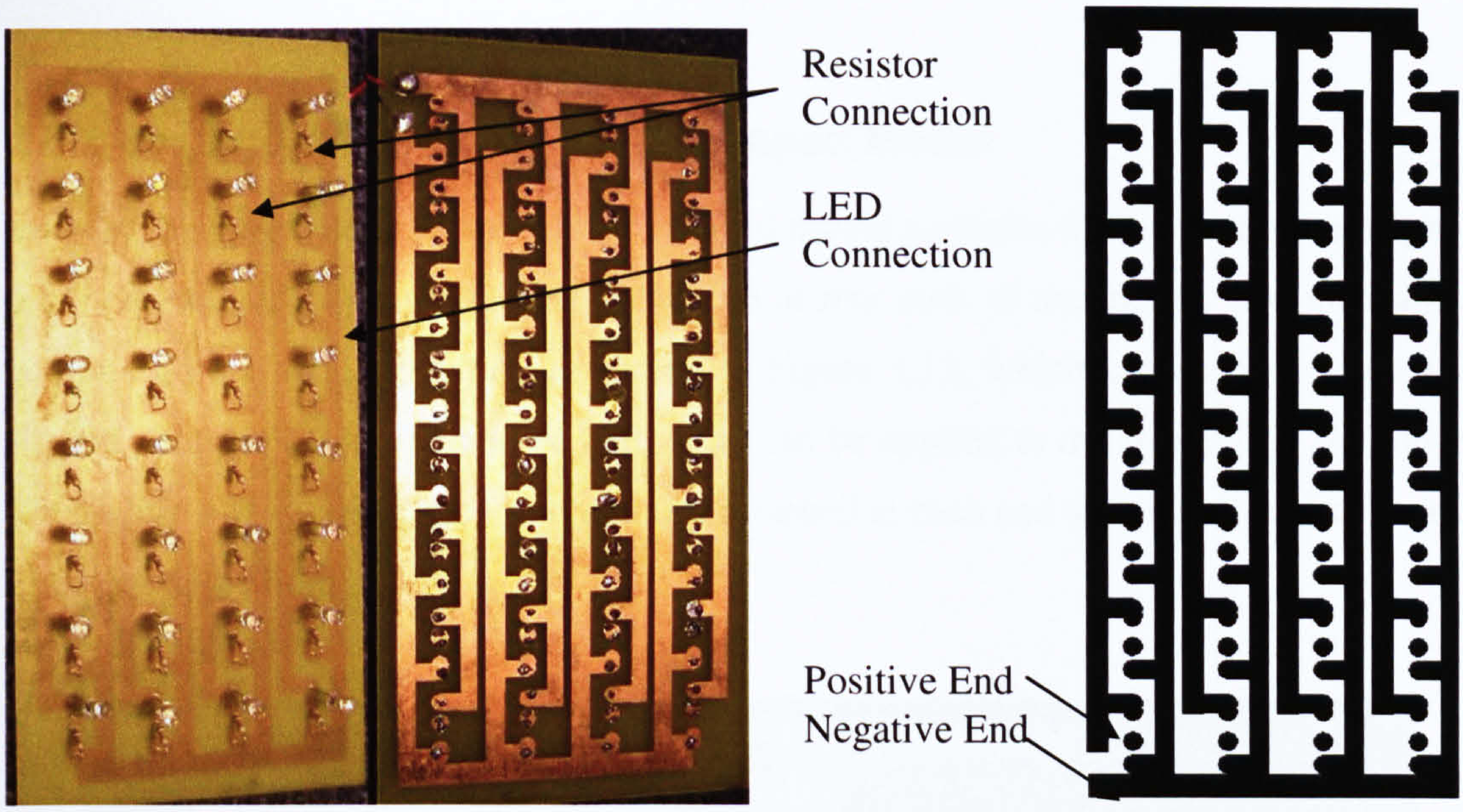

Figure 3-11: (a) LED based light source, (b) the circuit diagram custom designed to substitute an SOX light source

The black region in Figure 3.11(b) is where copper was retained as seen in Figure 3.11(a) to act as conductor for current. The LEDs were driven by a 12v DC supply and for optimal design they were coupled together both in series and in parallel. Resistors of 120 Ohms were connected in series with each LED to control the amount of current being passed through. The custom made LEDs were used not only as a reference light source for previous section but also for phase shifting experiments.

3.5 Experimental Rigs & Image Acquisition Systems

A number of experiments were conducted in this research and almost each of them required a different setup either in terms of loading or image acquisition. For instance, different loading mechanisms were required for different models and different lighting and image acquisition system were required for different photoelastic techniques. The various loading mechanisms and experimental setups designed and constructed in this research are discussed in this section. Finally, a system was designed using a flatbed scanner to provide high quality images and portability to the system.

3.5.1 Loading Mechanism for C- Shaped Model

In order to apply bending load to the C-shaped model a precise mechanism was designed, providing an accurate measure the deflection at free ends of the model. The mechanism comprised of a bending fixture as shown in Figure 3.12, which can accommodate a C-shaped photoelastic model and bending load can be applied to the free end of the model. The fixture had two precision micrometers attached at each end to ensure equal deflection of the model at both ends.

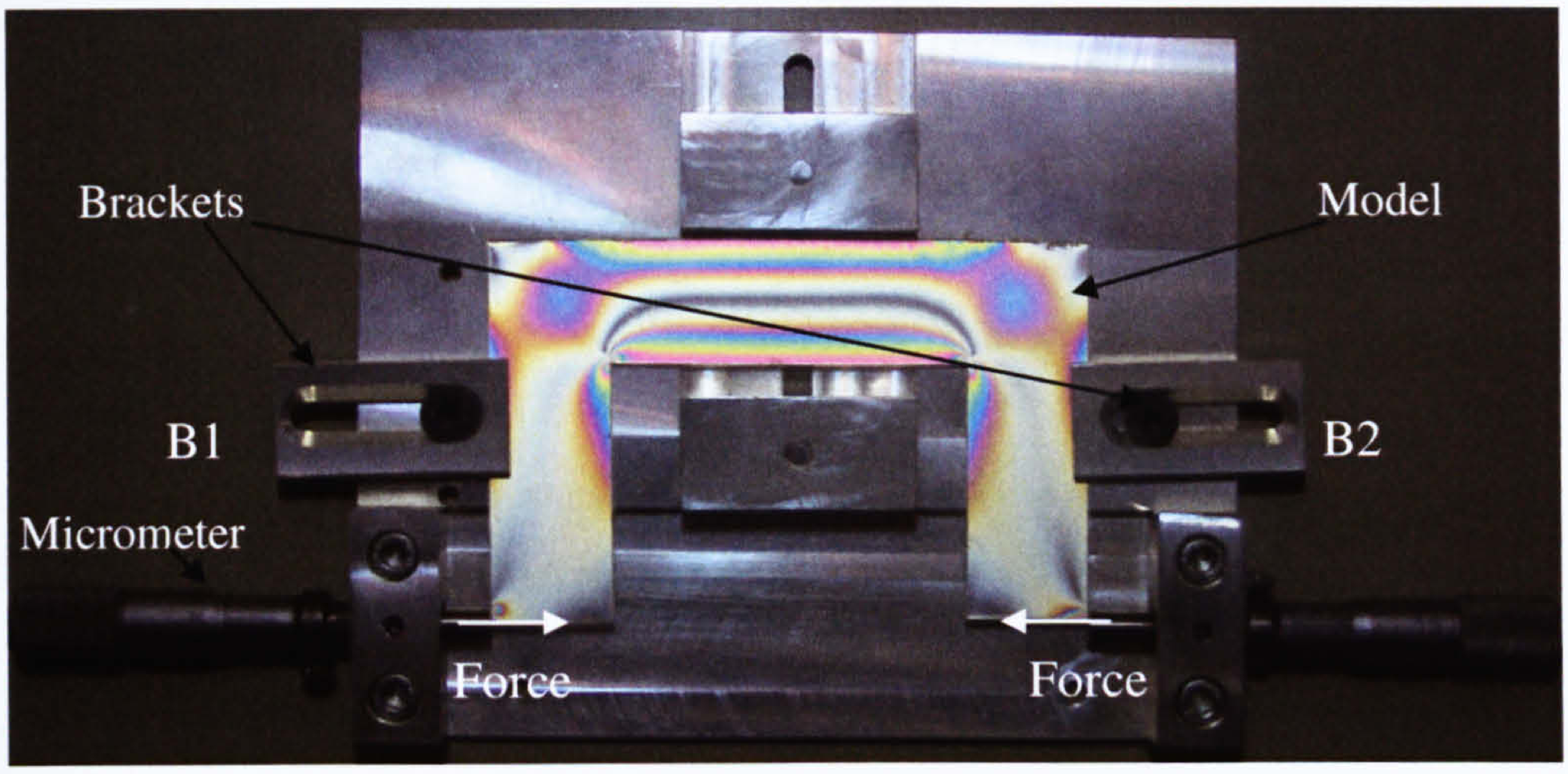

Figure 3-12: The loading mechanism for C-shaped model, illustrating photoelastic fringe patterns induced from deflection at free ends causing stress in material

To hold the model in plane of loading and avoid any displacements at high deflections, two adjustable screw brackets (B1 & B2) were provided on the sides. The brackets were carefully mounted as in not to load the model. The image in Figure 3.12 was illuminated with polarised light and acquired using a digital camera (Olympus, SP500) with separately mounted optical elements.

The designed loading mechanism was used for RGB calibration experiments in Chapter 4 and in Chapter 5 for developing neural network based methodology for inverse analysis of photoelastic fringes.

3.5.2 Loading Mechanism for Disc Model

A simple mechanism was designed for loading the disc model with diametral compression. Figure 3.13(a) shows the setup and Figure 3.13(b) shows the actual fringes obtained during experimentation.

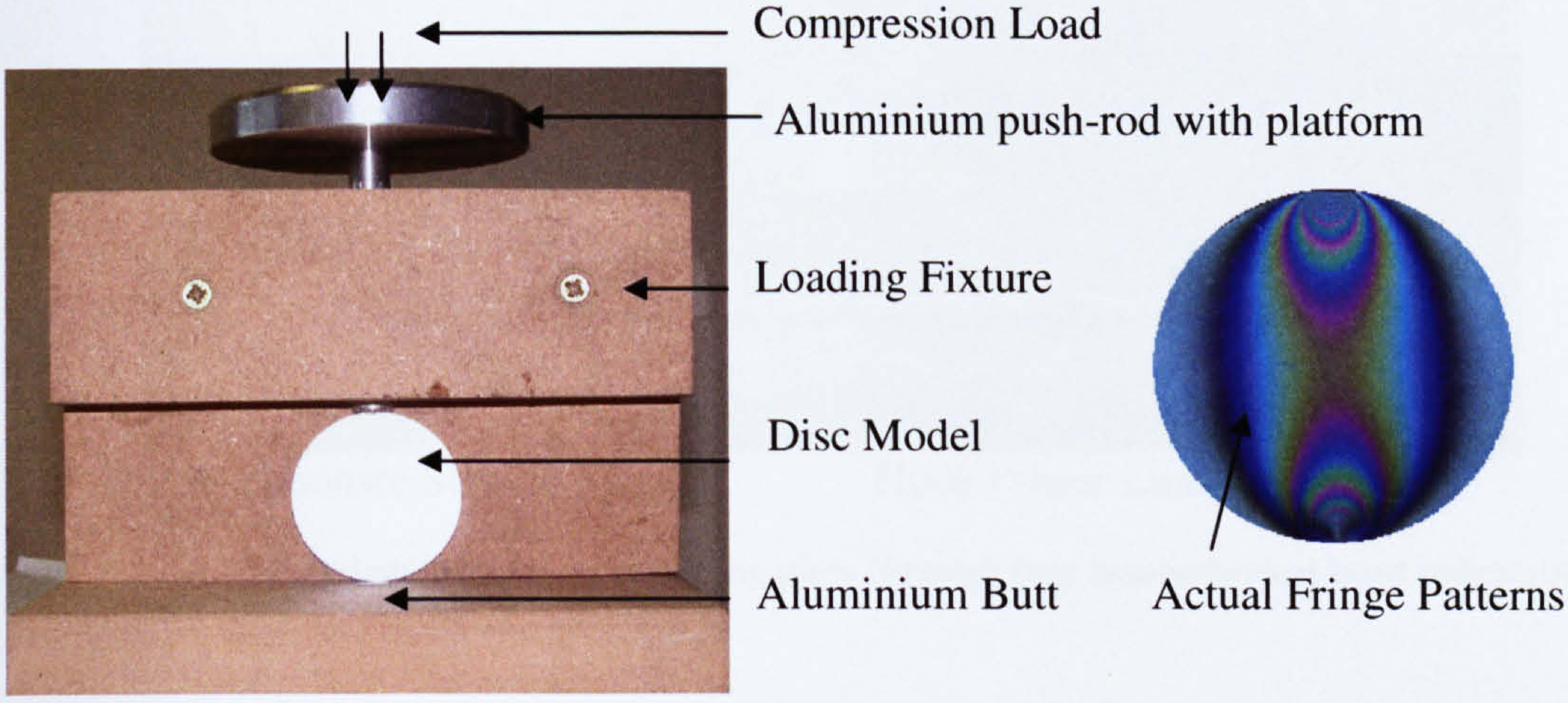

Figure 3-13: (a) The loading mechanism for disc model, (b) actual fringes from experimentation

An Aluminium push rod with loading platform passes through the fixture to apply point load on the disc. To achieve symmetrical loading at both ends, an identical Aluminium butt was provided at the other end. Sufficient gap was given between the loading platform and the fixture top to take higher loads. The dimensional diagram of the setup is shown in Appendix-II.

3.5.3 Loading Mechanism for Sensing Plate

The sensing plate built using PS-4 photoelastic material (Section 3.2.3) was loaded under vertical and shear forces with specifically designed indenter. Figure 3.14 shows the four-head indenter in contact with the sensing plate for vertical and shear loading.

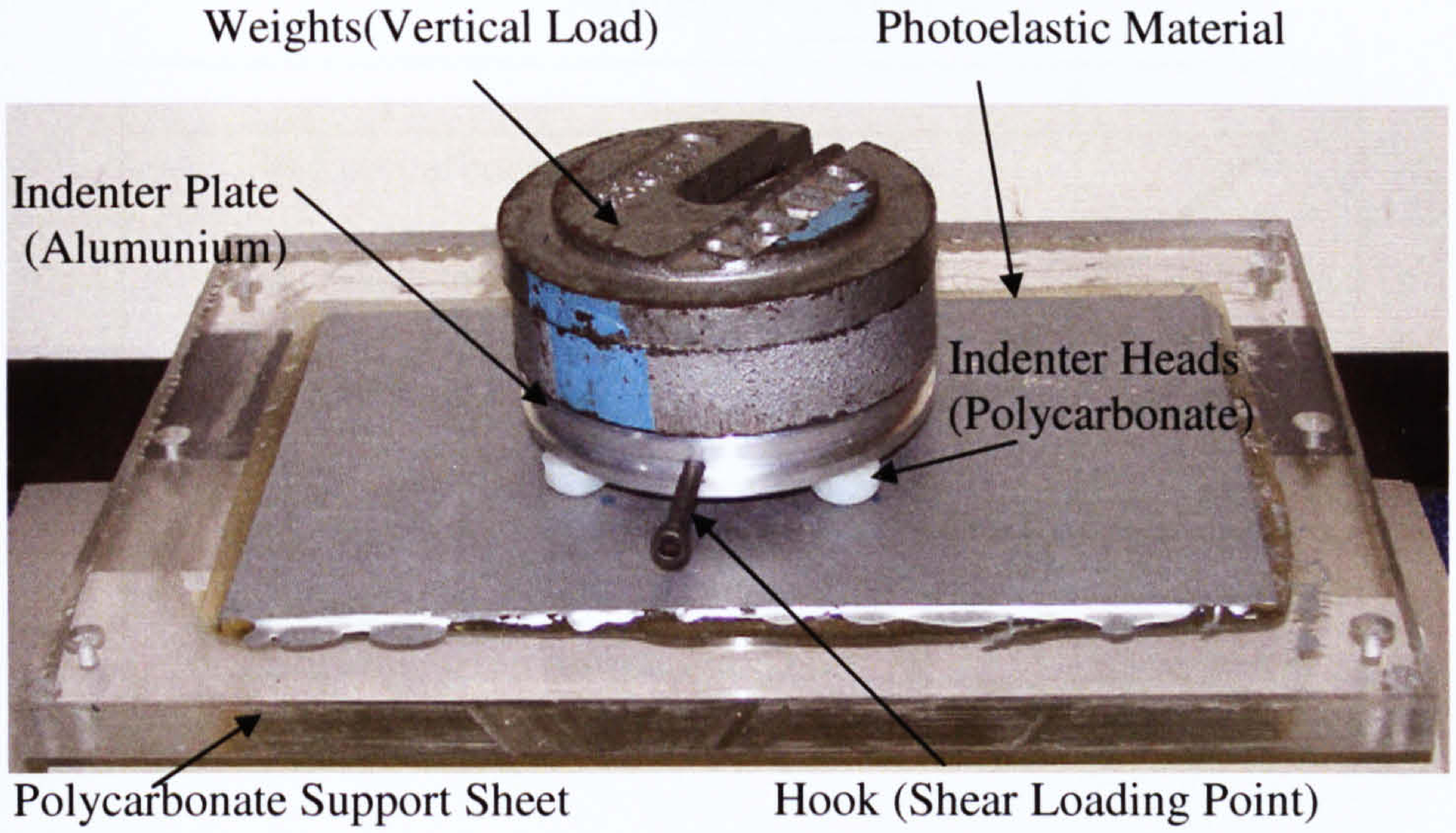

Figure 3-14: Indenter loading the sensing plate through four hemispherical head indenters

The indenter platform was made using Aluminium and polycarbonate was chosen as the material for indenter heads. The polycarbonate heads exhibited high frictional characteristics with the coated photoelastic model to avoid slipping during shear loading. The vertical load is introduced by flat-weights and shear load is introduced by a cord with hook-weight combination attached to the screw passing over a pulley. The complete assembly of loading and image acquisition is described in Section 3.5.5.

3.5.4 Image Acquisition System for Phase Shifting

An experimental setup design with image acquisition that used a compact fluorescent tube as light source and a digital camera is described below. The system incorporated the loading mechanism described in the previous section. Figure 3.15 shows a 2D drawing of the design in its side view.

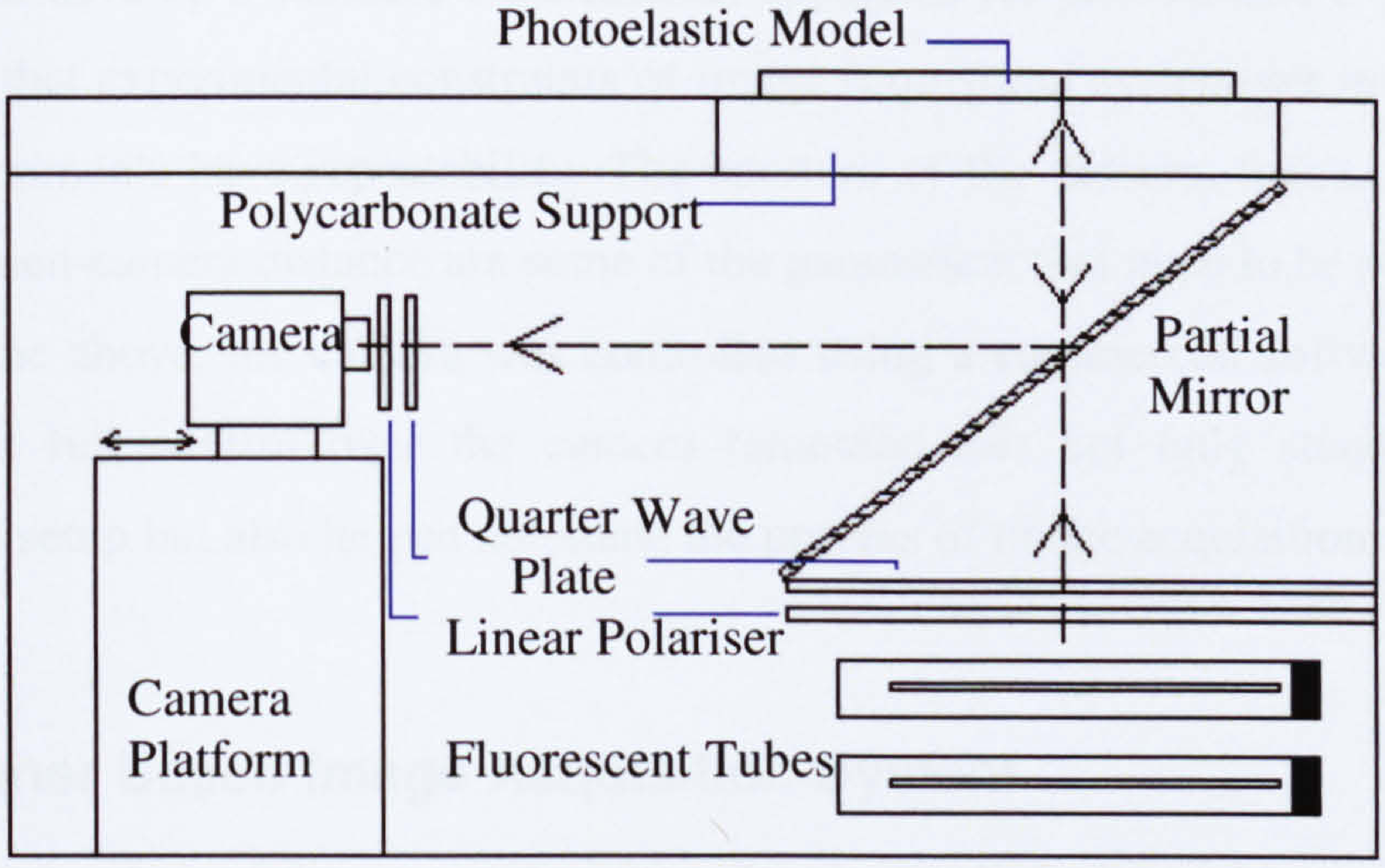

Figure 3-15: A schematic sketch of experimental rig designed and fabricated with partial mirror for phase shifting experiments

The setup was used for phase shifting experiments with white light and custom designed monochromatic light source. Figure 3.16 shows the exploded view of the actual setup; the top and loading mechanism has been removed for illustration.

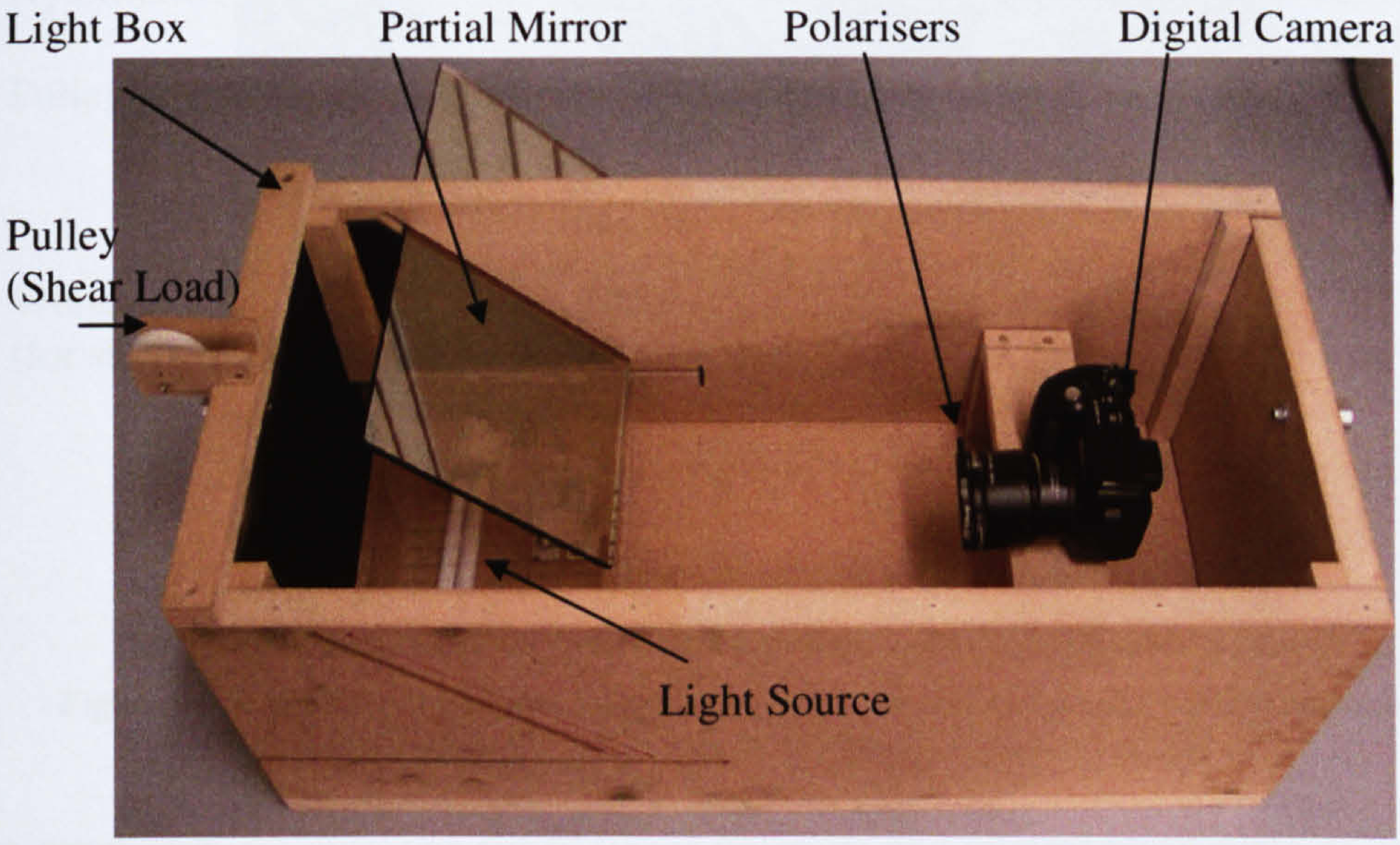

Figure 3-16: An exploded view of actual setup with partial mirror and mounted loading mechanism

In an effort to develop a standard experimental apparatus for photoelastic experiments it is important that experimental constraints of image acquisition system are maintained so that the experiments have repeatability. The aperture of the camera, focus, the level of zoom, specimen-camera distance are some of the parameters that need to be standardised. To achieve the above, the camera was controlled using a commercial software package that provides full control over the camera remotely, this not only standardised the experimental setup but also helped automate the process of image acquisition.

3.5.5 Scanner Based Image Acquisition System

One of the main aims of this research was to develop a clinically viable sensing system for biomedical applications requiring minimum maintenance. A commercial flatbed scanner (Epson 1660, Photo-Perfection) was used for image acquisition providing a compact and a portable system which requires no separate light source or camera. Figure 3.17 shows the actual system with mounted sensing plate and indenter loading mechanism.

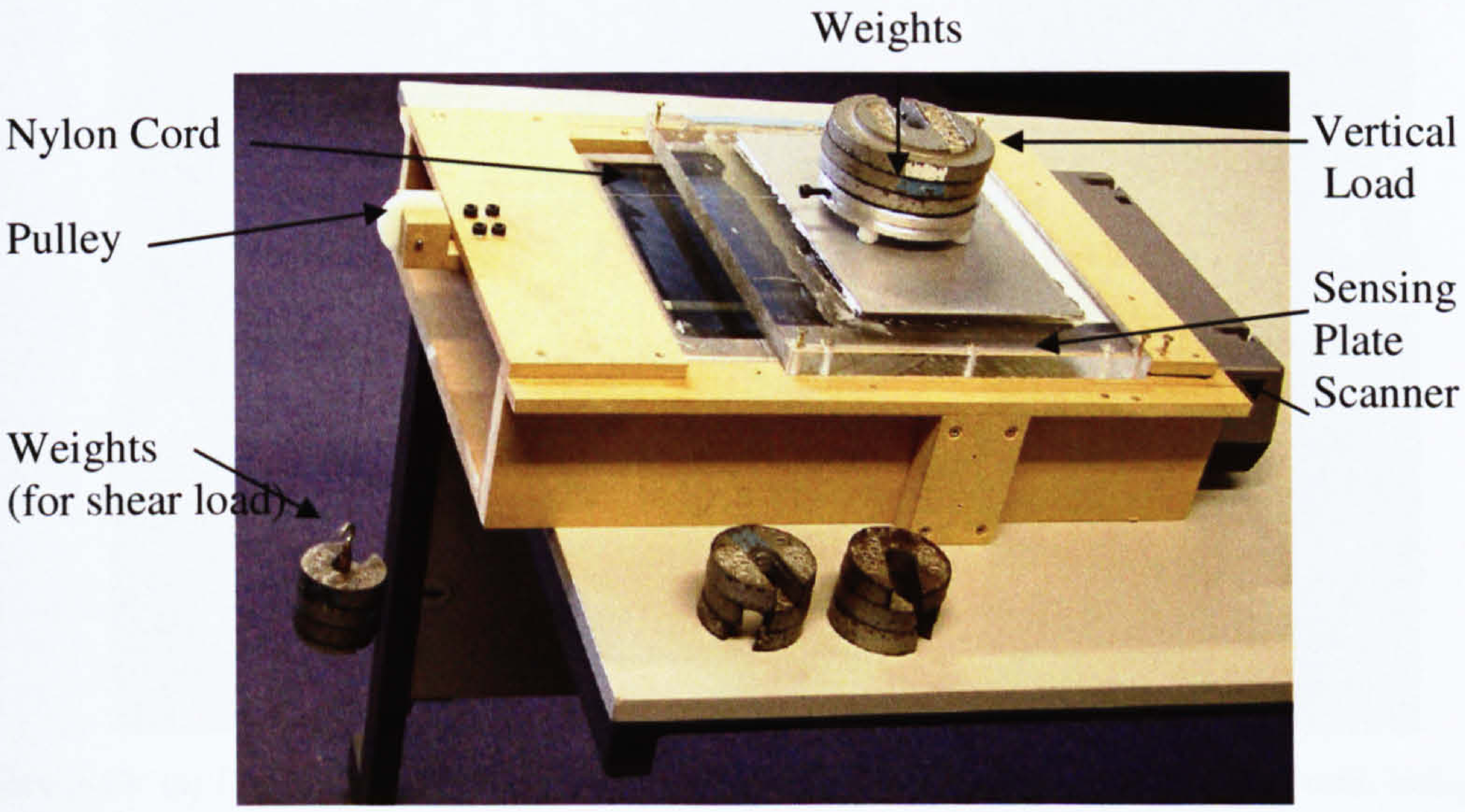

Figure 3-17: Scanner based system with mounted vertical and shear loading mechanism

The setup requires only one set of linear polariser and quarter wave plate as opposed to the previous experimental setup based on a partial mirror. The polariser and quarter wave plate were directly placed on the scanner bed. However, this setup can only be used for

LUT based technique and not phase shifting unless the model is small, under stress frozen condition and transparency unit of scanner is incorporated (Ng et al. 2003).

3.5.6 Digital Camera

The scanner based system provides portability and convenience of combined light source and image acquisition system, however it cannot be used for certain experiments where optical elements (polariser, quarter wave plates) needs to be mounted separately. For such experiments a digital camera (Olympus, SP500) with high image resolution of 6M was used and the optical elements were mounted separately for both light source and camera. Figure 3.18(a) shows the camera with the optical element assembly (Figure 3.18(b)) mounted on the camera lens.

Figure 3-18: (a) Digital Camera used in the experimentation, (b) optical mountings with independent rotation of polariser and quarter wave plate

The optical mount provides an advantage of independent rotation of each optical element, i.e. the polariser can be rotation independently from the quarter wave plate and visa versa. This feature is useful in phase shifting experiments where a number of images need to be collected at different orientation of the optical elements. Experiments like phase shifting and look up table technique also require certain experimental constraints to be maintained during the experimentation for instance, distance between the camera and the test object, camera aperture, shutter speed etc. The above was achieved using a camera control software package (Sabsik 2005) that not only maintains the camera settings but also provides image acquisition control from a computer. The technical specifications for the camera are given in Appendix-II.

3.6 Summary

This Chapter provided information on the material selection for sensing application as required in this research. The most appropriate material was chosen from the available list of material depending upon their mechanical and optical properties. The Chapter also provided a detailed description of different loading mechanisms and experimental rigs used for conducting conventional and non-conventional photoelastic experiments. The final system was built using a flatbed scanner, mounted with specifically designed sensing plate to be used as prototype sensors for controlled experimentation in Chapter 6. The next Chapter discusses the experiments conducted with conventional photoelastic techniques, leading to the contributions made to the current techniques and limitation of the techniques for unconventional experiments like sensing.

Chapter 4 Results Using Conventional Photoelasticity

4.1 Introduction

This chapter describes the implementation of photoelasticity under the conventional as well as unconventional loading. The first two sections include implementation of LUT based calibration technique discussed in Chapter 3 and the two major contributions made to this technique. Later sections evaluate the use of conventional photoelastic techniques under unconventional loading situations to evaluate their efficacy in sensing applications. The loading is unconventional in the sense that a low modulus photoelastic material is deformed by surface loading to induce photoelastic effect which is atypical of conventional methods. Both LUT based calibration and phase shifting techniques have been used to study the characteristics of patterns obtained under vertical and shear loadings. The results obtained under these conditions are discussed with their limitations when used for sensing applications. Finally a case study has been conducted to analyse the foot image and conclusions drawn from this have been presented.

4.2 Fringe Analysis Using Look-Up Table Technique

In this research mainly two different white light sources were used, compact fluorescent light and cold cathode tube. This section compares the LUT based calibration technique using conventional white light source with scanner based system as implemented in this research. The colour response may vary with the type of white light but the basic sequence of colour is same. However, as suggested in literature a high quality spectral response light source is almost a mandatory requirement to obtain a better calibration database and accurate results.

As explained in Chapter 2 that colour calibration technique (TFP) requires generation of a LUT and extracting fringe order to form a database. This however requires careful considerations on various aspects of the experimental procedure including the selection of components and setup design. This section describes calibration procedure used in this research for fringe order demodulation.

4.2.1 Calibration Procedure

The loading mechanism design in Chapter 3 section 3.5.1 was used for loading of a C-Shaped model (section 2.3.4) with high precision. The conventional techniques use four point bending load (Ramesh 2000) for calibration and LUT preparation however, in this research a C-Shaped model as shown in Figure 4.1 was used for the ease of loading compared to four point bending load.

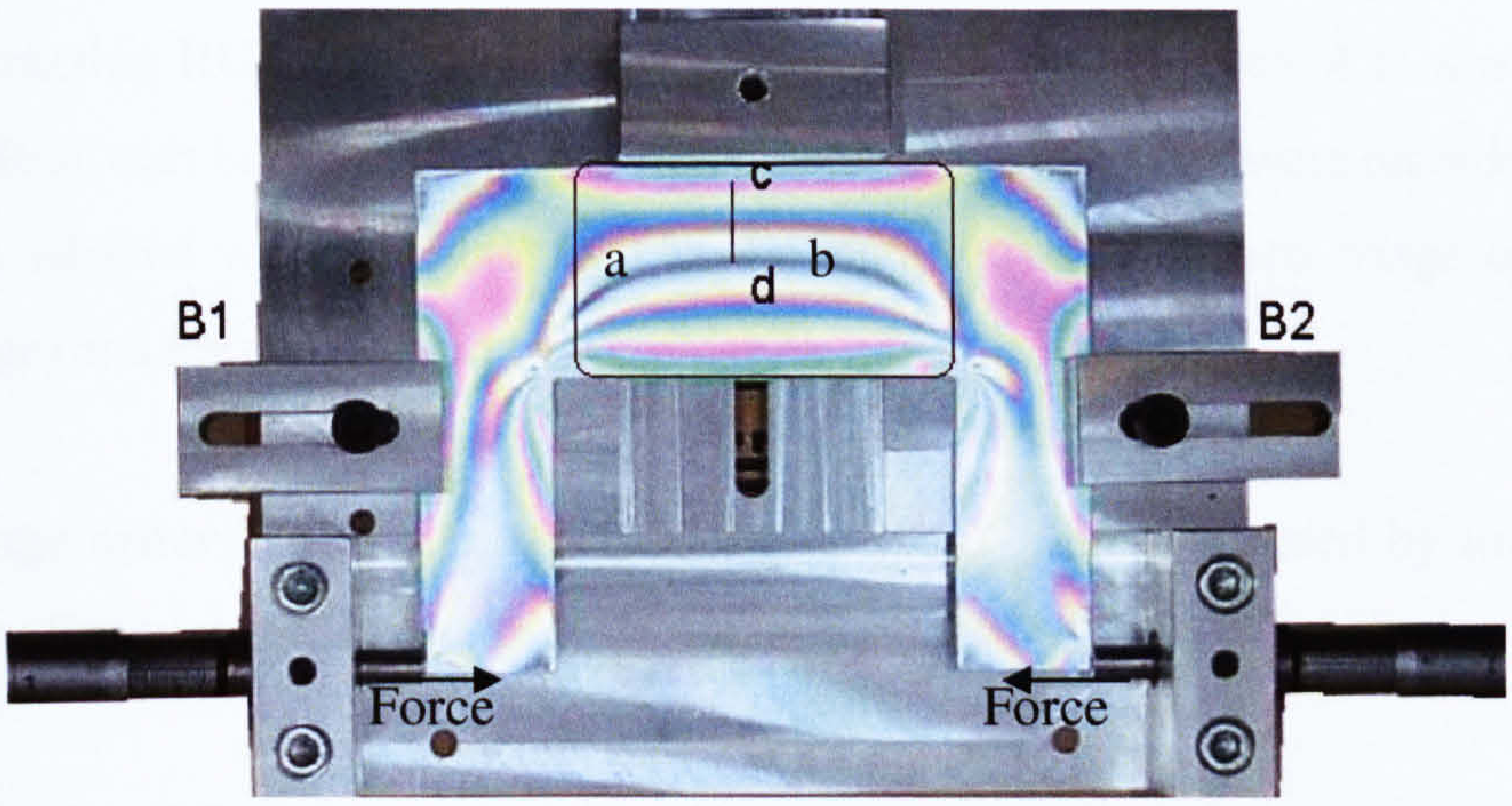

Figure 4-1: Photoelastic fringe patterns induced in a C-shaped model loaded using a fixture for preparation of LUT

The setup was illuminated with polarised light and image acquired using a digital camera. The optical components were separately mounted (dark-field circular polariscope setup) on the light source and the camera (section 3.5.6) to facilitate easy orientation of the model with respect to the light and the camera to minimise any reflection and ghost images. A compact fluorescent tube was used as light source in this experiment.

The loading generates patterns of uniform stress distribution along ‘a-b’ and linear stress distribution along ‘c-d’ as seen in the region of interest (ROI) in Figure 4.1. The step by step calibration procedure followed involved the following 7 steps:

1. **Bending load:** Appropriate bending load was applied to the model to induce a known fringe order (*N*) against the fringe colour. The fringe order is available from the standard isochromatic colour characteristics (Table 2-1).

2. **Data acquisition:** An RGB image of the fringe patterns generated was stored and a region of interest (ROI) was extracted using a high resolution digital camera.

3. **Filtering:** The region of interest was filtered using median filtering to remove electronic noise and smooth the image, as the CCD is highly sensitive to intensity changes.

4. **Extracting RGB triplet values:** A calibration line 'c-d' (Figure 4.1) was selected in the ROI with linear stress distribution and RGB triplet values were recorded. The line was selected with the start point at the neutral axis with zero fringe order (black fringe) and the end point at fringe order *N*.

5. **Fringe order:** The fringe orders along line 'c-d' were calculated by linear scaling using Equation 2.8.

6. Steps 4 and 5 were repeated for 50 transverse lines and the averaged results were saved in calibration database (this helps in further noise removal and making the calibration table robust).

7. Steps 1 to 6 were repeated with different values of maximum fringe order (*N*) by changing the bending load. For analysis up to third fringe order, three different calibration databases were built ranging from fringe orders 0-1, 0-2 and 0-3. The number of calibration tables required depends on the maximum fringe order expected in the test model.

4.2.2 Analysis

The test was conducted on a disc under diametral compression, loaded using the setup explained in Chapter 3 section 3.5.2. Figure 4.2(a) shows the image of disc under compression, the regions of fringe order higher than 3 are near the points of loading. Since the results are limited to maximum of third fringe order in TFP, these regions were masked as shown in Figure 4.2(b).

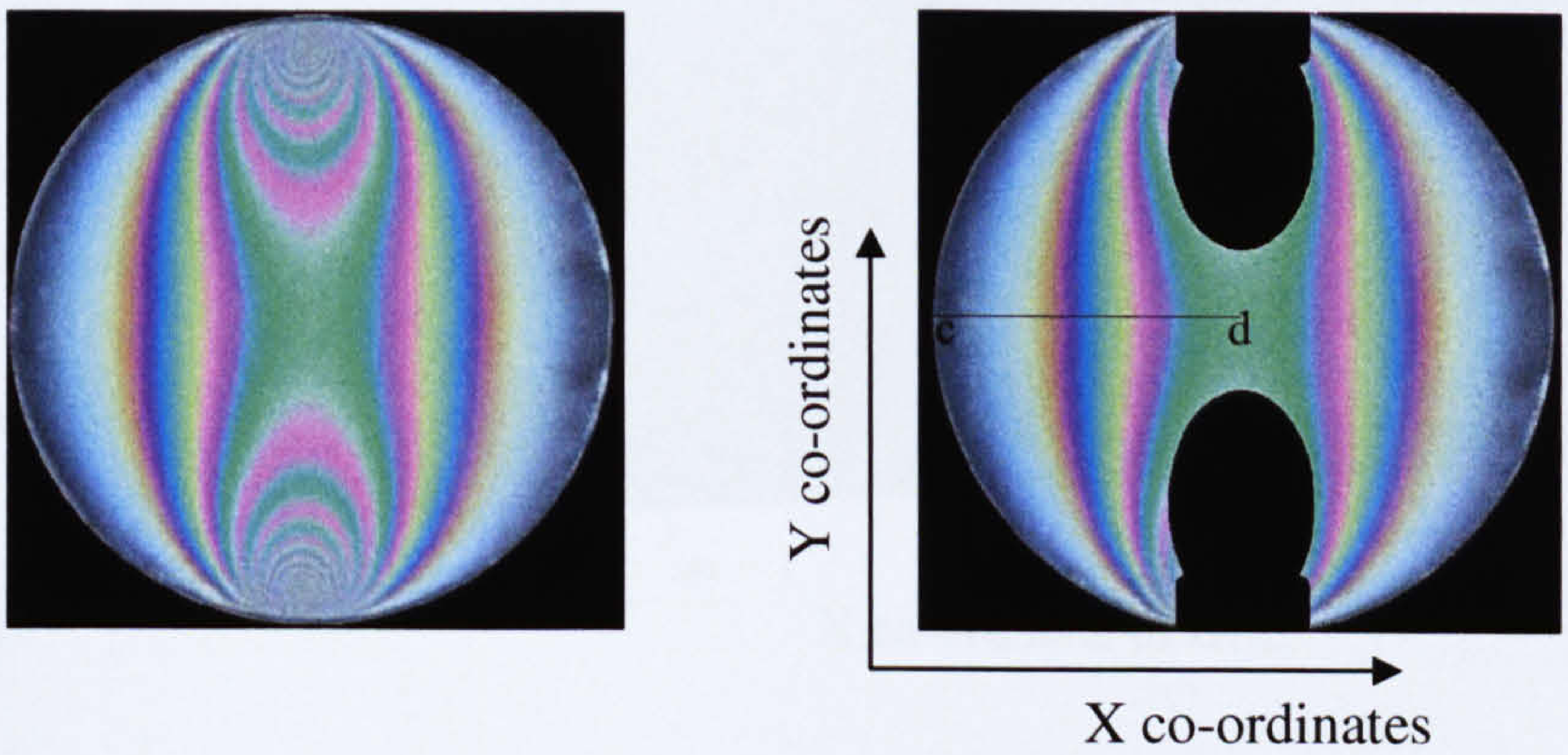

Figure 4-2: (a) Photoelastic image of disc under diametral compression, (b) high stress zones masked

The conventional technique for analysis compares the RGB triplet value at the test point with the RGB triplets stored in the LUT to find the closest match using Equation 2.9. Despite the light source used, the system would be liable to errors due to the colour mismatch and would require some sort of fringe order tracking (Ajovalasit et al. 1995a; 1995b; Quiroga et al. 2002a; 2002b) to accurately demodulate the isochromatics. These techniques require complicated algorithms and are tedious to apply, with only 2D results and not whole field. A simpler technique was proposed and implemented in this research based on median filtering to eliminate all the errors, whilst maintaining the original values of correctly determined fringe orders, to reduce the errors developed in the TFP analysis.

In order to demonstrate the efficiency of median filtering based noise removal the whole field analysis of the test specimen was conducted. During analysis it is most likely that the errors could be distributed over the entire field and significant in certain zones of specimen which would require careful consideration. Figure 4.3 shows a 3D plot of results obtained from LUT based technique over the entire disc from Figure 4.2(b).

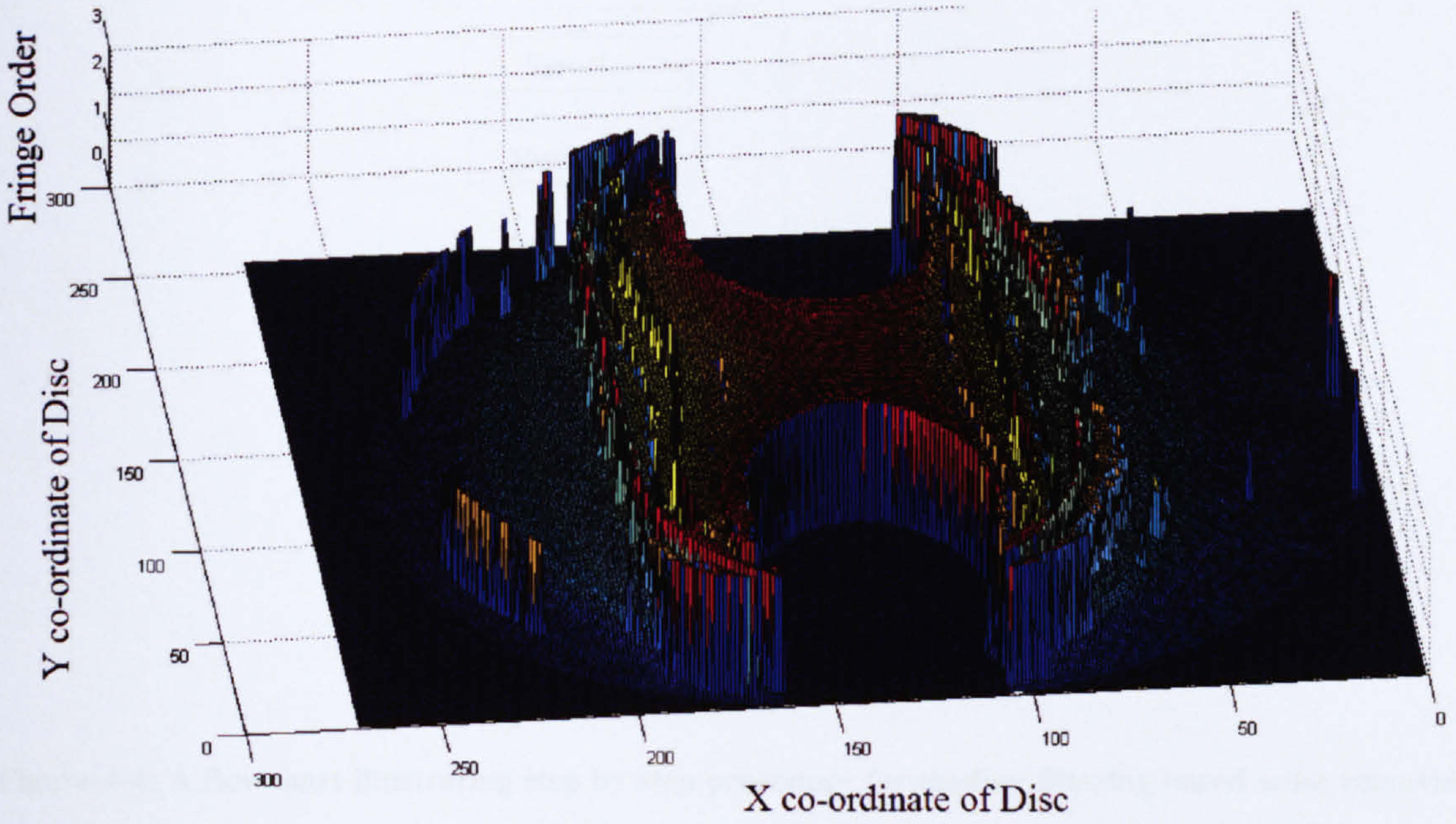

Figure 4-3: 3-D plot of results from LUT based technique using Euclidean cost function

From the above figure it is evident that some fringe tracking algorithm would be required to accurately demodulate all the fringe orders. Method based on median filtering proposed in this research is described below.

4.2.2.1 Noise Removal by Median Filtering

The technique is based on filtering of the results obtained from Euclidean cost function using a median filter, followed by a simple correction threshold to retain the correctly demodulated fringe orders from the Euclidean function. A flowchart illustrating the procedure of the technique is shown in Figure 4.4.

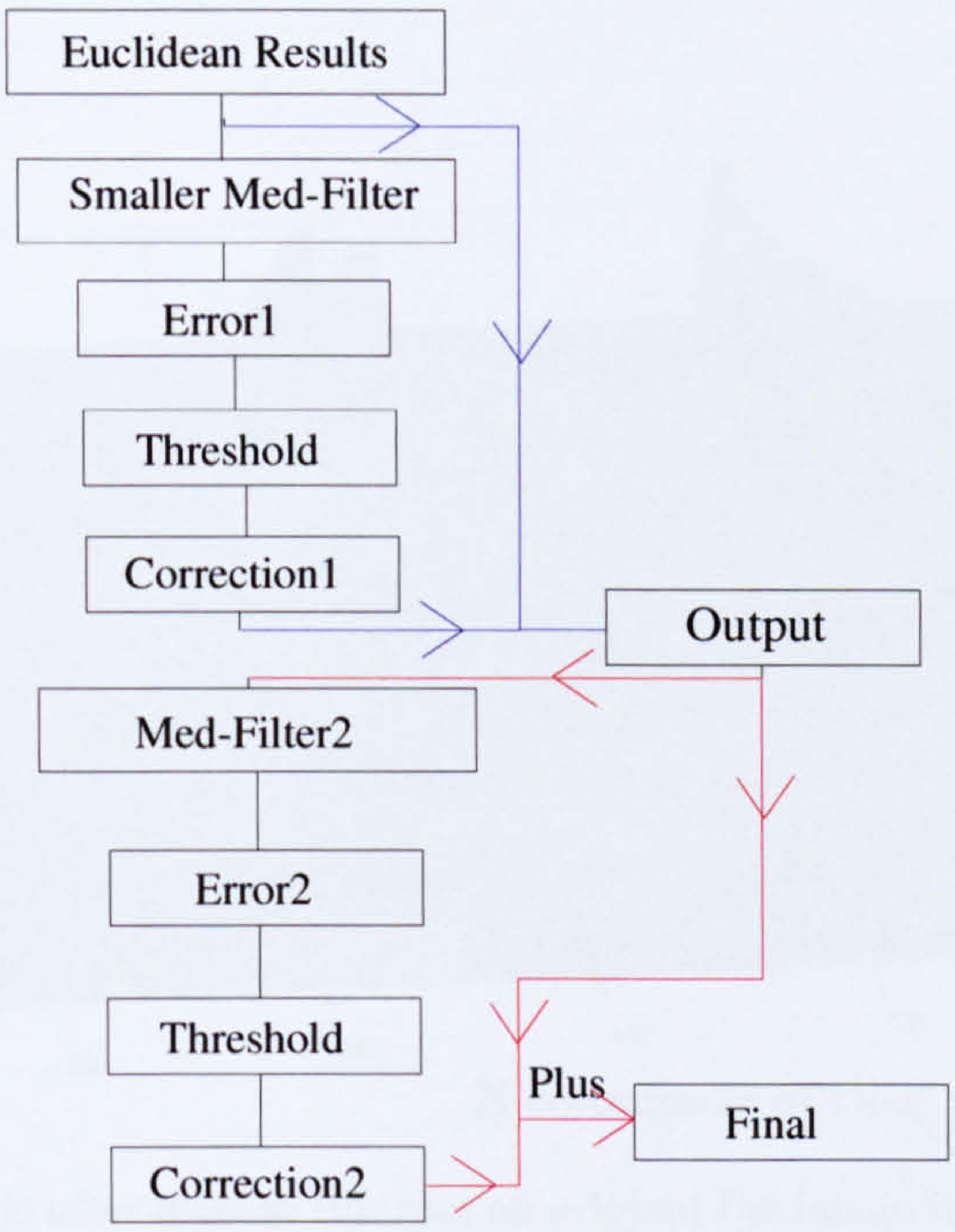

Figure 4-4: A flowchart illustrating step by step procedure for median filtering based noise removal in TFP

The initial results from Euclidean distance from Figure 4.3 are passed to the median filter with a small kernel of size 8 to eliminate sparsely distributed errors. Figure 4.5 shows the continuity in fringe order after applying the median filtering.

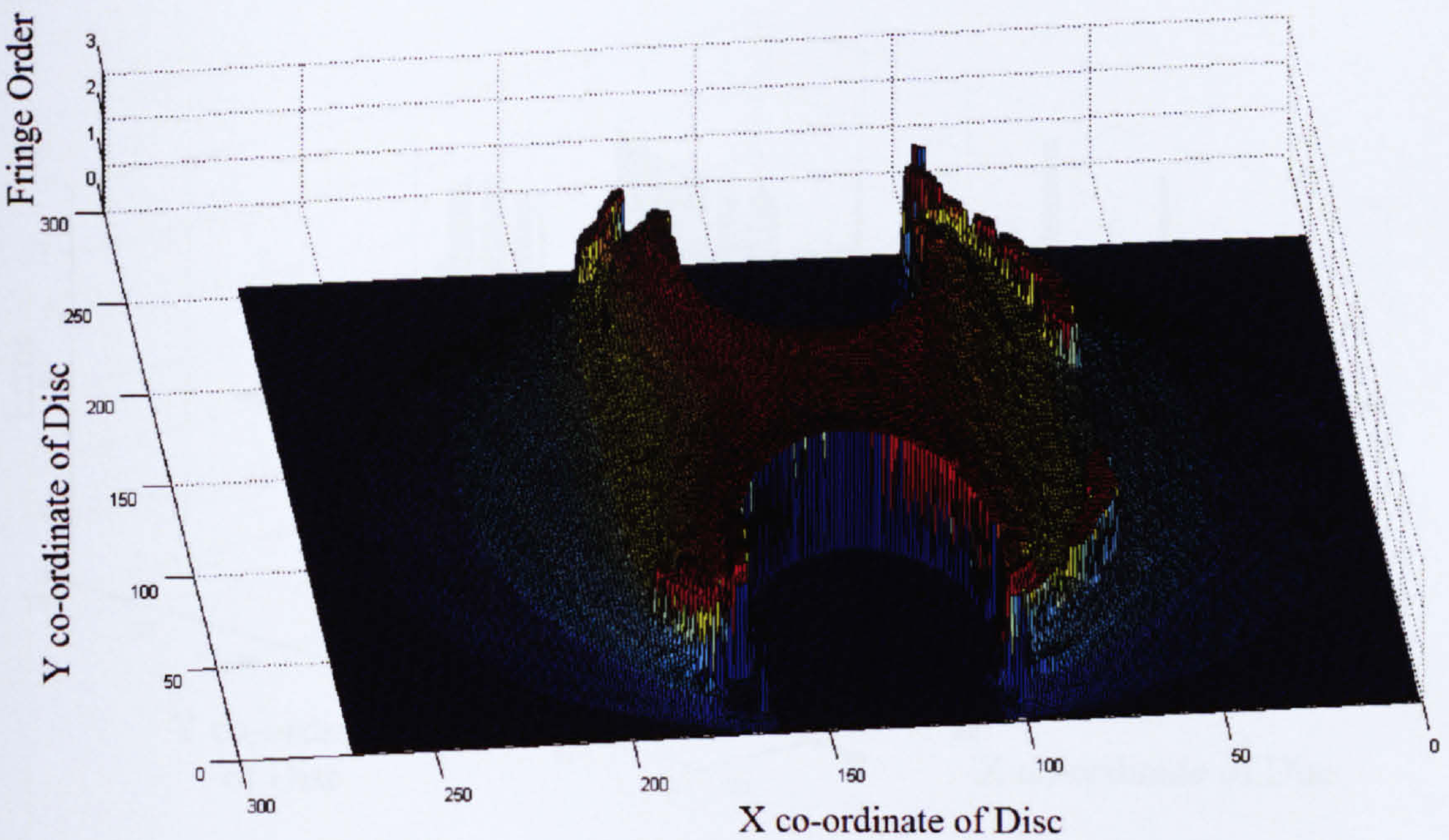

Figure 4-5: Results after median filtering on original Euclidean function results

However, there are two drawbacks; first, the original values of fringe order even at point of correct demodulation have been changed, secondly the dense error zones are still not eliminated. In order to overcome the first drawback, a difference 'error term' between the actual results from TFP and the median filtered results is obtained as shown in Figure 4.6. This represents the difference value at each pixel point. The pixels that were originally demodulated correctly would have changed slightly by median filtering compared to the erroneous pixel points.

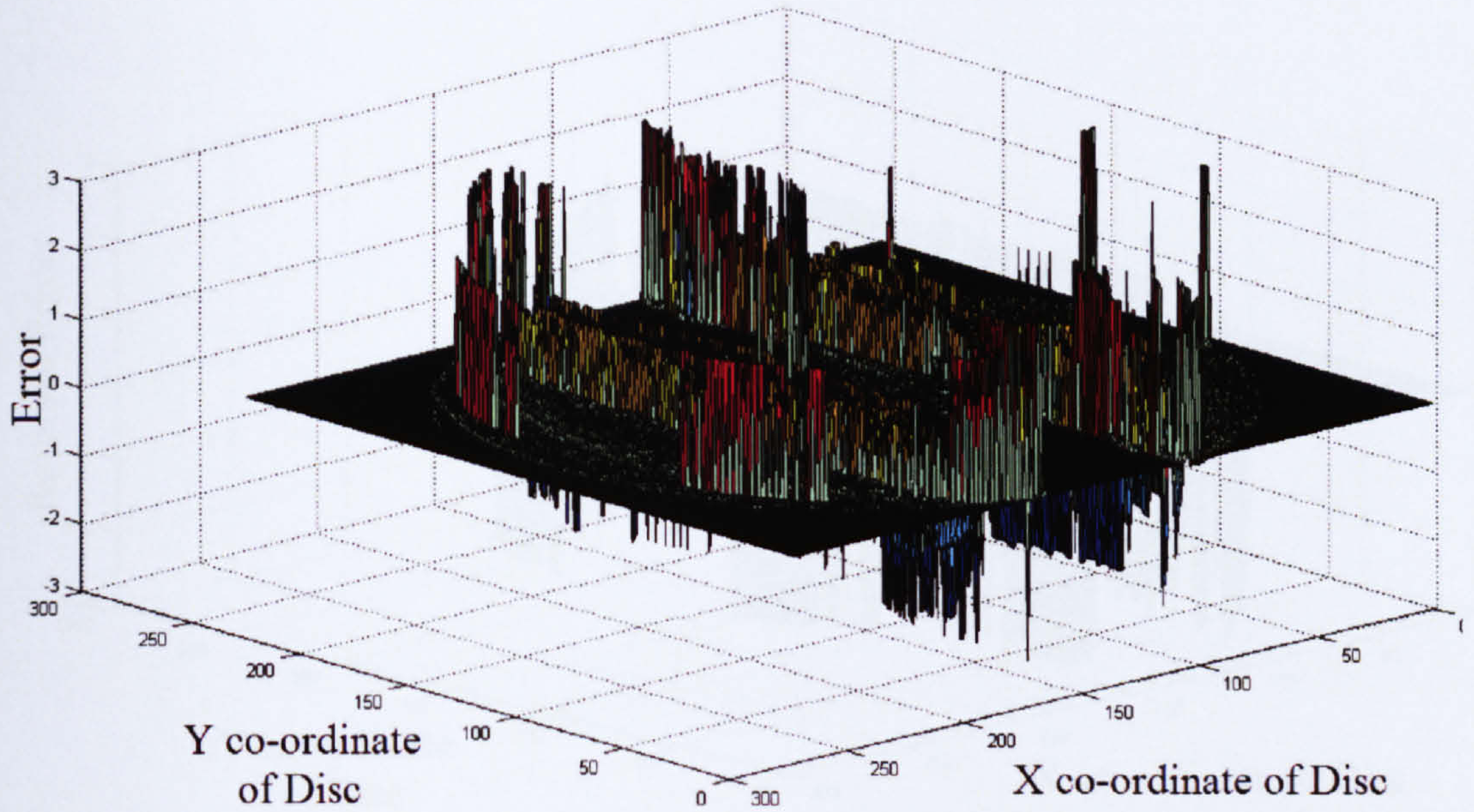

Figure 4-6: The error term obtained from difference of Euclidean function and median filtered results

Now an appropriate threshold is applied to the 'error term' and the values are reversed if it is above the threshold (0.5) otherwise set to zero as shown in Figure 4.7.

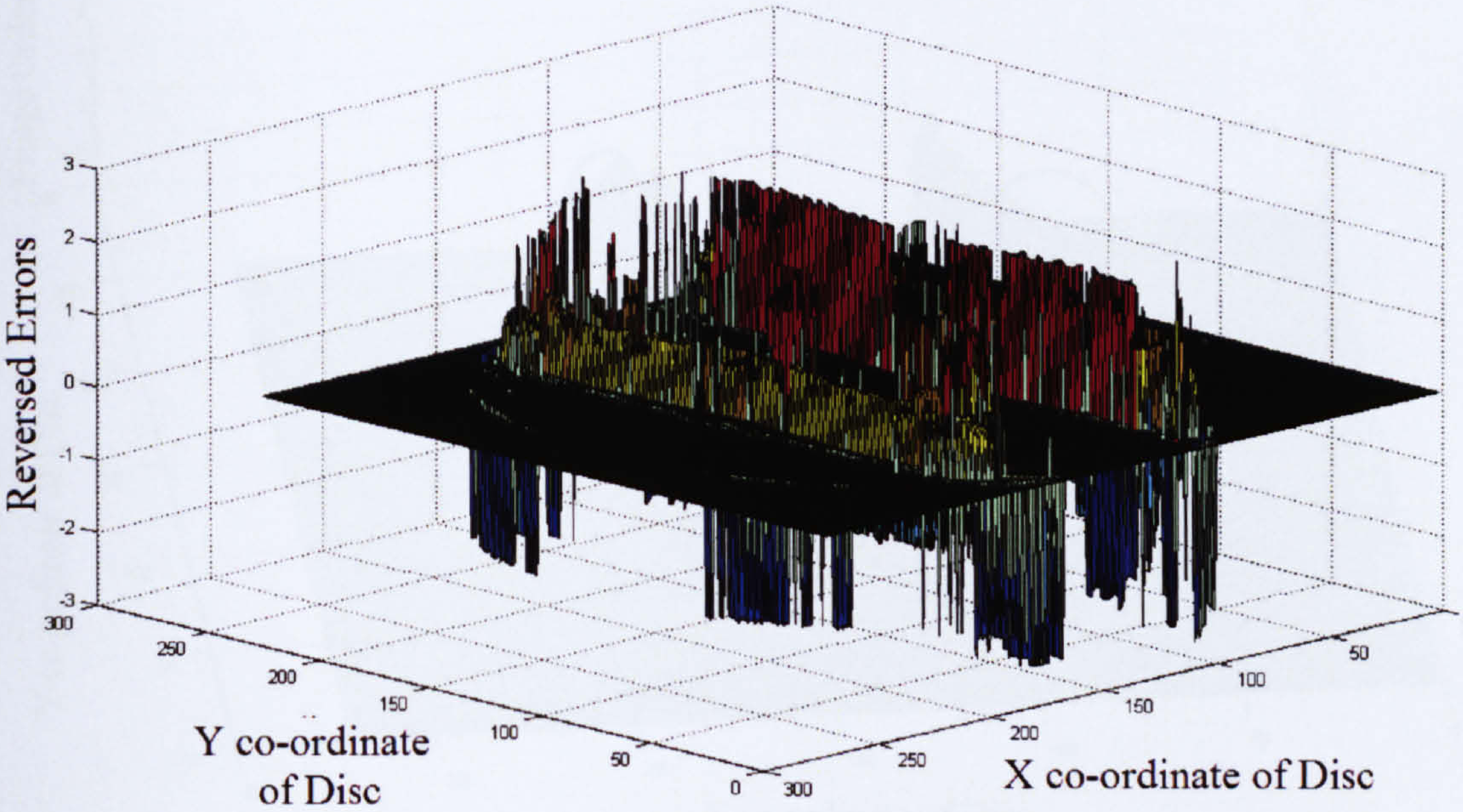

Figure 4-7: 'Modified error term' after threshold and reversal

When this 'modified error term' is added to the actual Euclidean function results, the correctly demodulated pixel points are retained as value of pixel at that point in modified term is zero and the median filtering is only applied to erroneous points as can be seen in Figure 4.8.

The process can be repeated with different thresholds (0.1, 0.2, 0.3, 0.4, 0.5) and would eliminate all sparse errors. Using more than one threshold is not detrimental to the results as the correct fringe orders are not altered irrespective of the value of the threshold used.

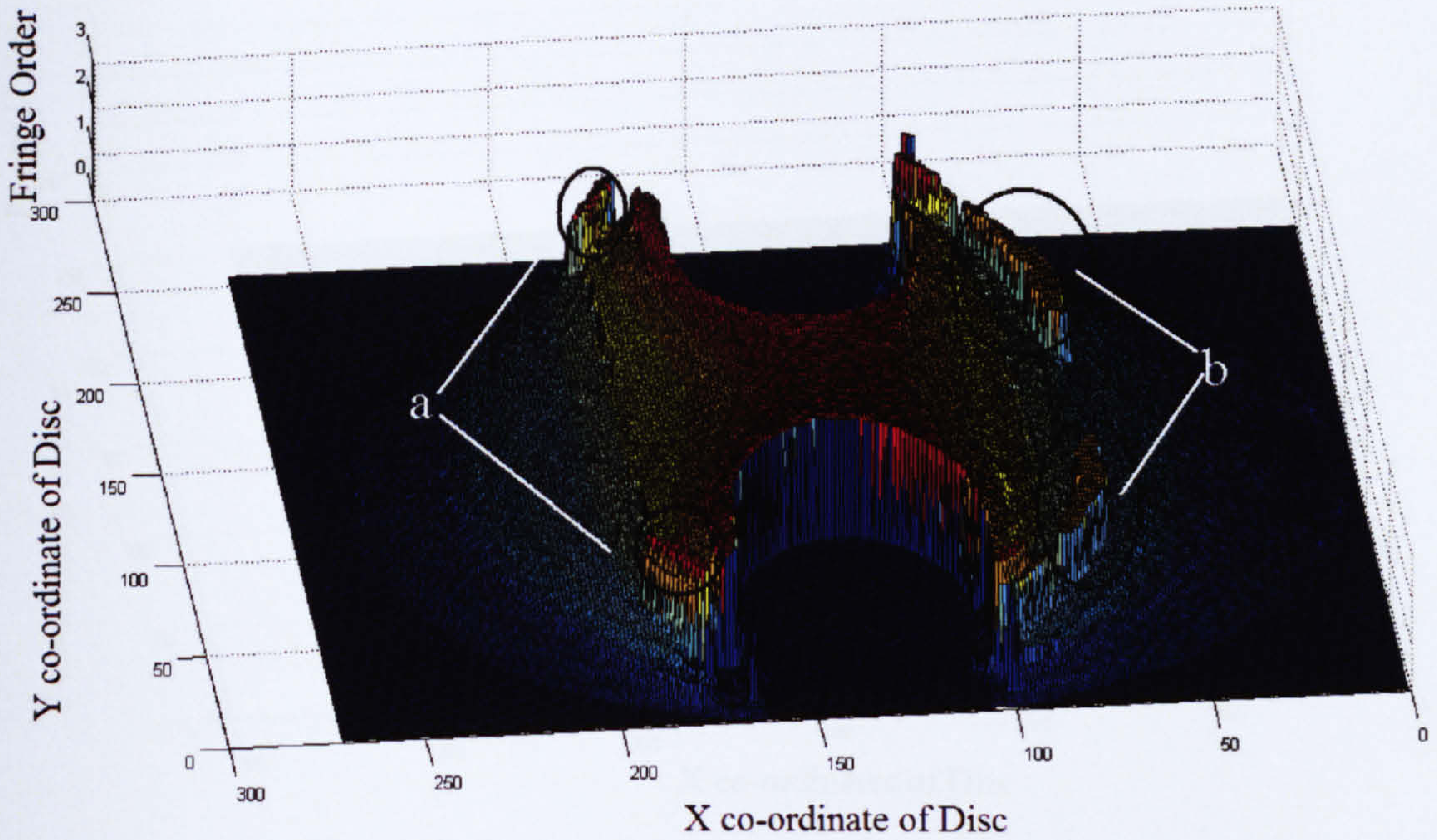

Figure 4-8: Fringe order achieved after eliminating spare errors

The second drawback of big clusters of errors ‘a’ & ‘b’ can be eliminated by repeating the whole process with a larger kernel size on the new results obtained in Figure 4.8. Figure 4.9 shows the ‘Final’ results achieved where both sparse and densely packed errors are eliminated when compared to the actual Euclidean function results in Figure 4.3.

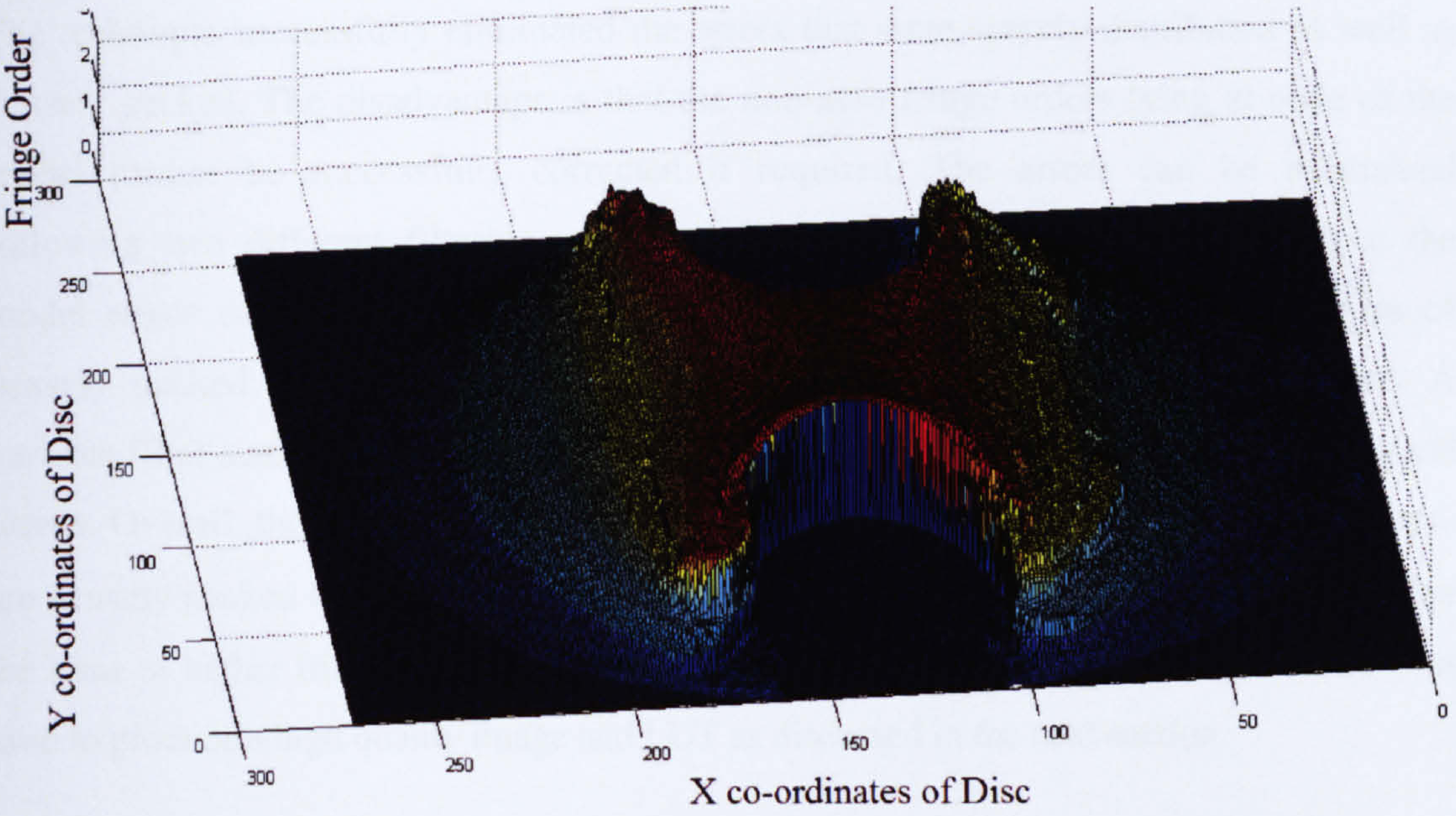

Figure 4-9: Final results with median filtering technique

Figures 4.10 (a) compares the 'Original Euclidean function' and the 'Final' results for line 'c-d' in Figure 4.2(b), and as can be seen only circled section of the results from TFP is modified, clearly illustrating the efficacy of the technique to eliminate the peak errors whilst preserving the originally demodulated correct fringe orders. Figure 4.10(b) compares the Final and the theoretical results, both the curves tend to follow the same function and very close to each other with minimum errors.

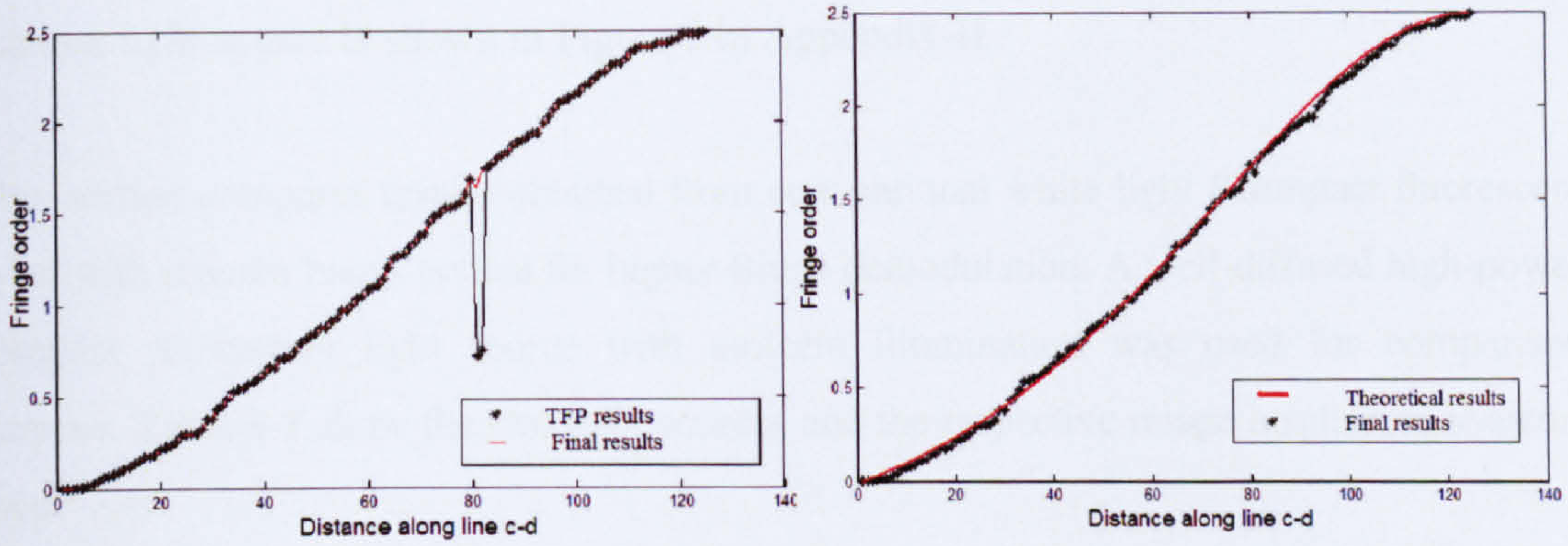

Figure 4-10: Comparison (a) Euclidean function and Final results, (b) Theoretical and Final results

The technique successfully eliminated the errors that were sparely distributed as well as densely packed. The disadvantage is that the non-zero fringe orders lying at edge of the model cannot be successfully corrected if required. The errors can be minimised following two different filtering procedures as done here. Additional padding at the model edges can further help reduce loss of information at the edges. The zones of densely packed errors would not be eliminated completely using this technique. A variable filter size, repeated filtering and error reversal would reduce the errors to a great extent. Overall, the technique is simpler at the cost of a little less accuracy where errors are densely packed but highly advantageous to eliminate sparse errors for $N \leq 3$. To resolve the issue of higher fringe order demodulation, a commercially available flatbed scanner was used to produce a high quality image and LUT as discussed in the next section.

4.3 Fringe Demodulation using Scanner

For applications that require demodulation of higher fringe orders require light source with a higher spectral response and algorithms for fringe tracking and error correction. It was found in this research that implementing scanner as a digital polariscope with a modified error term can provide a portable and inexpensive device for photoelastic analysis up to fringe order five. Implementing scanner also eliminates the need for complicated experimental setup; camera and light source, whilst providing a high spectral response. The RGB spectrum for scanner light source is shown in Figure 2 in Appendix-II.

This section compares results obtained from conventional white light (Compact fluorescent tube) with scanner based system for higher fringe demodulation. A well-diffused high-power compact fluorescent light source with uniform illumination was used for comparison purpose. Table 4-1 show the two light sources and the respective image acquisition systems used.

Table 4-1 Light sources used for demodulation comparison

Setup	Light source	Image Acquisition	Illumination
1	Fluorescent Lamp	Olympus SP 500	Diffused Fluorescent Lamp
2	Scanner-integrated	Scanner-integrated	Cold Cathode Fluorescent Lamp

4.3.1 Comparing RGB Signal Response

The spectral response of a light source for LUT based photoelastic analysis can be evaluated to some extent by the RGB response of calibration fringe patterns. This section compares the RGB signal response for the compact fluorescent tube and the cold cathode tube (scanner).

Figure 4.11 shows the ROI from the model under a bending load and the adjacent plot shows the RGB signals along the calibration line for the Fluorescent diffused light, maximum *N* possible was 4. The RGB signals extended over a considerable range of 0-255, but tend to attenuate with the increasing fringe order making it difficult to identify the RGB triplets.

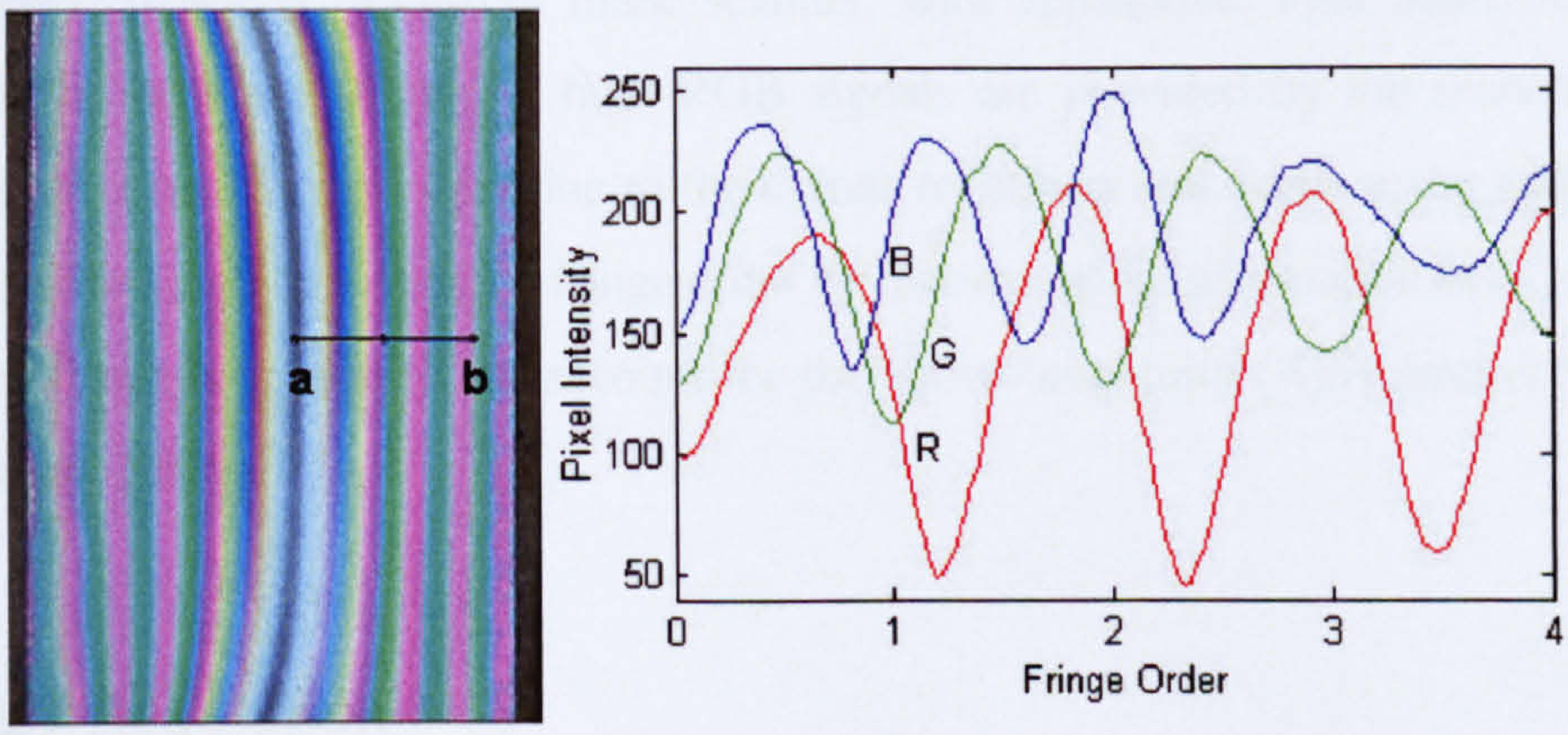

Figure 4-11: (a) Fringe patterns acquired under fluorescent light source, (b) RGB signal response

As discussed earlier, to overcome the problem of RGB signal attenuation a scanner can provide high image quality with low RGB signal attenuation. Figure 4.12 shows the image acquired using the scanner. It can be seen that the image quality is better than the conventional setup. The adjacent figure plots the RGB signal profile across the calibration line 'a-b'.

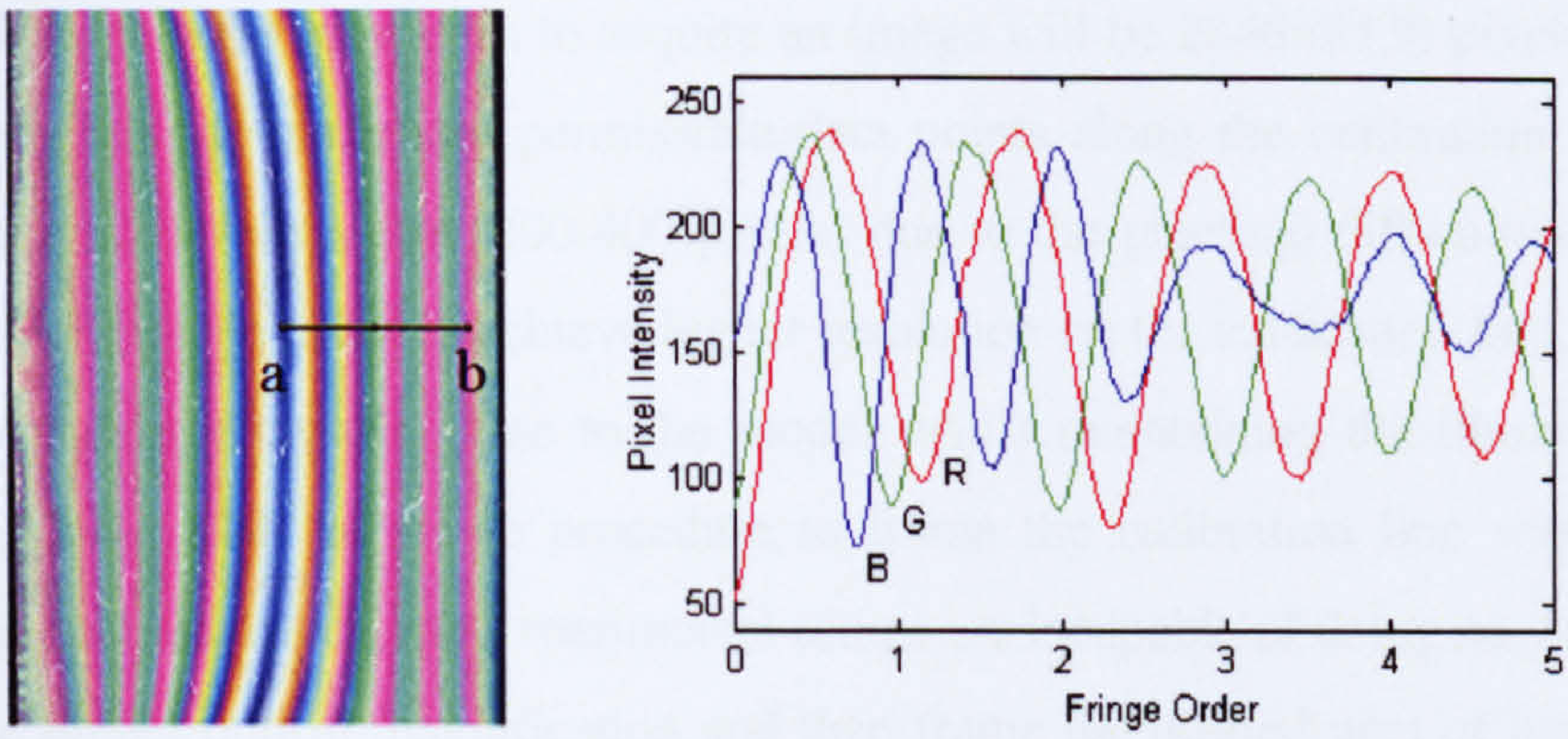

Figure 4-12: (a) Fringe patterns acquired using scanner, (b) RGB signal response

Figures 4.11 and 4.12 clearly show that a scanner can demodulate higher fringe orders and thus provide better LUT as compared to the conventional light sources due to low signal attenuation. This gives a significant advantage for LUT based analysis to achieve higher fringe orders with such a simple approach. A careful visual inspection of the plot in Figure 4.12 shows that the blue intensity signal is attenuating more rapidly as compared to red and green signals. However, a custom made scanner, with appropriate light source can easily overcome this problem. Although high RGB signals are provided by the scanner but the ambiguity of correct fringe order due to the colour repetition still needs to be addressed. A robust algorithm to keep a track on fringe order by incorporating information from previously demodulated points is required to account for the above ambiguity (Ajovalasit et al. 1995a; Quiroga et al. 2002b).

4.3.2 LUT Resolution

Another reported limitation of LUT based calibration technique is low resolution and low bit value of image acquisition systems. In order to generate an accurate and robust LUT it is essential that the cameras with higher resolution and higher bit value should be used, which adds to the cost and effort. The scanner system however, does not require any of the above and is still capable of providing up to 48-bit images. A 48-bit image has 16-bits for each available channel of *R, G* and *B* thus providing 65536 unique values per channel over 256 possible values from RGB cameras.

The maximum possible resolution to acquire an image will be 2848×2136 pixels with a 6M pixel camera, but the maximum permissible data points along the calibration line will be limited to a much lower value (200-400 pixels) due to the practical difficulties of framing such a small region. In order to achieve higher resolution on the calibration line, it would be required to place the camera close to the model whilst maintaining the illumination. It is worth mentioning that the above procedure to frame the calibration line with very high resolution is not trivial and most experimental setups are incapable of doing so. Alternatively, one can use higher optical magnification and then frame the desired area of interest, which increases the distance between model, light and camera. The digital camera used here achieved a fringe resolution of 2e-2 (0.02) compared to 4.5e-3 (0.0045) from of the scanner for maximum fringe order of 4; the fringe resolution is calculated by dividing the maximum produced fringe order by the number of pixels along the calibration line. Since scanner resolution is specified as pixels per inch, increasing the size of model increases the number of effective pixels in the ROI. More importantly, from these data points there were no repetitions of RGB triplets thus all of them had a unique value providing a unique fringe order of up to 5.

4.3.3 Modified Error Term

Since all the possible RGB triplet values cannot be included in the LUT due to various factors including the sensitivity of CCD, material properties, and fringe gradient. The conventional method for fringe demodulation in RGB calibration is achieved by the Euclidean cost function (Equation 2.9). Using commercially available white light source, the results can be quite erroneous even by the Euclidean approach, thus a robust algorithm is required to cope with this problem. The most common technique uses piecewise continuity to keep a track of the determined fringe orders. In order to evaluate LUT based approach it is important to visualise a 3-dimensional plot of RGB calibration curve from the database.

Figure 4.13 shows the plot of database up to fringe order of 4. A closer inspection reveals how tightly packed the database is. The 3-D curve with higher fringe orders gets even more complex and thus prone to errors. From the entire cube of RGB colour space, the database is limited only to a couple of lines which is why during the analysis the test point is usually not available within the database. The Figure 4.13 shows that the database is formed in the shape of helical rings close to each other and the stretching and bunching of the fringe gradient further drift the test point away from its corresponding match in the database making the system prone to errors. This can be explained by assuming the *black* dot as a test point under analysis (Figure 4.13). During the least square search the determined fringe order can be erroneously picked up from any of the closest helix rather than the original match. A light source with higher spectral response can provide demodulation of higher fringe orders but will need advanced algorithms to tackle the fringe order ambiguity due to the colour repetition.

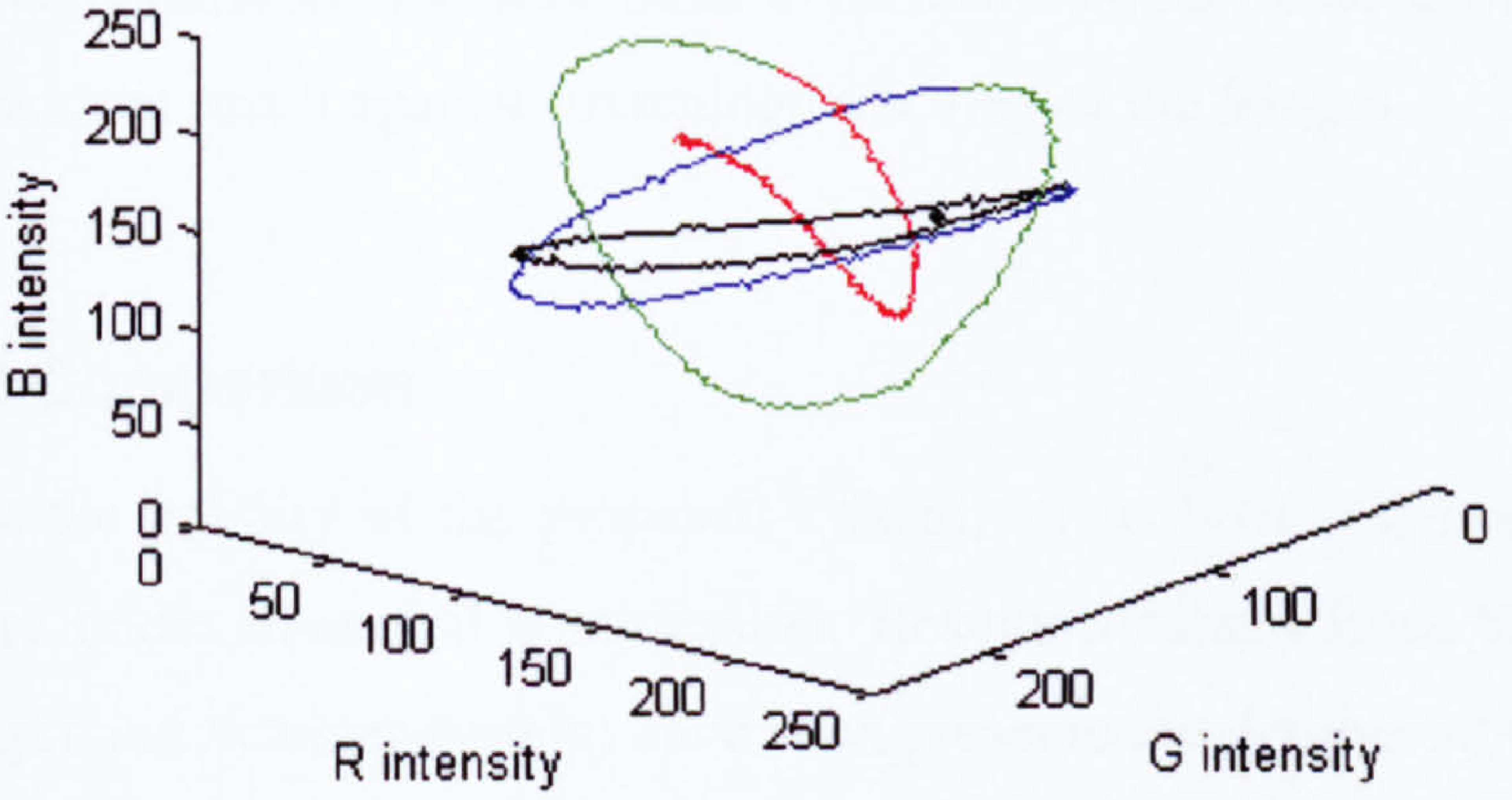

Figure 4-13: A three dimensional plot of RGB triplet from the LUT database showing how closely packed is the database

In this research the standard error term was modified to reduce errors and a simpler technique for error correction by using information from different colour spaces was developed. The conventional Euclidean function uses *R, G* and *B* comparison between the test point and the database, the proposed technique here implements *H, (R-G), (G-B), (R-B)* to be used for least square match. A modified equation with error function (e_h) involving *H, (R-G), (G-B), (R-B)* was used as represented by Equation 5.1 replacing Equation 2.9.

$$e_h = (H_i - H_m)^2 + [|(R_i - G_i)| - |(R_m - G_m)|]^2 + [|(G_i - B_i)| - |(G_m - B_m)|]^2 + [|(R_i - B_i)| - |(R_m - B_m)|]^2 \qquad (4.1)$$

where e_h is the new error function, (R, G, B, H) are the stored colour values in the calibration table, i is the index in the calibration table, and (R_m, G_m, B_m, H_m) are the measured RGBH values.

Since the hue component from HSV/HSI[3] images has the colour information, which represents the gradation of the colour within the visible spectrum of light, change in fringe gradient or slight variation in light intensity does not change the original colour information but only the shade of the colour. Any change in *R, G* or *B* signals is minimised by the difference term rather than their absolute values. Thus choosing *H, (R-G), (G-B)* and *(R-B)* parameters helps in minimising the errors in determining the higher fringe orders. For these reasons *H, (R-G), (G-B)* and *(R-B)* become the appropriate parameters for the search. The benefit of using information from other colour space for fringe demodulation depends on the fringe order to be determined and was found to be better suited for achieving higher fringe orders with consistent result against stretching/bunching of the fringes.

4.3.4 Output Comparison

In order to test the validity of the proposed system, an analysis was performed for the problem of disc under diametral compression. Results obtained from the two systems (Fluorescent light and Scanner system) have been presented to demonstrate the advantage of scanner system.

4.3.4.1 Fluorescent Tube

The results are good up to fringe orders of 3, beyond this the merging of colours occur which cannot be resolved by this technique. Figure 4.14(a) shows the disc image taken under the diffused fluorescent light source and Figure 4.14(b) is the corresponding fringe order obtained by the RGB Euclidean approach.

---

[3] Hue-Saturation-Value/Intensity

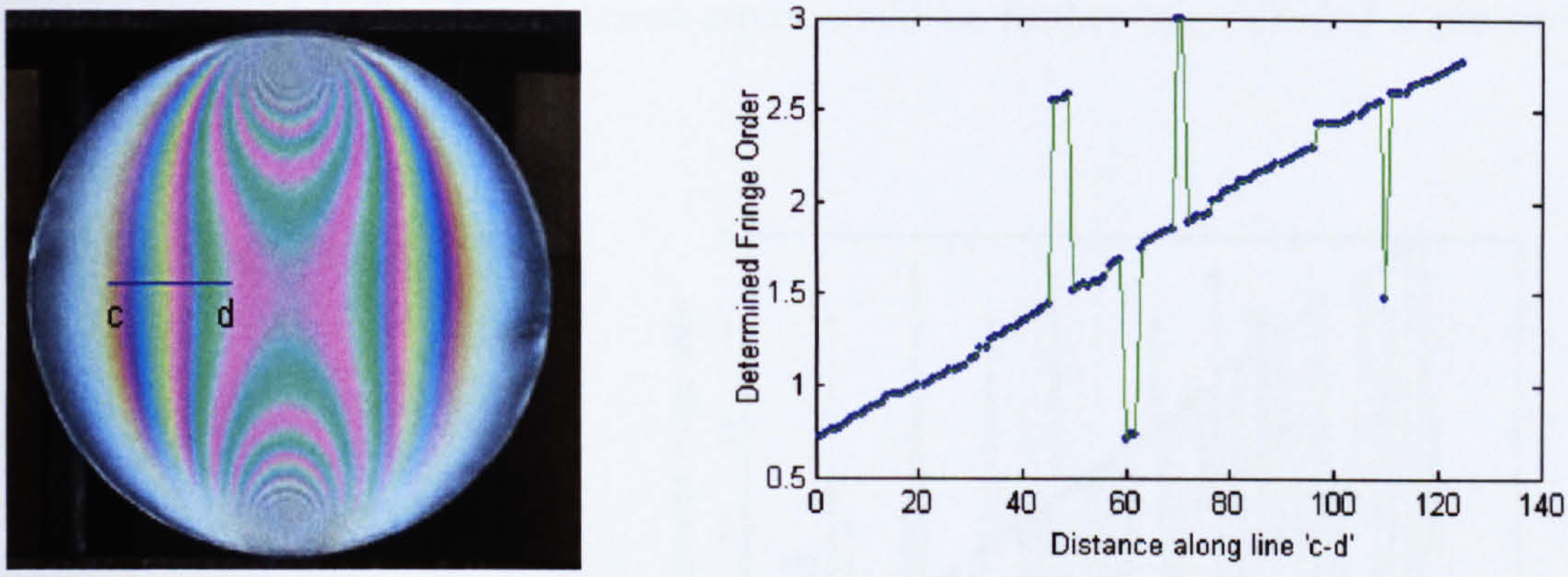

Figure 4-14: (a) Test image from fluorescent light, (b) fringe order determined by RGB match

Figure 4.14 shows the demodulation for higher fringe orders using fluorescent light source and standard Euclidean function. The errors are far more due to the colour mismatch and require fringe tracking algorithms. The median filtering technique for noise removal proposed in previous section would not be sufficient as the errors are too dense and clustered.

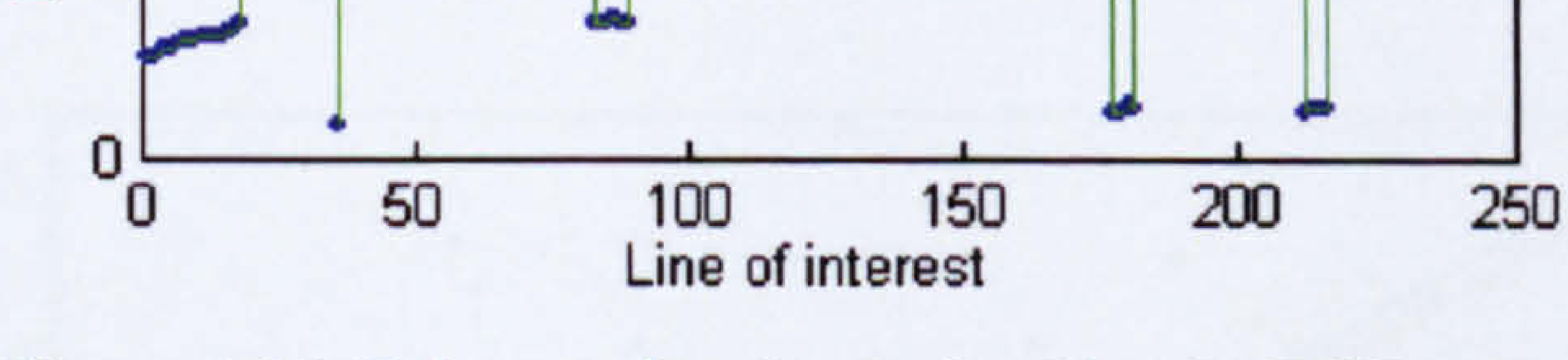

Figure 4-15: Fringe order determined by the RGB match

4.3.4.2 Scanner Based System

The results using the scanner system with colour information from other colour spaces were found to be accurate compared to the previous results. Figure 4.16(a) shows the test image acquired using flatbed scanner. Line 'c-d' on the disc is analysed for fringe order. Using the modified error function e_h for the closest match the errors were suppressed as seen in Figure 4.16(b). The scattered errors could be further minimised if a piecewise continuity is used.

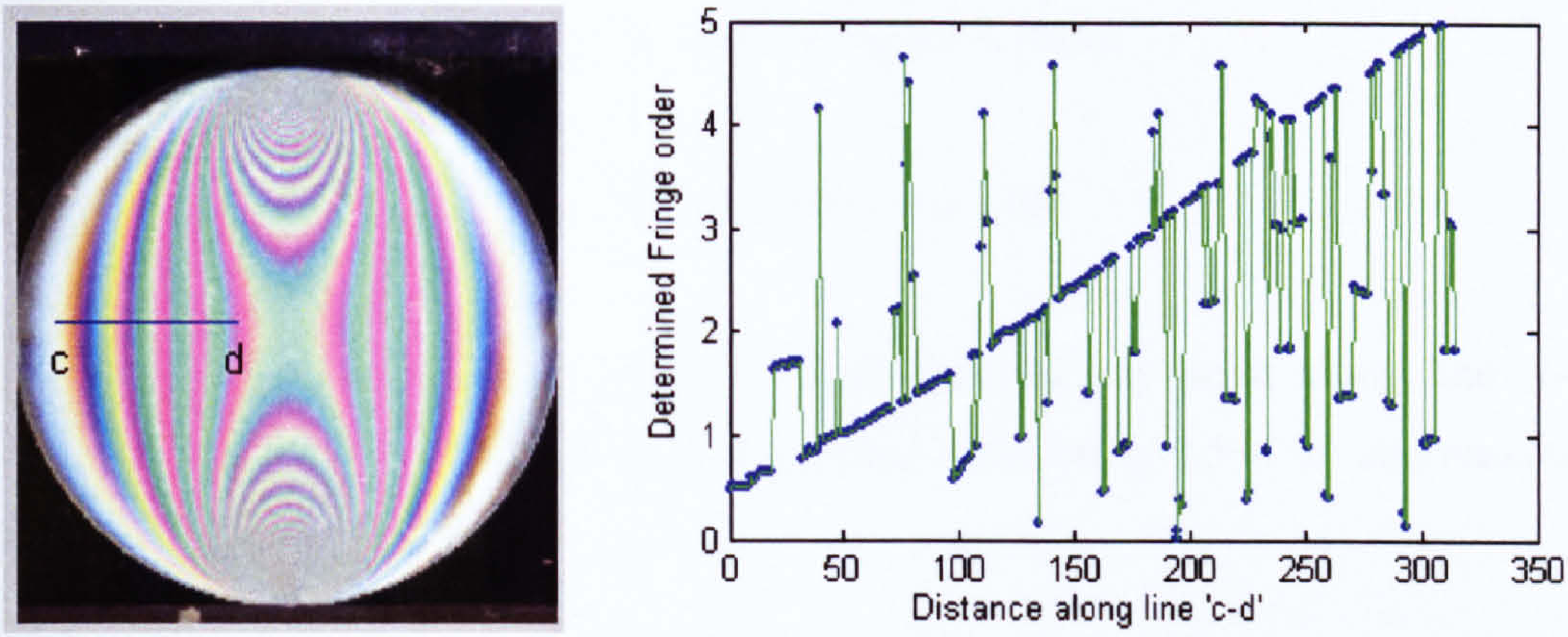

Figure 4-16: (a) Test image, (b) Fringe order determined by eh function

To develop a robust system, a curve fitting approach was adopted and the errors were further suppressed. A cubic polynomial was fitted to the results (excluding the scattered points) to obtain an equation for determining the fringe order. The technique was used to minimise the errors for a line profile on the image, which was representative of the stress variation over the model, however, for any irregular stress variation to cover the entire image, the same technique can be applied by splitting the entire curve into ascending and descending trends and analysing them separately.

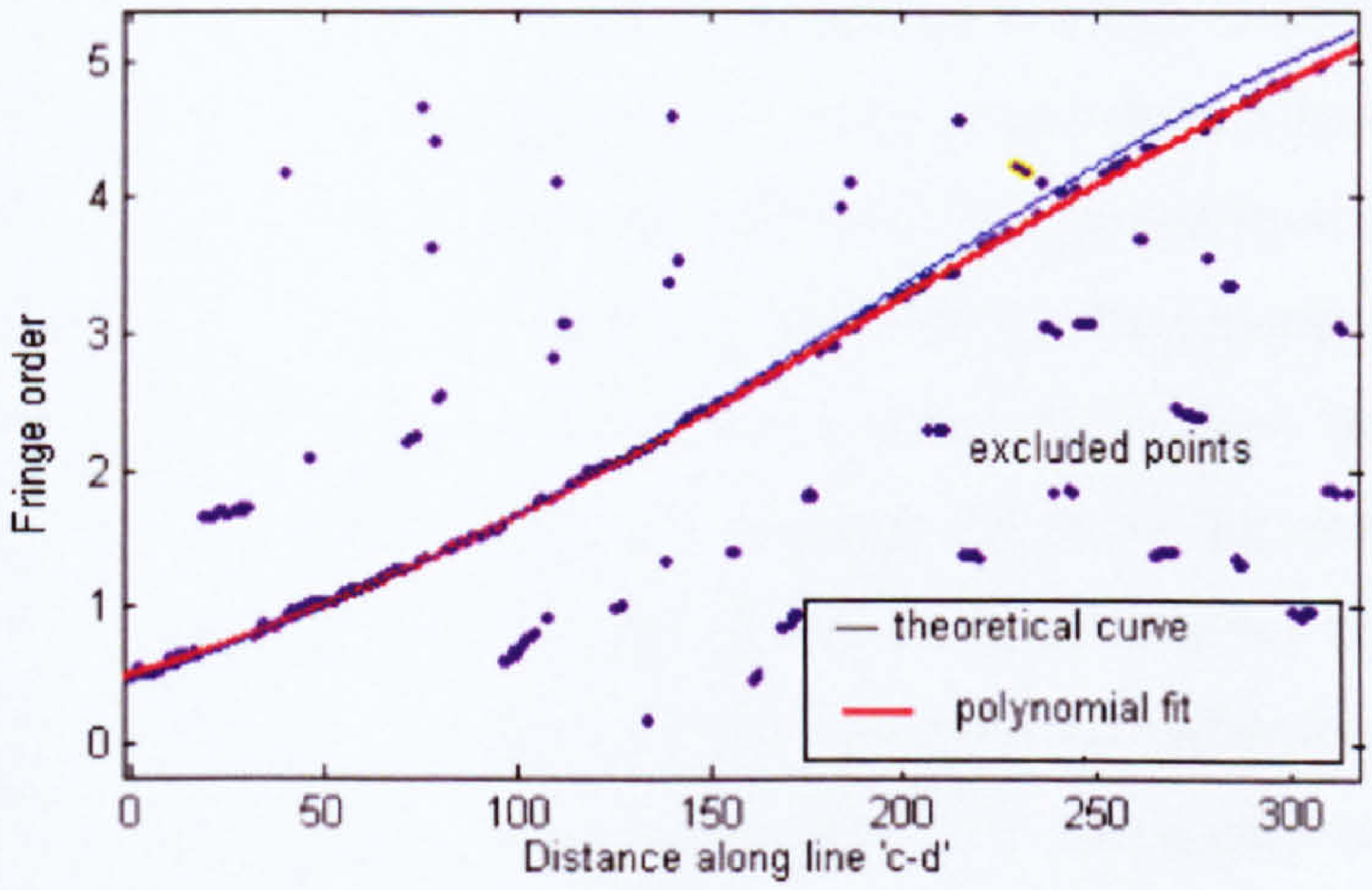

Figure 4-17: Comparison of theoretical and experimental fringe orders

Equation 4.2 represents the polynomial curve and Figure 4.17 shows the polynomial curve through the data points (thick/red line through the data points) and the blue line representing the theoretical results. Using this equation fringe orders can be accurately determined excluding the erroneous peaks in Figure 4.16(b).

$$N = -(7.49e-8)x^3 + (4.44e-5)x^2 + (7.99e-3)x + 0.5 \qquad (4.2)$$

This equation can be used to find the fringe order at any point along line 'c-d' by substituting the pixel number of the point, fringe order being 0.5 at 'c' and maximum at point 'd' in the shown plot.

As can be seen in Figure 4.17, a slight difference does exist between the theoretical (thin blue line) and the actual curve; this is inevitable due to difference in fringe gradient of the calibration LUT and the actual test specimen. The results validate our presumptions that the LUT based technique, being the fastest demodulation techniques, can be implemented effectively using a scanner. Since the experimental data is very close to the theoretical curve, the determined fringe order will be accurate. In the current implementation the minimum absolute error in the fringe order was found to be 8.15e-4 and maximum error was 0.041.

Since calibration is done on linear data and the test data is non-linear, the RGB calibration system is subject to errors when compared to phase-shifting method. A better LUT can be developed if calibration is done using an arc-shaped model (Quiroga et al. 2002a). The load is incremented in steps and data is collected from a section of image with uniform stress, the next loading-step represents the incremental fringe order. This means slow incremental steps can provide a better LUT; also better demodulation algorithms can cope with fringe gradient changes and make the systems less prone to errors. However, the results obtained using 16-bit channels were not significantly different from 8-bit channel results as suggested (Ramesh 2000). It was rather found that information from other colour spaces, better noise filtering algorithms and appropriate light source play an important role in accuracy of the technique.

4.3.5 Advantages of Scanner Based System

Use of the flatbed scanner as a device for photoelastic fringe demodulation gave advantages in many aspects. First of all, it does not require a digital camera and can still provide resolution up to 10 Million pixels per square inch (3200 dpi). More importantly, a 6M digital camera is not capable of framing 2848 pixels across the selected calibration line, whereas a scanner does not require any settings such as zoom, focus, aperture or shutter speed to generate sharp images with high clarity. The diffused light source scans over entire model with uniform illumination and as the scanning is performed at a close proximity, this makes the system insensitive to geometric variations. Further, there is no need to devise a new experimental setup and the whole process is simple and easy to implement with no experimental constraints. It is also insensitive to the surrounding light sources unlike the conventional techniques, which require great care in maintaining lighting conditions for the RGB calibration systems. Finally, due to the high spectral response of scanner, higher fringe orders up to 5 can be demodulated without any special light source requirement and the system is portable, cost effective and highly efficient. The only drawback of this approach is the time required to scan the image. Image acquisition could be time consuming and can take up to several minutes if very high resolution is required, however the choice of resolution is user dependent. The scanner system can be used as an educational system for demonstrating the LUT based photoelastic analysis technique.

4.4 Photoelasticity for Unconventional Loading

This section considers the use of conventional photoelastic techniques of LUT based analysis and phase shifting under unconventional loading situations to evaluate their efficacy in sensing applications. A low modulus photoelastic material is deformed in z-plane to induce photoelastic effect. The results obtained under these conditions are discussed with their limitations when used for sensing. Finally a case study has been conducted to analyse a foot image and conclusions drawn from this have been presented.

4.4.1 Experiment Preparation

The PS-4 photoelastic material (Table 3-1) has been used in these experiments, having low modulus which makes it ideally suited for the intended sensing application. The details of the experimental setup are described in Chapter 3 section 3.5.5 including the sensing element design and its layout (Section 3.2.3). For the intended sensing the photoelastic material was laid out horizontally in the form of a sensing plate to induce photoelastic effect when loaded. The sensing element was loaded under the vertical and shear forces with specifically designed indenter (Section 3.5.3). The fringe patterns obtained from loading the sensing plate with indenter heads and acquired using scanner based image acquisition system are shown in Figure 4.18.

Due to the physics of the experimentation, the applied vertical load on the surface of photoelastic model would induce circular fringe patterns panning out from the point of loading. Under ideal conditions similar fringe patterns are generated for all the four indenter heads at a particular vertical load. However, even slightest uneven loading from the weights or mechanical flaws in the indenter design combined with high sensitivity of material leads to un-identical fringe patterns.

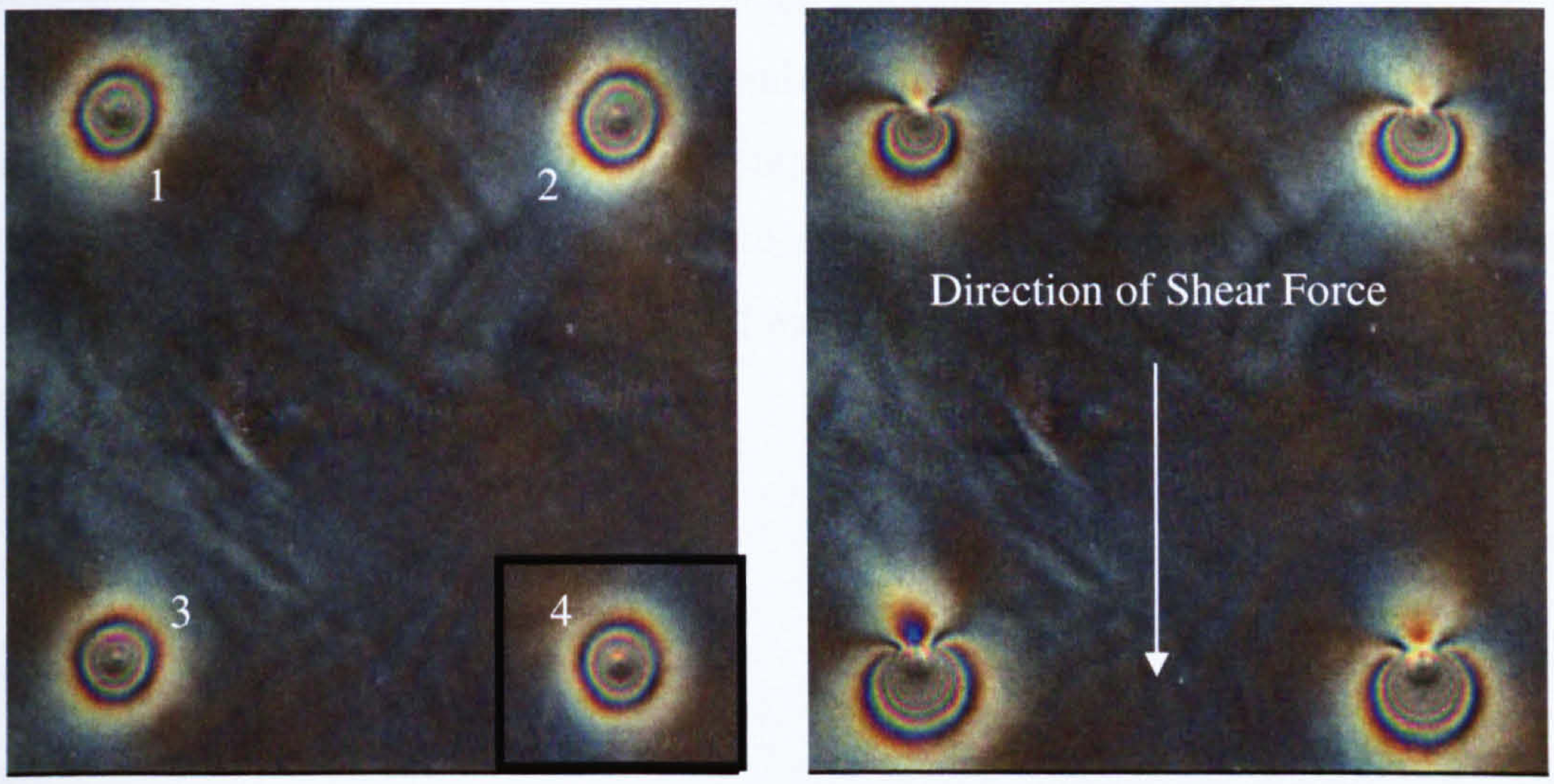

Figure 4-18: Fringe patterns under (a) vertical load of 17.5 N and,(b) shear load of 15.2 N

Figures 4.18(a) and Figure 4.18(b) show the fringe patterns developed under the indenter heads for a vertical load of 17.5 N and a shear load of 15.2 N respectively. When shear load is introduced – the fringe patterns appeared different for the front two heads compared to the rear two heads, since the shear force was applied at a point and not on the plane.

Even though the photoelastic material has been glued to the polycarbonate sheet and acts as coating but there is no transference of strain from the object to the coating as under conventional photoelastic experiments. Instead the photoelastic effect is induced due to deformation of material in z-plane, thus the photoelastic effect is appreciable even outside the point of indentation. It is this property of the photoelastic material to visually represent the effect of the load that makes it ideally suited for sensing and can be exploited for measuring vertical as well as shear forces. These images are representative of a whole-field sensor where the entire area covered can be mapped against the stimulating forces.

4.4.2 Fringe Analysis using Look-Up Table Technique

The modified LUT based calibration technique discussed and developed in the preceding section of the Chapter was used for determining complete fringe order for fringe patterns obtained under the vertical load. For the purpose of illustration only the fringe patterns under one indenter head (indenter 4) were analysed. Figure 4.19(a) shows the fringe patterns obtained under the vertical loading with determined fringe order along line a-b in Figure 4.19(b).

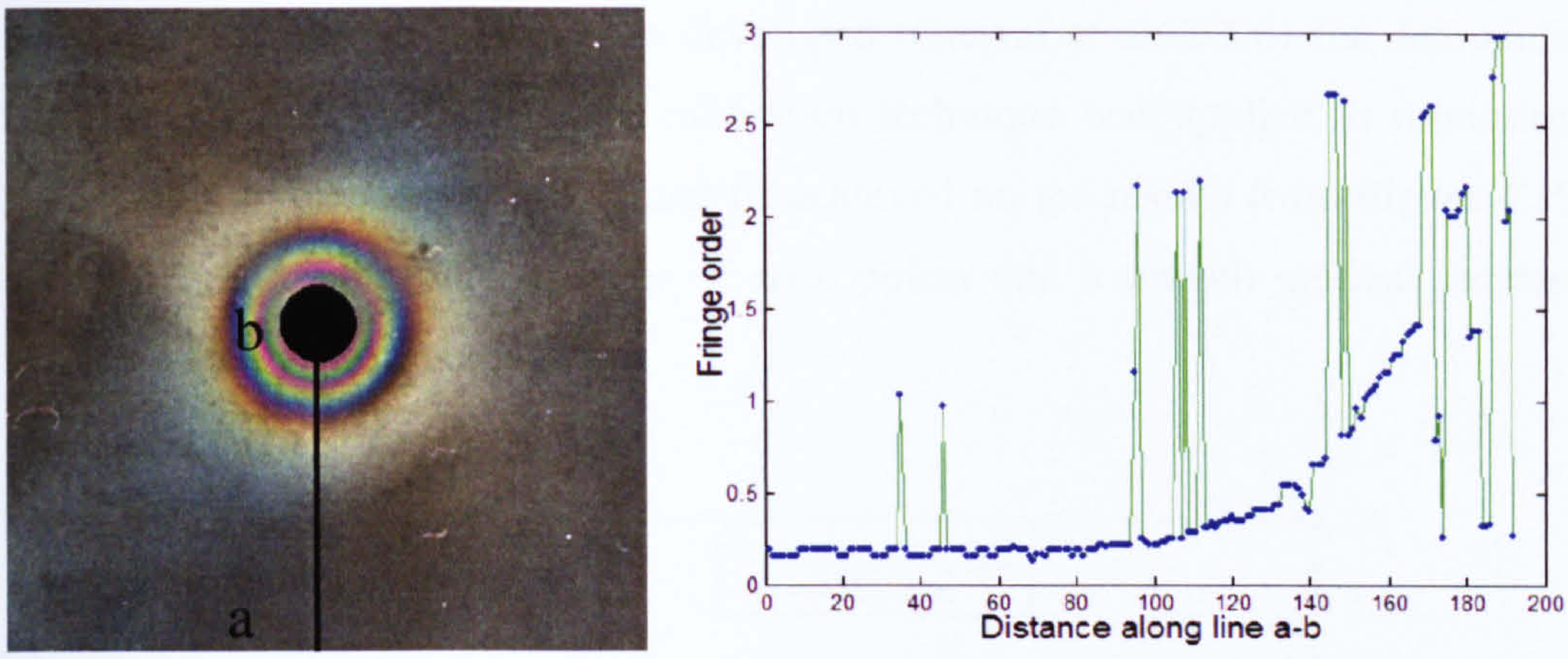

Figure 4-19: Fringe order determination under unconventional loading (a) fringes due to indenter loading, (b) fringe order plot for line a-b

The fringes induced under the indenter head are not pronounced since the load was applied in an unconventional manner. Therefore, stress information cannot be extracted accurately from this region. Thus, the centre of patterns was masked due to stress concentration and limited fringe information under the indenter head.

As can be seen the determined fringe order had limited accuracy in terms of maximum fringe order due to the following main reasons;

1. The LUT based technique being less accurate compared to phase shifting. The accuracy of results is limited by the technique itself in addition to the type of light source and the image acquisition system used.
2. The unconventional loading of surface deforms the material to a great extent thereby the colour chat of LUT that is prepared through conventional loading (C-shaped specimen) does not truly represent the colours being induced under such a deformation; this compromises the accuracy of the results obtained.

3. The fringe patterns generated under surface loading through the indenter are densely packed making the analysis more difficult and thus require alternative techniques for analysis.

However, the enhanced technique as developed (Grewal et al. 2006) for demodulating fringe patterns through LUT based calibration technique was applied to minimise the errors. Figure 4.20 shows a polynomial fit achieved on the results from Figure 4.19(b), this significantly reduces the number of error points and a smooth gradual increase in fringe order can be achieved.

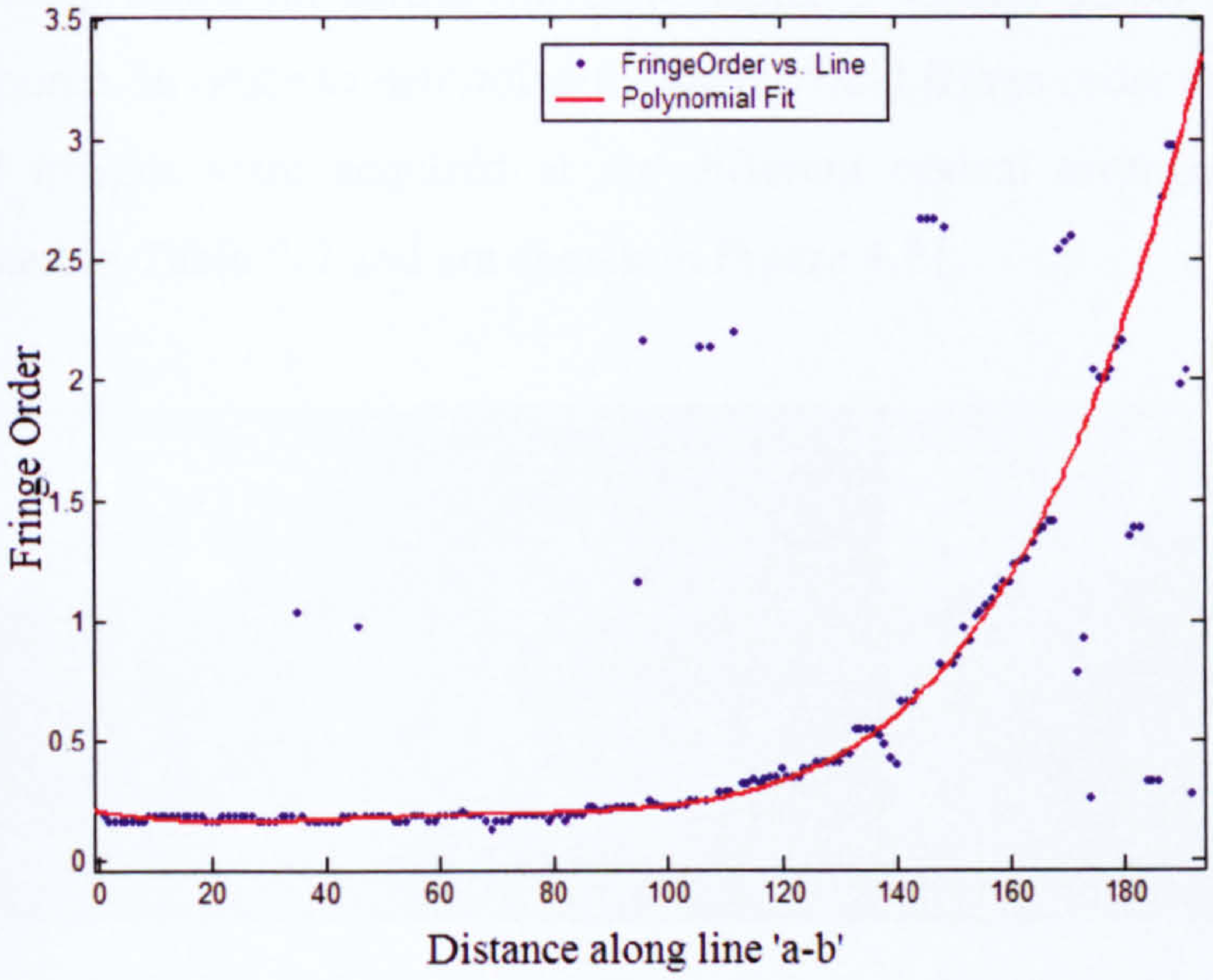

Figure 4-20: Complete fringe order determined by curve fitting

The results obtained in Figure 4.20 can be integrated over a range of $0^0 - 360^0$ to achieve fringe order for the entire ROI. However, due to inherent limitations of RGB calibration technique coupled with densely packed fringe patterns (from unconventional loading) this technique cannot be relied upon for accurately demodulating the fringe patterns.

4.4.3 Phase Shifting for Unconventional Loading

To overcome the limitations of LUT technique in demodulation of densely packed fringes phase shifting was used. This study should show the capabilities of phase shifting and how far it can be implemented for load determination. The technique was applied only to the fringes induced from the vertical load, however, the results would lead to the conclusion that if the technique is useful for vertical loading it can be equally applied for the fringes induced from shear forces.

4.4.3.1 Phase Map

For phase shifting the fringe patterns under the indenter head ‘4’ were acquired using the experimental setup based on partial mirror (Chapter 3 section 3.5.3) using fluorescent tube as light source. In order to determine the whole field fringe order for the entire ROI, phase stepped images were acquired at six different optical arrangement of circular polariscope listed in Table 2-2 and are shown in Figure 4.21.

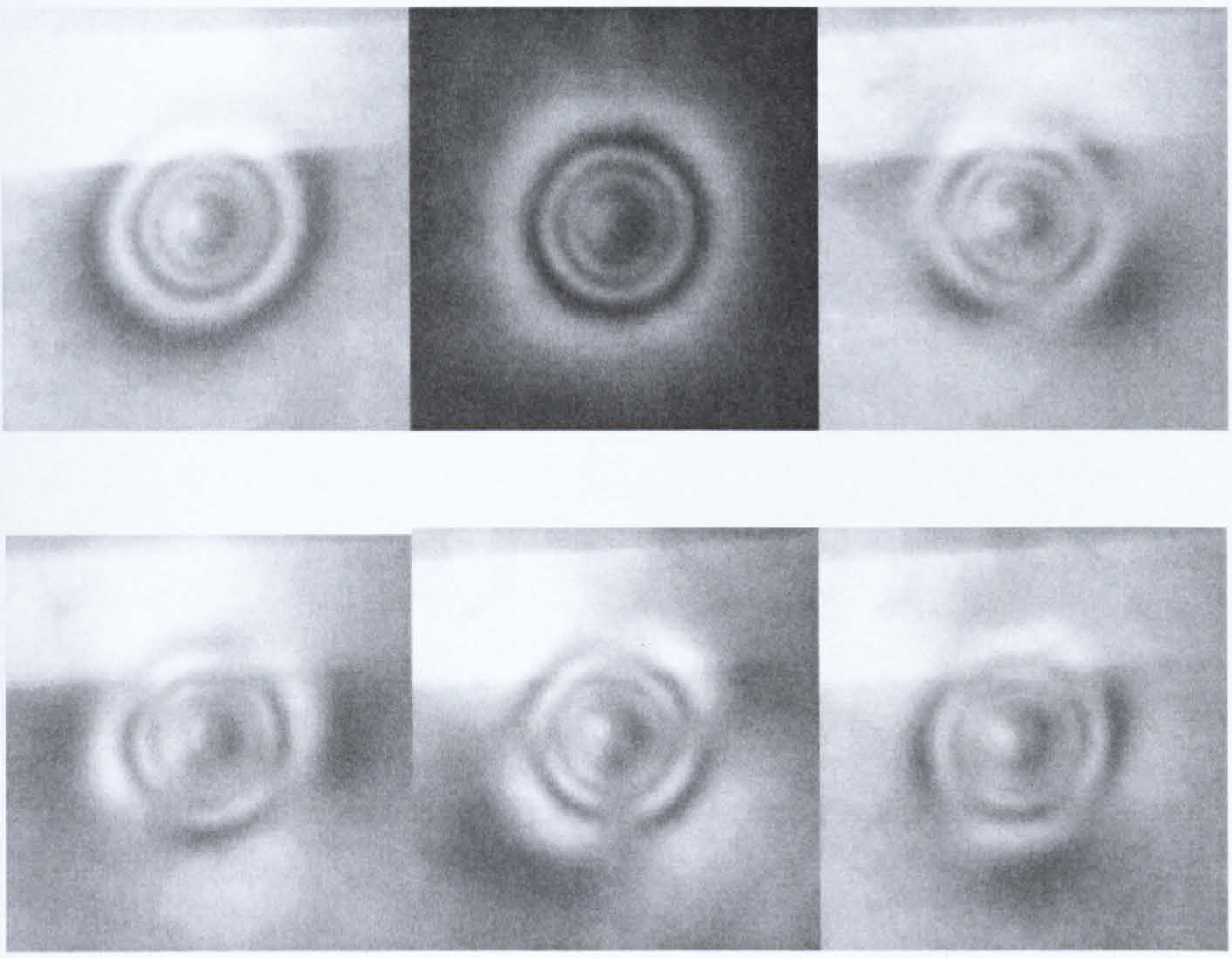

Figure 4-21: Six phase stepped images acquired under white light for optical arrangement of elements as tabulated in Table 3.2, reflections of light source and glare due to partial mirror can be observed

The central region of the fringe pattern has the highly stressed zone, however as can be seen, the photoelastic effect in this region is the least due to the indenter head pressing in the z-plane of model.

The experiment revealed that the images acquired under white light were of low contrast due to presence of a partial mirror in the design of experimental setup and the rotation of optical elements caused glare and ghost images of the light source; causing a significant loss in image quality. However, the effect was found to be less prominent with the use of custom designed monochromatic light (Chapter 3 section 3.4.). Figure 4.22 shows six images from the monochromatic light which gave better fringe patterns in terms of image quality and contrast compared to white light.

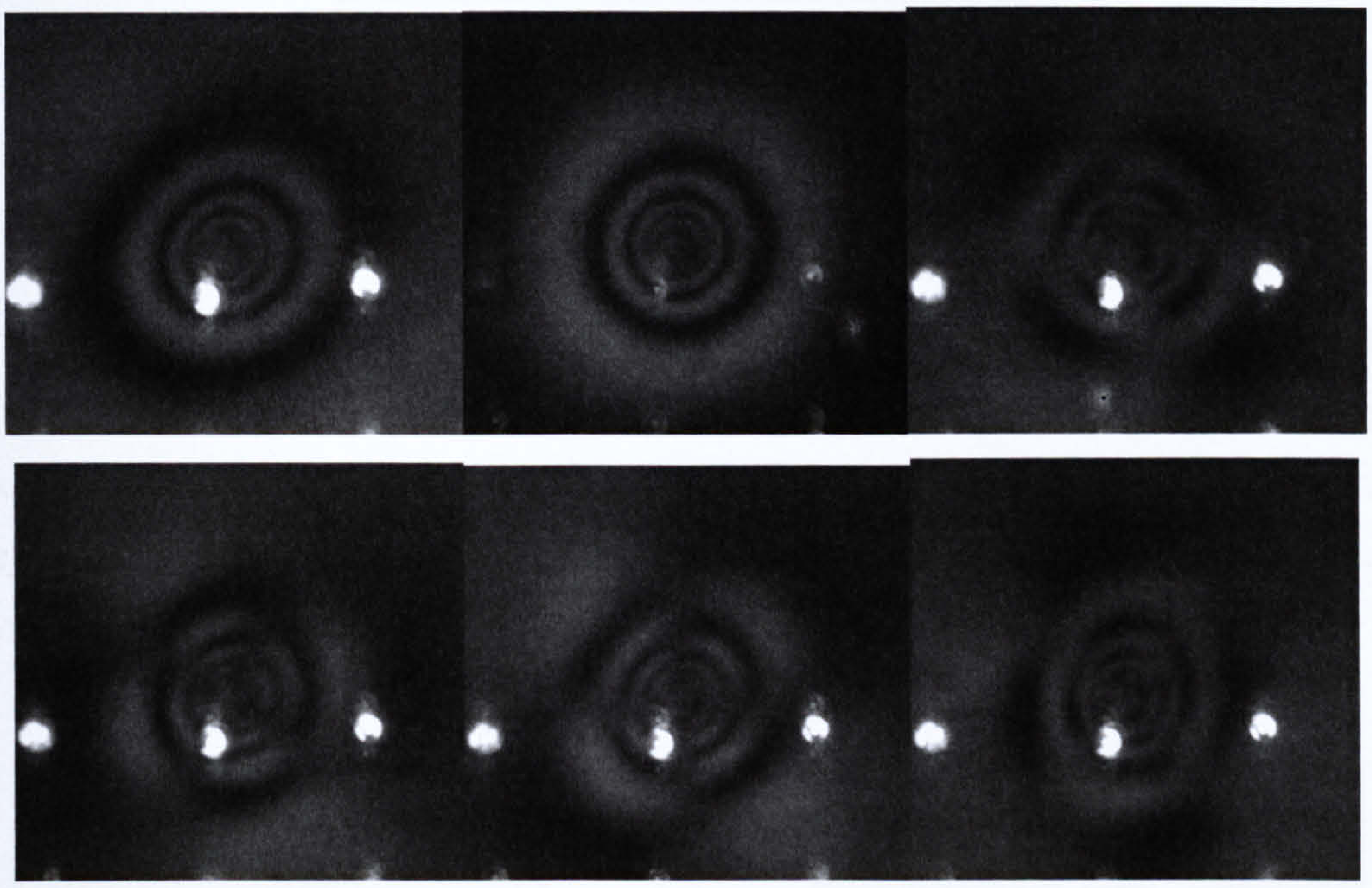

Figure 4-22: Phase stepped images acquired using partial mirror setup under monochromatic light of 589 nm

Using Equations 2.9 & 2.10 (Chapter 2), the phasemap for isoclinics and isochromatics was obtained as shown in Figure 4.23 and 4.24. The isoclinics were influenced by the model geometry, the point of application of load and the relative retardation as a result of the applied load.

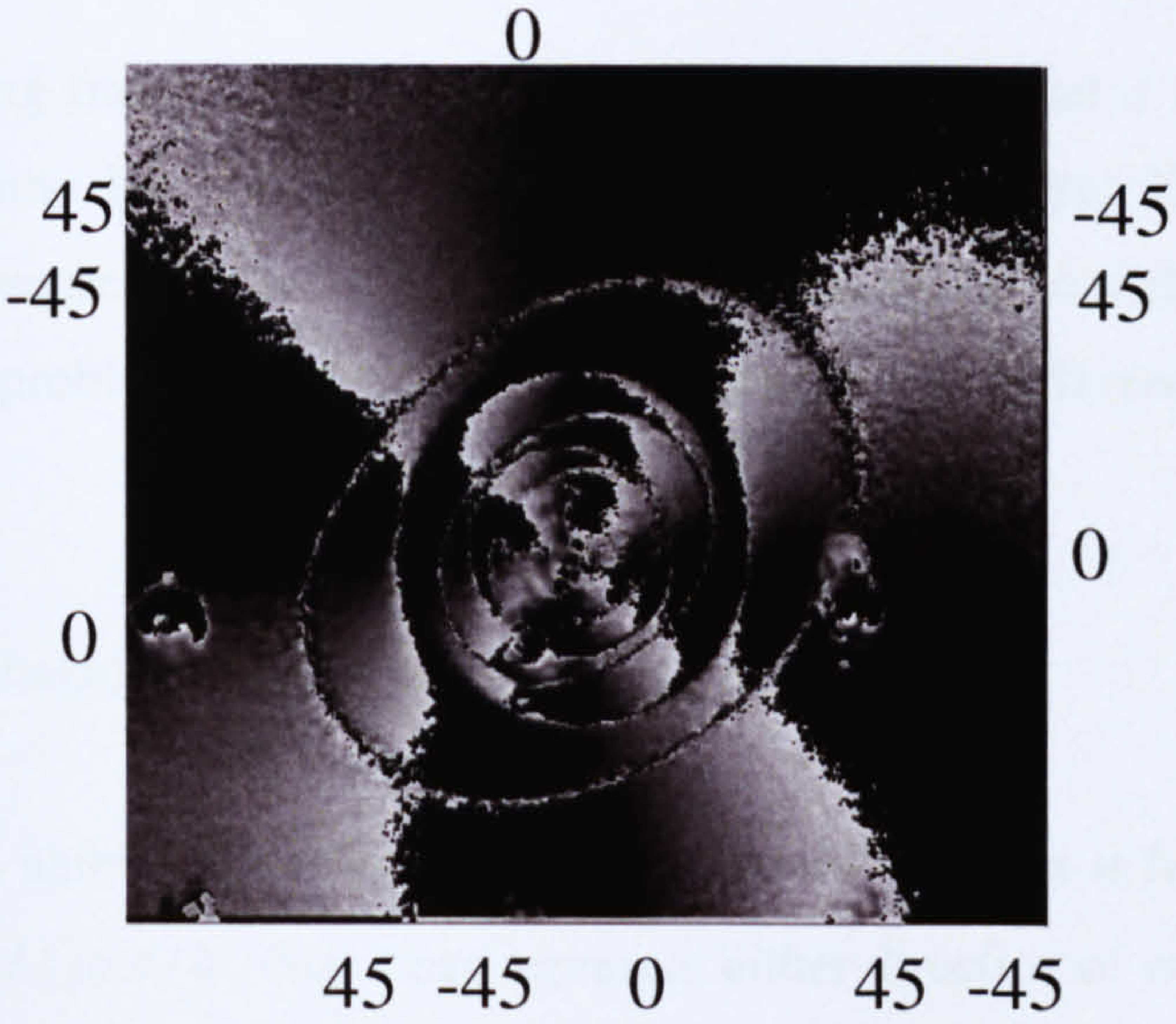

Figure 4-23: Isoclinic phasemap using monochromatic light with orientation

The isoclinic and isochromatic phasemap obtained appear to be elliptical in shape as opposed to expected circular shape, this can be attributed to the errors induced from the alignment of the optical elements during phase stepping. A fully controlled precise workbench is required to conduct this experiment to minimise this error, however, the effect will persist if the initial image under the load itself is elliptical due to unsymmetrical loading.

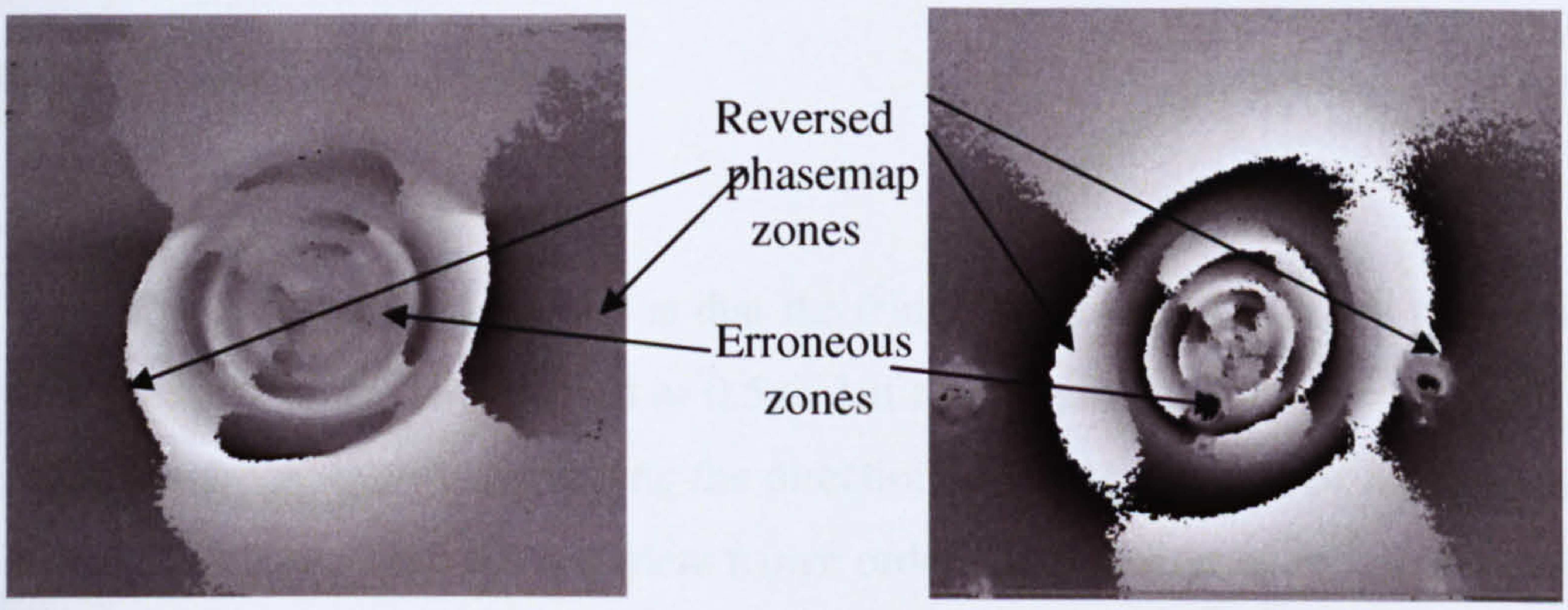

Figure 4-24: Phasemap for isochromatics with reversed zones and high error zones, (a) white light, (b) monochromatic light

The phase map obtained under monochromatic light source in Figure 4.24 is of higher quality than white light. However, as opposed to the expected phase map of radially (inwards) increasing fractional fringe order both phase maps had a reversed fractional fringe order at some locations and erroneous output elsewhere. This has been also reported in the literature (Ramesh 2000) for some models like disc with a hole. Therefore, to investigate this problem the experiment was repeated with different orientation of the optical elements.

The unexpected behaviour of the phase map was found due to;

1. The ambiguity in determination of the isoclinic as it falls in the range of $-\pi/4$ to $\pi/4$, thus it can represent either direction of σ_1 or σ_2.
2. Equation 3.10, is sensitive to fast or slow axis of the model, for which results can be erroneous and in certain zones phasemap can appear reversed.

These drawbacks were overcome by using the modified Equation 4.3 for determination of isochromatics, this Equation is insensitive to fast or slow axis of the model.

$$\delta = \tan^{-1}\left(\frac{\pm\sqrt{(i_5-i_3)^2+(i_4-i_6)^2}}{(i_1-i_2)}\right) \tag{4.3}$$

The limitation of using Equation 4.3 is that the fringe order can only range between 0 to 0.5 if the positive square root is used or 0.5 to 1 if the negative is used rather than 0 to 1. Therefore, the advantage of identifying the direction of fringe gradient from the Equation 2.10 is lost, thus to achieve the complete fringe order the direction of fringe order is now required. For fringe patterns induced in these experiments the fringe order always increases radially from edge of the ROI towards the centre, thus complete fringe order can be obtained by phase unwrapping using an algorithm.

Figure 4.25(a) shows the phase map obtained using Equation 4.3 and Figure 4.25(b) is the fractional fringe order along line 'a-b' under a monochromatic light source. The spots appearing in Figure 4.25(a) are the reflections of LEDs used as monochromatic light source.

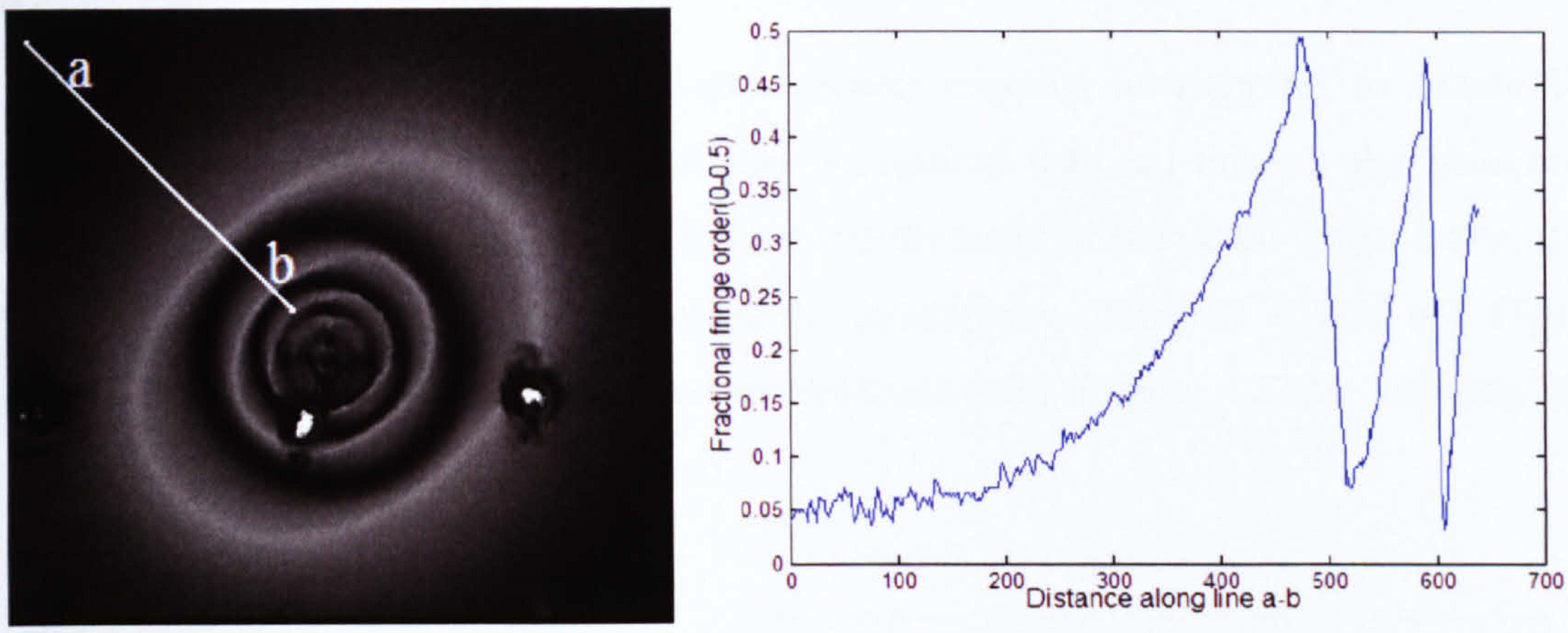

Figure 4-25: (a) Phasemap obtained under monochromatic light with partial mirror setup, (b) fractional fringe order along line a-b

Figure 4.26 shows the results of the experiment repeated with a different load and without partial mirror to investigate if there was any considerable difference in the phasemap quality as this would eliminate the light source reflections.

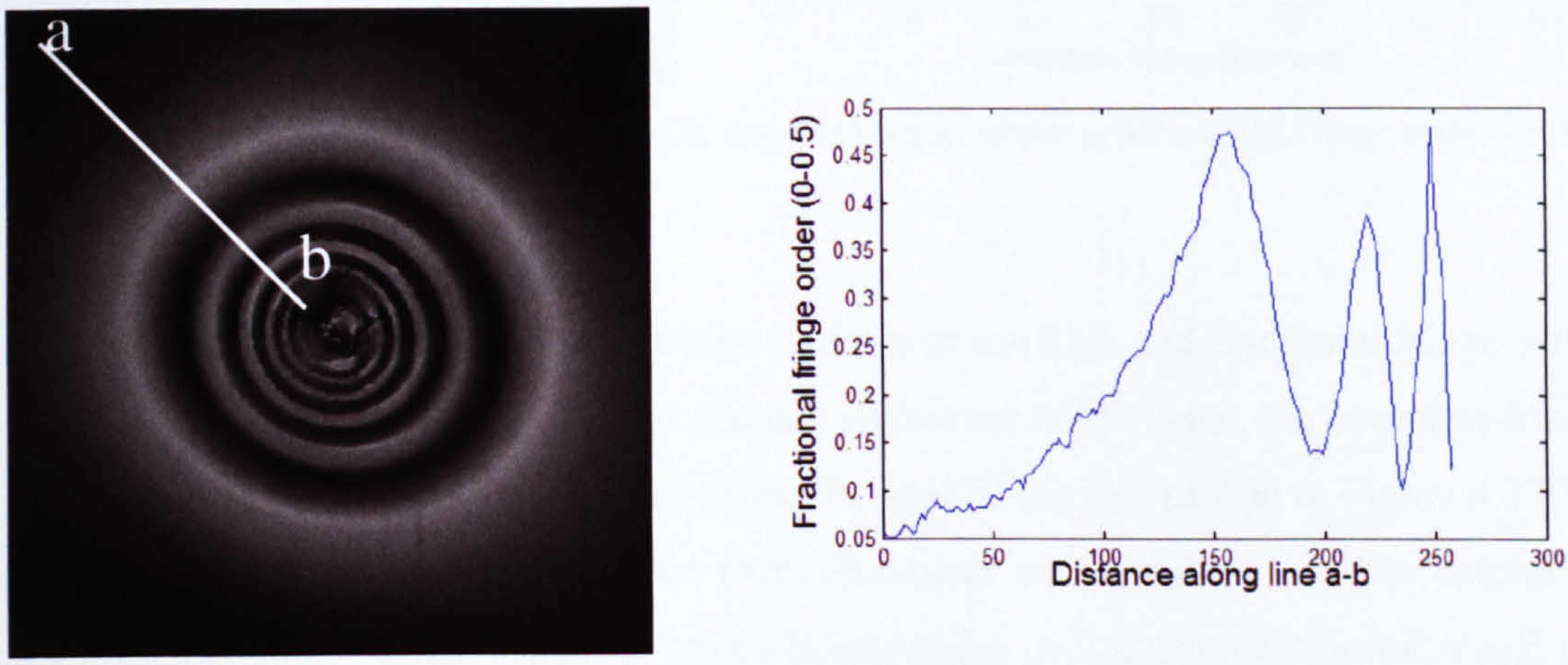

Figure 4-26: (a) Phasemap obtained in reflection mode under monochromatic light without partial mirror setup, (b) fractional fringe order along a-b

The improvement in the quality of phasemap is evident, however, the stress field cannot be completely determined due to the direction of loading and highly stressed zone at the centre.

4.4.3.2 Phase Unwrapping

The phasemap obtained in the previous section requires unwrapping to obtain the complete fringe order. A robust algorithm is required that can unwrap the phasemap correctly following the integral fringe orders and the trend of fractional fringe order from the image. A code was written to achieve the unwrapping of Figure 4.26(a) and Figure 4.27(a) shows the unwrapped phasemap obtained with Figure 4.27(b) showing the complete fringe order along the line 'c-d'.

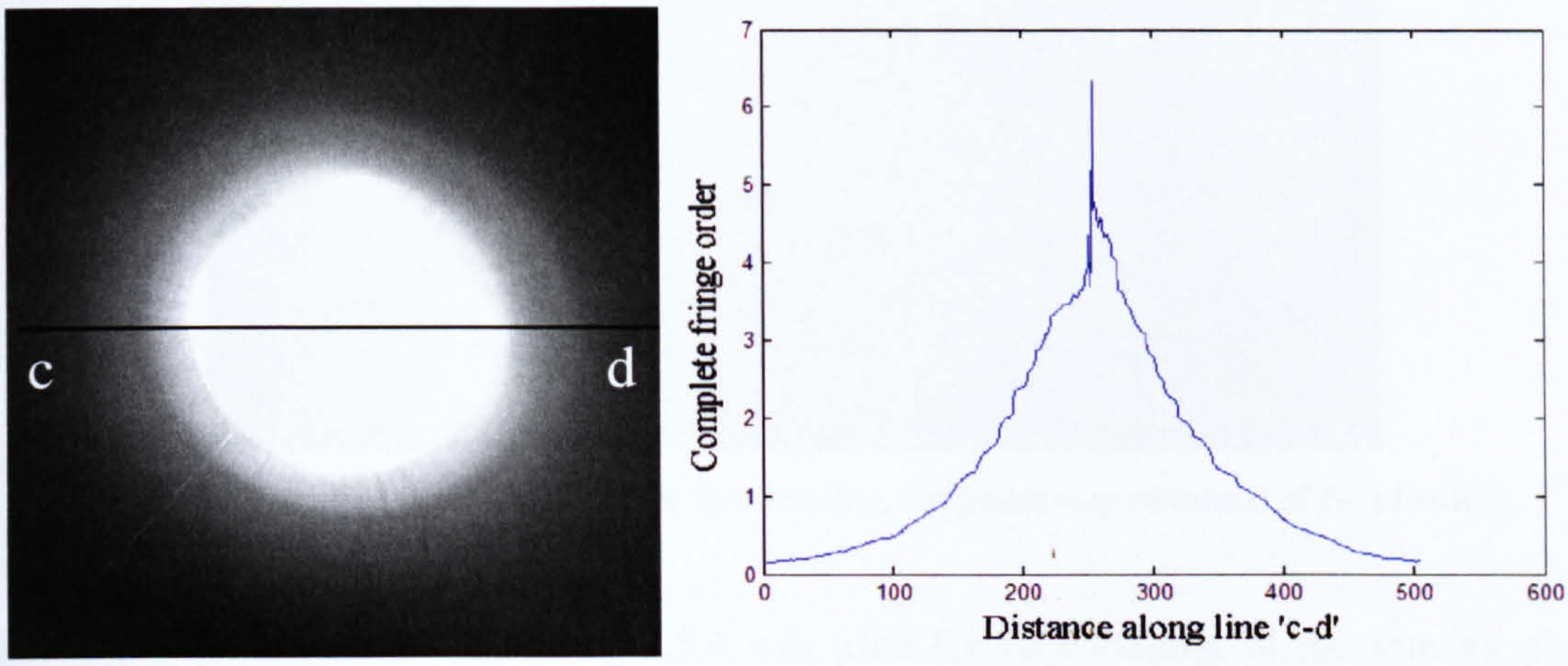

Figure 4-27: (a) Unwrapped phasemap with complete fringe order achieved, (b) fringe order profile along c-d

Since the stress at the centre of the fringe patterns is too high and fractional fringe order obtained from phase shifting is unreliable and erroneous in this zone, the complete fringe order cannot be accurately unwrapped as can be seen in the line profile in Figure 4.27(b). The determined complete fringe order from phasemap can be further used to determine the principal stress-strain difference using Equation 2.1 or 2.2, by substituting N and the determined values of λ and f from section 3.3.1 and 3.3.2. Thus the whole field principal stress difference can be obtained.

4.5 Foot Image Analysis

A case study of the foot induced fringe patterns was carried out to evaluate the use of photoelastic techniques on such complex fringe patterns and to investigate how far these techniques can be implemented in terms of quantitative measurements. Figure 4.28 shows a portion of fringe patterns obtained under the actual foot loading, which was subjected to phase shifting experiment by collecting six phase stepped images.

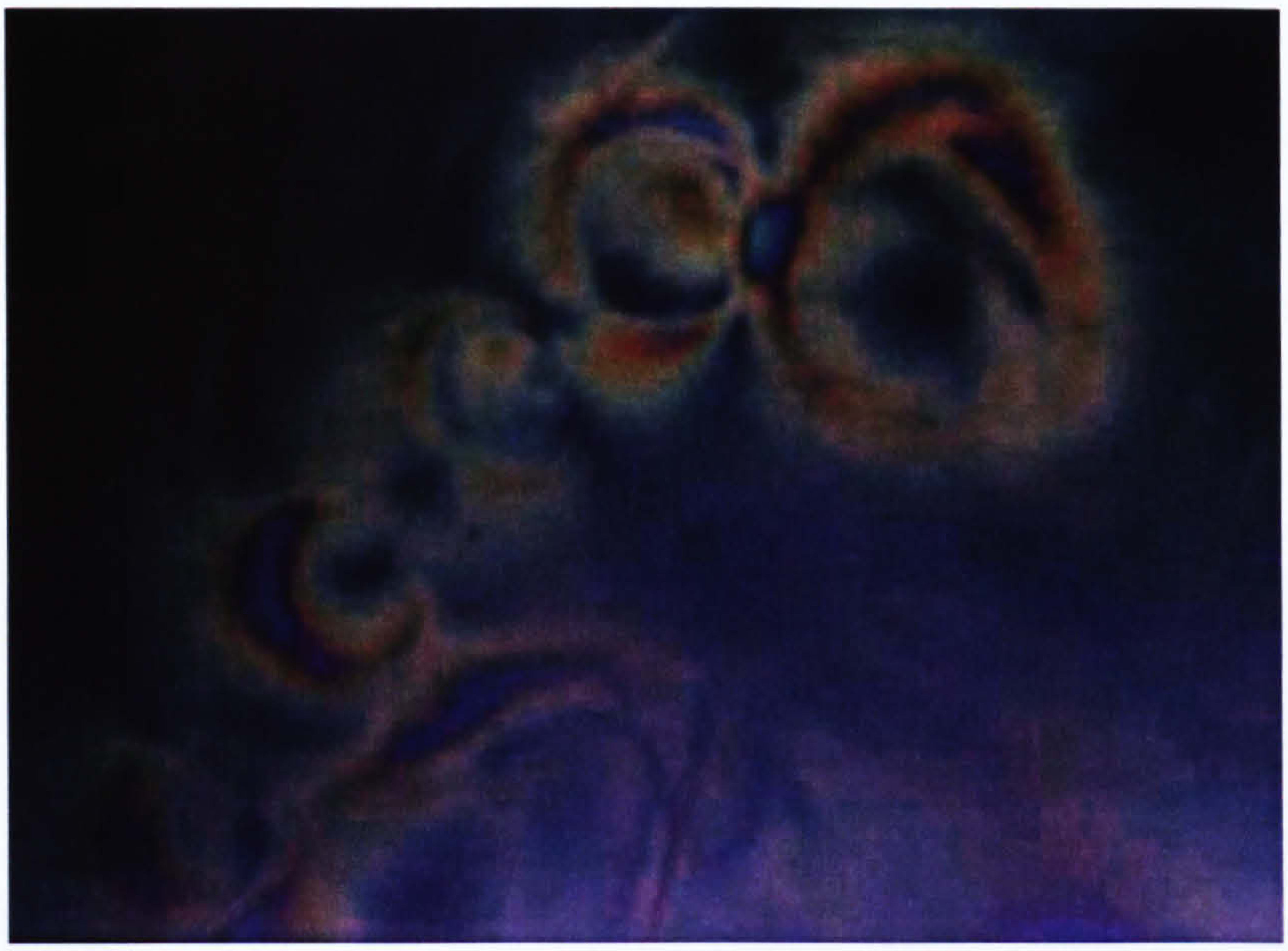

Figure 4-28: (a) Fringe patterns under foot loading, (b) phasemap obtained of foot loading.

The experimental rig from section 3.5.4 was used for foot loading of the sensing plate and the six phase stepped image acquired are shown in Figure 4.29.

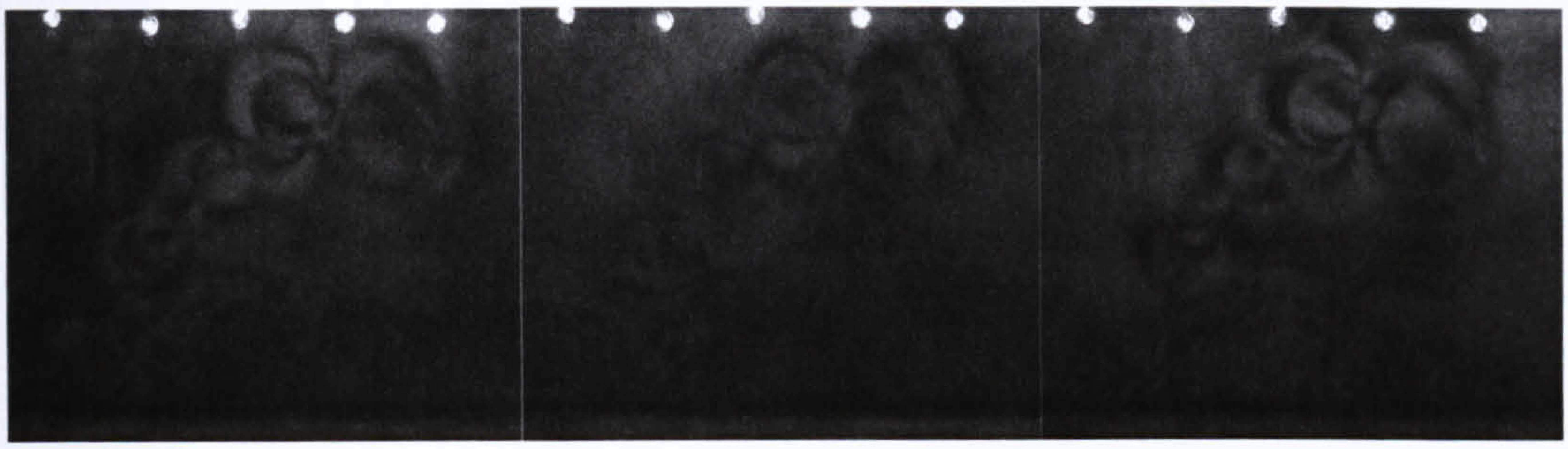

Figure 4-29: Six phase stepped images acquired for foot loading of sensing plate using experimental setup equipped with partial mirror and monochromatic light source

The isochromatic phasemap was obtained using Equations 2.10 and 2.11 and Figure 4.30 shows the unwrapped phase map. Since the phase shifting experiments using this particular experimental rig gave better results using monochromatic light source as compared to white light, the former was used in the experiment.

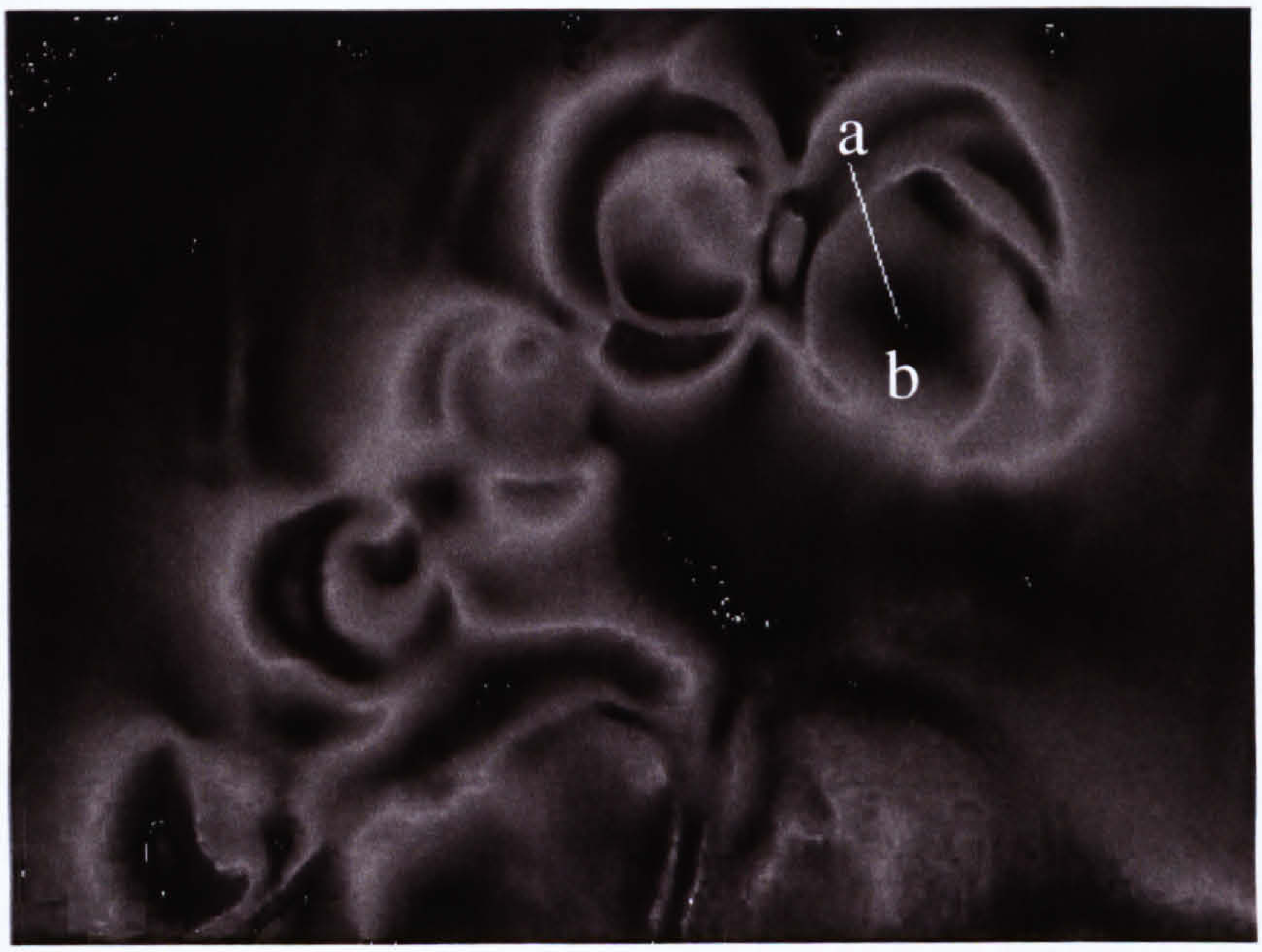

Figure 4-30: Isochromatic phase map obtained using phase shifting from foot loading of sensing plate

The phasemap obtained had the same limitations as the one obtained in Figure 4.27(a) and for determining the complete fringe order further processing would be required. However, visual inspection of Figure 4.28 & 4.30 shows how complex and random the fringe patterns appear under the actual foot loading compared to the patterns with controlled loading from indenter. The complexity also makes it difficult to unwrap the phasemap and would necessitate manual efforts. Figure 4.31(a) shows the fractional fringe order profile obtained along the line 'a-b' and Figure 4.31(b) shows the complete fringe order achieved along 'a-b' by unwrapping the data.

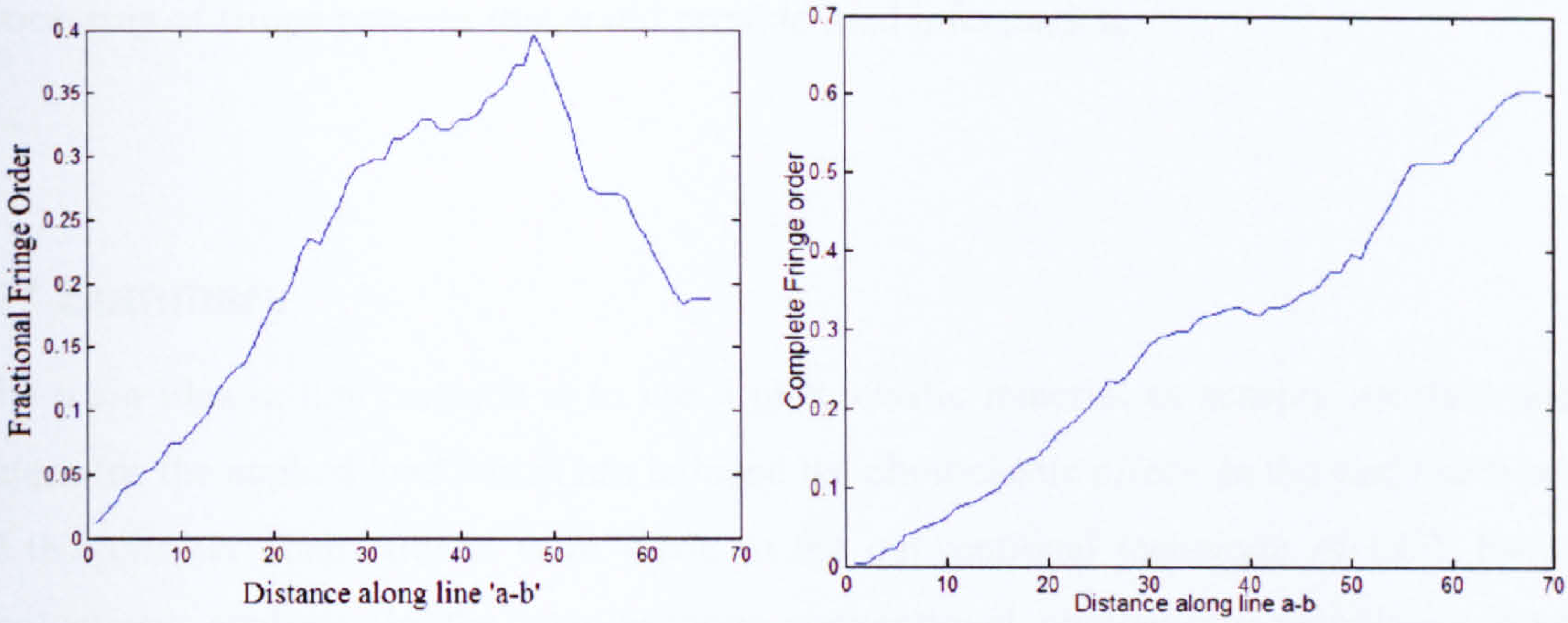

Figure 4-31: (a) Fractional fringe order, (b) Complete fringe order along line a-b

The algorithm for unwrapping was same as the one developed for the preceding section. The complete fringe order for the entire phasemap image can be obtained, however, the process would be tedious and still inadequate to provide full stress information from the induced fringe patterns. If LUT based calibration technique was to be applied to the foot induced fringe patterns it would render similar results as obtained here. However, it would be difficult to obtain the complete stress field for the whole foot; also the results would not be accurate due to inconsistent mapping of the RGB values between the model and the specimen due to the model deformation.

4.6 Limitations of Conventional Techniques

The results obtained from section 4.3 and 4.4 show that the conventional photoelastic stress analysis techniques can only determine principal stress-strain difference (maximum shear stress-strain) and all the six stress-strains (x,y,z strain and xy,xz,yz shear strains) cannot be determined using photoelasticity. Further for applications that require unconventional loading like sensing, conventional photoelastic techniques have limitations in terms of determining the applied load. For loading conditions where deformations of unknown shape may occur or repeatability of the fringe patterns may not exist; under these circumstances of complex fringe patterns, mere determination of fringe order or stress-strain difference is not sufficient. This would require some intelligent processing of fringe patterns that could provide load information.

4.7 Summary

The main idea in this research is to use a photoelastic material as sensing medium and determine the applied load which has induced the photoelastic effect. In the early sections of this chapter contributions were made to the conventional technique of LUT based photoelastic analysis. In the later sections conventional photoelastic techniques were tested on the fringe patterns obtained from surface loading of photoelastic material through a hemispherical head indenter. Both LUT based analysis and phase shifting could only provide fringe order thus limiting the results to principal stress difference. These techniques were also applied to the fringe patterns obtained from the actual foot loading and determination of the applied load was not possible due to the limitations of conventional photoelasticity. The results from the case study not only described the limitations but also identified the complexity of the problem. The results show that although fringe patterns may provide quantitative data in terms of photoelastic information but determination of load was not possible through either of these techniques. This requires that some intelligent image processing techniques be employed to achieve the whole field analysis and determination of load causing the photoelastic effect.

Chapter 5 Photoelastic Inverse Using Neural Networks

5.1 Introduction

In certain applications it is difficult to obtain an analytical relation between the fringe patterns and the triggering parameter. Under such circumstances empirical relations or even artificial intelligence may be required to develop a non-linear relation between the input and the output. With photoelastic materials as sensing mediums in determination of the applied load as triggering parameter this leads to inverse photoelastic problem where the developed image can be analysed for the input forces. However, there could be infinite number of possible solutions which cannot be obtained by conventional techniques. The conventional photoelastic techniques presented in the previous chapters are not applicable to the inverse problems as the requirement here is force extraction rather than stress analysis. This chapter presents neural networks based approach to solve this problem. The first few sections provide a brief description of neural network architecture used in this research followed by the construction, training and testing of the network implemented in this research. In order to generalise the force estimation from photoelastic images, a simple photoelastic model was considered for inverse analysis for which direct analytical relations exist between stress field and the applied load.

The technique can be implemented for any generalised case involving complex fringe patterns under different loading conditions for analysis of the fringe pattern, which may find application in a variety of specialised areas including biomedical engineering and robotics. The presented technique uses image information from photoelastic fringes and overcomes the drawbacks of previously reported techniques of photoelastic inverse analysis using neural networks. A supervised network was trained to determine the force from direct photoelastic images. The methodology and implementation strategies of neural networks are presented in this chapter.

5.2 Photoelastic Inverse

When a component or structural member is subjected to external loads the material is stressed. Photoelastic techniques have been used to estimate the stress-strain level on such components by analysing the fringe patterns. However, there may be a certain class of application where photoelastic images need to be analysed to extract the loading conditions (Dubey et al. 2007); which is the inverse problem. Inverse problems are difficult to solve since there may be more than one possible solution for the same resulting effect. Consider the loading of a photoelastic material as shown in Figure 5.1(a) by a normal force *F* and the resulting patterns, the same fringe patterns can be obtained by infinite number of forces acting at different angles (θ_n) as shown in Figure 5.1(b). Equations 5.1 & 5.2 describe the number of possible solutions for such conditions.

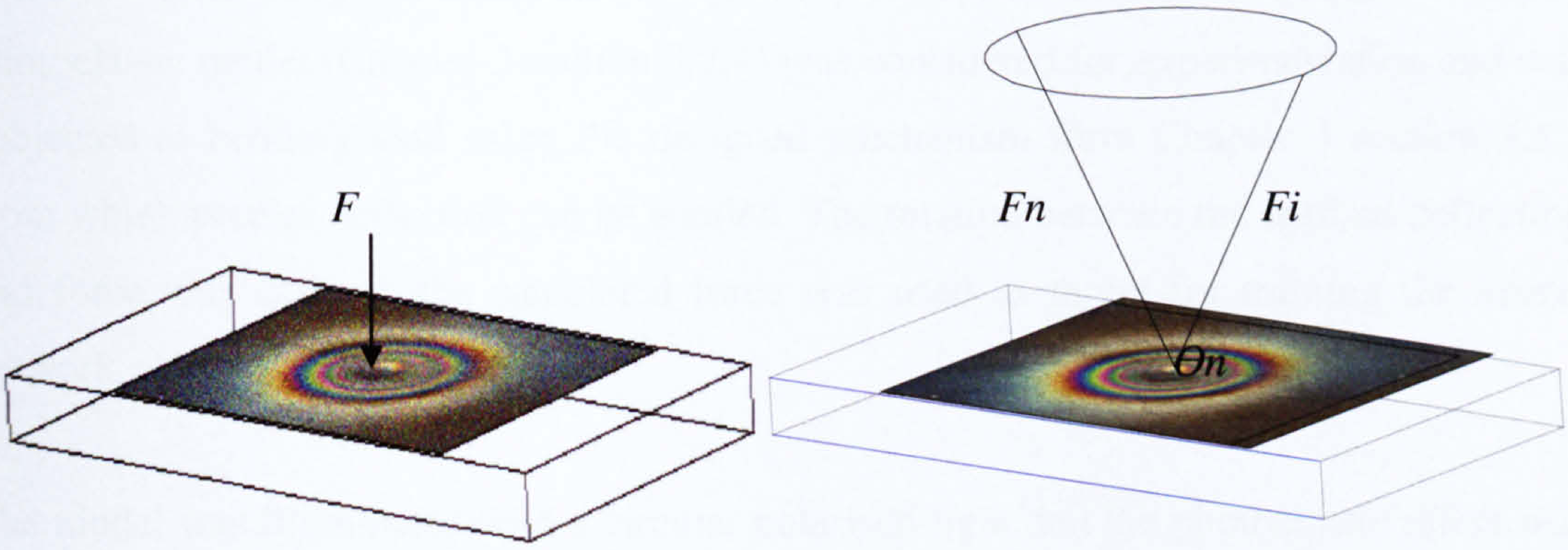

Figure 5-1: (a) Fringes due to a normal force (b) same fringe pattern with large number of forces

$$F_i = \frac{F}{n} \tag{6.1}$$

where, F_i is equi-spaced forces for (i>1)

$$F = (F_1 + F_2 + F_3........F_n)\sin\theta_n$$

Where (i=1, 2, 3 … n), n is an integer

$$\theta_n = \sin^{-1}(\frac{1}{n}) \tag{6.2}$$

where, θ_n is the angle between the horizontal plane and the axis of forces.

Thus inverse problem cannot be solved by analytical methods for generalised loading conditions because it is difficult to develop relations between the information available (fringes) and the input (forces). Artificial neural networks may prove to be a useful tool, since neural networks are well suited to develop non-linear functions between input and output (Bishop 1995; Patterson 1996). It is also known that neural networks can tolerate experimental changes (Noroozi et al. 2003), which are likely to occur in real systems.

5.2.1 Experimental Procedure

The aim of this chapter is to develop and a test neural network based methodology for determining the applied forces inducing the photoelastic effect. A simple C-Shaped photoelastic model (Chapter 3 section 3.2.4) was considered for experimentation and was subjected to bending load using the designed mechanism form Chapter 3 section 3.5.1 from which precise deflection can be applied. The relation between the applied deflection and force was derived; the calculated force was used as target for training the neural network.

The model was illuminated with a circular polarised light and the photoelastic effect was visualised through a digital camera (Olympus, SP500) mounted with optical elements (Chapter 3 section 3.5.6). Images of photoelastic fringe patterns were acquired and stored in a computer using camera control software (Sabsik 2005). The training data was extracted from the acquired images and used as input to the neural network. The presented technique is easy to implement, does not require extensive computation and can cope well within slight experimental variations. The technique just requires image acquisition, filtering and data extraction, which can then be fed to the neural network to provide load as output. The novelty of this technique is that the neural network is trained with direct image data from actual experiments which requires no prior calculations. The optimal network size was considerably small and system was generalised to analyse completely unseen data even at different camera settings.

5.3 Artificial Neural Network Based Analysis

Artificial Neural networks are inspired by biological nervous system where elements are connected in parallel. The system can be trained through examples; input training sets are fed and the network learns the target. The connections (weights) between elements are modified with every training cycle to minimise the error between the desired target and the output of network. Figure 5.2 shows a block diagram of neural network learning principles. In the present case the network would be trained from direct image information of photoelastic fringes against the applied load to analyse the unseen image data.

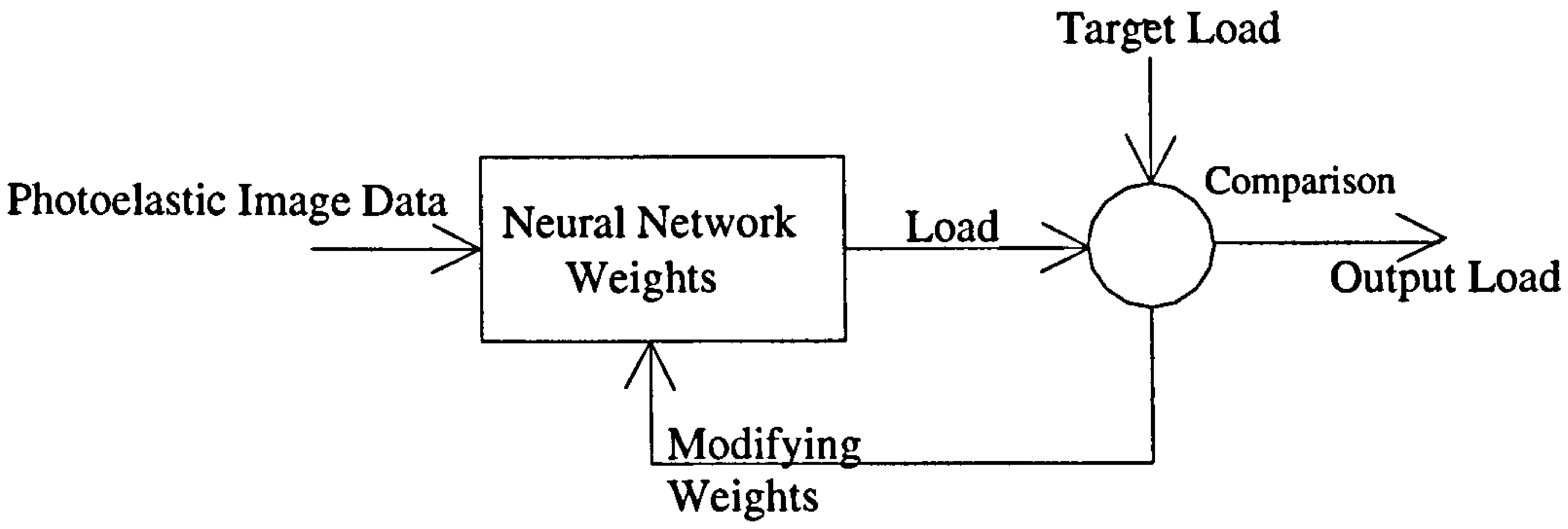

Figure 5-2: The basic structure of neural network for image analysis

5.3.1 Network Architecture

Besides the relevant input, the accuracy of the output is also dependent on the architecture of the network which is defined by the number of layers, number of neurons in each layer and the transfer functions used. A simple architecture of a single neuron connected to an input vector is shown in Figure 5.3. The element inputs are multiplied by individual weights and summed up; an additional scalar value (*b*) called bias can be added to the scalar product *wp*, which is then fed to a transfer function to produce an output. The input biased networks are found to be more efficient than without biased networks as they can learn to feed some input to the transfer function even if all inputs are zero.

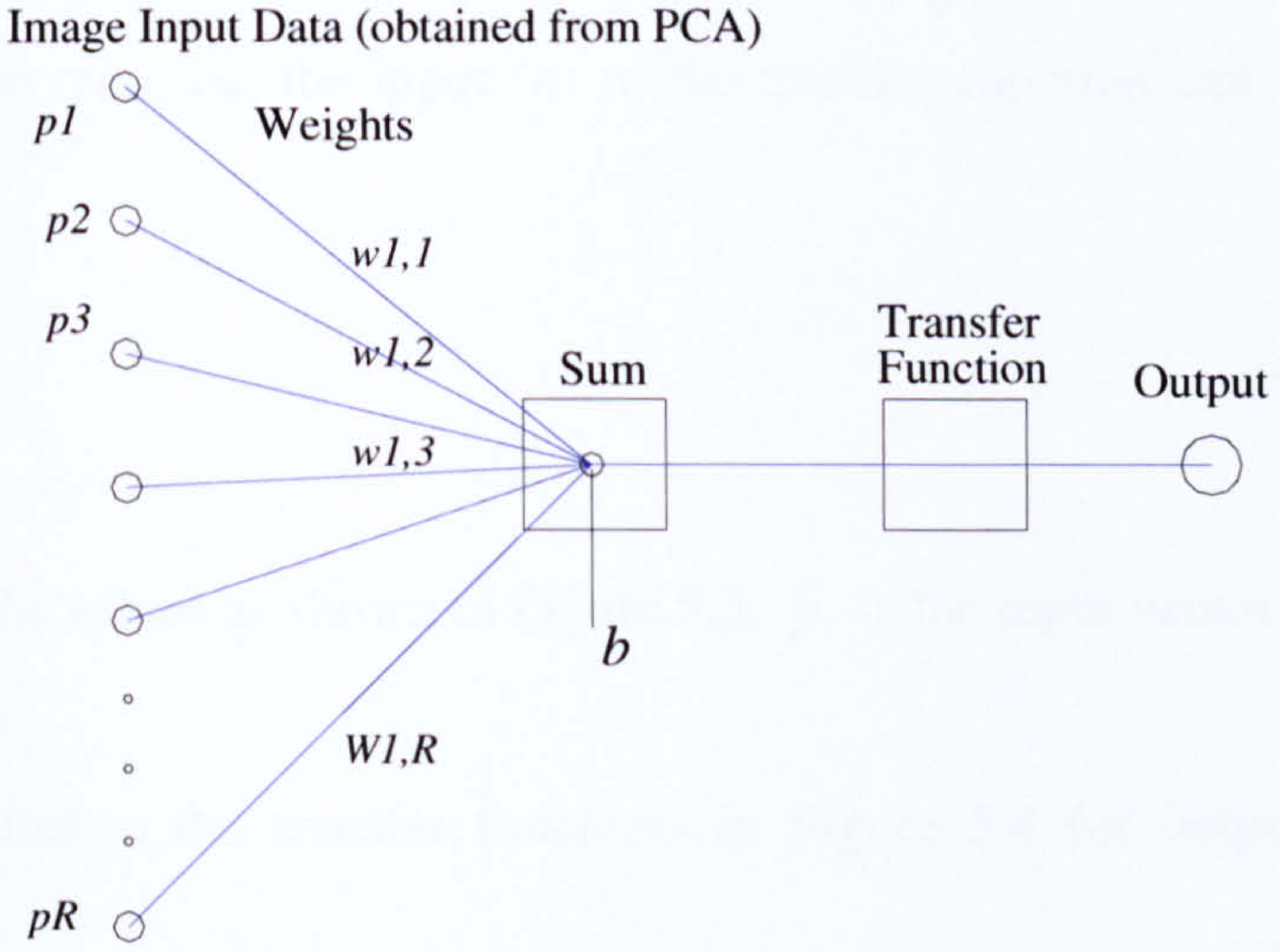

Figure 5-3: A schematic diagram representing a neuron connected to an input vector (*p*) and a transfer function via weights (*w*)

Further, many neurons can be used to form a web of connections between the nodes and the input elements. The web of connections enables neural network to develop a non-linear relation between input and output as maybe required in some applications. Selection of transfer function is important as it affects the behaviour of the function. Figure 5.4 shows the two transfer functions used in the construction of network for this research. The *tansig* function (Figure 5.4a) generates output between -1 and 1 and was implemented for its ability to add non-linearity to the system which is required in this case. The *tansig* transfer function was used in neurons in hidden layer. The second transfer function used was '*purelin*' used for output layer (Figure 5.4b) which generates output of any range, thus can be mapped for the desired load values.

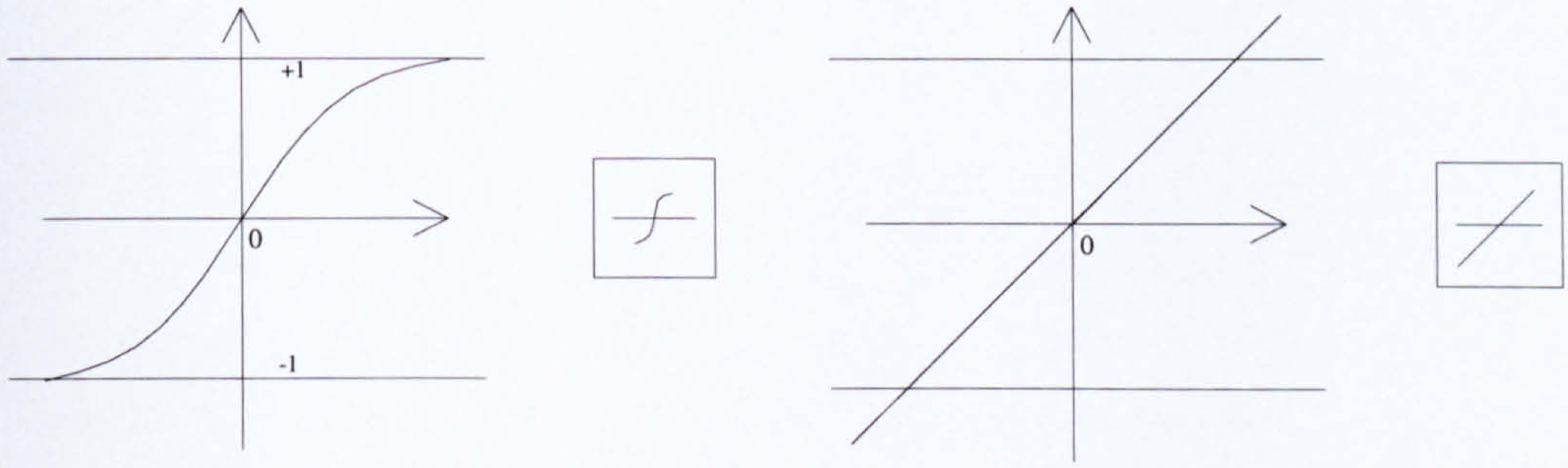

Figure 5-4: Transfer function (a) 'tansig', (b) 'purelin' used in construction of the neural network

Since more than one neuron is required for developing non-linear relations additional neurons might be required, the input (*n*) to the transfer function can be represented by Equation 5.3.

$$n = W_{ji} p_i + b \qquad (5.3)$$

Where,

W_{ji} are the weight values as shown in Figure 5.3, p_i is the input vector (i=1 to R)

The input *n* is fed to the transfer functions in Figure 5.4 for output *a* as shown by Equation 5.4.

$$a = f(n) \qquad (5.4)$$

The concept of one neuron connected to an input vector *p* with *R* elements is extended to form a multi layered network as shown in Figure 5.5. Here each element of input is connected separately to each neuron via weight matrix *W*. The number of neurons (*S*) can be different than the number of elements in the input vector (*R*). The mathematics involved in connecting each element to each neuron is seldom re-written, however, the network becomes capable of adapting to a high level of non-linearity of the system as is required in the present application. For implementation of the network standard functions from MatLAB® Neural Network toolbox have been used. Two different training methods, '*adapt* and *batch*' are available, *batch* training mode was used in this research due to its high efficiency and necessity for type of input data (static) fed and the output required.

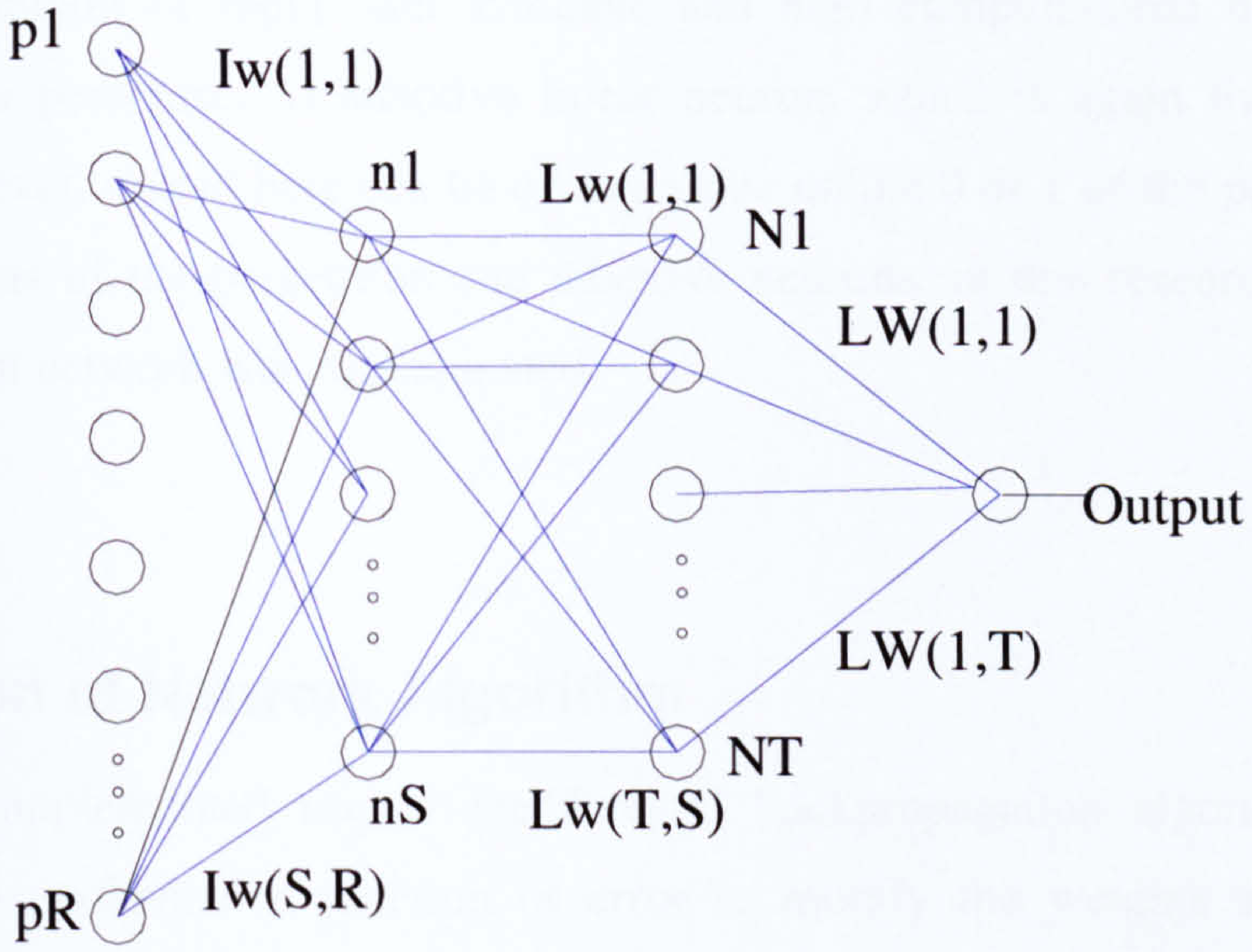

Figure 5-5: Structure of the multilayered neural network used for inverse photoelastic image analysis in determining the applied load from fringe patterns

The size of the network is defined not only by the number of neurons and layers but also by the number of weights required to achieve the target output. The weights are categorised as input weights (connected to inputs), layer weights (connected to layers) and bias weights thus defined by the connection ends. Further, the initialisation of weighs is an important issue and is discussed in Section 5.4.2 in regard to the experiments conducted here.

5.3.2 Selection of Neural Model

A variety of neuron models are available to select from but the selection is application dependent (Grewal et al. 2006). Various other parameters need to be accounted for in selection of appropriate neuron model including the transfer function, learning function, learning rule (supervised or unsupervised) and the training technique. For linear classification perceptron neuron models with hard limit transfer function are sufficient. The output is limited to 0 or 1 due to the nature of transfer function and a wide range of outputs cannot be achieved. Here the training is performed using the *adapt* technique, where weights are adjusted after every single input, which cannot be used in this research due to large amount of input data available and high computational times involved. Alternative to a perceptron is adaptive linear neuron, which is again limited to linear problems; however, output here can be of any value unlike 0 or 1 of the perceptron. Due to the limitations of the perceptron and adaptive neurons, in this research feedforward backpropagation network was implemented.

5.4 Selection of Network Algorithm

This research implemented use of feedforward backpropagation algorithm that uses gradient of the performance function or error to modify the weights and bias while training the network. The calculations are performed using chain rule (Hagan et al. 1996) and weights are adjusted in the direction of negative gradient i.e. opposite to the direction of the slope of performance function. The change in weights is described by Equation 5.5. Thus the weights are adjusted in the direction in which performance function decreases most quickly. Several modifications have been made to the basic algorithm of backpropagation to optimise the technique for faster convergence. The techniques falling under improved algorithm are steepest descent, conjugate descent, quasi-Newton and Levenberg-Marquardt (Bishop 1995; Mathworks 2002).

$$x_{k+1} = x_k - \alpha_k g_k \tag{5.5}$$

Where, x_k is the current weight vector, α_k is the learning rate and g_k is the current gradient

5.4.1 Constructing the Network

In order to construct a backpropagation network four inputs are required (Equation 5.6) viz min-max of the input vector (1), the number and size of layers (2), the transfer functions (3) and the training function (4). The constructed network is represented by

Equation 5.6 and Figure 5.6 shows the optimised network achieved for inverse image analysis in this research.

$$net = newff(\underset{1}{[\min(pn)\max(pn)]},\underset{2}{[l1,l2]},\underset{3}{\{'tansig','tansig','purelin'\}},\underset{4}{'trainlm'}) \qquad (5.6)$$

Where, *newff* is the command for creating a feedforward network

$\min(pn)$, $\max(pn)$ are the minimum and maximum values of input

l1, *l2* are the number of neurons in hidden layer 1 & 2

tansig, *tansig*, *purelin* are the transfer functions used in each layer

trainlm is the training algorithm used based on Levenberg-Marquardt optimisation algorithm

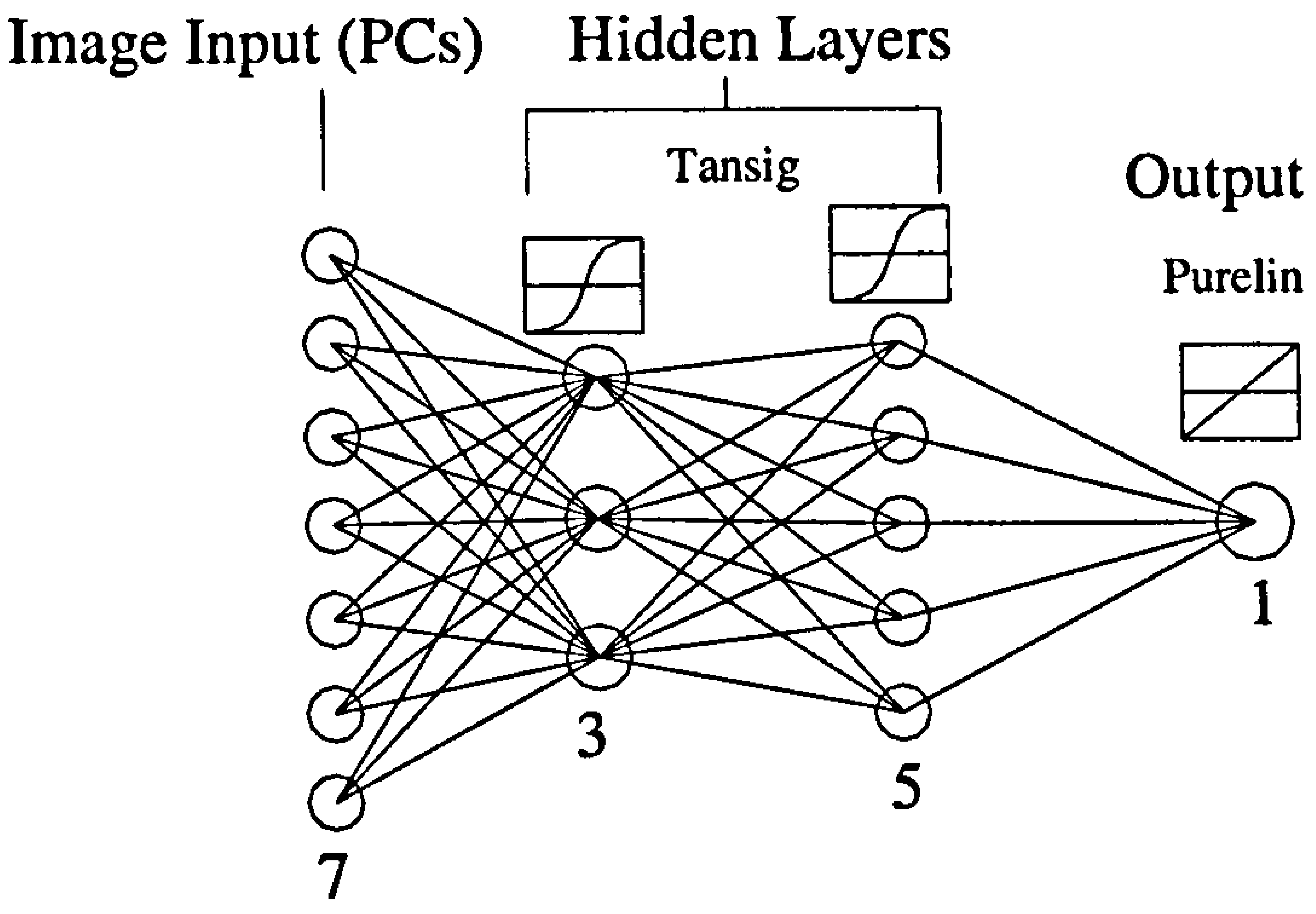

Figure 5-6: The optimised network configuration for the inverse photoelastic analysis

Single hidden layered network was also tried but accurate results were obtained using two hidden layers. The selection for number of neurons in each hidden layer was optimised by experimenting with different possible configurations of the network (section 5.6).

5.4.2 Initialising the Network

One of the very important parameters for fast training a network and for efficient convergence is initialisation of the weights and bias. By default, initialisation is done randomly when a network is created. The main problems with multi-layered neural networks using non-linear transfer function is the local minima; on an error surface there can be many local minima points besides one global minimum (Hagan et al. 1996).

Figure 5.7(a) shows an example of error surface for a single-layered network (1,2,1) and Figure 5.7(b) shows a 2D view, with the red dot pointing to the global minima and white dots local minima.

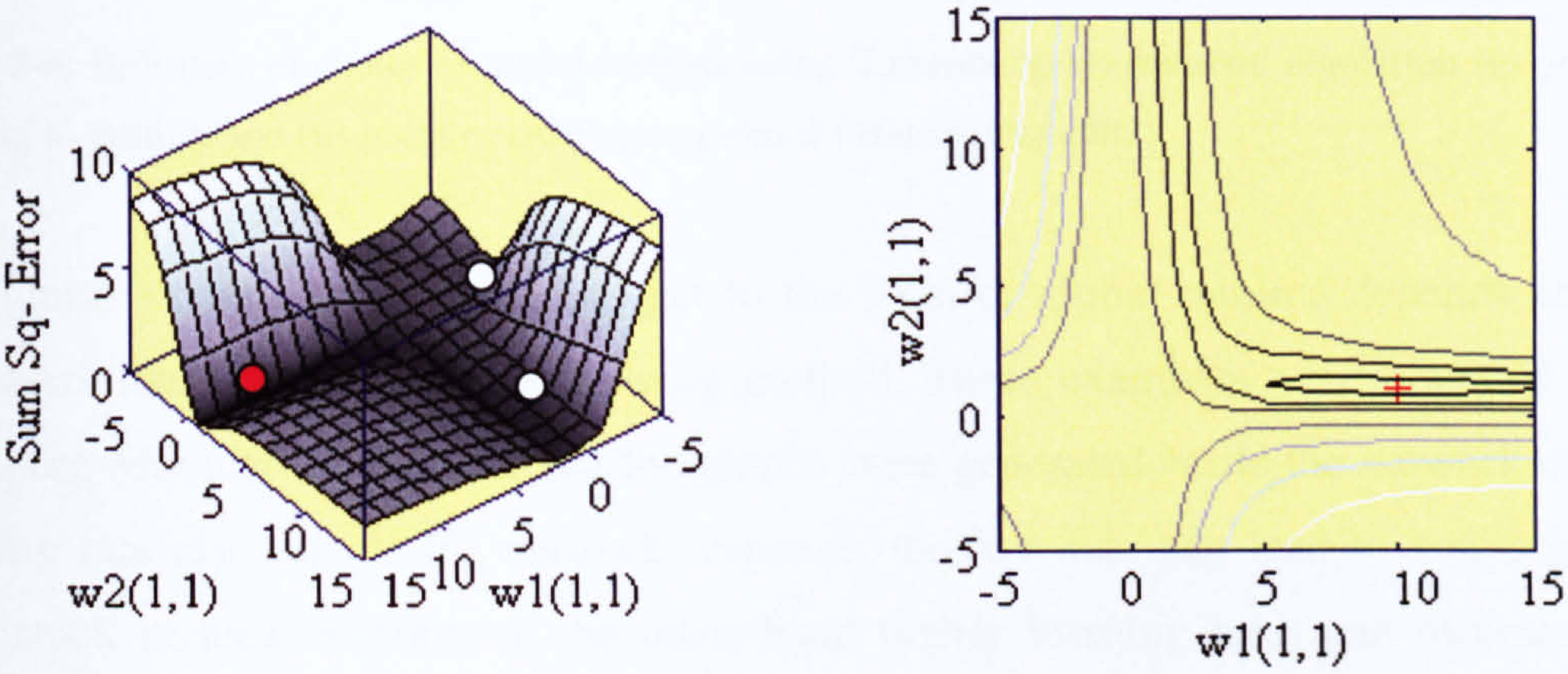

Figure 5-7: (a) 3D and (b) 2D representation of error surface, illustrating the effect of weight initialisation

While training, the network can get trapped in one of the local minima instead of reaching global minimum error. For instance, the initialisation started from 'a' in Figure 5.8(a) leads towards error point 'b' (out of plot) which is a local minima; on the other hand initialisation of weights from 'c' in Figure 5.8(b) leads to the global minima at 'd'. The small circles are the iteration points during the network training. Since appropriate starting point is unknown it is reasonable to train the network a number of times with random initialisation which can help avoid a local minima. As it is impossible to confirm global minima in complex functions, training the network with different initialisation parameters and variables can lead towards the global minima. A random seed point is given every time while initialising the weight matrix and bias to help reach close to the global minima and avoid local minima.

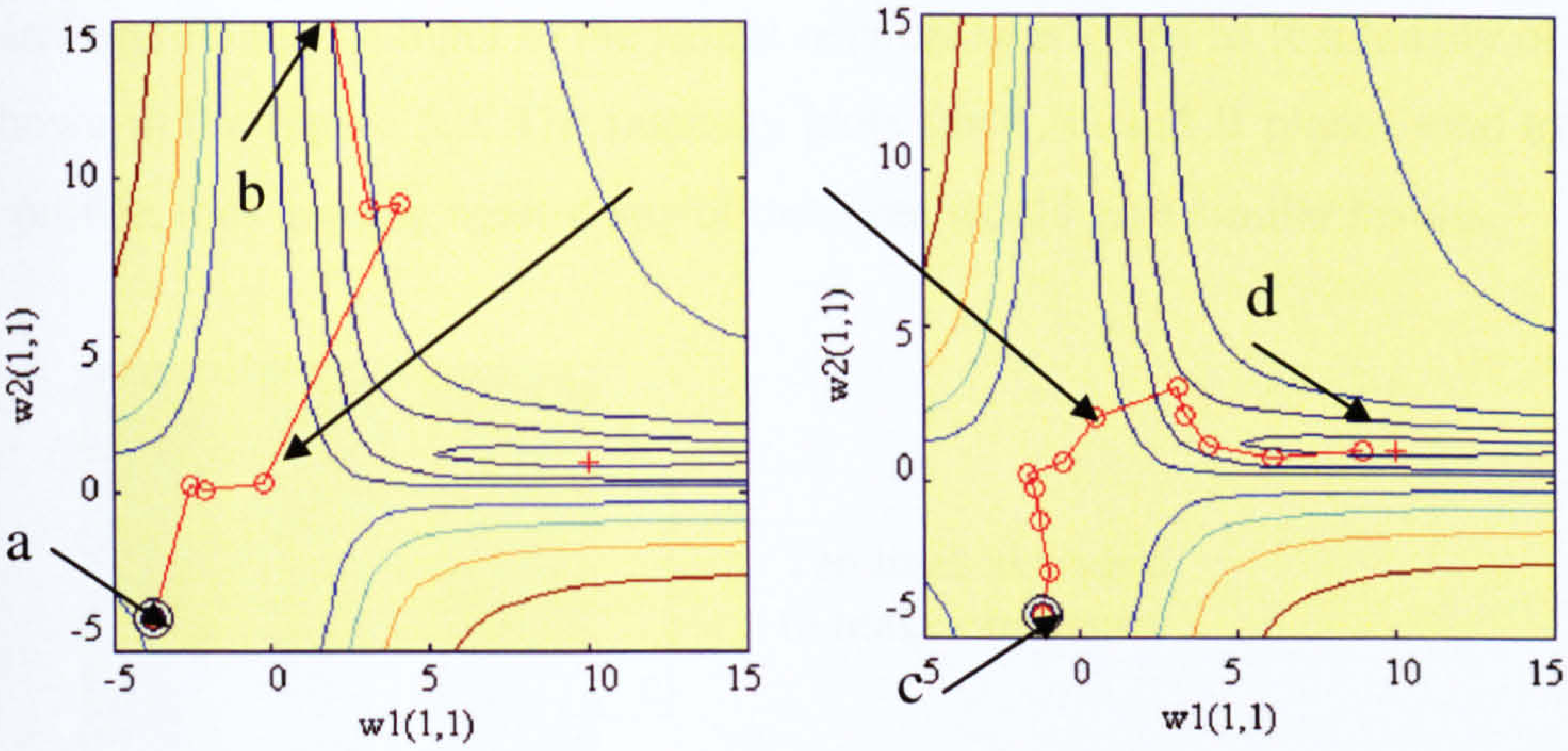

Figure 5-8: Influence of choice of initial weights using 'Levenberg-Marquardt' algorithm (a) point a reaching to point b and (b) point c reaching to point d (Mathworks 2002)

The number of iterations required to get to the local or global minima depends on the parameters like learning rate and training method. These examples were obtained with Levenberg-Marquardt algorithm and the graphs were generated while the network trains. Learning rate also affects the network response, too low rate can lead to convergence being stuck in local minima on the other hand higher learning rates can increase the convergence rate to a level that the system can become unstable and miss the global minima.

5.5 Factors Influencing Network Performance

Once the network is created, the next step is training the network with relevant data. The data being fed must be adequate and relevant; even though network learns to ignore irrelevant data through iterations still careful selection of the data is of vital importance. The following section discusses the data selection and extraction procedure, network parameters and the training techniques.

5.5.1 Input Data

The model was subjected to a bending load and the induced fringes were acquired in form of digital images. An ROI was selected along the vertical arm of the specimen as shown in Figure 5.9. The input to the neural network was given as R intensity of line 'a-b' as shown in the Figure 5.9. The intensity plots for R, G and B planes tend to exhibit similar profile, thus training against any of the three would give similar results.

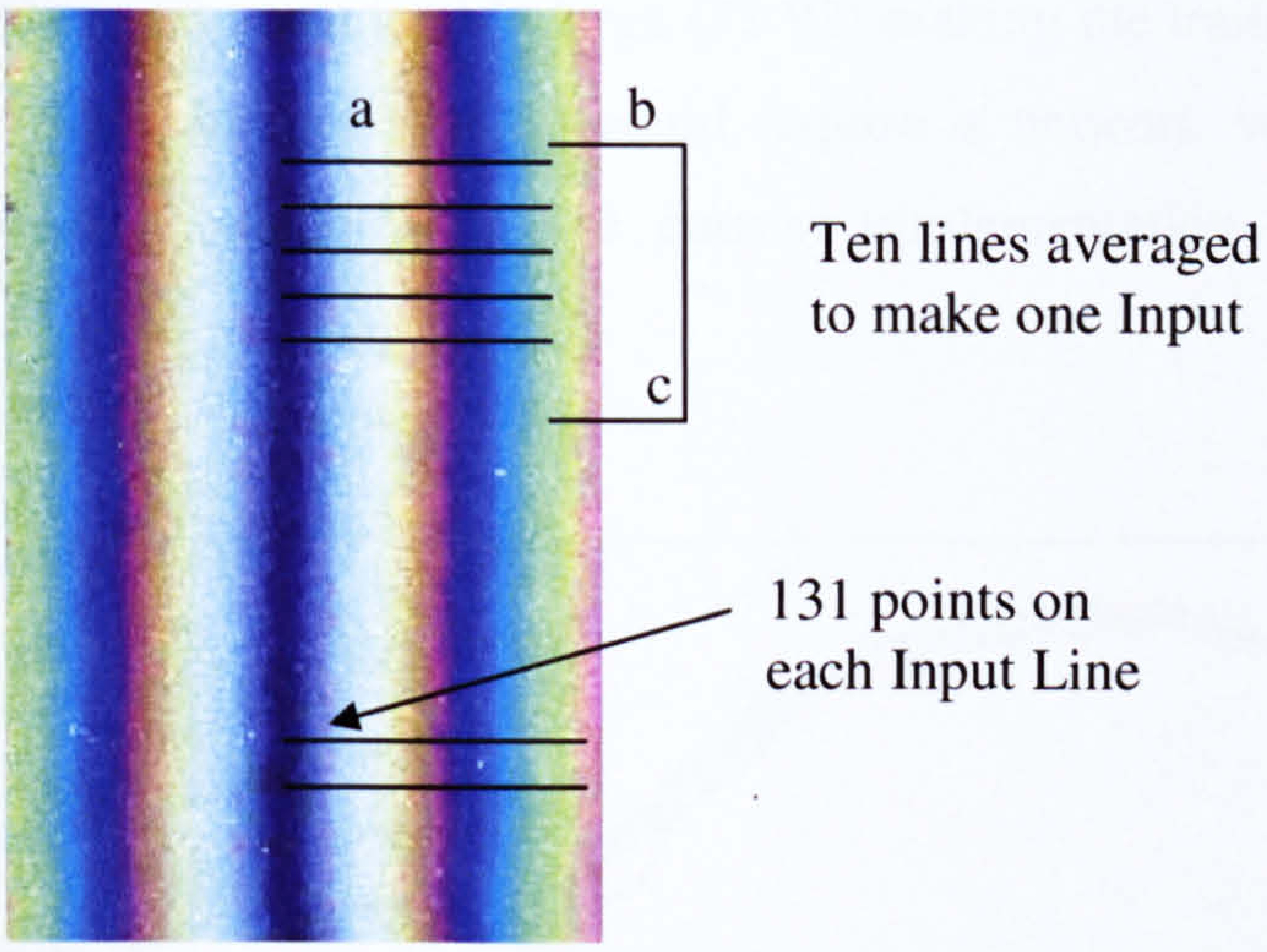

Figure 5-9: (a) ROI in the model with fringe pattern, (b) loading conditions of the specimen

In this research data reduction techniques were implemented to reduce input dimensionality, unlike (Chung 1998), which made the technique more efficient. To train the network it is essential that sufficient amount of training sets are provided. The fact that stress distribution along line 'b-c' is uniform facilitates extracting more than one input line from the same image. Inevitably noise is introduced due to multiple input extractions or if there was any uneven loading at the two ends. However, it has been reported that noisy data can help in better 'generalisation' of the network (Freeman and Skapura 1992). Average R-intensity of 10 input lines was extracted along 'a-b' to make one input data line (131 points each) as shown in the figure. Similarly, 15 input data lines were extracted from each image under the load and the procedure was repeated for the successive loads. Figure 5.10 shows the 15 input intensity curves obtained at a deflection of 0.4 mm applied to the model, the noise induced can be seen in the plot. The main consideration in the selection of image data as direct input was to minimise the computational effort of extracting features or other parameters for training. Noroozi (2003) implemented neural networks for inverse analysis of photoelastic data, but prior knowledge of Finite Element Analysis was required for training neural networks and knowledge of photoelasticity for testing the network. Additional noise generator was also used to introduce artificial noise to the network. During analysis the authors required determining *N* at different locations and feeding the fringe order to the neural network during testing. On the other hand Chung (1998) used direct image data but input dimensionality was considerably large (32-92) making the training more computationally expensive. Such an input range would require a network with more neurons. These limitations were overcome in the current implementation by using data reduction techniques.

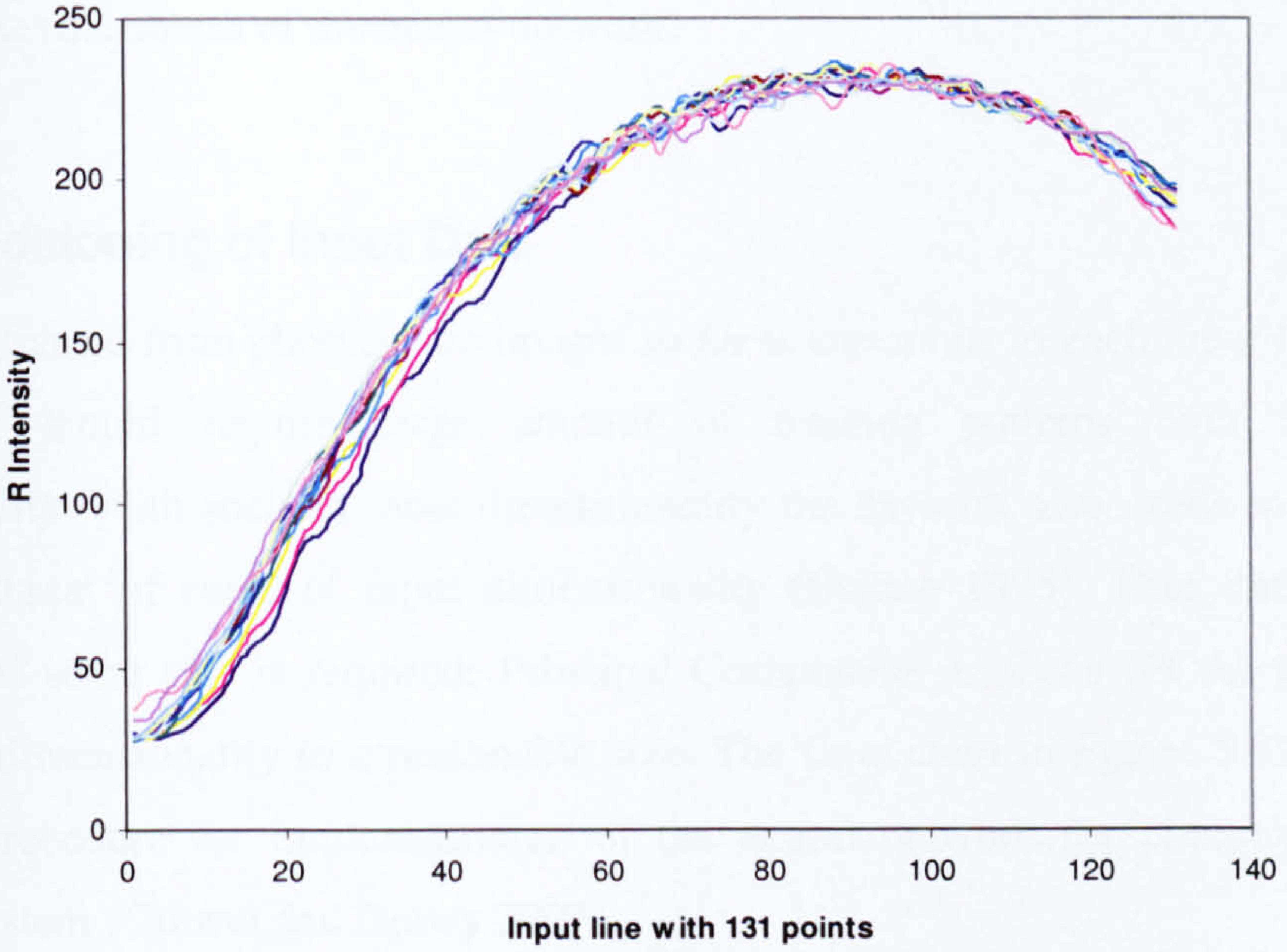

Figure 5-10: A set of 15 input data lines (R intensity) extracted along line 'a-b' at a single value of deflection

The deflection to the specimen was incremented in steps of 0.04 mm and recorded, later converted to applied force using Equation 5.7 to be set as target for training.

$$\delta=\frac{Ph^2}{3E}\left[\frac{2h}{I_1}+\frac{3L}{I_2}\right] \tag{5.7}$$

Where E is the modulus of elasticity of the model and I_i is the second moment of area of different sections of the model.

Ten similar sets of experiments were performed with 25 load values (increasing and decreasing). Thus a total of 250 images were acquired. The neural network was trained with noisy data in order to make it robust against experimental variations that may occur during image acquisition e.g. changes in image orientation and scaling due to loading, lighting, reflections or camera settings. Generally, one load value would provide only one input data thus 250 input data sets from 250 images, but multi-input extraction gave 15 input sets from each image. This increased the training data from 250 to 3750 and improved the robustness of the neural network.

5.5.2 Conditioning of Input Data

The data extracted from photoelastic images so far is enormous as each input line has 131 points and would require large amount of training patterns with such input dimensionality. With such an input dimensionality the network also needs to be big and there is a threat of curse of input dimensionality (Bishop 1995). Thus data reduction technique of some sort is required; Principal Component Analysis (PCA) was used to reduce the dimensionality to a reasonable size. The flow chart in Figure 5.12 shows the complete procedure for implementation of the neural network for photoelastic fringe mapping system (Grewal and Dubey 2007).

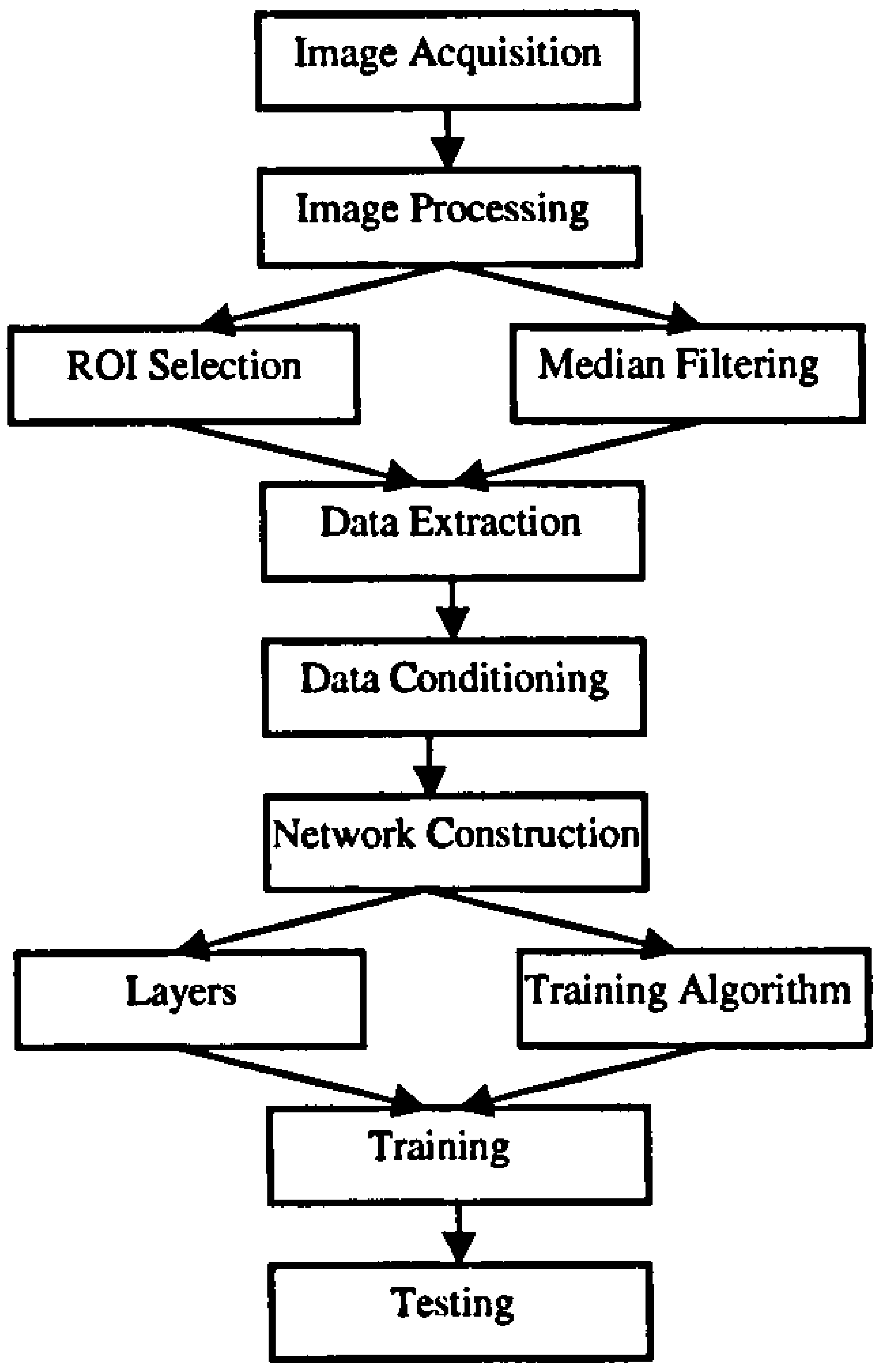

Figure 5-11: The flow chart illustrating the process of inverse analysis; image acquisition, processing, data extraction, conditioning and neural network processing

Since neural networks are found to be more efficient with normalised input (Mathworks 2002), the input data and target were scaled by normalising so that the mean and standard deviation are within 0 and 1. The whole procedure shown above was automated in MatLAB® from image processing to training and testing.

5.5.3 Performance Function

The error defined by performance function was set as the mean square error '*mse*' between the target and the output of neural network. The value was set to an appropriate level (0.01) depending upon the accuracy required and as per output response of the network to avoid over-fitting. The weights and bias were modified as per gradient of performance function to minimise the error. The performance function was defined by Equation 5.8.

$$mse = \frac{1}{n}\sum_{i=1}^{n}(t_i - a_i)^2 \tag{5.8}$$

Where, *n* is the total number of target, *t* is the target desired and *a* is the neural network output.

5.5.4 The Training Algorithm

Selection of training algorithm is application dependent and requires experience, so does all the other parameters. To achieve fastest convergence and less computational time 'Levenberg-Marquardt' training algorithm was adopted (Hagan and Menhaj 1994). Levenberg-Marquardt algorithm has been found more efficient as it interpolates between Gauss-Newton Algorithm and Gradient Descent Algorithm. This offers the fastest training algorithm for networks of moderate size and has a memory reduction feature when the training set is large. Other methods were tried but their slow response and lower accuracy led to adoption of Levenberg-Marquardt algorithm.

5.5.5. Generalisation of the Network

The idea of using neural network is to develop a system that can efficiently map input data on to the desired targets through some non linear functions. The network is expected to learn and produce output for unseen data. However, sometimes the network memorises instead of learning and thus over-fitting on input data. Larger networks tend to over-fit, thus keeping network to a reasonable size should be attempted. Two methods for improving generalisation are resorted; regularisation and early stopping. Regularisation is referred to modification of performance function and early stopping involves sub dividing the data into three sets; training, validation and test data. In this research early stop was chosen over regularisation as the latter requires an additional parameter to be carefully monitored and selected. In early stopping the validation data is the key. Research on quantifying cross validation (Prechelt 1998) criteria suggests that the modifications in validation technique can improve results slightly but at the cost of longer training times. The validation data was used in parallel to the training data and validation error was computed along with training error. The network training was stopped when validation error has increased more than a specified number of iterations. After early stopping the weights and bias automatically roll back to the point of minimum validation error. Various other parameters are available that can be set to control the behaviour of training algorithm, like learning rate, number of iterations and the performance goal.

5.6 Training the Network

After careful selection of input data and network parameters, the next step was to train the network. The network trains by slowly modifying the weights in response to the performance function and learns from the input data sets. The input data was shuffled for efficient learning otherwise the network might memorise the last trained class of input data (Freeman and Skapura 1992; Patterson 1996); a separate code was written to shuffle the data. Figure 5.13 shows a plot of training cycles with training curve, validation curve and the goal to be achieved. The network training must be stopped when the error reaches a particular value of goal or if it does not fall any further, thus, the number of iterations were chosen accordingly.

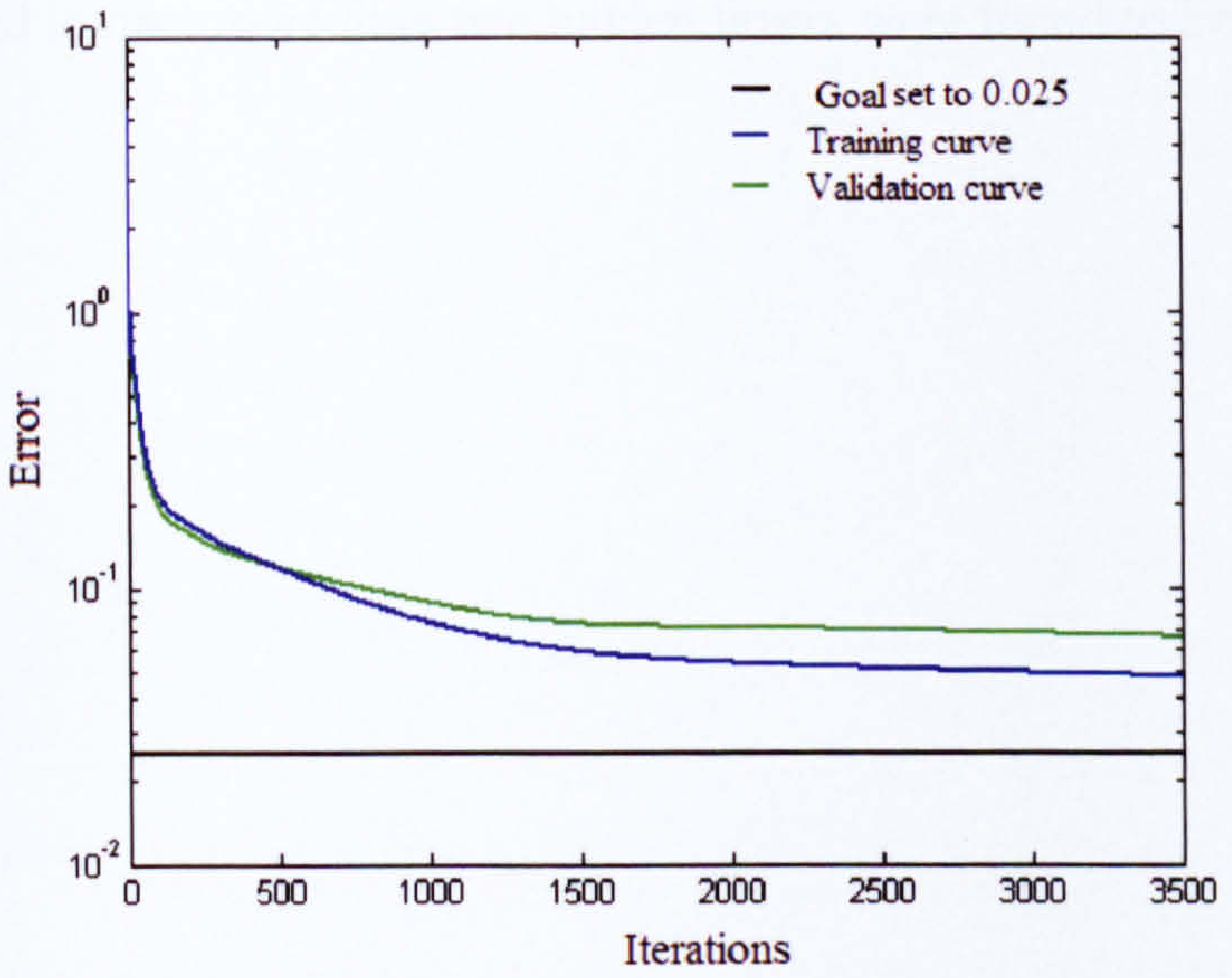

Figure 5-12: The training behaviour of the network for photoelastic inverse analysis, the plot shows training and validation curve progressing against a set goal

The goal was set to 0.025 although different values of goal were used to reach to one optimised network. The performance for the network shown in Figure 5.13 reached 0.0478 after 3500 iterations, the increasing distance between training and validation curves from the figure suggests that the training will stop in next few iterations, as a sign of early stop.

The network was trained with different combination of neurons in the first and second hidden layers and with each combination the network was trained 30 times using different weights. The above procedure would make sure that the network is not stuck in local minima as 30 different networks have been checked every time, thus optimising the final network. In order to efficiently train the network the input dimensionality and the size of network was optimised. This was achieved by testing 49 different network size configurations for each input dimensionality and computing the error for 24 different test images. Table 5-1 shows a part of the tested network configurations with different input dimensions. The error computed for 24 different test images is listed in the table. It was found that the network gave consistent and accurate results when two hidden layers were used as compared to one; more than two hidden layers were found to be computationally overloading.

Table 5-1: Network optimisation and percentage error

Input Dimensionality	Neurons in Layer 1	Neurons in Layer 2	% error 24 test images	% error 23 test images
5	4	3	5.56	4.18
6	3	3	4.97	4.68
7	**3**	**5**	**4.20**	**2.78**
9	3	6	5.98	4.15
10	3	4	6.67	2.93
11	3	4	5.54	3.26
12	3	4	9.08	3.49
13	3	3	6.08	3.90
14	5	5	5.23	5.08
15	3	5	7.51	3.92
16	3	3	6.53	5.08
17	3	8	5.97	5.02
18	4	3	5.70	5.67

By comparing the input dimensionality and the network size, the network {7,3,5} was found to be the best choice. This means that the final network had input dimensionality of 7 with 2 hidden layers, each with 3 and 5 neurons respectively. The average percentage error was found to be 4.20 and it further dropped to 2.78 when the initial load was eliminated from the analysis; since there was very little fringe information available at such a low deflection of 0.04 mm where the network did not learn efficiently.

5.7 Testing the Network Performance

Once the network with minimum validation error is saved, it is ready to be tested with unseen data. After testing 24 test images the range of error was found to be between 4-9 % for most of the networks as could be seen from Table 5-1. When the error falls in the same range for different networks, it is better to use network with fewer numbers of weights as they are more generalised. Once the optimal size of the network is achieved and the network is trained, the weights are saved and the test data can be fed without any further training. No further retraining of network is required for this setup and it can analyse any unseen test data. The network with 7 input dimensionality was found to be better suited and delivered accurate results with moderate sized network. The number of weights required were fewer and thus the network was better generalised. There were 25 different loads and the network was tested for 24 loads (excluding the zero load). The network was unable to learn for one of the 24 loads and error was comparatively higher than other loads, the percentage error for 23 test loads is shown in Table 5-1 excluding the erroneous load. The test result for 10 random test load-images is plotted in Figure 5.14, a comparison of ideal load value and neural network output is given.

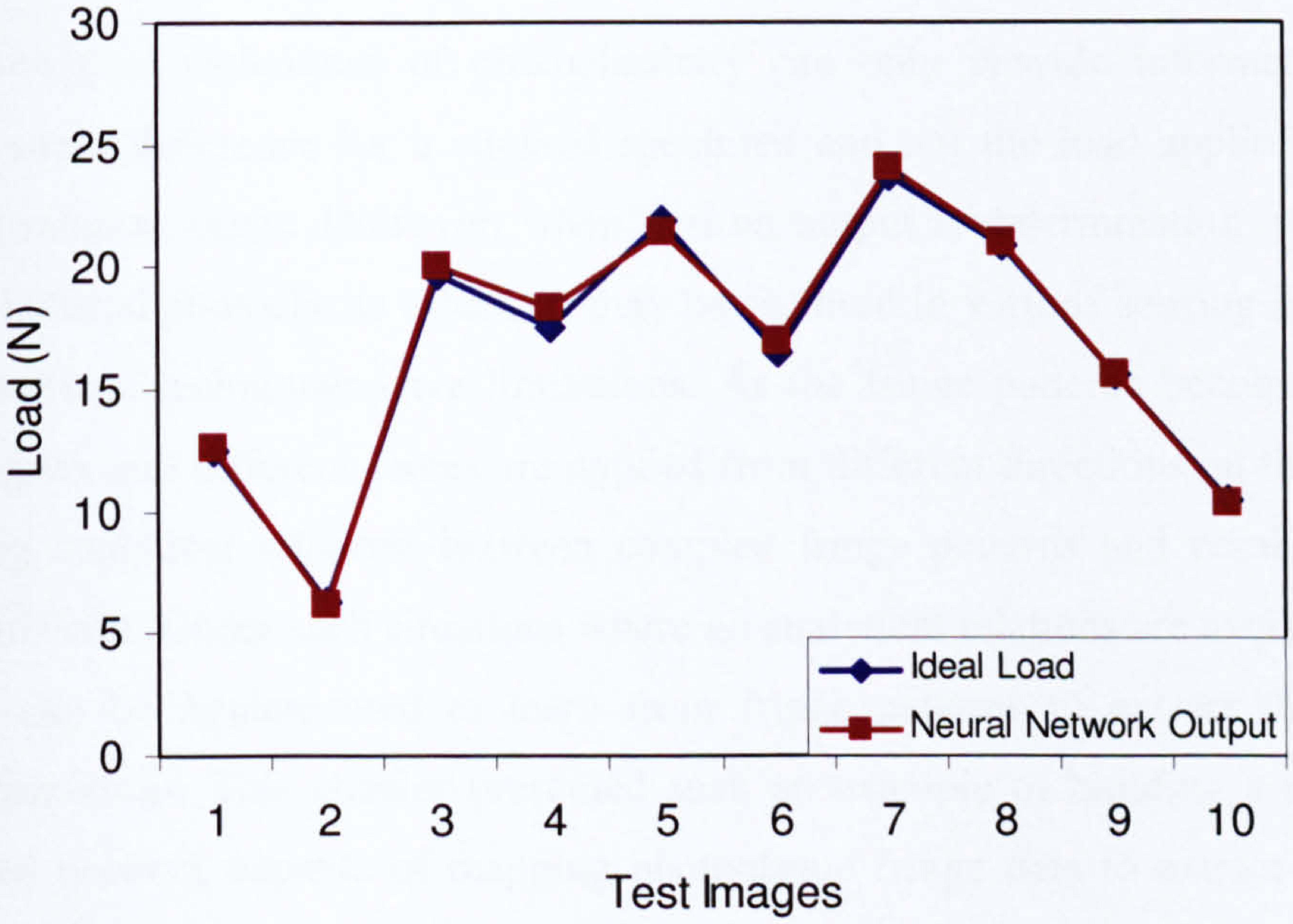

Figure 5-13: Results plot for 10 different test images

Regression analysis on the training data and the test results are shown in Table 5-2. Under ideal conditions of perfect fit (neural network output should equal the desired target) the slope and correlation coefficient should be 1 between training and test data.

Table 5-2: Regression analysis on training and test data

Data	Correlation coefficient	Slope
Training	0.993	0.985
Test	0.999	0.985

Following the co-efficient values obtained from regression analysis and results shown in Figure 5.12, it can be concluded that the network performed considerably well in mapping the input photoelastic image data on to the applied bending load.

5.8 Summary

The conventional techniques of photoelasticity can only provide information on the principal stress difference for a stressed specimen and not the load applied, unless an analytical relation exists. However, when desired output is determination of the forces from the induced photoelastic effect, as may be required in various sensing applications, the conventional techniques have limitations. As the fringe patterns become more and more complex and different forces are applied from different directions on the specimen developing analytical relations between complex fringe patterns and combined forces become difficult. Under such situations where no analytical relations are available, neural networks can be implemented to learn from fringe patterns to extract the specified loading conditions. This chapter presented such an example of building a tolerant and generalised network capable of mapping photoelastic fringe data to extract the desired output load. The presented system overcame the demerits of previously published work and offered an enhanced technique for inverse photoelastic analysis using neural networks. This technique can be further built up with more and diverse inputs to the network for a more generalised and complex problem under varying conditions of load.

Chapter 6 Force Visualisation and Measurement

6.1 Introduction

This chapter further develops the technique of artificial neural networks discussed in the preceding chapter for evaluation of different loading conditions viz vertical and shear forces by analysing the photoelastic fringe patterns induced in the sensing plate. The methodology is based on the inverse photoelastic technique, however, a generalised case is considered here, where normal as well as shear forces are applied to the sensing plate and images produced are analysed by taking into account the various parameters of the image. The main parameters considered were image intensity, geometric and statistical parameters and later combinations of these parameters was tried and results obtained in each case are discussed with their limitations. The last section of the chapter presents qualitative load visualisation from actual foot loading.

6.2 The Loading Characteristics

The experimentation for this chapter uses the developed photoelastic sensing plate and subjects it to known vertical and shear loads. Neural network based methodology developed in previous chapter is implemented to determine the triggering parameter (the applied forces) from the produced photoelastic fringes. Since the fringe patterns pan out on application of vertical load as seen in Figure 6.1(a), it is important to understand the effect of various parameters that govern the fringe panning through the indenter loading. The following parameters have direct bearing on the characteristics of the fringe patterns:

1. **Geometry of indenter**: Fringes generated under a hemispherical head indenter would pan out to a different length compared to a flat head indenter.
2. **Diameter of indenter**: Larger diameter indenter head would cause the fringes to propagate to a different length than a smaller diameter.

3. **Material properties**: High modulus material used under indenter would generate higher fringe order and higher propagation of fringes. However, with too high modulus (2.5 GPa) such loading may not generate appreciable fringes as material straining may be insignificant.

Further comparative study on the influence of the above parameters on the fringe patterns is given in Appendix-III.

Two types of forces (vertical and shear) were applied to the photoelastic plate separately or in conjunction by the specially designed indenter (Chapter 3 section 3.5.3) and experimental setup discussed in section 3.5.5. The vertical force deforms the material and fringes propagate radially from the point of application of load in a symmetrical way. The fringe patterns appear as concentric circles of sequential colours when white light is used, as in these experiments. When shear force is applied in conjunction with the vertical force the fringe patterns smear in direction of application of force. Figure 6.1 shows the effect of vertical and shear force on the surface of photoelastic plate.

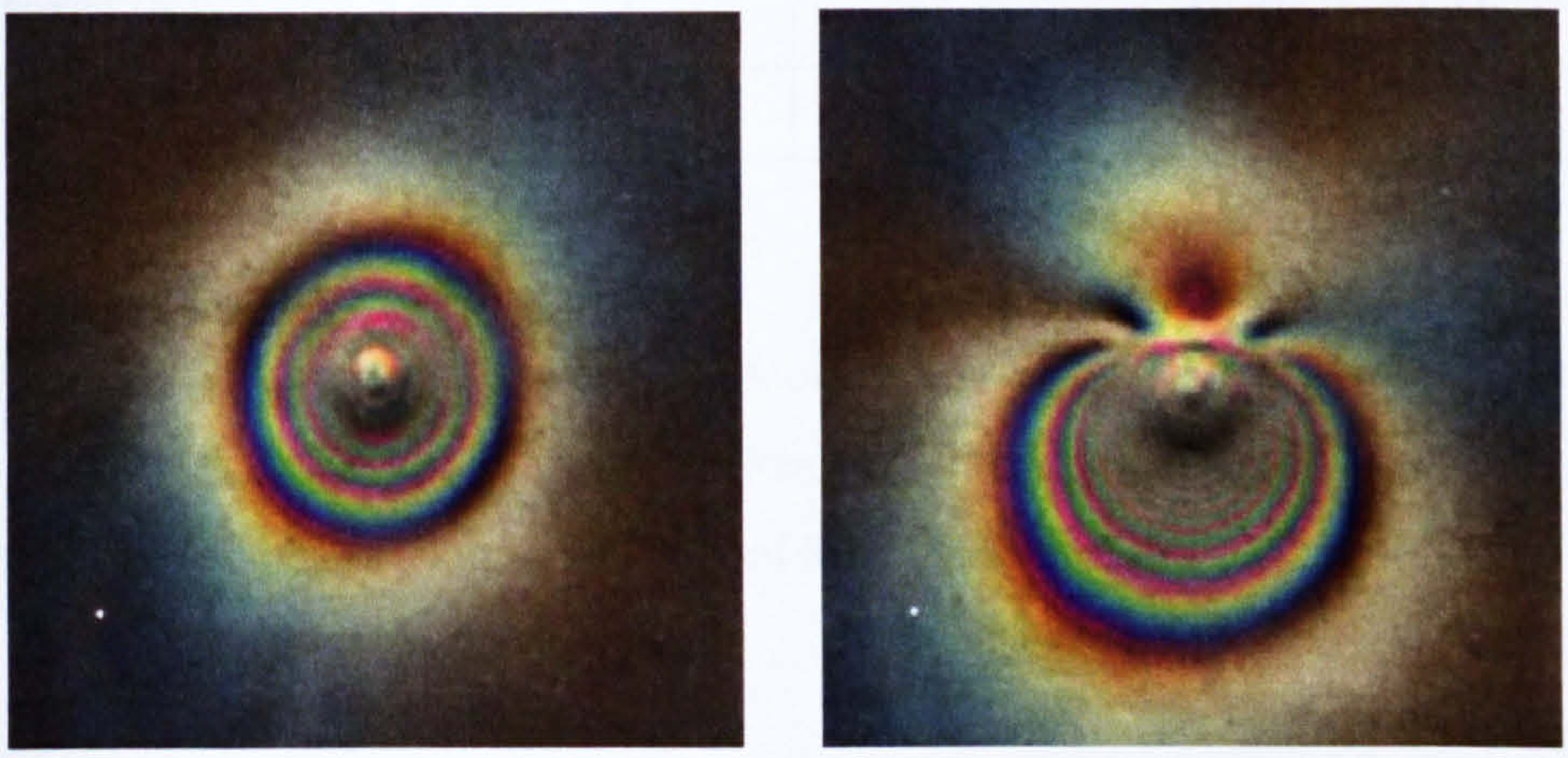

Figure 6-1: The effect of vertical (23.4 N) and shear (19.13 N) forces on the surface of photoelastic model with hemispherical head indenter using scanner based system

The co-efficient of friction was found to be 0.89 between the polycarbonate indenter heads and the photoelastic model with reflective paint, which was determined experimentally. Co-efficient of friction helps in determining maximum amount of shear force that can be applied at a particular value of vertical force without slipping the indenter. This also ensures that for the intended sensing application the coefficient of friction would be sufficient so that appropriate level of shear force can be measured without slippage. Table 6-1 shows a part of the range of vertical and shear forces applied on the material for the following experiments.

Table 6-1: Applied vertical loads with a range of shear loads

Vertical force (N)	**8.68**	**9.66**	**10.64**	**11.62**	**.......**	**21.43**	**22.42**	**23.4**
Shear force (N)	1.47	1.47	1.47	1.47		1.47	1.47	1.47
Shear force (N)	3.43	3.43	3.43	3.43		3.43	3.43	3.43
Shear force (N)	5.39	5.39	5.39	5.39		5.39	5.39	5.39
Shear force (N)	7.35	7.35	7.35	7.35		7.35	7.35	7.35
Shear force (N)			9.32	9.32		9.32	9.32	9.32
Shear force (N)						11.28	11.28	11.28
Shear force (N)						13.24	13.24	13.24
Shear force (N)						15.20	15.20	15.20
Shear force (N)						17.16	17.16	17.16
Shear force (N)								19.13

The vertical load was incremented in steps of 100 gm starting from 500 gm (excluding weight of indenter 385 gm) and the shear load was incremented in steps of 200 gm. The limiting value of shear at a particular vertical load was determined using Equation 6.1.

$$S_{\max} = 0.89V_i \qquad (6.1)$$

Where, $S_{\max}$ is the maximum permitted shear load under the vertical load of V_i.

The vertical load was placed directly on the top surface of indenter while shear force was applied by a pulley–cord setup as shown in Figure 6.2. A nylon cord was used for connecting indenter and the shear load. Figure 6.2(a) shows the top view of experimental rig and Figure 6.2(b) shows fringe patterns induced under all the four indenter heads from the loading.

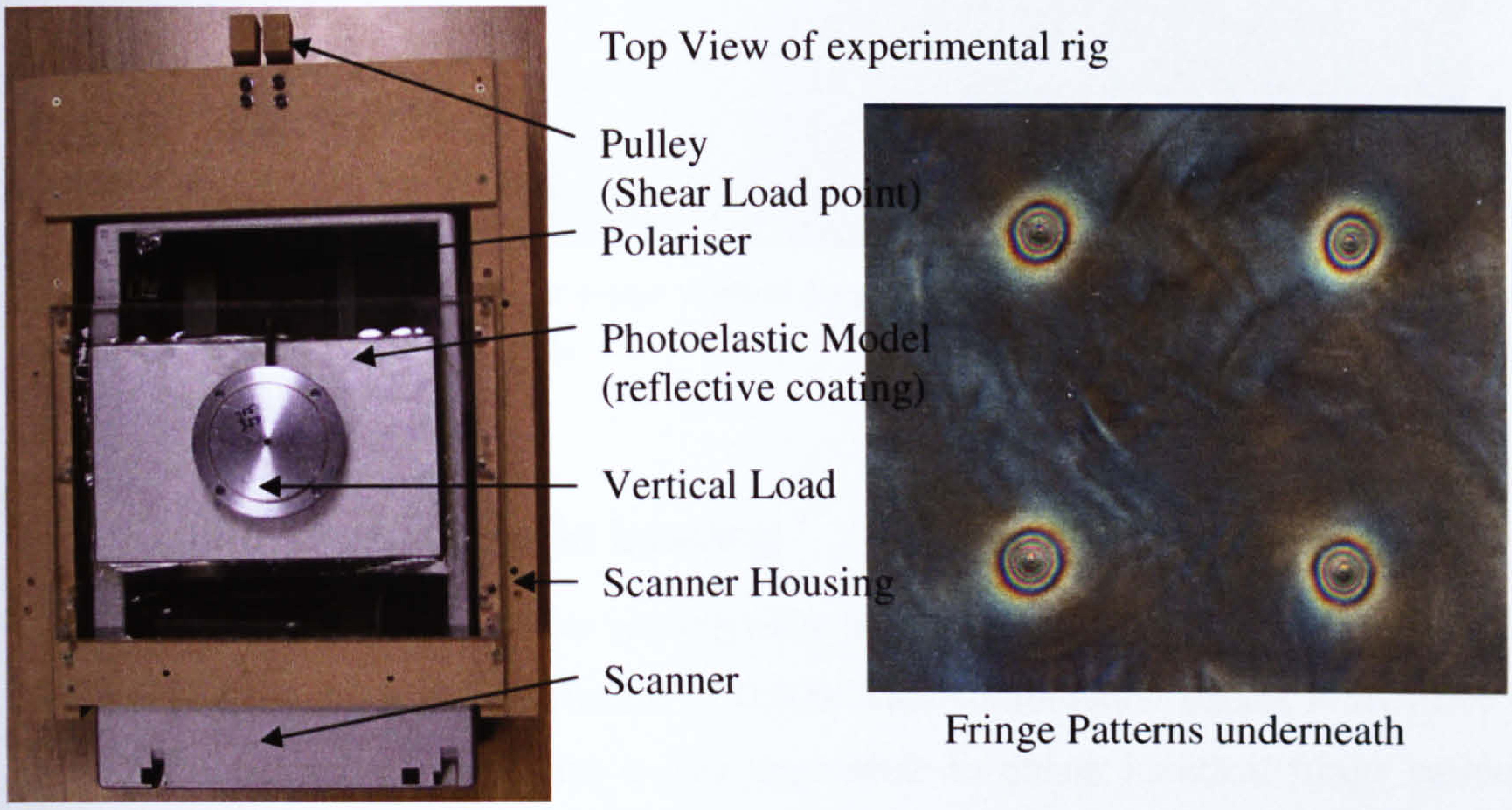

Figure 6-2: (a) Top view of the scanner based experimental rig, (b) fringes induced under all the four indenter heads

Figure 6.3 shows a series of fringe patterns obtained under a vertical load of 22.42 (N) for indenter head 4 and how the fringe patterns change when incremental shear force is introduced to the vertical force.

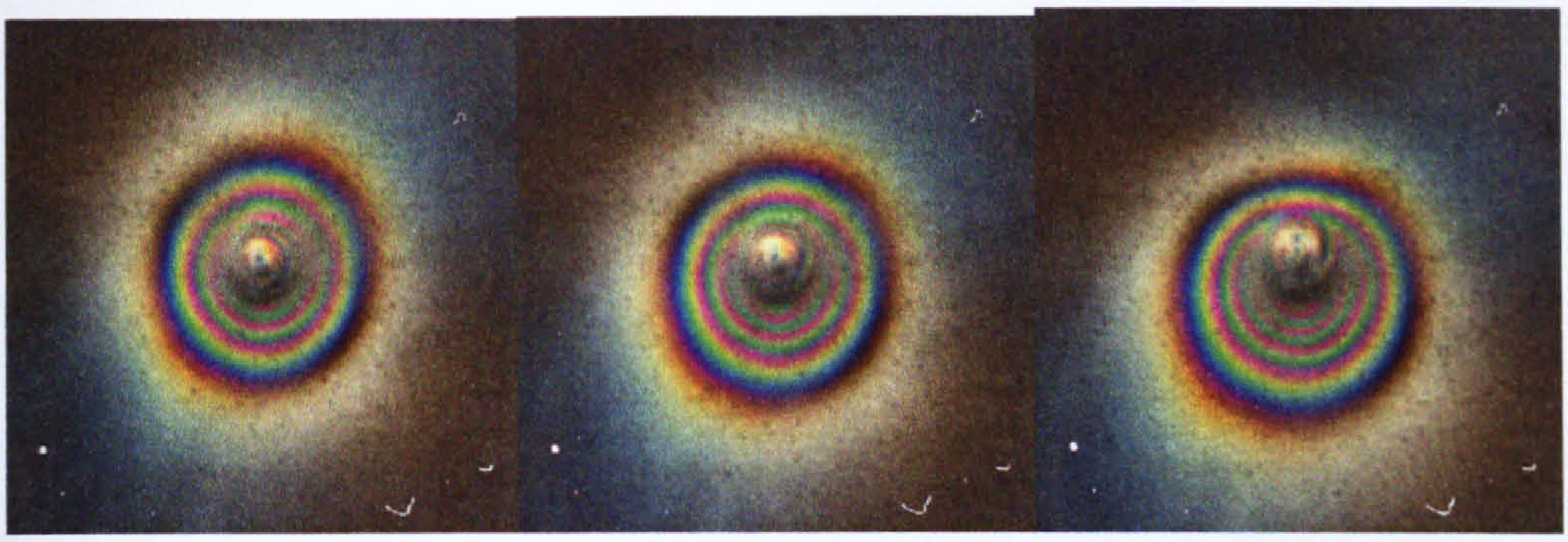

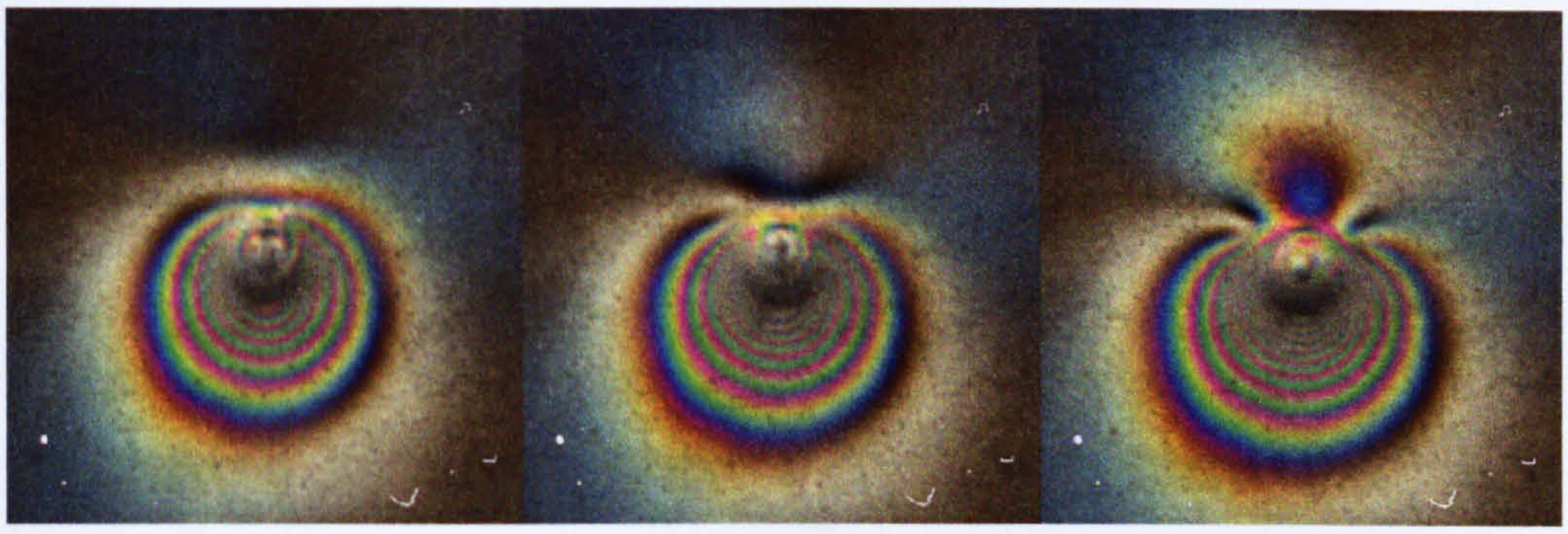

Figure 6-3: Fringe patterns obtained under vertical force of 22.42 N with incremental shear force in steps of 3.92 N from 3.43 N to 19.12 N

6.2.1 Experimental Errors in Loading

The photoelastic material used for sensing plate had a low modulus of elasticity of 0.004 GPa and high strain optic co-efficient of 0.009. This combination makes it sensitive to even small changes in force, thus it was impossible to obtain identical fringe patterns under all the four indenter heads for a known vertical load as evident from Figure 6.2. These errors in loading can be determined by measuring the diameter (horizontally) of fringe patterns under all the four heads and repeating the experiment several times. In order to do that the images were converted to HSV plane for ease of image processing. Further images were segmented in H-plane and then the diameter of the outermost fringe was measured by the developed algorithm (Appendix-III). Measured diameter for all the four fringes under different indenter heads for 9 sets of experiments was averaged to get an ideal diameter. Percentage error for all the measured diameters was evaluated against the ideal diameter. Figure 6.4 shows the measured diameter for vertical load of 17.5 N with averaged diameter from the four indenters represented by the black-cross for each set of experiment.

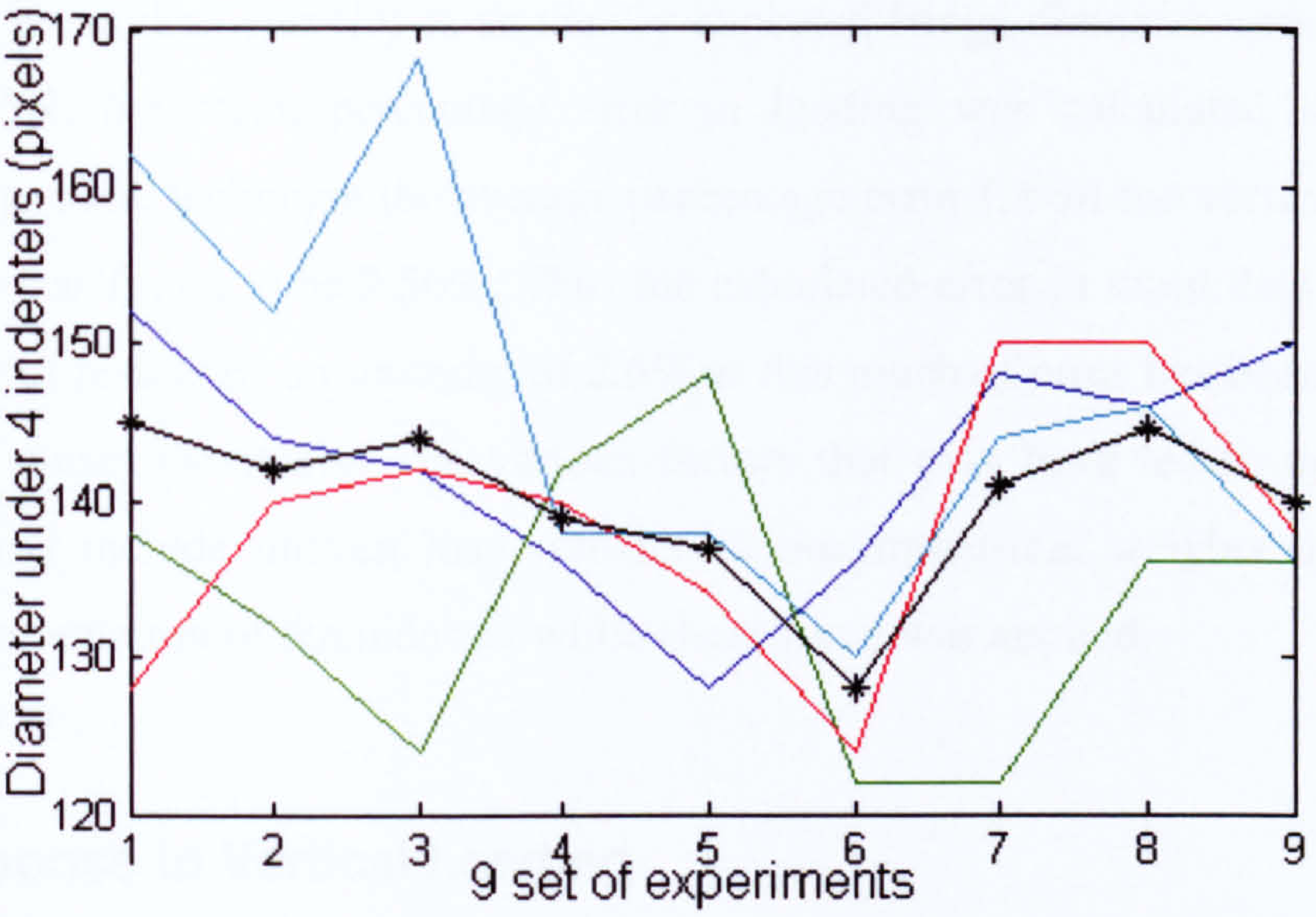

Figure 6-4: The average fringe diameter under 4 indenter heads from 9 experiments, black line representing average diameter

The fringe diameters are represented in pixels and for each experiment from 1-9, four diameters were recorded as represented by red, green, blue and cyan lines corresponding to fringe patterns under each indenter head. Following the above two conclusions were drawn first, the fringe patterns induced by the four indenter heads were not identical in terms of diameter (as red, green, blue and cyan lines are far apart), second; the averaged diameter from four fringe patterns had a significant difference (black line) even though the vertical load was kept same for the repeated experiments. A statistical evaluation of error in loading and fringe generation was performed following the significant difference in statistical parameter in the fringe patterns. Table 6-2 shows averaged diameter for each experiment; in other words it represents the black line.

Table 6-2: Average fringe diameter from 4 indenters for 9 experiments

145	142	144	139	137	128	141	144.5	140

The fringe diameters in the table were averaged to obtain an ideal diameter D, the mean of 36 (4x9) fringe diameters.

D= 140.05

Considering mean diameter (*D*) as an ideally expected fringe diameter under the vertical load of 17.5N, the mean percentage error in loading was calculated to be 2.57%. Following the same technique the average percentage error for all the vertical loads for 9 experiments was found to be 2.56%. Thus the calculated error in input data would affect the accuracy of results by a minimum of 2.6% as this much of error has been added in the input at the outset inevitably. The various factors that may have led to unsymmetrical fringe patterns include uneven load transfer to unsymmetrical weights design and to slightest disorientation of the indenter while shear force was applied.

6.2.2 Response to Vertical Loading

As explained earlier the fringe patterns tend to pan out under the influence of vertical force, Figure 6.5 shows the influence of increasing vertical load on the diameter of fringe patterns obtained from 9 repeated experiments.

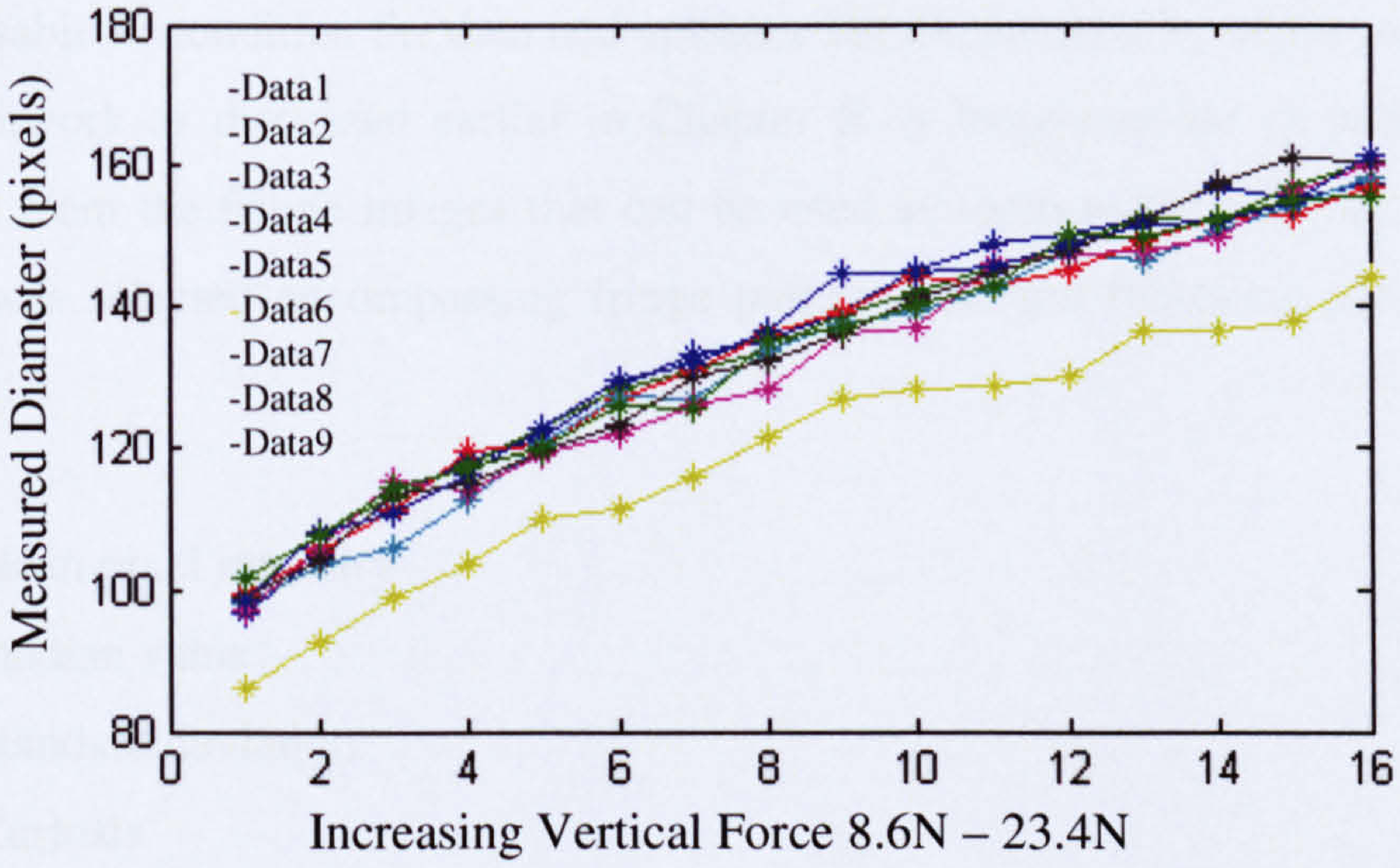

Figure 6-5: The influence of vertical load on measured diameter of fringe patterns

Every point plotted in each data line in Figure 6.5 is averaged measured diameter from all the four fringe patterns under four indenter heads. It is evident that the plot of averaged diameter measured from 9 repeated experiments has significant differences. Data collected from experiment 6 seems to be out of place and can be attributed to the measurement error or loading itself. Even if the data did fall in the range of the rest of the plot, still reliability in measurement of vertical load from the fringe diameter cannot be ensured. Using just one geometric parameter in determination of load from the fringe patterns may not be a reliable method, since material is too sensitive to this kind of loading and achieving identical fringe patterns under repeated loading is difficult. Thus a more reliable and high tolerant algorithm is required to extract load information, which can use maximum possible fringe information. In the following section the neural network approach as developed in Chapter 5 was used to determine vertical and shear force using various parameters extracted from the fringe patterns.

6.3 Data Conditioning and Optimisation

The fringe data acquired in form of images was used for training and testing of the neural network. Since an entire image cannot be used as input due to high input dimensionality, it is advisable to condition the data and optimise the dimensionality of the input being fed to the network as discussed earlier in Chapter 5. A large number of parameters were extracted from the fringe images that can be used as input to the network. A region of interest was selected encompassing fringe patterns and the following parameters were extracted;

1. Mean pixel intensity
2. Median value
3. Standard deviation
4. Kurtosis
5. Skewness of data
6. Horizontal radius- Horizontal stretch in fringe from point of load
7. Vertical radius- Vertical stretch in fringe from point of load
8. Pixel area of segmented ROI
9. Intensity information from region of interest

The above parameters were fed in combination and individually to reach to an optimal input for network training. Principal component analysis (PCA) was used as data reduction technique in the following implementation. Since training data is limited by the number of experiments, it is important to narrow down to an optimal dimensionality through PCA whilst maintaining the subtle differences in the fringe patterns under the consecutive loads.

6.4 Optimisation of the Selected Network

A large number of networks were tested for the best possible results; the training method adopted was 'Levenberg-Marquardt' as it proved to be the most suitable for the type of data (fringe patterns) available for analysis. Both single layered and multi-layered architecture were used and the results were found to be accurate when a network with two hidden layers was used.

Training data was accompanied by validation data to keep a check on network over-fitting or memorising. The network was initialised randomly 10 times under each layer configuration and 200 different layer configurations were tested. Testing network for a wide range of configurations becomes essential here due to the following two factors:

1. The application requires 128 different numerical values as output from image data, as opposed to most of the applications where the desired output is classification of images in just 2-5 different bins.

2. There is a subtle difference between consecutively loaded images. An image acquired under a particular value of vertical and shear load tends to be very similar to other images acquired under different vertical and shear load combinations.

Thus the data in this case is equivalent to classifying similar looking patterns into 128 different groups, which makes the training harder. The following sections present data analysis using various image parameters viz statistical, geometric and intensity to obtain loading information from the sensing plate. Later a combination of these parameters was fed to the neural network to compare the results obtained under these circumstances.

6.5 Data Analysis using Statistical Parameters

The input training data used for the network was derived from the statistical analysis performed on the acquired images. Each image was stacked down to individual planes and intensity data from only one plane was used for statistical analysis. Since there is no considerable difference between fringe patterns in different planes (R, G & B) due to optics of the problem, the plane with highest contrast was considered for analysis. Different statistical parameters, Kurtosis, Skewness, Mean Pixel Intensity, Standard Deviation, Median (definition of these parameters is available in Appendix III) were extracted and fed as input to the neural network to map the shear force. Figure 6.7 shows the optimal results that were achieved using statistical parameters as input to the network *with 23 random test images.*

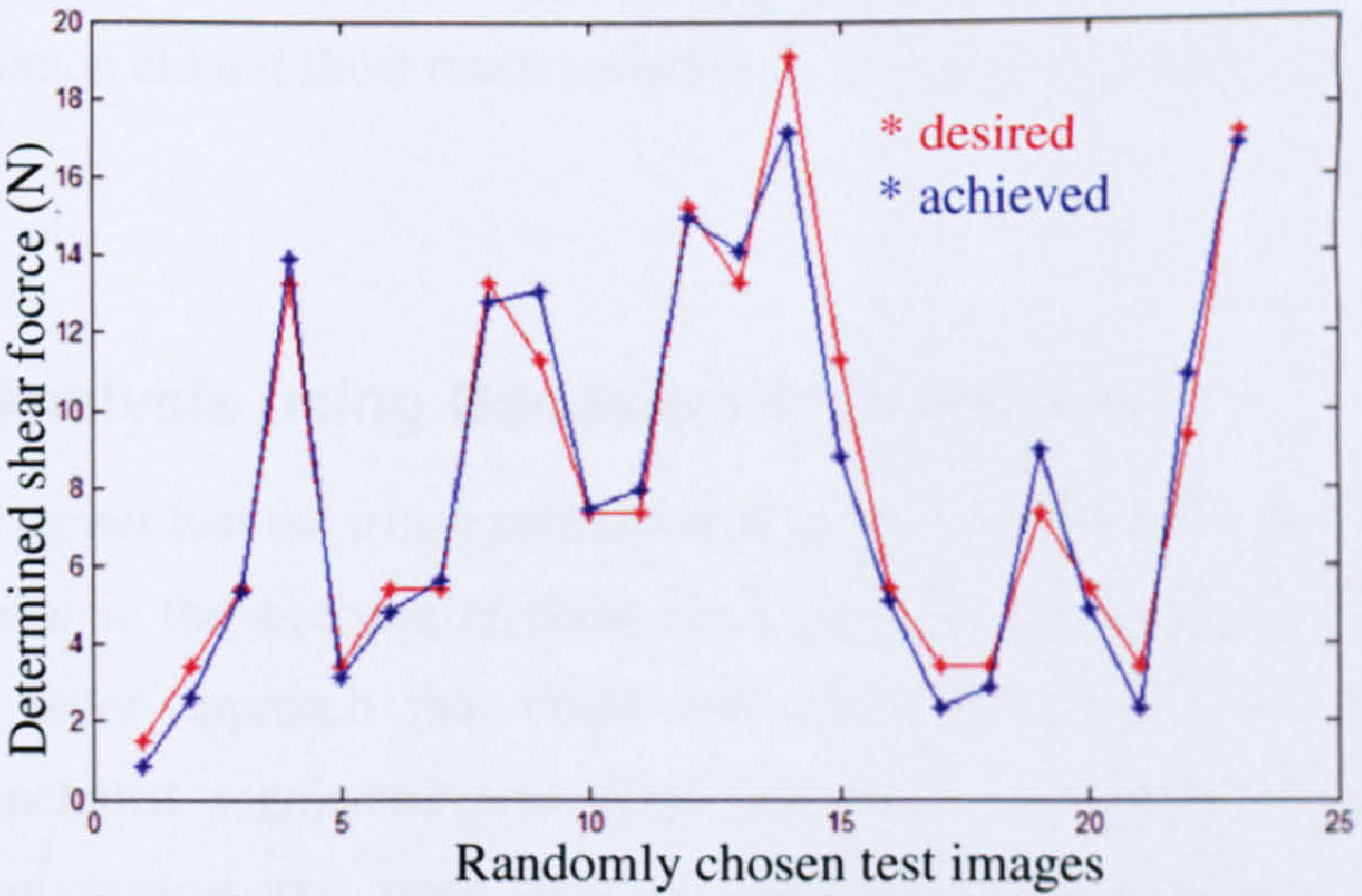

Figure 6-6: Determined shear force using statistical parameters

The Figure 6.6 shows desired shear force compared to determined shear force at different vertical load values. Table 6-3 list the vertical forces at which each shear force was determined. The same vertical forces were used for all the following experiments.

Table 6-3: Vertical force at which shear forces were determined in 23 test images

Test Image	1	2	3	4	5	6	7	8	9
Vertical Force (N)	8.68	10.64	9.66	14.56	12.6	16.53	12.6	15.54	21.43
Test Image	10	11	12	13	14	15	16	17	18
Vertical Force (N)	17.51	19.47	19.47	22.41	22.41	13.58	17.51	20.45	17.51
Test Image	19	20	21	22	23				
Vertical Force (N)	12.60	15.54	9.66	18.49	21.43				

The average percentage error found for 23 test images was 13.15% and for the entire load range (112 test images) was 13.45%. The results obtained were reasonable to continue using neural networks for force determination but were not accurate enough. As can be seen in the figure, for some test images the error is too high due to insufficient input data and training patterns. Many of the statistical parameters like mean pixel intensity and standard deviation did not show much variation with change in load values.

6.6 Data Analysis using Geometrical Parameters

As discussed earlier that the fringe patterns tend to pan out under the influence of vertical force and smear in the direction of shear force, thus measuring geometrical parameters could be a better approach that could lead to meaningful results. The measured parameters included segmented area from hue plane and radius measured in both horizontal and vertical axis since they are controlled by different forces. Horizontal radius being influenced mostly by the vertical load, whereas vertical radius is influenced by the shear load which stretches the fringe patterns in direction of application of load starting from the point of loading.

The network was trained with an input dimensionality of 8 contributed by the four area values corresponding to fringe patterns under each indenter head, two horizontal and two vertical radii measured for the bottom two fringe patterns as they happen to change more significantly under the influence of shear force. Figure 6.7 shows the results obtained from training the network with geometrical parameters and testing for shear load. The optimal network had a configuration of {8,2,5,1}, where 8 is the input dimensionality, 2 neurons in the first layer, 5 in the second and 1 is output dimensionality. The network is small and results are accurate with respect to the input provided.

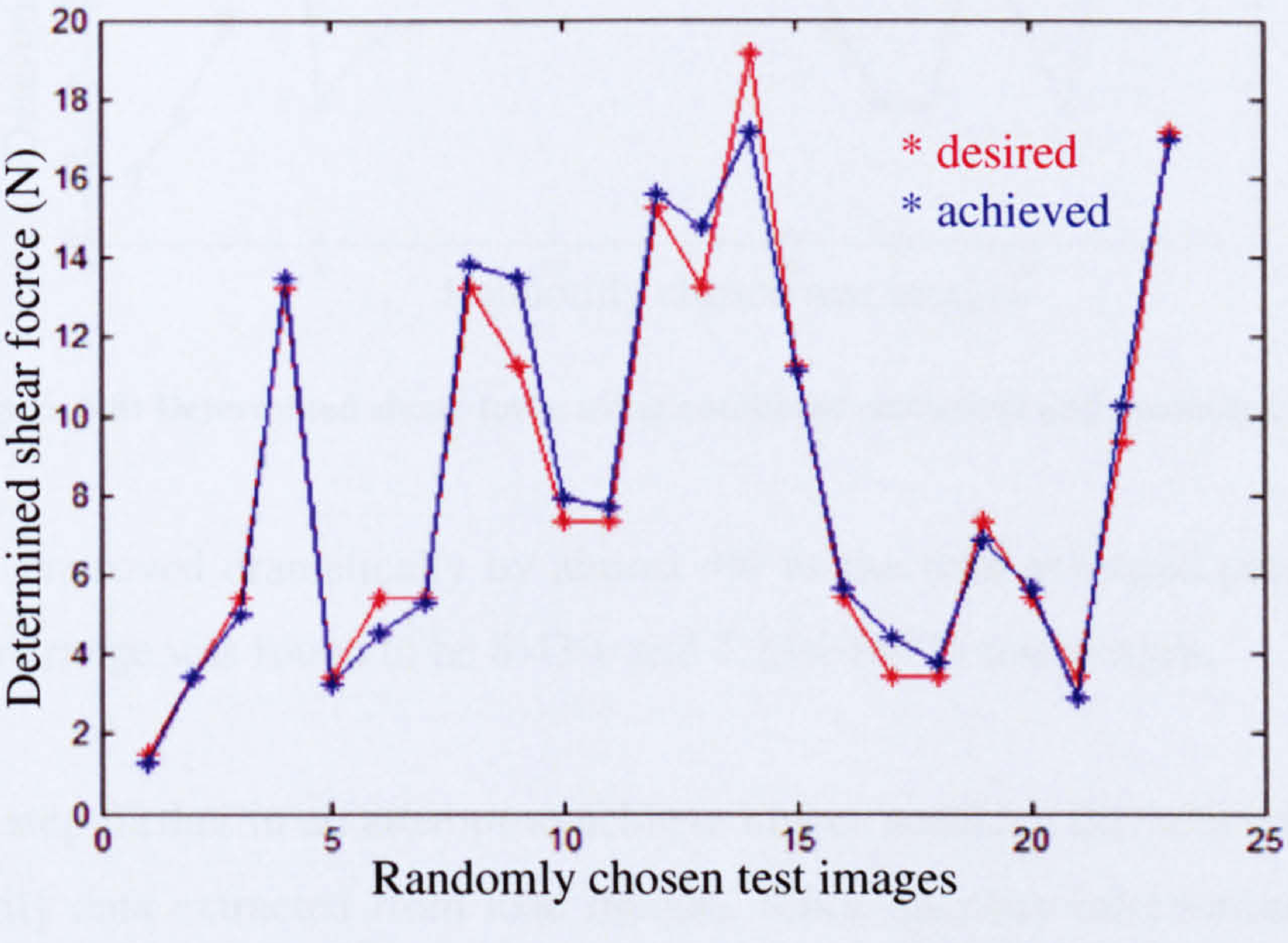

Figure 6-7: Determined shear force using geometric parameters

The percentage error was found to be 8.15 % for 23 test images and 11.4 % for entire range of loading (112 images). The results obtained were better than what were achieved with statistical parameters, since the geometrical parameters were influenced more significantly with the change in load. However, the accuracy desired was still not achieved and thus combined statistical and geometric data was tried for training the network.

6.7 Combined Statistical and Geometric Parameters

Since encouraging results were obtained using statistical and geometric data, it was envisaged that error would reduce if the training data was combined from the two. Thus a network was constructed and trained with combined statistical and geometric data. The results obtained are shown in Figure 6.8.

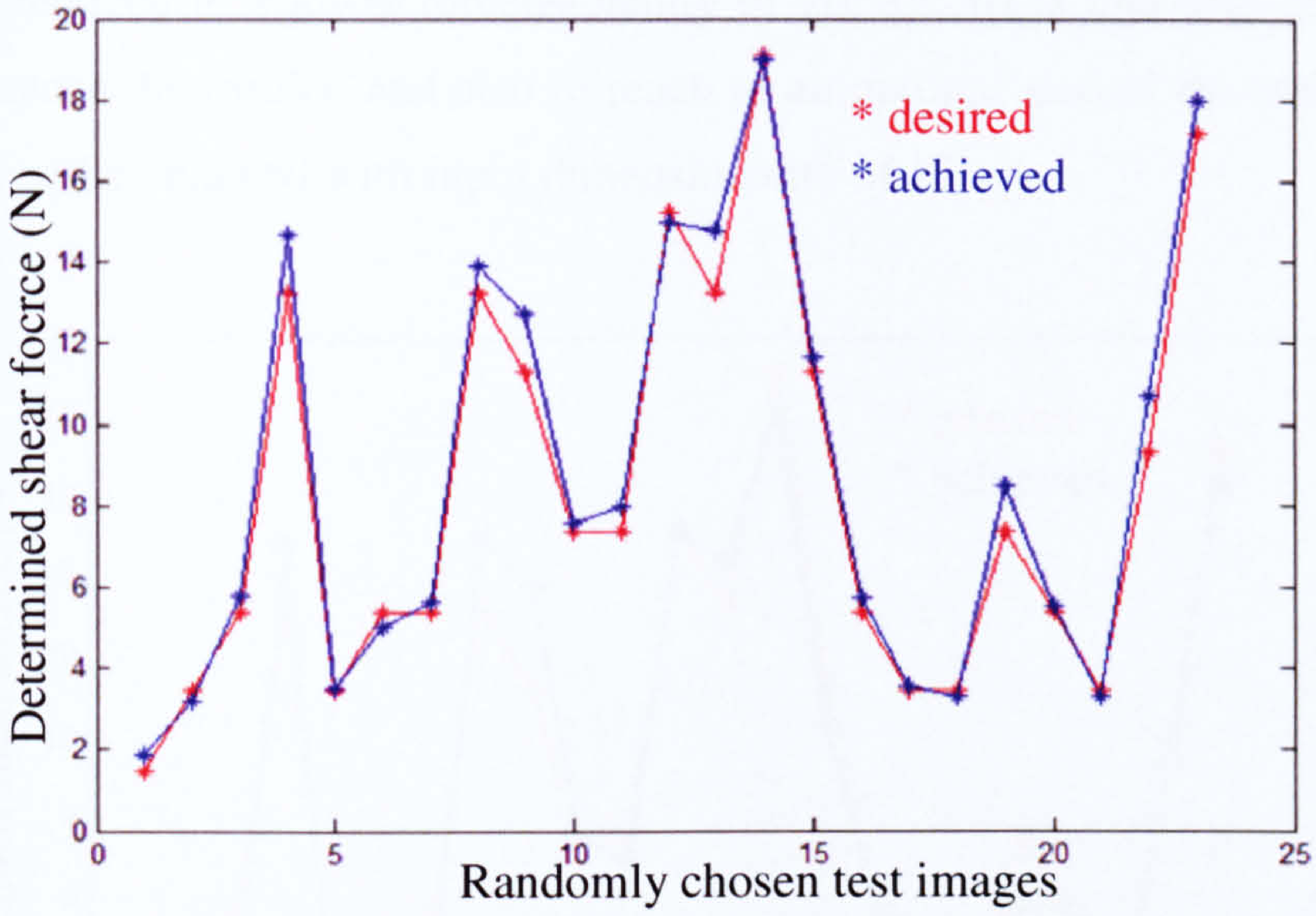

Figure 6-8: Determined shear force using combined statistical and geometric data

The results improved dramatically by almost 4% as the total averaged percentage error for the entire range was found to be 8.43% and 7.23% for 23 test images.

To move a step further in an attempt to achieve higher accuracy the network was trained with intensity data extracted from load images. Since intensity information is the most abundant information and seemed most relevant in this case, the results were expected to improve.

6.8 Analysis using Intensity Data

The intensity data available is massive for each image, however, using an entire or even a part of image directly for training would be huge (Grewal and Dubey 2007) which may lead to dimensionality curse. The number of training patterns were also limited because of time constraint in collecting data and the computations required. Thus input data was collected from a region of interest and dimensionality was reduced using PCA.

The training data was collected along a line profile across the vertical diameter of the image and reduced to a lower dimensionality of 20, 15, 10, 8 and 6 to check how this would influence the results; and also to reach to an optimal size of the input. Figure 6.9 shows the results obtained with input dimensionality of 15.

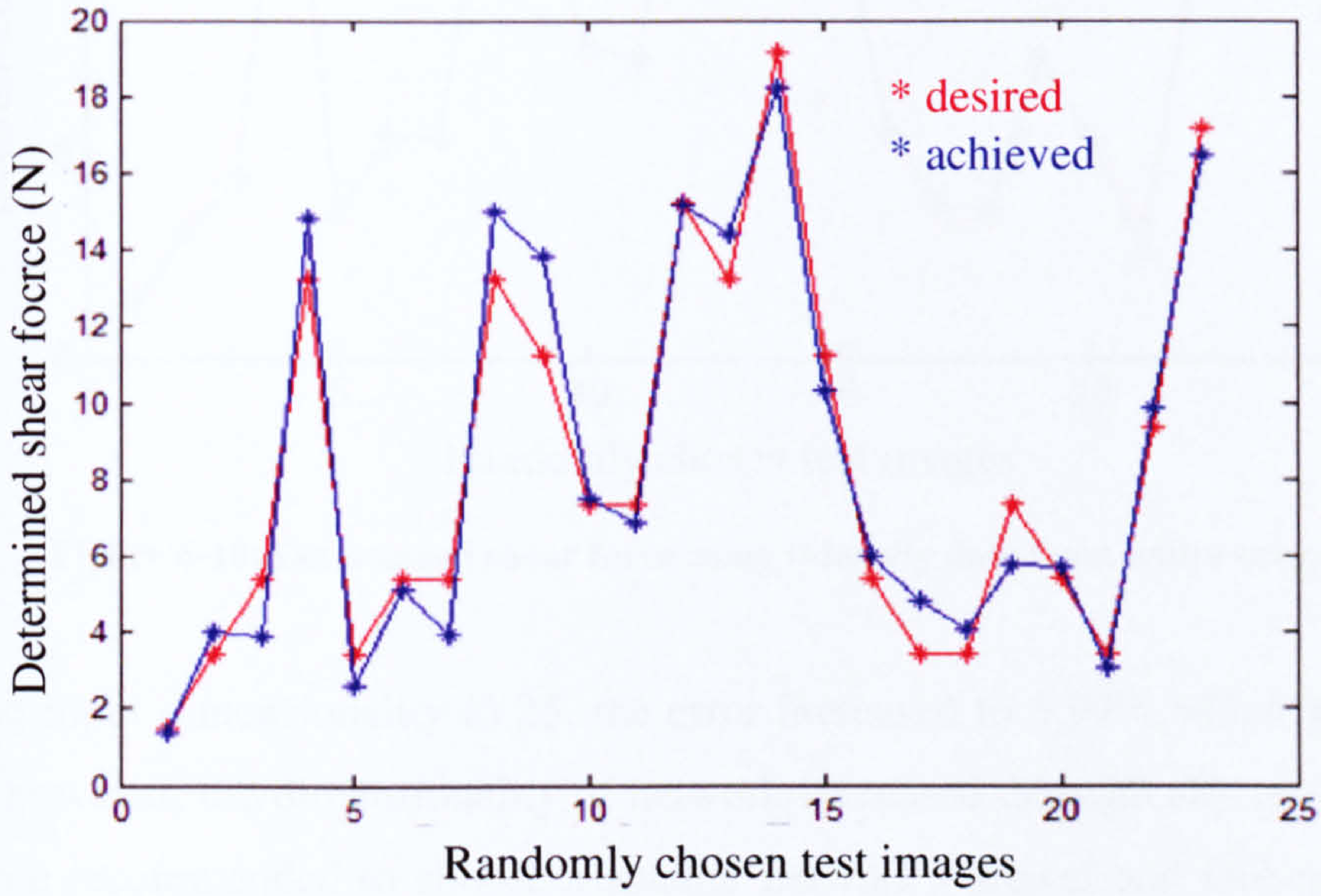

Figure 6-9: Determined shear force using intensity data

The results gave an average error of 19% for the entire range and 13.3% for 23 test images thus a lower accuracy compared to the previously fed input of statistical or geometrical values. The reason why intensity data came out with such a low accuracy was that the input fed as intensity from a small region of interest would not be as relevant and crisp as features extracted from geometrical and statistical parameters.

To improve results the entire image was considered for extracting input rather than just a region of interest or line of interest. The image was resized to a size of 75x75 pixels and PCA was preformed to reduce the dimensionality to 20. Figure 6.10 shows the results obtained with average error reduced to 5.1% for entire range of loads and 5.35% for 23 test images with network dimensions as {20,2,6,1}.

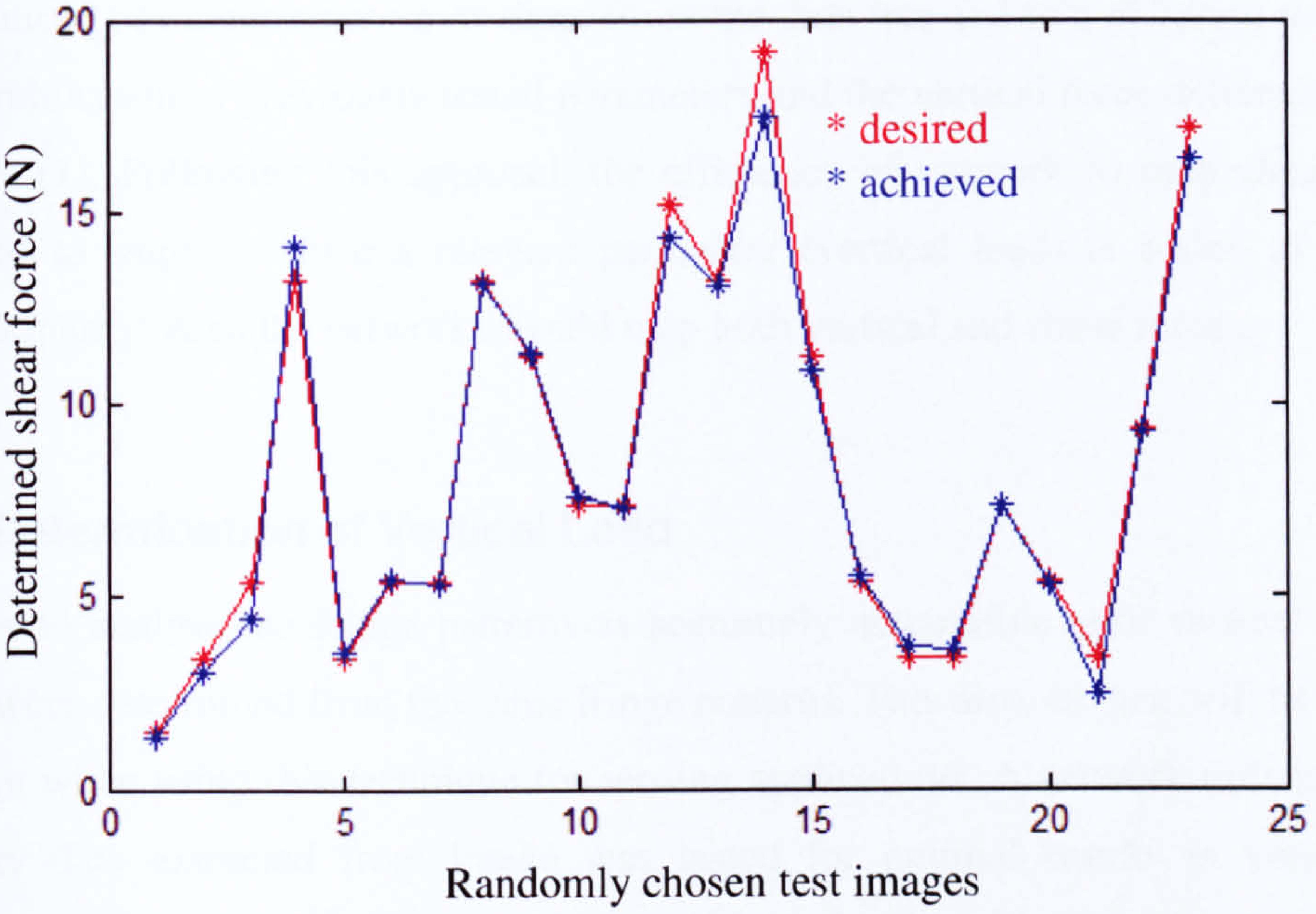

Figure 6-10: Determined shear force using intensity data from entire image

Increasing input dimensionality to 25, the error increased to 5.99% which is marginally different however, the dimensionality of network increased dramatically to {25,6,5,1}. It is therefore recommended to choose a smaller network (Grewal and Dubey 2007) over larger when results are comparable thus former network was set as optimal network. Results obtained using different input dimensionality (25, 15) are shown in Appendix-III.

However, in order to achieve even higher accuracy and tolerance a different methodology was adopted where an attempt was made to make the input more relevant.

6.9 Modified Strategy

The determination of shear force through different approaches like statistical parameters, geometric parameters and intensity data did provide clear indication for implementation of neural networks but the results desired were still not very accurate. A modified approach was adopted in order to improve the accuracy and efficiency of the system; a network (1) was set to determine vertical force from the image data using intensity information. For determination of shear force the data was fed to a different network (2) as a combination of previously tested parameters and the vertical force determined by the network (1). Following this approach the efficiency of network to map shear force is expected to improve since a relevant parameter (vertical load) is added to the input dimensionality. Also the networks would map both vertical and shear forces.

6.9.1 Determination of Vertical Load

In order to analyse the fringe patterns as accurately as possible both vertical and shear forces were determined from the same fringe patterns. This also, in fact, will be the actual situation when using this technique for sensing applications. A network trained from the intensity data extracted from image was tested for optimal results in vertical force determination. Since the desired number of targets were considerably fewer compared to the shear force, the network was trained efficiently and required less computational time. Figure 6.11 shows the results obtained for determination of vertical load from the fringe patterns.

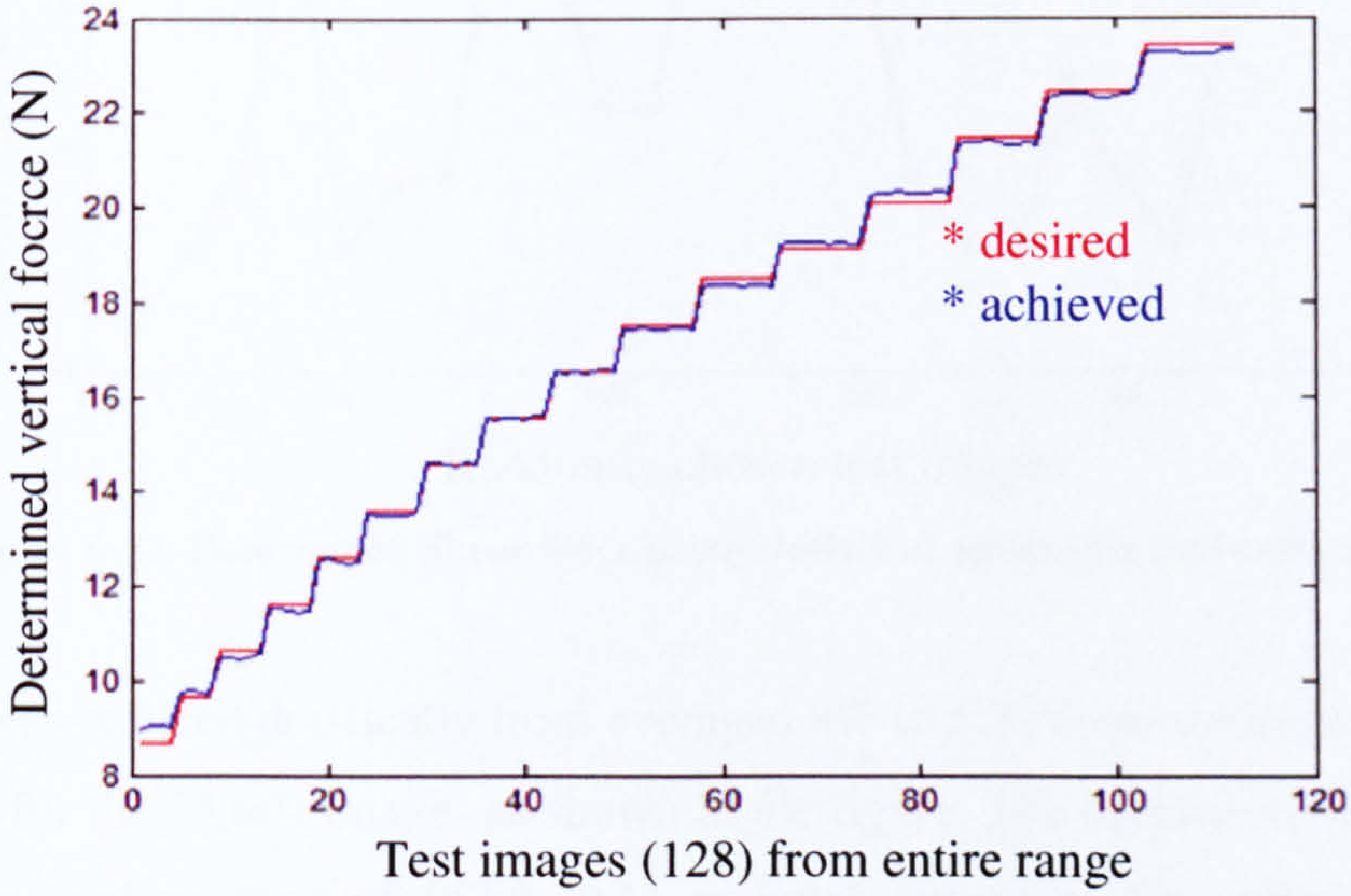

Figure 6-11: Determination vertical force for 128 test images, the graph appears as steps as there was more than one shear force applied at each vertical load

The averaged percentage error for 128 test images was found to be 0.67%, thus giving an accurate value of the applied vertical load. The results plotted appear in stepped form with increasing length because at each vertical load different shear loads were applied (Table 7-1). In absence of shear load the graph would result as a straight line for each vertical load thus appearing as steps. The vertical load determined from the network can now be combined with other inputs (statistical, geometric, intensity) and fed to a new network for determination of shear load.

6.9.2 Statistical and Geometrical Parameters with Vertical Input

The network was trained with combined statistical and geometric parameters as input (as discussed in section 6.6) but an additional input parameter, the determined vertical load was added as another relevant input. Figure 6.12 shows the results obtained from the trained network tested over 23 test images.

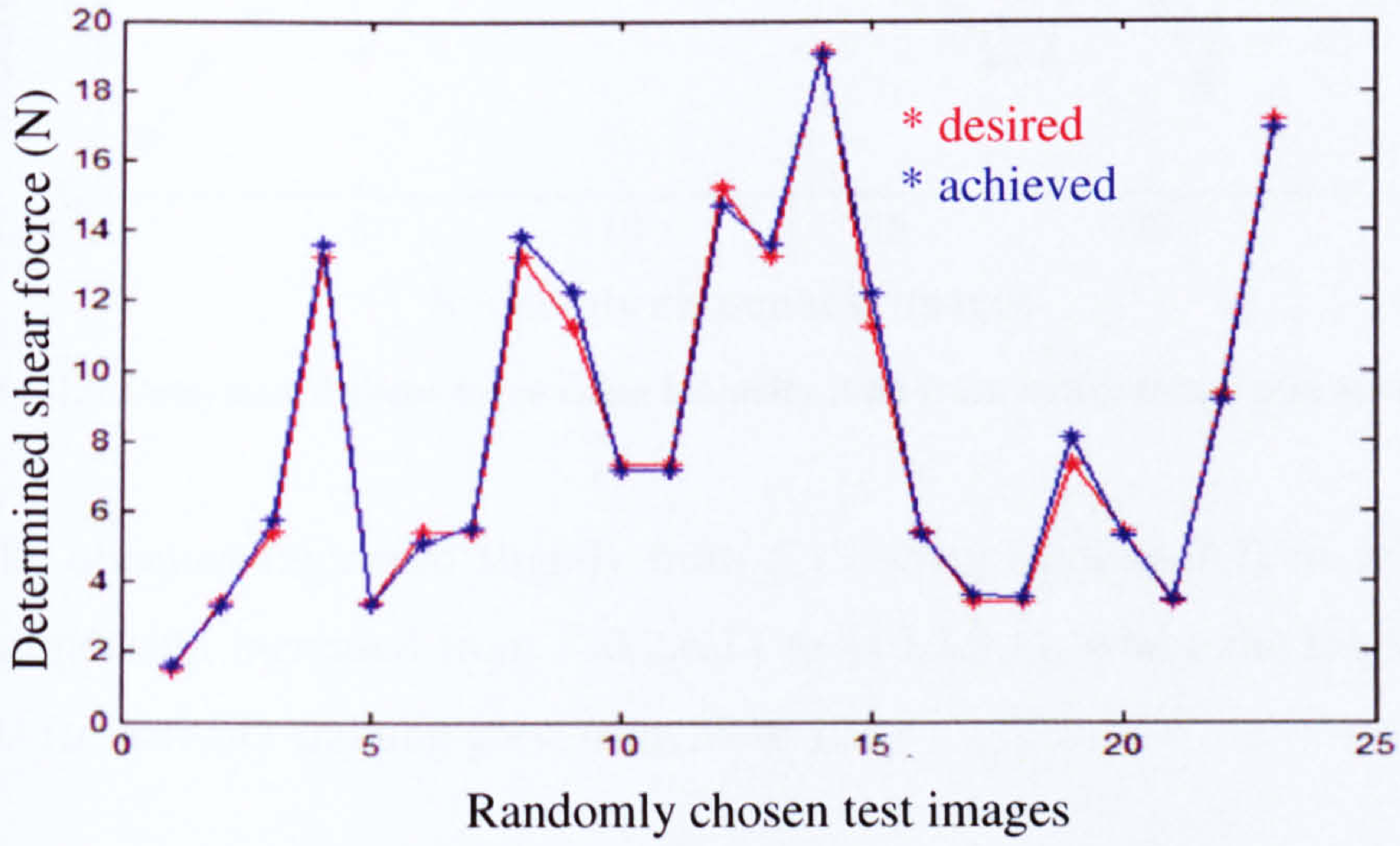

Figure 6-12: Determined Shear force using statistical, geometric and vertical input

The error was reduced drastically from averaged 8% to 5.37% for the entire range of load and 3.86% for the 23 test images as shown in the figure. The optimal network was found to have the configuration of {13,9,20,1} as input dimensionality, neurons in the first layer, neurons in the second layer and the output dimensionality respectively. However, if the accuracy was compromised for 6.46% the network size could be reduced to {13,2,9,1}.

6.9.3 Intensity with Vertical Input

The determined vertical force input was added to the conditioned intensity data of input dimension 15 as 16th input dimension and Figure 6.13 shows the results obtained.

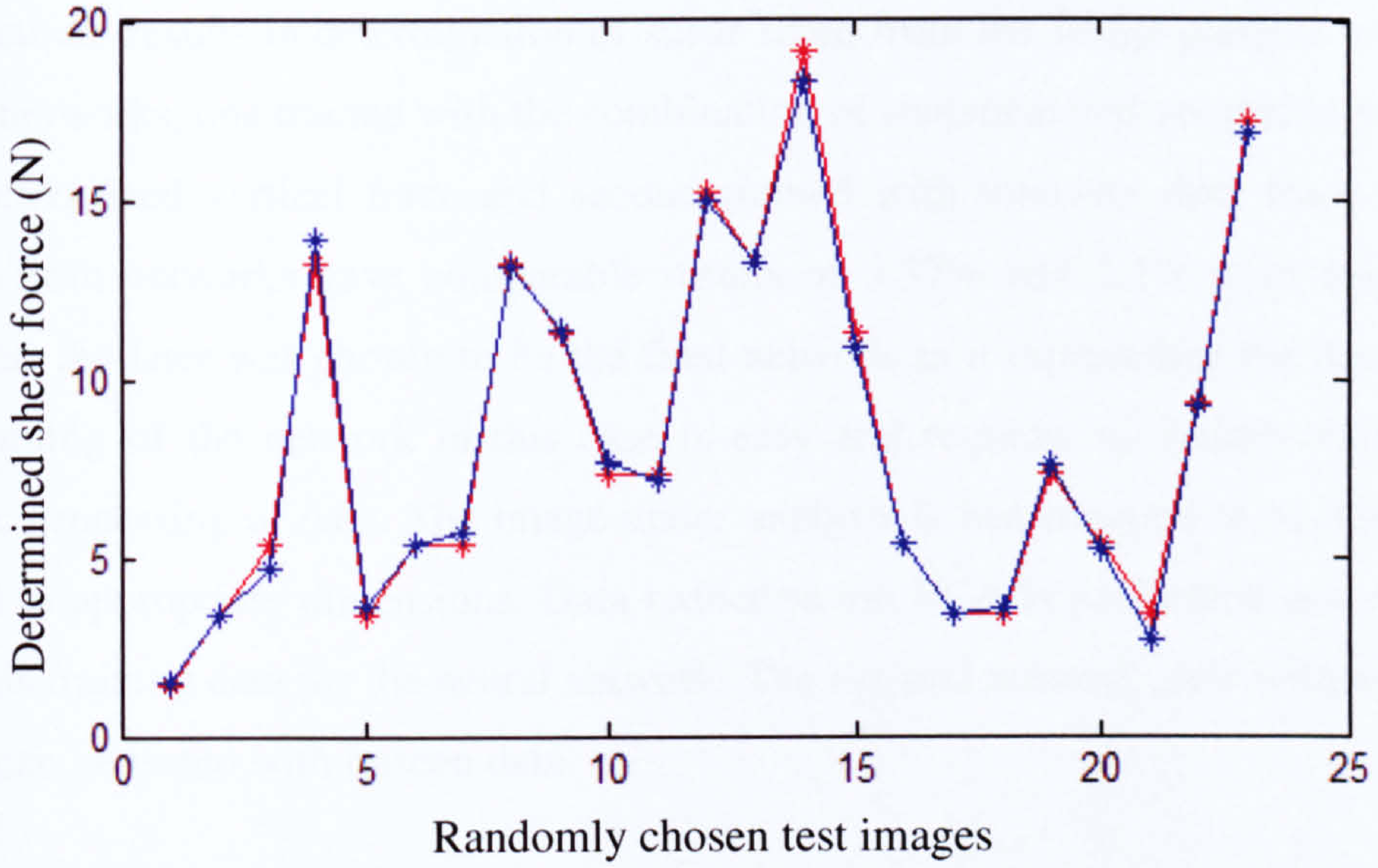

Figure 6-13: Determined shear force using intensity data from entire image and vertical input

The results obtained improved slightly from 5.1% error (section 7.7) to 5.08% but the network dimension increased from {20,2,6,1} to {15,5,8,1}, where the required number of weights for network training grew from 58 to 123.

The addition of determined vertical force as input improved results significantly for the networks trained with statistical and geometrical input parameters and the error reduced dramatically (8% to 5%). However, for the network trained with intensity data there was no significant improvement in results (5.1% to 5%) with additional input of vertical force. This is because the intensity input was extracted considering the entire image, thus it is more likely to represent the whole image and addition of similar image information (vertical force) is unlikely to change the results. On the other hand for statistical and geometric inputs the vertical force was found to be an important input as the other parameters do not represent whole image, thus the network trained with intensity data is an optimal and more efficient network.

6.10 Results and Discussion

The accurate results in determination of shear force from the fringe patterns were found in two networks, one trained with the combination of statistical and geometric parameters with determined vertical force and second trained with intensity data from the entire image. Both networks gave comparable results of 5.37% and 5.1% error respectively, however, the later was chosen to be the final network as it represented the image better. The training of the network in this case is easy and requires no feature extraction or specific processing of data. The image under analysis is just required to be selected and resized to appropriate dimensions. Data reduction via PCA is performed and results are stored as training data for the neural network. The optimal network after training is saved which can be tested with unseen data.

Until now the determination of vertical and shear has been discussed in context of load and not stress because the load applied was point load and the aim was determination of the triggering parameter. However, for real sensing applications such as analysing the foot prints or pressure patterns of a loading, accurate determination of loading at pressure points and providing the whole-field load information may be of more relevance. This will require further investigation using intelligent techniques like neuro-fuzzy and knowledge based system to extract the loading information from these complex fringe patterns. However, an effort is made here to extract qualitative data from the foot print and a basic analysis is presented to extract the information from such images.

6.11 Qualitative Data from Foot Loaded Images

Determination of quantitative information from foot image would require a lot more training patterns and much more sophisticated artificial intelligence techniques beyond the scope of the present research. However, in order to extract some meaningful qualitative data from different foot images, fringe patterns were acquired (scanner based system) and analysed.

Three different sets of data were collected under low, medium and high foot loading and qualitative data analysis was conducted to compare the images under vertical and shear loading. In these experiments attempts have been made to keep the vertical force qualitatively controlled to low, medium and high ranges and the applied shear forces were corresponding to these ranges. Figure 6.14 shows the foot images under a low vertical load followed by a low shear load. The changes in fringe patterns are discernable as it can be seen that fringes tend to propagate in the direction of shear compared to the reference image under the vertical load.

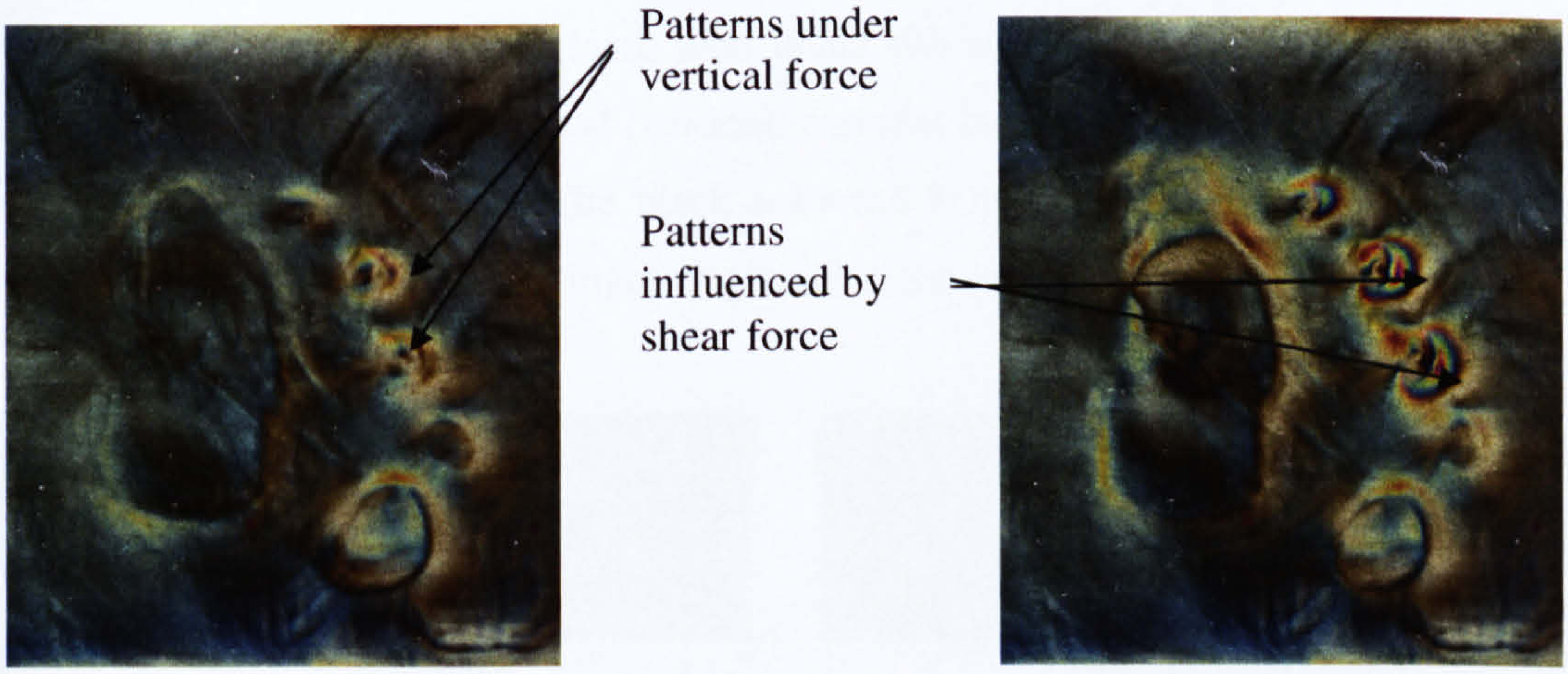

Figure 6-14: Fringe patterns obtained under (a) low vertical load and (b) with low shear load introduced

When medium foot loading was applied to the sensing plate, similar fringe characteristics can be observed in Figure 6.15 under the vertical and shear loads, however, significant changes were visible compared to the previous low level of foot loading.

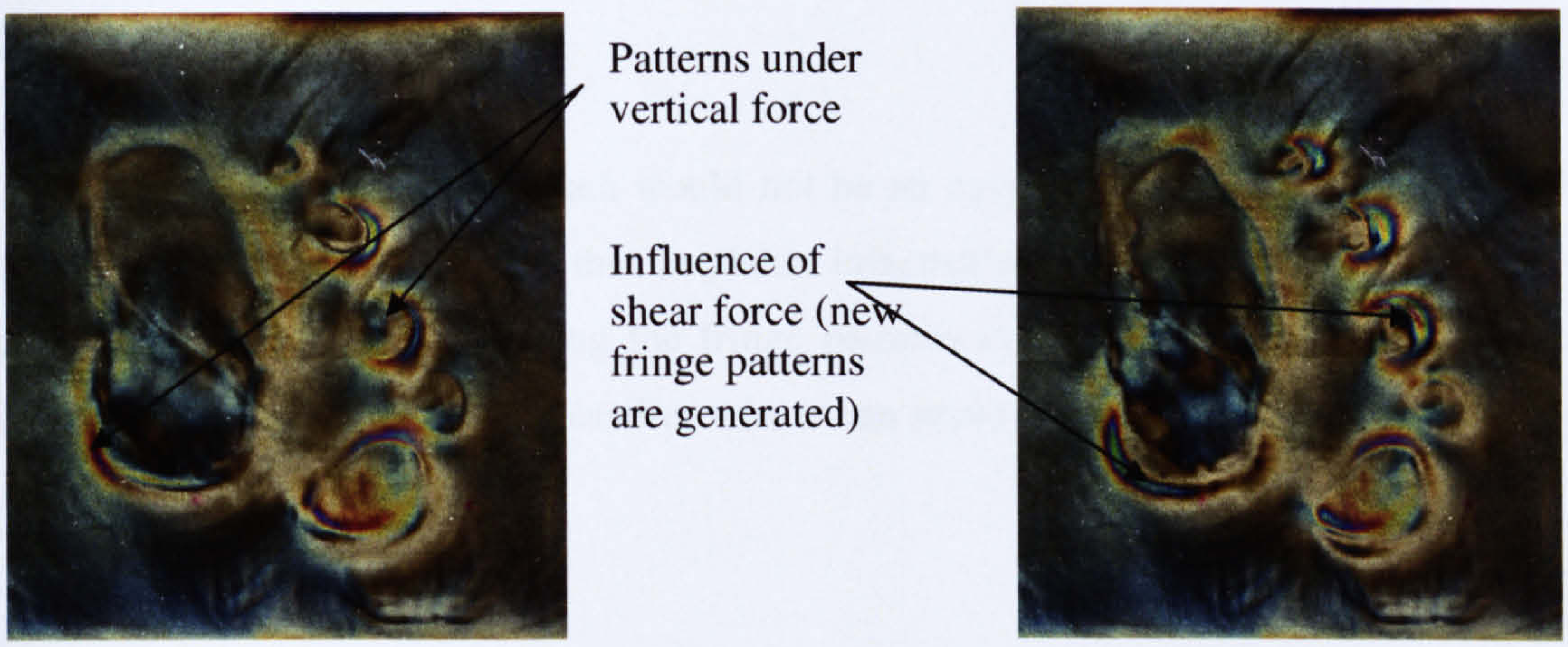

Figure 6-15: Fringe patterns obtained under (a) medium vertical load and (b) medium shear load introduced

Under high foot loading it can also be seen (Figures 6.16) that new fringe patterns emerge under vertical as well as shear load, seen under the first metatarsal head and laterally along the metatarsals. Point of load (vertical) can also be extracted if fringes are carefully examined (Inset Figure 6.16). The black coloured fringes in the inset representing the 'source point' (from where the fringes originate) is the point of vertical loading.

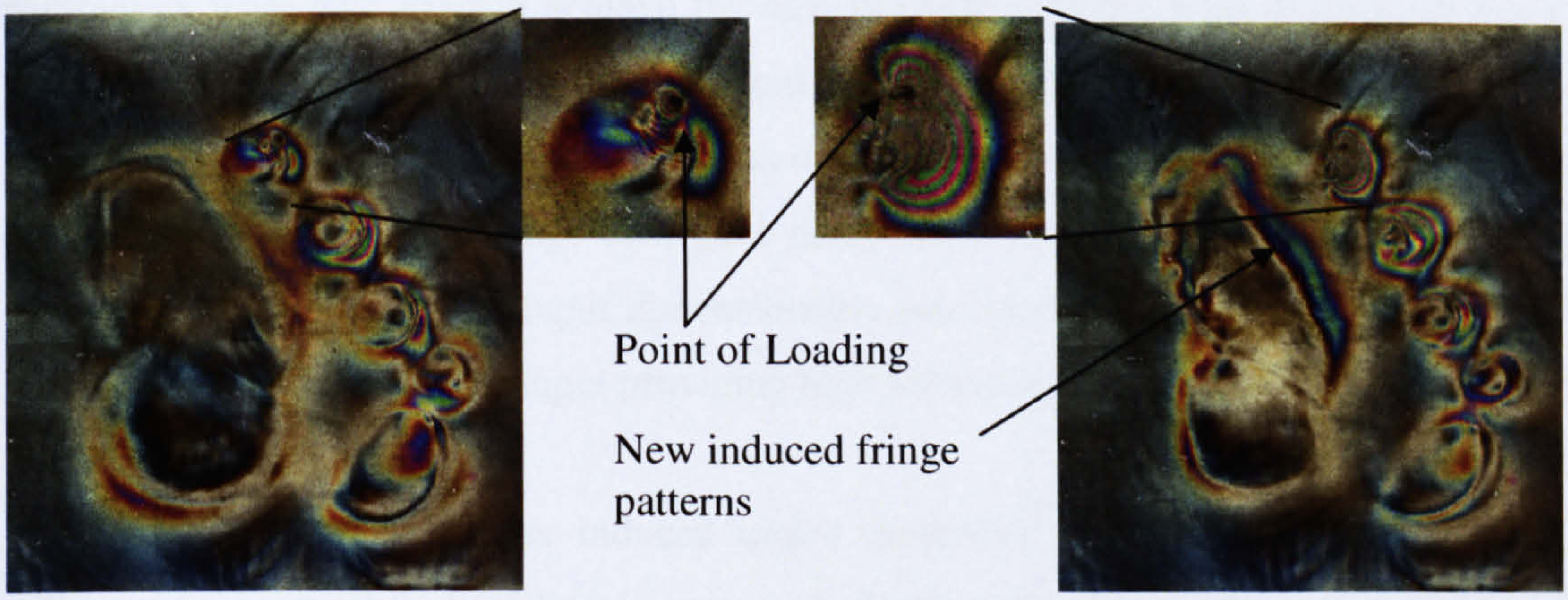

Figure 6-16: Fringe patterns obtained under (a) high vertical load and (b) high shear load introduced

Studying the fringe patterns above it is evident that the fringe patterns are influenced differently under different loading conditions (vertical, shear, low, high) and would be different for different subjects. Since fringe patterns induced are also influenced by the loading element, soft tissues would generate different patterns compared to tissue with callus, thus intelligent processing would differentiate the foot likely to develop ulcers compared to normal subjects.

The extraction of quantitative data would not be an easy task as the fringe patterns are complex and represent only the in-plane information due to the nature of the phenomenon. However, analysing the fringe patterns carefully and intelligently would lead to the development of a classifier which can serve as a predictor for diabetic foot ulceration.

6.12 Summary

This chapter focused on analysing the fringe patterns obtained under the vertical and shear loads in order to determine the load characteristics. Various strategies were adopted to refine the results by taking various image parameters for implementation. Since an image has enormous data in itself it cannot be used as a whole for training neural networks of moderate size. Thus a range of data were extracted from the images including statistical, geometric, intensity and fed as training data. A mix of input parameters were also tried to achieve the best possible network with desired accuracy. The network trained with combined data from statistical inputs, geometric parameters and previously determined vertical load gave accurate results. However, the network fed with intensity data from entire image also gave comparable results, due to the fact that the input was most relevant and input dimensionality was moderate. Thus the later network was chosen with the relevant input providing high tolerance.

Following the fringe patterns induced under controlled loading, a set of data was collected from actual foot loading to extract qualitative information. The changing fringe patterns under vertical and shear load gave qualitative data in terms of determining pressure points and regions of high stress. However, in order to get meaningful clinical results (in terms of ulceration) from foot images, system refinement would be required with sophisticated algorithms in conjunction with the medical history of the subjects forming a knowledge-based intelligent system.

Chapter 7 Conclusion and Future Directions

7.1 Review

The research presented in this thesis has been concerned with the use of digital photoelastic techniques for biomedical sensing applications. The research started with the need for a sensing device for pressure induced pathologies that could measure the actual conditions of loading; and thereby identifying the causation factors that could lead to the anomaly. The research has specific implications for early detection of diabetic foot ulceration by measurement of shear force under the sole of foot, however, the developed technique could equally be applied to other pressure induced anomalies as well as for tactile or haptic interface for man-machine interactions. The initial section of the thesis has presented the problems in foot pressure measurement, highlighting the need to sense the actual conditions of foot loading in standing or walking. A comprehensive survey has been conducted on various foot-pressure measuring devices with their relative merits and applicability for clinical assessments. This led to the conclusion that photoelasticity may be a suitable technique to meet such requirements. Following this, elements of photoelasticity have been reassessed for sensing applications. Conventional photoelastic techniques have been investigated in the sensing context i.e. under unconventional loading situations. Enhancements to the existing techniques have been presented with the recommendations to use intelligent techniques to extract loading information from photoelastic images. This further led to the implementation of neural networks for load analysis taking into account the relevant image parameters for quantitative image analyses. A prototype device was developed capable of extracting qualitative information from fringes. This was coupled with artificial intelligence to measure applied vertical and shear forces and provided quantitative load information from fringe patterns under controlled experimental conditions. The developed sensor could provide quantitative load information and prediction towards foot ulceration if integrated with a knowledge base system. Following this, future research directions are given to develop an integrated methodology for designing a classifier for predicting foot ulceration at an early stage.

7.2 Research Achievements

Pressure induced tissue anomaly is of crucial clinical importance in many pathological investigations, including pressure sore identification in neuropathic subjects with a high risk to foot ulceration. A number of devices have been developed to identify pressure points at foot-sole interface however, measurement of shear has always been a challenge due to the limitations of the existing technology and the measurement difficulties. Shear force is considered to have more damaging effect than the vertical force in ulceration due to the nature of force as it stretches and bunches the soft tissues. The first chapter discussed the problems associated with foot interface pressure measurement followed by comparing the existing foot-pressure measuring vertical and shear force devices and elucidates their merits and applicability for assessment of interface force measurement and role in diabetic foot ulceration. Most of the commercial sensors only measure pressure and only a few research based shear sensors are available which in fact, are displacement sensors that provide discrete measurement. The measurement of the actual condition of foot loading and visualisation of the whole-field is not possible with a single sensor and specifically it is difficult to isolate the role of each type of forces in causation and growth of ulceration. This set the research objectives to make use of digital photoelasticity for developing a biomedical sensing device. The unique properties of photoelastic materials to exhibit visual information under stress conditions can be exploited to develop such a potential sensing tool for foot load analysis.

Chapter 2 dealt with the basic physics of photoelasticity, components and material properties. The current photoelastic techniques were discussed with their relative merits and demerits followed by application of photoelasticity in medical and industrial fields. Chapter 3 was focussed on selection of appropriate material properties and optical components to design and build the sensing plate. To develop a sensing tool based on photoelastic phenomenon various elements of the technique were identified and tailored to locate the best suitable material, components and techniques. The type of loading involved in this research was unconventional compared to the traditional photoelastic applications, thus the relations determining the material properties, thickness and other parameters required were not directly useful. After testing with materials of different physical and optical properties, the suitable material to develop the sensing plate was identified. This further required selection of a light source and an image acquisition system as both were crucial for high quality fringes and both affect the portability of the sensor. The chapter also gave detailed description of various experimental setups used in this research. Since the fringe patterns induced under surface loading in reflection mode (as used for sensing applications) were of low quality (sharpness and colour) with high stress regions at the point of interests; this was due to the deformation of the material. Due to low modulus of elasticity of the material and out of plane loading the stress propagates less extensively which required high resolution image acquisition systems and sharp focus. A portable photoelastic experimentation system was built using a commercial flatbed scanner providing a combined system with light source and imaging facility inbuilt into it. Another imaging system was developed as a part of this research using partial mirror and separate light sources. This resulted in two different experimental setups using scanner and partial mirror and development of a photoelastic sensing plate, which is capable of generating load-imprint representing the actual condition of loading.

Chapters 4 discussed in detail conventional photoelastic techniques under unconventional loading situations for sensing applications. A number of contributions were made to enhance the existing techniques (Grewal et al. 2006). The conventional photoelastic stress analysis techniques were tested with fringe patterns obtained from the experimental loading and their limitations were identified both for conventional and unconventional loading conditions. A simple yet enhanced RGB calibration technique was developed capable of noise removal and demodulating higher fringe orders. However the conventional techniques, though successful in the traditional way for demodulating fringe patterns, were inadequate in evaluating the actual load that triggered the phenomenon. Since there did not exist any direct relation between the principal stress difference and load for the specific loading conditions, the problem demanded a way of mapping the load on to the fringe patterns.

Following the limitations of conventional techniques in load determination from photoelastic fringes patterns, a methodology based on artificial neural networks was developed. Inverse analysis techniques were simplified by using neural networks and necessary modifications and improvements were made to the existing techniques and contributions were made in the field of inverse analysis of photoelastic image data (Dubey et al. 2006; Grewal and Dubey 2007). Different types of input parameters (statistical, geometric, intensity and combinations of these) were tested for training the neural networks to optimise the performance in terms of accuracy of the system. Finally, a methodology was developed and used for vertical and shear force evaluation from the fringe patterns. A network trained with conditioned intensity data from the entire image gave the optimal results. In order to develop a system that can predict foot ulceration and diabetic condition of subjects, recommendations were provided to develop a classifier based on neural networks to be trained with medical data. The network could be fed with specific information about the subject in regard to diabetic duration, glucose level, age, height and weight. Such a trained network would prove to be a better classifier, however, it is envisaged that including more input parameters like gender, clinical history of the patients combined with photoelastic fringe patterns under a knowledge-based system (such as neuro-fuzzy) would lead to the development of a complete classifier for early prediction of diabetic foot ulceration.

7.3 Clinical Implementation

The system under consideration is capable of determining shear as well as vertical force under controlled loading environment. Results discussed in the preceding chapter provide basis for clinical implementation of the system. In its present form, the system only provides qualitative information under direct foot loading. It would require a significant computational effort to fully automate the data collection, processing and clinical presentation. A typical clinical testing procedure will require reasonable expertise of the physician to identify high stress regions, represented in the form of specific colours in photoelastic fringes. High visual acuity offered by the system provides the benefit of a visual stimulus to the patient and therefore, can potentially be used for educating the patient. Following the clinical test, the physician can recommend appropriate orthotic interventions. It must be emphasised that this technique provides supplementary evidence of high risk foot and can be used as an adjunct to routine diagnostic techniques.

From the clinical standpoint, the need for a more comprehensive system capable of intelligently predicting the risk category based on photoelastic fringes cannot be discounted. The scanner based system used in the current research should be modified to develop a platform based device with inbuilt capability to apply shear load. The preceding system is a simple, easy to use and a low cost device that can be used in smaller GP clinics, whereas the proposed system is appropriate for specialist diabetic foot centres for detailed investigation and research purposes. An appropriate measurement protocol that addresses the clinical issues such as tissue compliance, areas of loading and safety should be formulated with advice from podiatrist and diabetologist. Typically, the patient's foot will be placed on the measurement platform and shear load applied from an external slider mechanism resulting in baseline and shear data. The baseline data represents photoelastic patterns resulting only from vertical loading and shear data represents the effect of externally applied shear force on the plantar surface.

7.3.1 Clinical Assessment Procedure

The proposed system consists of a measurement platform where each subject applies foot pressure. This results in load application on the sensor plate and production of coloured fringes. Ideally, the sensing plate should be loaded with same vertical and shear loads for each subject. However, the vertical load varies in the subject population and hence, there is a requirement of vertical load compensation mechanism. The shear load can be induced through an independent slider mechanism for the sensing plate underneath the foot. Each subject applies load in seated position, with feet parallel to the ground. It is intended to assess the coloured fringes at a consistent value of vertical load during each investigation. Data is acquired through the flatbed scanner arrangement.

Shear load is induced by sliding the sensing plate underneath the plantar surface to a known length, consistent for each subject. Two independent images are collected representing the coloured fringes for vertical and shear load respectively. The acquired patterns under the vertical load act as reference and shear patterns act as change that has occurred from shear loading. There is a need for reference image (under vertical load) as for every subject the fringe patterns would be different even though the vertical load and shear load are same due to physical anatomy of the individual foot and varying tissue properties of each subject. Thus, keeping a reference image acts as a starting point to compare the latter acquired shear image.

Artificial neural network can be trained with the two acquired photoelastic images along with a clinical history of the subject. Considering, the training data is acquired both from a neuropathic patient group and a control group, it is possible to determine the risk category of the subjects once the network is trained to optimum specifications. Training the network with sufficient data from a wide number of subjects provides a knowledge base relevant to a decision support system for use in GP clinics and specialist diabetic foot centres. During the test, the system requires two photoelastic images (each representing the affect of vertical load and shear load) and clinical history of the subject to determine the risk category of the patient. The system is not expected to replace the existing assessment techniques.

7.4 Limitations and Future Research Directions

Current research investigates the use of digital photoelasticity in biomedical sensing applications like foot ulceration. A simple scanner based system provides information of applied load and qualitative data represented as stress patterns. However, the following limitations were encountered and the future research directions are provided:

1. The available photoelastic materials have limited physical and optical properties which limit the range of vertical and shear forces/stress that can be applied and measured. There is a need to investigate different photoelastic materials to achieve the best results.

2. Although the scanner based system is portable, it may not be appropriate for dynamic loading. A platform based system with small light sources such as LEDs and high speed cameras may be considered to make a real time system.

3. The system can only be used as an external barefoot device due to limitations involved in image acquisition and the fact that measurements are done on a relatively rigid surface.

4. Using artificial neural networks to analyse fringe patterns proved to be a successful approach and provided the desired output. However, the amount of training data was limited due to the time constraints. Using large training data is expected to improve the results.

5. The developed methodology of determining vertical and shear stresses under controlled environment cannot be directly applied to the foot image as the fringe patterns generated are very different in the two cases. However, training directly with the foot images would be a better option to proceed in that direction.

6. Since the network training required actual image data, in real application involving diabetic subjects this may not be a practical proposition, hence the system would require enhancement in terms of data mining and forecasting system that can assess conditions of the foot by analysing only a limited number of images.

The neural network based methodology developed for inverse analysis has shown encouraging results, however, at this point it is limited to loading in a controlled environment. Future recommendations include training patterns obtained from directly under the foot and determination of peak points of vertical and shear loads. Determination of peak shear stress points and actual fringe patterns from foot loading would provide ideal training data for the artificial intelligence shell for developing an early detection system for foot ulceration.

The system developed during this research can be used as a clinical device for qualitative analysis of foot prints, however, in order to develop a complete system capable of predicting foot ulceration at an early stage it will be important to consider fringe patterns from foot loading and medical history of subjects together. The collected information can then be conditioned to extract the most relevant data. The artificial intelligence technique of analysing the photoelastic data to understand the behaviour of fringe patterns under different loading conditions (through different tissue properties in different subjects) coupled with medical history of the subject should be capable of predicting the risk factor of the foot. The research presented in this thesis has shown that the technique has a strong potential for developing a clinical diagnostic tool for early detection of diabetic foot ulceration and thus reducing the chances of amputation, improving the quality of life and providing cost savings to the health services.

Appendix-I

1. Diabetes Mellitus

The body's inability to produce or utilize insulin, leading of excess of glucose is referred as diabetes mellitus. Insulin is a hormone secreted by pancreas that enables blood sugar to be absorbed by the body cells. High glucose levels in the body can have a detrimental effect on the nerves and the blood vessels causing long term complications related to heart, kidneys, vision, sensory loss, limb ulceration. About 230 million people worldwide are known to suffer from diabetes mellitus, adding 7 million every year and about 3 millions deaths per year (International Diabetes Federation 2003a). Recent figures from the World Health Organisation indicate that the prevalence of diabetes mellitus is approaching two million in the UK and is continuing to rise (World Health Organisation 2007). A significant proportion of this population will be at risk of developing diabetic foot complications with high surgical and treatment costs associated. Serious complications of diabetes mellitus include neuropathy (motor, sensory, autonomic) and ischaemia (peripheral vascular disease), which can lead to foot ulceration and infection and in extreme cases, amputation. Diabetic foot ulceration is a severe complication in diabetes mellitus, caused by excessive pressure loading at the plantar interface in neuropathic subjects. To improve diagnosis and treatment the Royal College of General Practitioner's Guidelines (April 2002) for the Prevention and Management of Foot Problems, recommend that diabetic clinics adopt a routine screening for indicators of ulceration. The importance of this has been further emphasised in the Department of Health, National Service Framework for Diabetes: Standards (2003). Extensive work has been done for the treatment, detection and prevention of foot ulceration. A wide range of therapies have been developed for curing foot ulcers by medical treatments and mechanically unloading of the areas with excessive pressure. Over the years a number of devices to sense, measure and monitor the vertical pressure have been developed, however, the role of shear force could not be studied due to limitations of the existing technology.

Types of Diabetes

There are two main types of diabetes mellitus:

1. Type-1: occurs due to the inability of pancreas to produce insulin required for glucose absorption causing an increase in glucose level. About 5-6% of the diabetic patients suffer from type-1. Subjects need regular injections of insulin for controlling the glucose level. This kind of diabetes is also referred to as insulin dependent. Type-1 can be found in any age group but usually is prevalent in young adults and children (International Diabetes Federation 2003b). The beta cells of pancreas cease and there is no phase-I response which usually leads to immediate release of insulin on any intake of carbohydrates or proteins. These malfunctions lead to high swings of sugar level in body starving the body cells due to non-absorption of glucose (Bernstein 2003).

2. Type-2: occurs due to the body's inability to respond to the insulin produced and is referred to as insulin independent type i.e. incapability of cells to absorb glucose. About 90% of diabetic patients suffer from type-2 and is commonly found in adult subjects (World Health Organisation 2004). Obesity has been linked to type-2 diabetes as 90% of the patients are found to be over-weight and tend to produce higher levels of insulin. The fat building property of insulin further increases obesity (Bernstein 2003). Regular exercise, medication and diet control are found to be effective in its control. About 1.7 billion people are reported to be at the verge of weight related diseases like diabetes (International Diabetes Federation 2003c). Type-2 is usually detected by one of its complications like vision impairment or diabetic foot infections.

Symptoms of Type-1 are generally marked by excessive urine secretion, thirst, blurred vision, sudden weight loss, while for Type-2 diabetes such symptoms might be less marked (World Health Organisation 2004). Thus in Type-2 later detection of the disease might end up with a prior existence of complications. The exact foot pathologies in foot ulcerations are unknown but some of the main known factors are neuropathy, ischaemia, foot deformities, callus, high plantar pressures and repeated plantar loading. Neuropathy along with poor blood circulations plays a major role in infections and ulcerations, however, how blood circulation is affected due to the plantar loading needs to be investigated to understand the precise role of plantar forces.

2. Neuropathy

Neuropathy is considered as a major risk factor leading to foot ulceration. It can lead to sensory loss, foot deformities, infection by damage to precipitation nerves causing dry cracked skin prone to infection (Bernstein 2003). Blood circulation is impaired by long term elevated sugar levels damaging not only the major arteries of leg but small arteries and capillaries too. This deteriorates the blood supply to damaged skin causing further damage and thus sensory loss to pain and heat (Bernstein 2003). Sensory loss can further leads to undiagnosed increasing pressures under the plantar foot. Increased pressure with repeated loading ultimately leads to tissue damage and foot ulceration.

Neuropathy is found to affect nerves throughout the body, from toes, feet, legs to all the way up kidney, heart and eyes. Peripheral neuropathy (sensory) causes damage of feet nerves much before arms and hands causing numbness, loss of sensitivity and reflexes, muscle weakness etc (National Diabetes Information Clearinghouse 2002).

3. Sensory Neuropathy

Sensory neuropathy is often referred as peripheral neuropathy, resulting from the damage to peripheral nerves. This type of neuropathy can be painful or painless, however painless type is found to be associated with ulceration (Boulton et al. 1994). Absence of sensory response of the body to external forces on the skin surface leads to undetected high loadings. This leads to other diabetic complications like ulcerations, Charcot foot (foot joint disease) etc. It has been reported that plantar pressures otherwise regarded lower than threshold may severely the affect foot, due to repetitive loading in absence of sensory response.

4. Autonomic Neuropathy

Autonomic nervous system controls the involuntary functions of the body like heart rate, blood pressure, perspiration, digestion, vision etc. Autonomic neuropathy affects the autonomic nerves. It has been well established that peripheral sympathetic dysfunction is present in diabetic foot ulcers (Boulton et al. 1994) that causes reduced sweating and thus dry skin (cracks) and is associated with high blood flow owing to arteriovenous shunting. This might hinder body's response to hypoglycemia (low sugar level). Cracks and fissures developed serve as portals for bacteria causing foot infections. It may impede cardiovascular system, sometimes leading to fall in blood pressure due to insufficient blood supply in certain body parts. Researchers have proved loss of usual systematic tone leading to shunting and bypassing of capillary bed (Laing and Clwyd 1998). Autonomic neuropathy may also hinder response to hypoglycemia.

5. Motor Neuropathy

This involves weakness of foot muscles leading to imbalance of tendons, which further leads to high arched foot. Motor neuropathic subjects also tend to develop clawed foot which draws the fat pads underneath metatarsal heads impairing the cushioning effect. This leads to increased plantar pressures making tissues thicker and less flexible, contributing to limited joint mobility (Laing and Clwyd 1998). In another study authors found degree of joint immobility increases more with presence of neuropathy than the duration of diabetes (Viswanathan et al. 2003). Neuropathic ulcerated groups are found to have less joint mobility than neuropathic subjects, which in turn hampers the shock absorption (Muller et al. 1989). High shearing is reported with loss of joint moment by many researchers (Laing and Clwyd 1998).

Higher skin temperatures have also been associated with autonomic and sensory neuropathic group when compared to controls as increased blood flow due to arteriovenous shunts dissipates the heat as a result of higher metabolic rate. Relation of skin temperature and blood has been reported to be non-linear in nature. Archer reported temperature of 33.5^0C with patients of sensory neuropathy against 27.8^0C of subjects without neuropathy (Boyko et al. 2001). Contrary to the above findings Boyko et al (2001) found lower skin temperatures at all the sites for sensory neuropathic subjects as compared to without. Similar temperatures were found for both with and without autonomic neuropathy.

6. Ischaemia

Ischaemia is a vascular disease prevalent in diabetic group and is found to develop at a younger age. Peripheral ischaemia tends to alter elastic and compressive properties of soft tissues which in turn deteriorate the shock absorption properties (Pitei et al. 1999). Tissue thickness reduction makes the feet prone to damage by shear forces. Absence of callus is found in neuroischaemic group due to an increased blood flow, in contrast to neuropathic subjects. Although ischaemia is one of the major risk factors to foot ulceration, it alone cannot cause ulceration.

7. Neuropathy in Lower Extremity

The most common complication of Type-2 diabetes mellitus is neuropathy. It is a peripheral nerve disease related to malfunctioning of nerves. Complications leading from neuropathy together with excessive plantar loading increase the risk to ulceration. Studies have shown that the changes in tissue thickness and properties serve as a predictor for elevated plantar pressure (Boulton et al. 1994). Stiff tissues are found in regions of previous ulceration. A potential reason could be change of properties in soft tissue like elasticity and shock absorption due to peripheral ischaemia i.e lack of blood supply (Pitei et al. 1999). Poor glycaemic control is linked to neuropathy in an indirect way of damaging nerves (American Diabetes Association 2004).

8. Foot Ulceration

Research has shown that metabolic disorders due to diabetes affect 2-5% of Europe population (Merza and Tesfaye 2003) Foot ulceration is a major and potentially disabling complication, prevalent in more than 5-10% of diabetic patients. Understanding the pathophysiology of diabetic foot is significant in order to predict ulceration. Ulcer being traditionally considered as a result of vascular disease, peripheral neuropathy and infection is now also linked to factors like poor glycaemia and repeated stresses on the insensitive zones. Neuropathic foot ulcers found on the plantar areas were reported with pressure values of (428.8±68.6) kPa in a group of 14 neuroischaemic and 18 neuropathic subjects (Pitei et al. 1999). Maximum pressure values associated with neuroischaemic patients was found to be (757.6±135.9) kPa. The main factors considered to be associated with the foot ulceration are:

- Peripheral neuropathy
- Peripheral vascular disease
- Neuromuscular dysfunction
- High plantar pressures
- Biomechanical factors

Peripheral neuropathy (PNP) is found in nearly 40% of diabetic patients (Merza and Tesfaye 2003) and is regarded as the strongest initiator for foot ulceration. It impairs foot sensitivity to react to high pressure, unlike in Normals where an individual tends to changes the position to relieve pain. Sensory neuropathy affecting more than one-third of elderly diabetic patients is found to cause reduction or complete loss of sensation to high pressures.

Peripheral vascular disease (PVD) alone is not considered to be harmful but when combined with PNP leads to ulceration and slow healing. Reduced transcutaneous oxygen tension has also been postulated as risk factor for ulceration (Merza and Tesfaye 2003).

Neuromuscular dysfunction has also been considered as one of the major risk factors in foot ulceration. It leads to malfunctioning of arterial walls with inadequate smooth muscular action. This prevents arterial wall's regular response of dilation and vasoconstriction to stimuli (Stein et al. 2001). Endothelial dysfunction leading to impaired vasodilation caused by diabetes mellitus is another factor leading to neuropathy (Caselli et al. 2003).

High plantar pressures are also associated with foot ulcerations as the level of pressure significant depends on the type of patient. For patients with history of ulceration, even pressure considered to be low can be significantly harmful. High planter pressures have been recorded in all neuropathic patients with history of ulcerations. Presence of callus also increases the plantar pressures on foot and aggravates ulceration as it restricts the pressure distribution and damages deeper soft tissues; removal of which have shown significant fall in pressures (Boulton et al. 1994) . Formation of callus has also been reported as a precursor to foot ulceration (Stein et al. 2001).

Other biomechanical factors like foot deformities cause limited joint motion and result in callus formation and thus leading to high pressures. Age, sex, smoking habits, race have also been associated with foot ulceration. In evaluation of determinant variables for peak pressures, Payne et al (2001) linked peak pressure for hallux with neuropathy and limited motion of the first metatarsophalangeal joint.

9. Diabetic Foot Medical Treatment

Basic diabetic foot treatment involves methods for quick healing and tissue formation. Adequate oxygen tension has been reported to be beneficial in wound control and healing (Kalani et al. 2002). A number of techniques have been developed and implemented for diabetic foot treatment. Surgical and medical treatment methods aim at increasing tissue thickness, increasing the oxygen tension, accelerating wound healing process, surgical debridements, callus removal etc. Hyperbaric oxygen (HBO) techniques accelerates healing by increasing the amount of dissolved oxygen in plasma and aids in formation of new capillaries (Stein et al. 2001; Kalani et al. 2002). Hyaluronan therapy (Vazquez et al. 2003) is a dressing technique that increases the granulation of tissues. Injecting methods include silicone and methyl nicotinate (Schie et al. 2002; Caselli et al. 2003). Surgical percutaneous includes lengthening of Achilles' tendon to reduce the risk to ulceration by altering peak pressures on weight bearing zones (Stein et al. 2001).

The main disadvantages reported for the above treatment methods include requirement of skilled personnel and high installation for HBO method and need for booster injections to improve the subcutaneous tissue cushioning for silicone injection treatment.

Pressure Redistribution under Foot

Pressure redistribution at the plantar surface of diabetic foot alleviates the forces at peak pressure points. Pressure redistribution is achieved by using specially designed shoes and soles. Higher plantar pressures in diabetic patients than normal are found in barefoot when compared to shoes. Factors leading to high pressures are associated with body weight, soft tissue thickness, joint mobility, sensory neuropathy and foot deformities. Fast walking speed has also been linked to increased plantar forces as this involves tissue shearing. Research suggest that the knowledge of above mentioned variables which lead to high pressures can aid in better direction of interventions against significant mechanisms (Payne et al. 2001). Intervention of certain gel and foam like materials also helps to reduce the peak pressures during the gait. Even sock interventions are known to reduce and redistribute the foot pressure to a great extent (Tappin and Robertson 1991;

Hosein et al. 1992). A recent research on modelling of foot socks and insoles combined with different frictional properties has revealed that the shear reduces to a greater extent if low coefficient of friction can be maintained between the foot and the sock and a high coefficient between the sock and the insole (Dai et al. 2006).

Foot loading as discussed above is actually a combination of forces, mainly vertical and shear. The vertical force is the normal force acting on the plantar foot and shear on the other hand acts tangential to the surface. Shear force in conjunction with the vertical force has been found to be detrimental to soft tissues and exacerbates pressure loading.

Appendix-II

10. Casting Setup for Photoelastic Materials

The low modulus photoelastic materials required for specific experiments were required to be casted manually. The setup is Figure 1 was used for casting PS-6 material with different thickness.

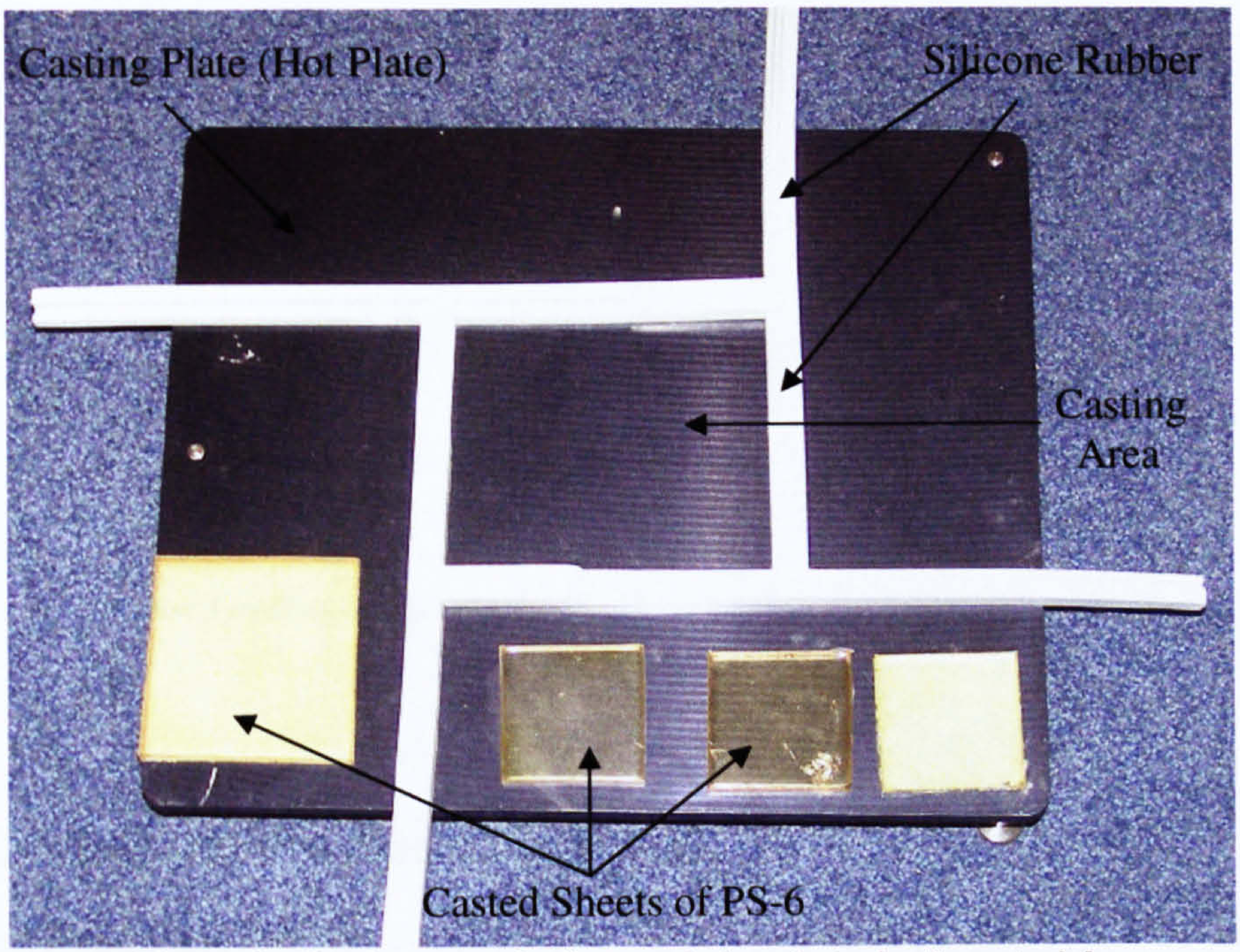

Figure 1: Casting setup for low modulus photoelastic materials

The material (PS-6) had low modulus which was one of the requirements in this research but the sensitivity was too low and required considerably high load to induce fringe patterns. Some of the basic experiments conducted with the castings prepared led to the conclusions of unsuitability of PS-6 for this research.

However, PS-4 was found to be appropriate for the experiments as it had low modulus (0.004 GPa) and high optical sensitivity (0.009). PS-4 was available in form of sheets so no further casting was required, but coating of reflective paint was done manually.

11. Dimensional Sketch of Disc Loading Mechanism

The basic disc loading mechanism was fabricated using MDF (Medium Density Fibreboard) and load bearing platform (the push rod) was made from Aluminium. Figure 2 shows the dimensions sketch of the loading mechanism.

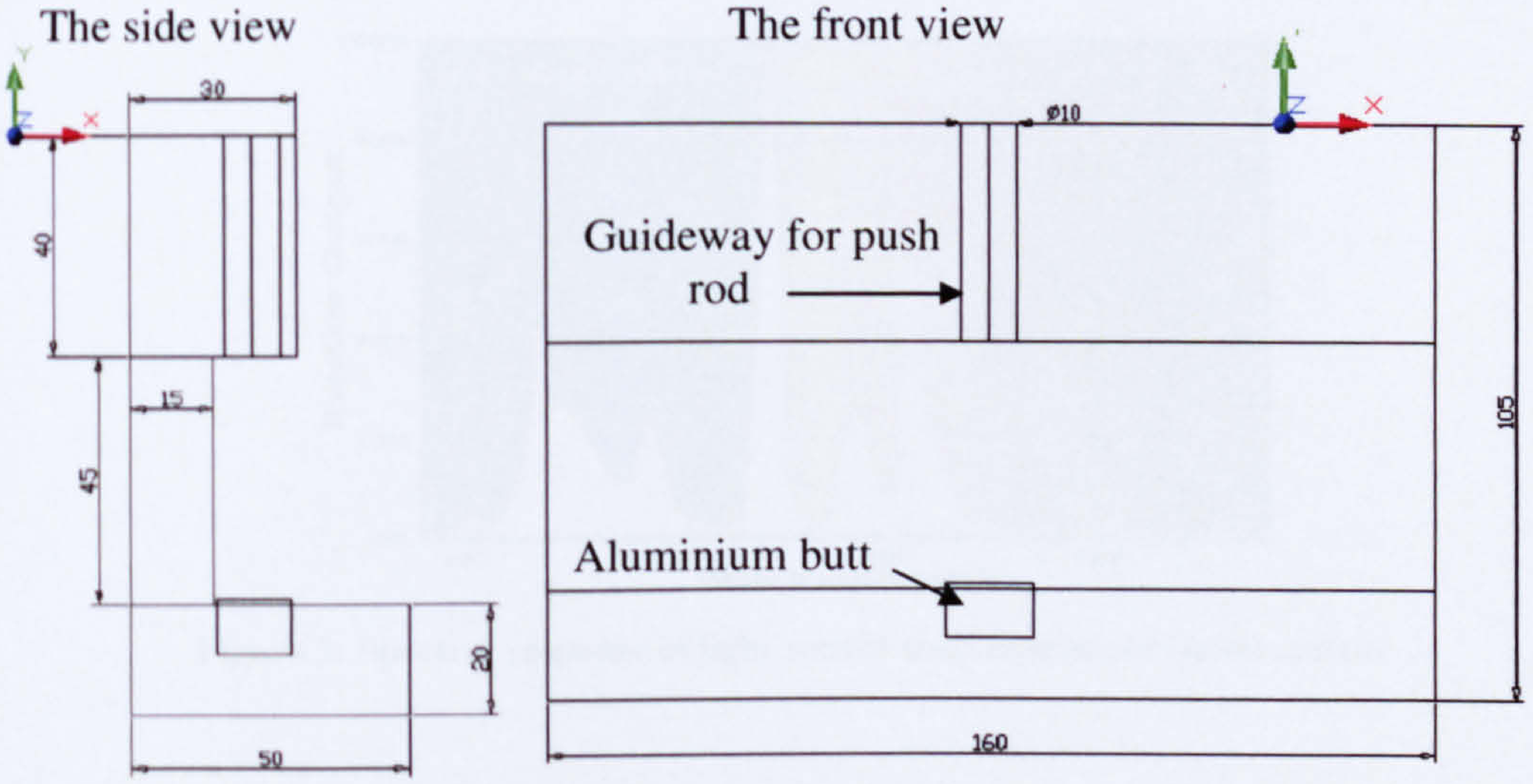

Figure 2: The Disc Loading setup (a) the side view, (b) the front view with dimensions in mm

12. Digital Camera Specifications

Olympus SP-500 UZ

Resolution: 6 Mega pixels

CCD: 1/2.5 inch colour

Image Format: Jpeg, raw

Focal Length: 6.3 mm – 63 mm

13. Spectral Response of CCFL

The Scanner was equipped with a cold cathode fluorescent tube providing a high spectral response compared to a conventional white light source. Figure 3 shows the spectral response of a typical CCFL used as scanner light source.

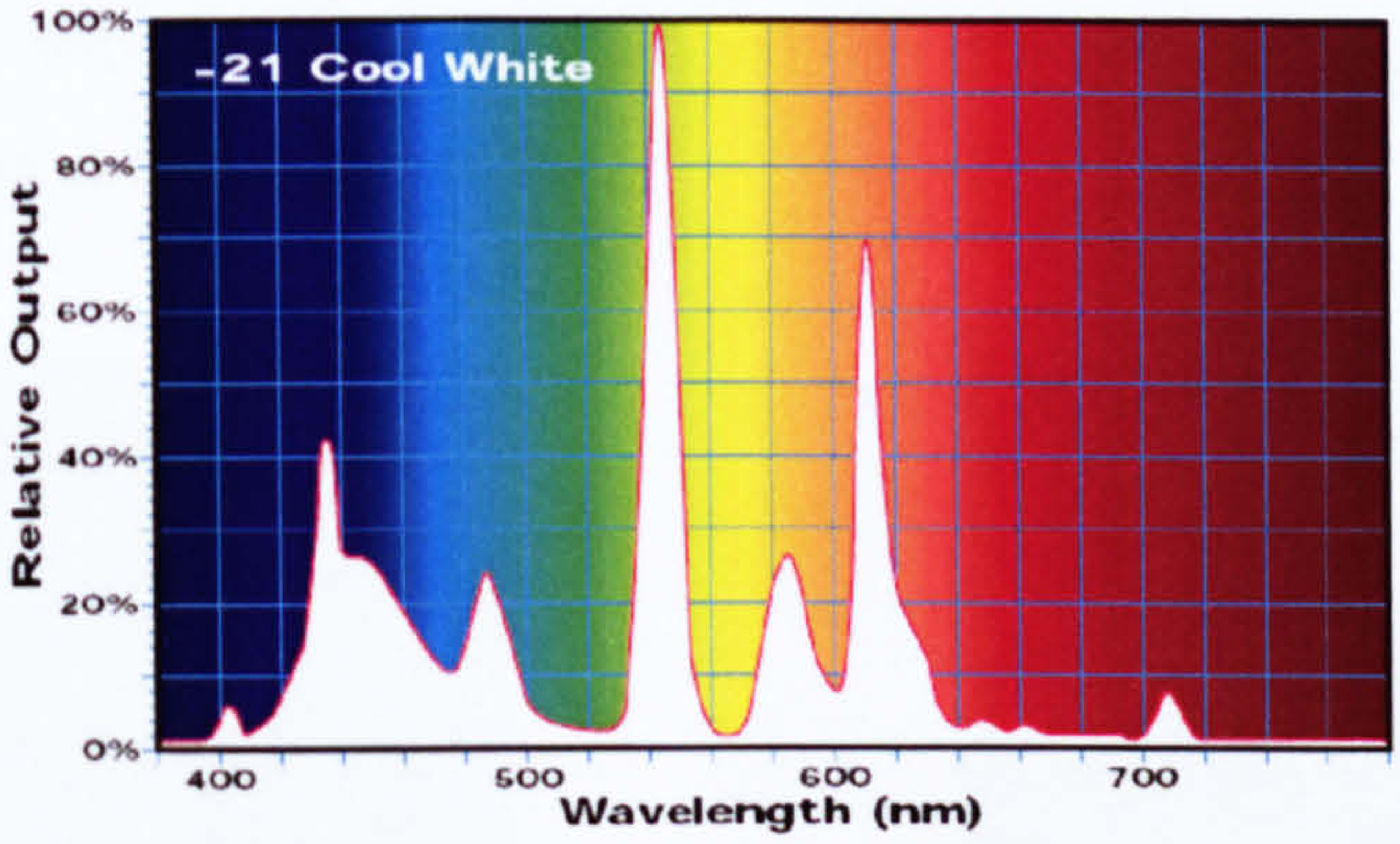

Figure 3: Spectral response of light source used in scanner based system

Appendix-III

14. Factors Influencing Fringe Response

The behaviour of fringe patterns is influenced not only by the amount of loading but also by the profile and geometry of the loading intender. Figure 4 show the profiles of two different intenders with diameter 13 mm and 16 mm and the corresponding fringe patterns obtained are shown in Figure 5.

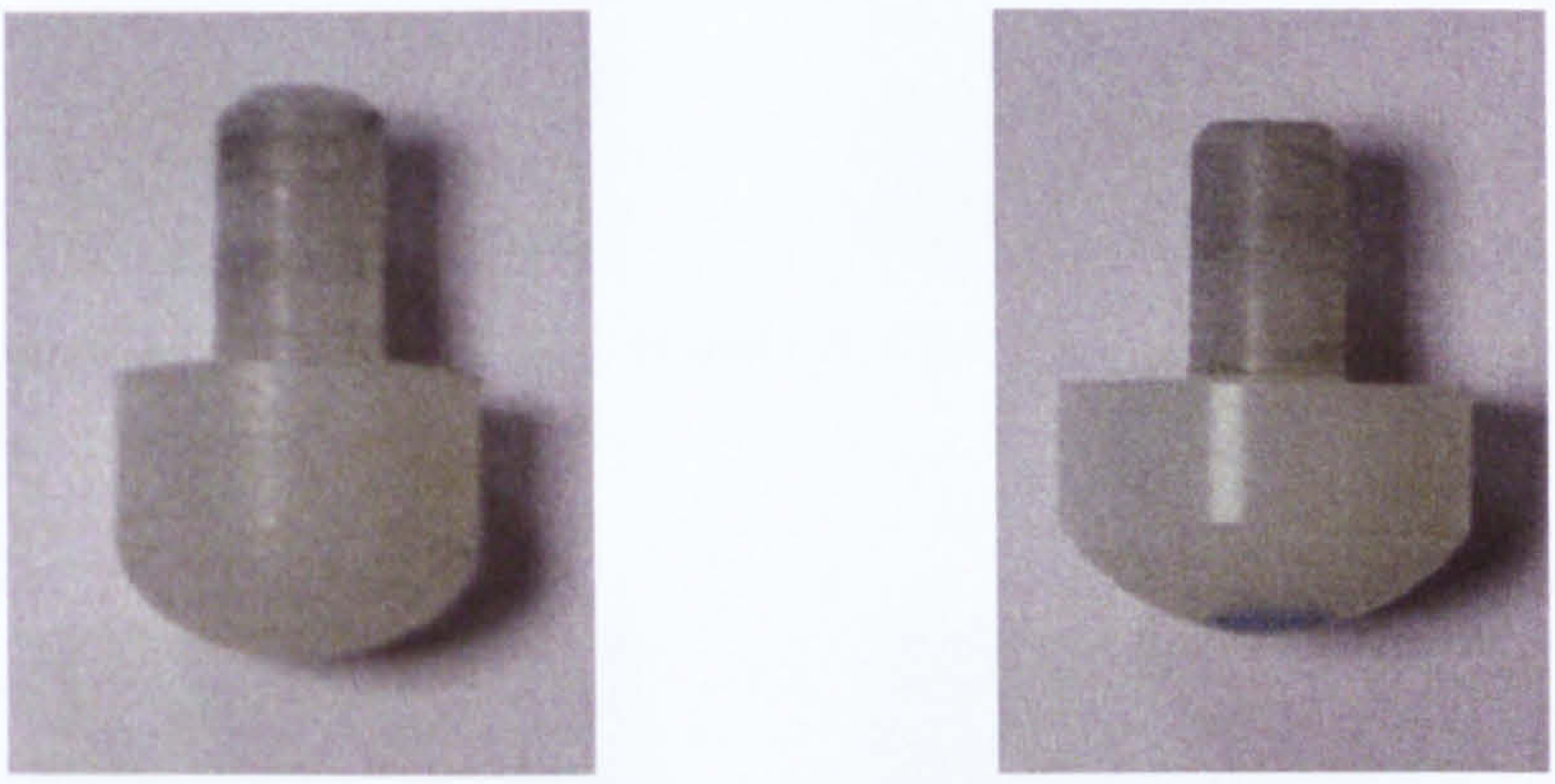

Figure 4: Indenter profiles of two hemispherical polycarbonate heads with diameter 13 mm and 16 mm

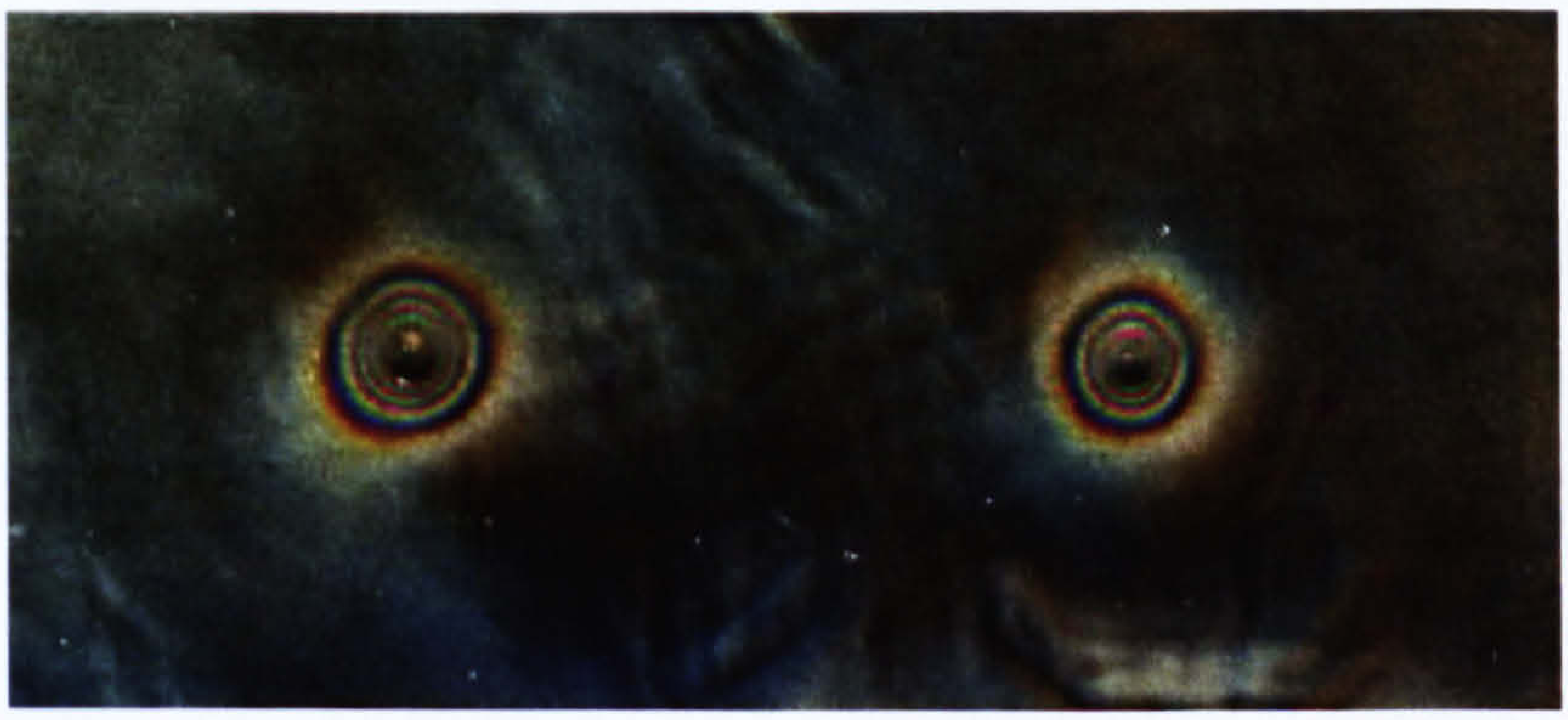

Figure 5: The photoelastic fringe patterns obtained from two indenter heads with different diameters, acquired using scanner based system

The difference in fringe patterns is discernable to a high degree, the fringe patterns pan out to a greater extent when loaded with a narrow profiled intender as the area of contact is less and thus stress is more.

Figure 6 and 7 show similar comparison for a steel head (5 mm) with a polycarbonate head (10 mm). The steel head has a flat bottom compared to hemispherical head of polycarbonate.

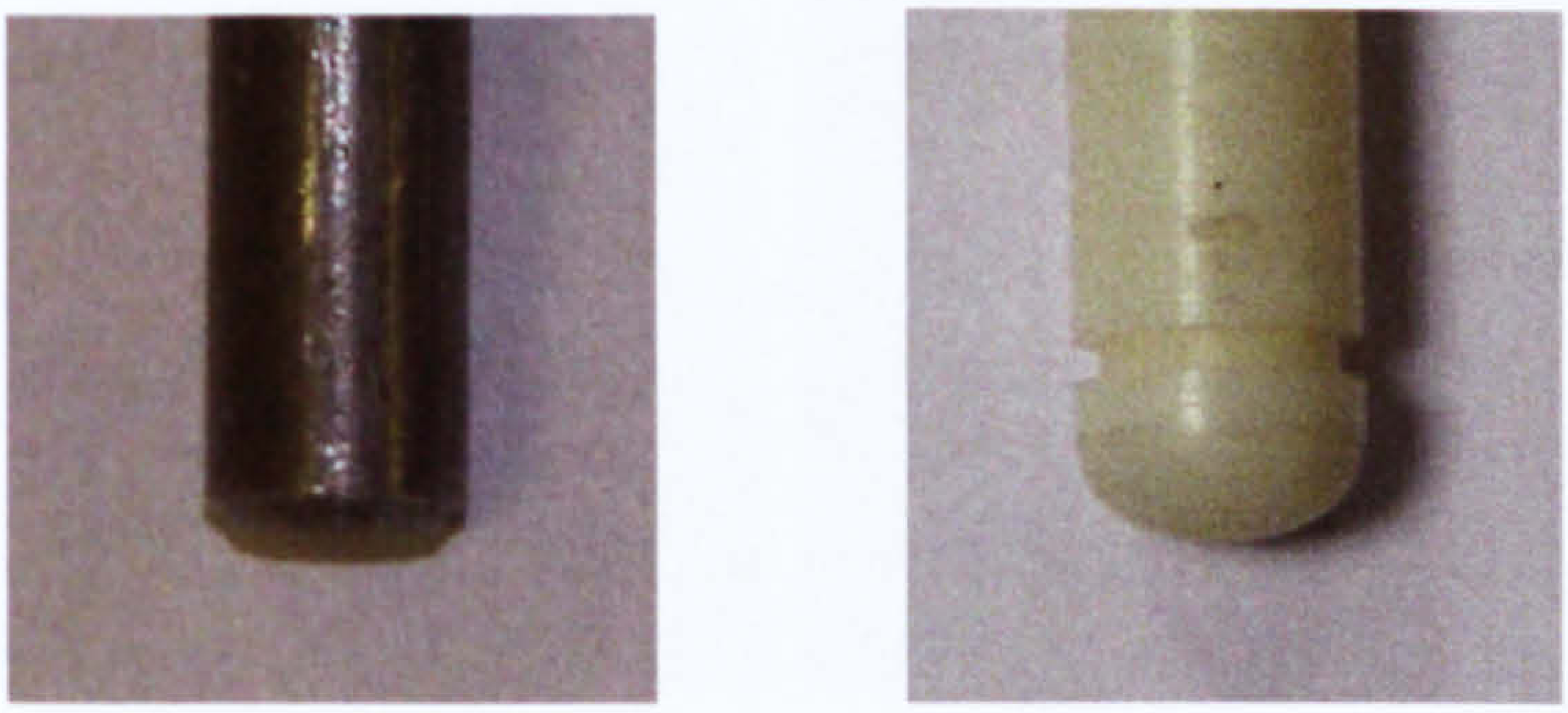

Figure 6: A comparison of a flat head steel intender and hemispherical head polycarbonate indenter

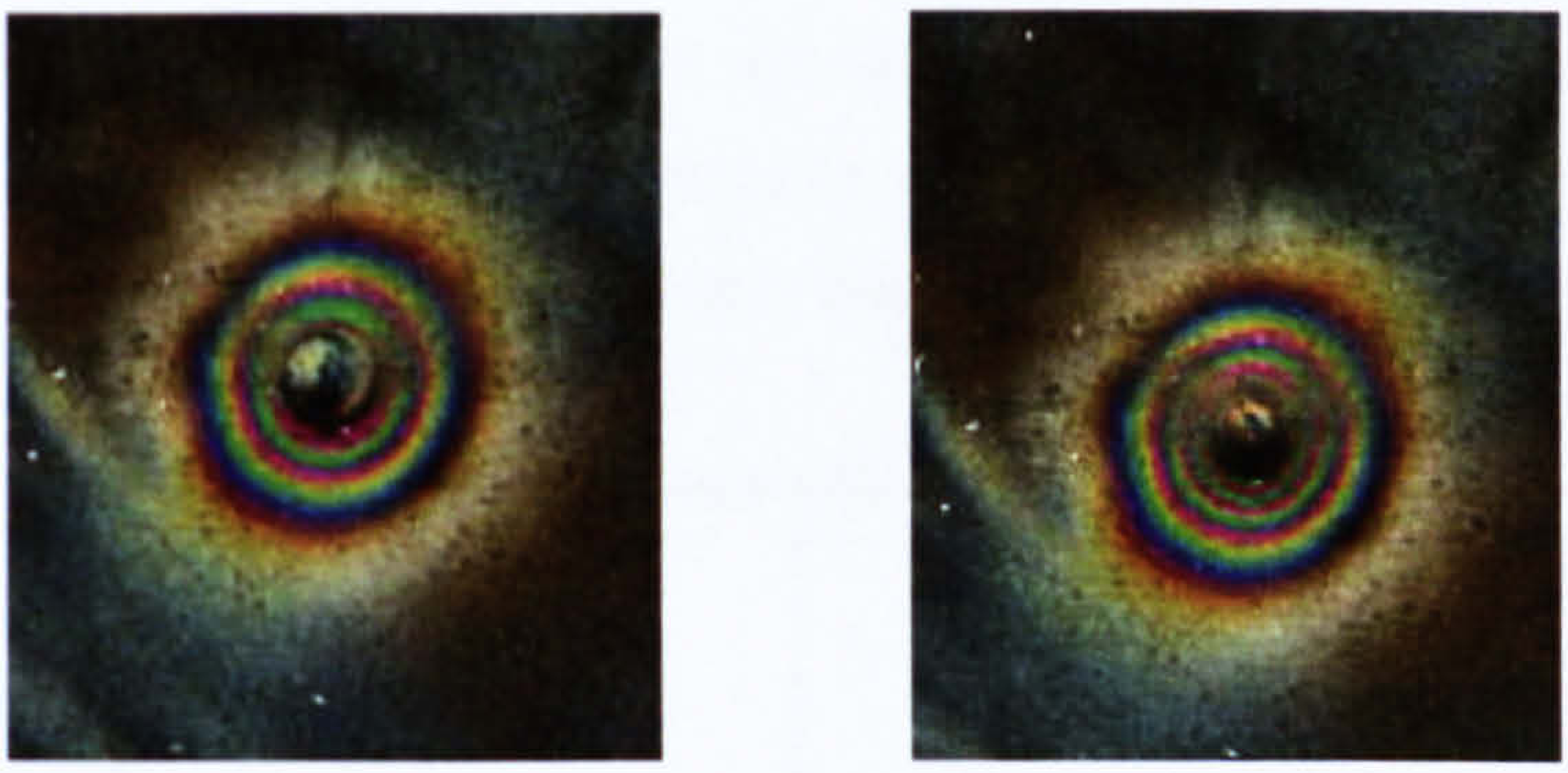

Figure 7: Photoelastic fringe patterns obtained under steel and polycarbonate indenter heads

The fringes are bunched together near the point of loading using hemispherical head as the area of contact is less than using flat head.

15. Diameter Estimation of Fringe Patterns

Since the fringe diameter changes under the influence of vertical as well as shear force, it is necessary to have some sort of measure of diameter or the area of the fringes induced. An algorithm was written in MatLAB® to measure the vertical diameter, horizontal diameter and the area of interest. The basic procedure involves converting images in HSV colour space and analysing H-plane images by image processing. Figure 8 shows a fringe image with corresponding H-plane projection.

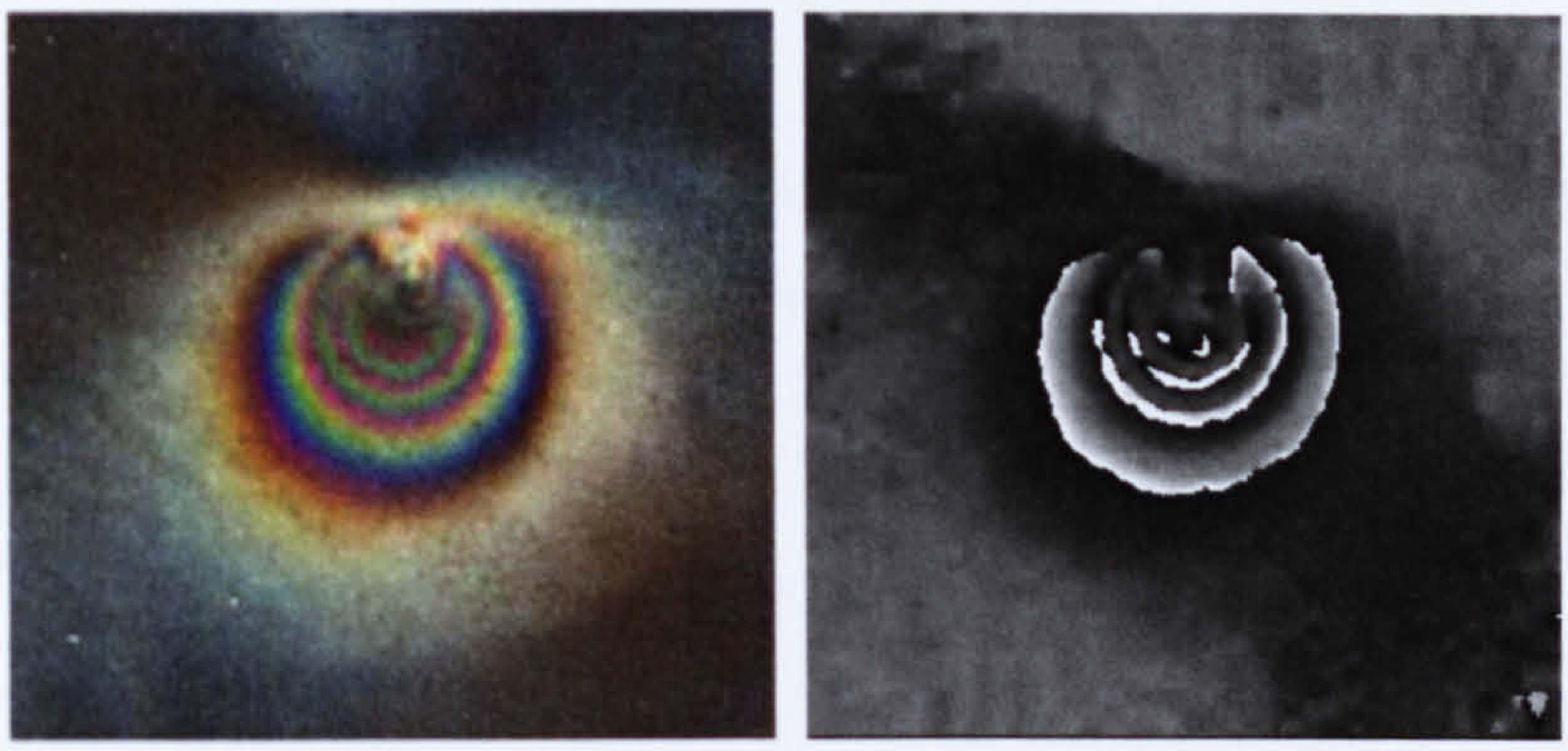

Figure 8: An RGB photoelastic image from indenter loading and the corresponding H-plane used to determine fringe diameter

The H-plane image was segmented using optimal threshold to segment a particular colour range of data from the image; a further algorithm developed in MatLAB® was used to determine the defined parameters of diameter and area. Figure 9 shows the segmented image with measured horizontal and vertical distances.

Figure 9: Segmented images with measured vertical and horizontal span

16. Definition of Statistical Parameters

In order to determine the applied forces from the fringe patterns it was necessary to measure some the parameters that showed variation on application of load. A list of such measured parameters and their definition is given below:

Mean: The mean of an image is often referred to as the mean pixel intensity of image, i.e. the average intensity of image represented by a single value. The mathematical relation for 2-dimensional mean is:

$$M = \frac{\sum_{i=1\,j=1}^{nm} I(i,j)}{nm}$$

Where, *M* is the mean pixel intensity, *n* and *m* are the number of rows and columns in the image (size of image), *I* is intensity at point *(i,j)*

Standard Deviation: The standard deviation of data is the general spread of the data, the mathematical relation is given by:

$$S = \sqrt{\frac{1}{nm \sum_{i=1,j=1}^{nm} (I(i,j) - M)}}$$

Where, *S* is standard deviation, *M* is the mean pixel intensity, *nm* is the size of image, *I* is intensity at point *(i,j)*

Median: The simple definition of median is the midpoint of the data and mathematical relation for median is step by step calculations as:

1. Count the number of data elements
2. Arrange them in ascending order
3. Find the data value at the mid point

Kurtosis: The kurtosis is the measure of how outlier-prone a distribution is or the measure of peakedness of distribution.

$$K_r = \frac{E_t(x-M)^4}{S^4}$$

Where, K_r is kurtosis, S is standard deviation, M is the mean pixel intensity, x is data set and E_t is the expected value of quantity t.

Skewness: The skewness is defined as the measure of asymmetry of data around its mean and mathematical relation is:

$$Sk = \frac{E(x-M)^3}{S^3}$$

Where, S is standard deviation, M is the mean pixel intensity, x is data set and E_t is the expected value of t.

17. Analysing Intensity Data

Figure 10 shows results obtained using conditioned intensity data from the entire image under indenter loading. The input dimensionality was set to 25.

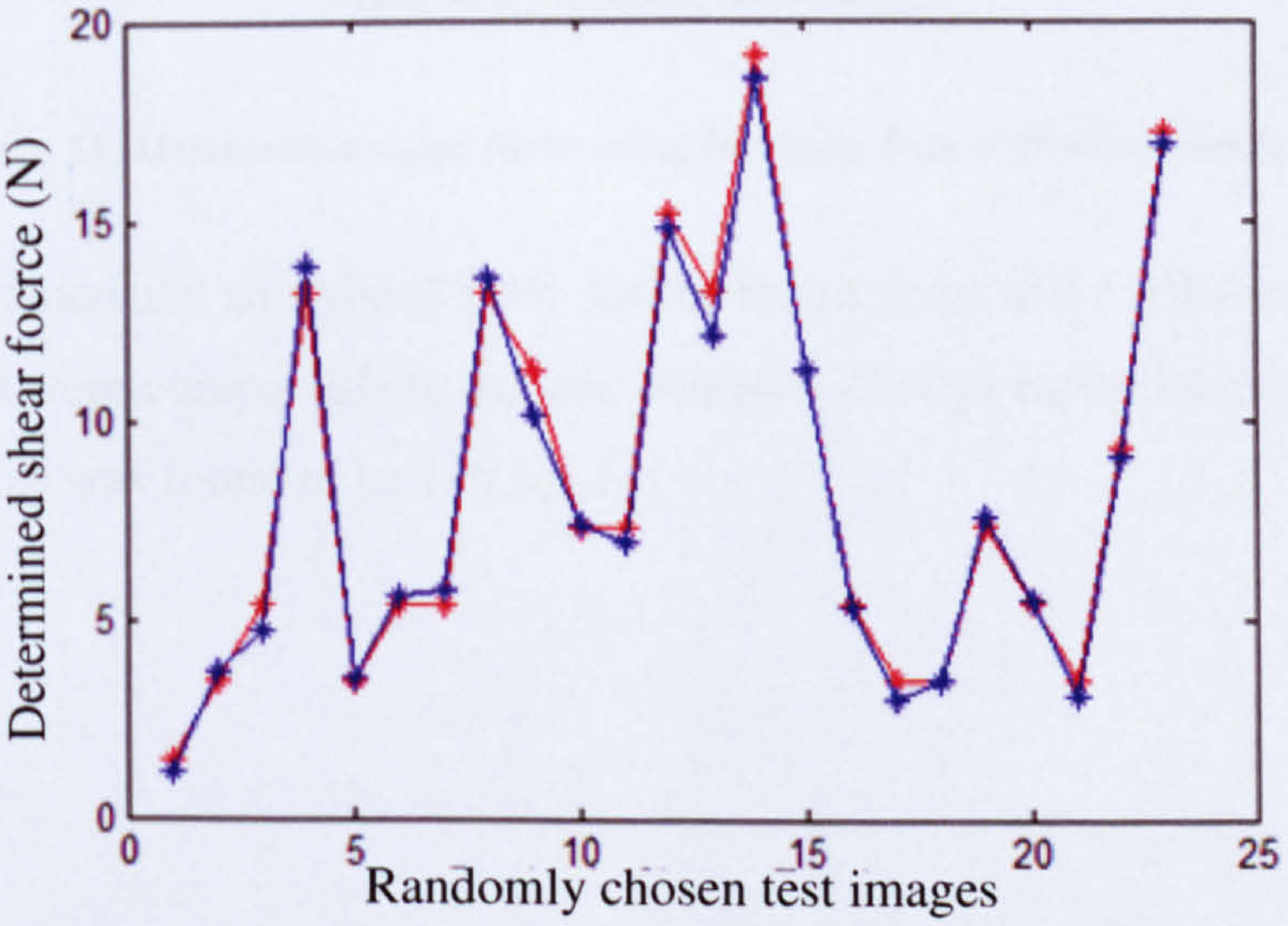

Figure 10: Determined shear force using intensity data of dimensionality 25

The error was found to be 5.99% and the network size of {25,6,5,1}; the input dimensionality influences the results due to network size and amount of training data available. Since the data is extracted from image and entire image cannot be used as input, data reduction techniques like PCA must be used carefully as subtle differences in input can be lost. Optimal size of input dimensionality can be determined by hit and trial methods. Figure 11 shows results obtained using input dimensionality of 15.

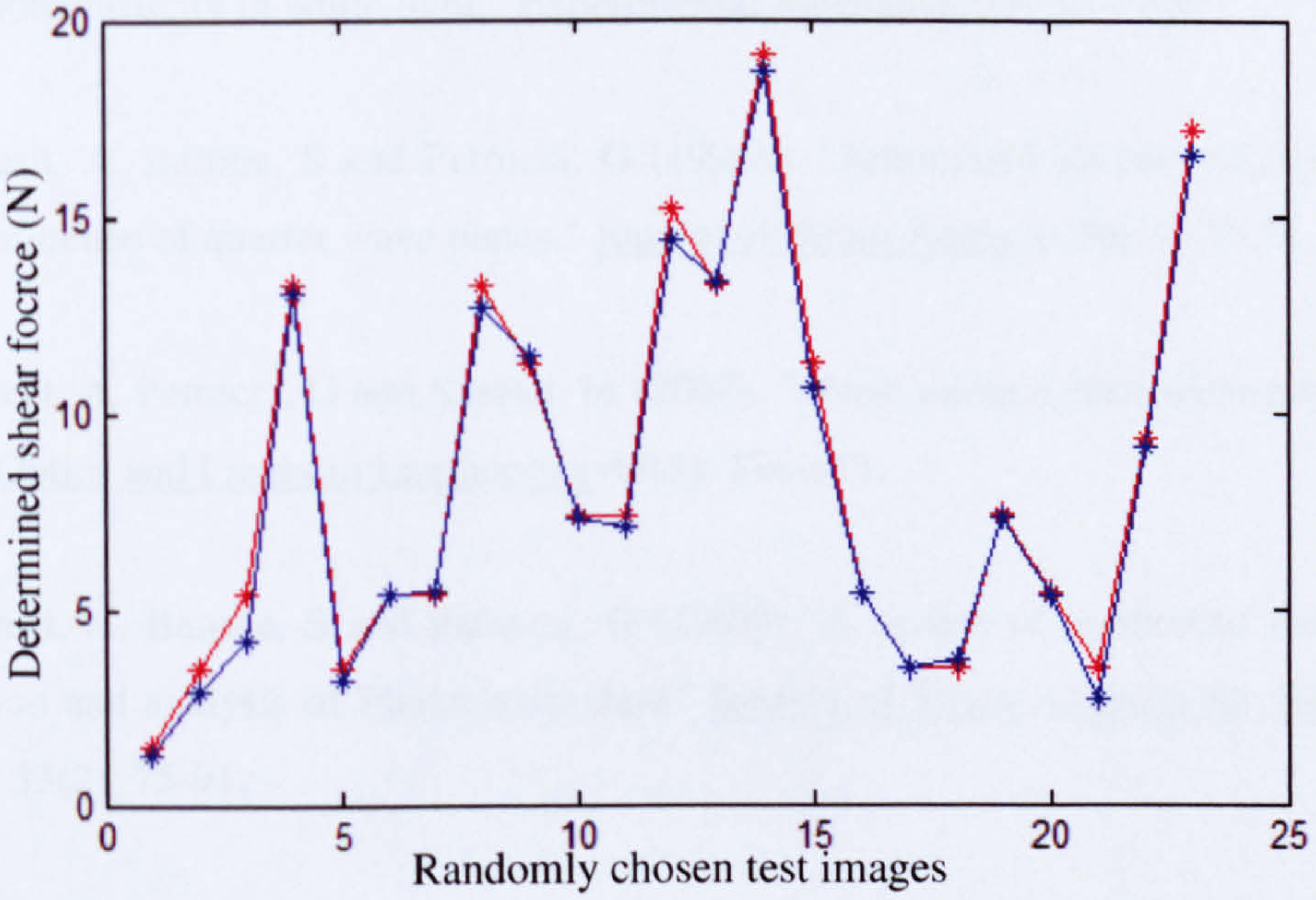

Figure 11: Determined shear force using intensity data of dimensionality 15

The results obtained had an error of 5.9% for the entire range and 5.4% for 23 test images thus the results were comparable to the one obtained through input dimensionality of 25. The network size was found to be {15,5,8,1}.

References

Acquisto, LD, Petrucci, G and Zuccarello, B (2002). "Full field automated evaluation of the quarter wave plate retardation by phase stepping technique." Optics and Lasers in Engineering **37**: 389-400.

Ajovalasit, A, Barone, S and Petrucci, G (1995a). "Towards RGB photoelasticity: Full-field photoelasticity in white light." Experimental Mechanics **35**: 193-200.

Ajovalasit, A, Barone, S and Petrucci, G (1995b). "Automated photoelasticity in white light: influence of quarter wave plates." Journal of Strain Analysis **30**(1): 29-34.

Ajovalasit, A, Petrucci, G and Scafidi, M (2007). "Phase shifting photoelasticity in white light." Optics and Lasers in Engineering **45**(5): 596-611.

Ajovalasit, A, Barone, S and Petrucci, G (1998). "A review of automated methods for collection and analysis of Photoelastic data." Journal of Strain Analysis for Engineering Design **33**(2): 75-91.

American Diabetes Association (2004). Neuropathy & diabetes, diabetic neuropathy-American diabetes association, www.diabetes.org. **2004**.

Arcan, M and Brull, A (1976). "A fundamental characteristic of the human body and foot, the foot-ground pressure pattern." Journal of Biomechanical **9**: 453-457.

Armstrong, D. G., E. J. Peters, K. A. Athanasiou and L. A. Lavery (1998). "Is there a critical level of plantar foot pressure to identify patients at risk for neuropathic foot ulceration?" The Journal of Foot and Ankle Surgery: Official publication of the American college of foot and ankle surgeons **37**(4): 303-307.

Asundi, A (1998). Recent advances in photoelastic applications. International Conference on Fiber Optics and Photonics.

Asundi, A and Sajan, MR (1997). Phase unwrapping in photoelasticity. International Conference on Experimental Mechanics.

Bader, D. L., Bouten, C. V., Colin, D. and Oomens, C. W. (2005). Pressure Ulcer Research: Current and Future Perspectives. Berlin, Springer.

Bernstein, R. K. (2003). Dr. Bernstein's complete guide to achieving normal blood sugars, www.diabetes-book.com. **2004**.

Bishop, CM (1995). Neural networks for pattern recognition, Oxford University Press.

Boulton, A. J. M., H. Connor and P. R. Cavanagh (1994). The Foot in Diabetes, Wiley.

Boyko, E, Ahroni, J and Stensel, V (2001). "Skin temperature in the neuropathic diabetic foot." Journal of Diabetes and its Complications **15**(5): 260-264.

Buckberry, C and Towers, D (1996). "New approach to the full-field analysis of photoelastic stress patterns." Optics and Lasers in Engineering **24**: 415-428.

Cameron, A, Danial, R and Durrant-Whyte, H (1998). Touch and motion [tactile sensor]. Proceedings IEEE International Conference Robotics and Automation.

Caselli, A., T. Hanane, B. Jane, S. Carter, L. Khaodhiar and A. Veves (2003). "Topical methyl nicotinate-induced skin vasodilation in diabetic neuropathy." Journal of Diabetes and its Complications **17**(4): 205-210.

Cavanagh, P. R., J. S. Ulbrecht and G. M. Caputo (2000). "New developments in the Biomechanics of the diabetic foot." Diabetes/Metabolism. Research and Reviews **16**(S1): S6-S10.

Chen, T, Tsao, S and Lee, H (2001). "Complete analysis of Photoelastic fringe patterns using two wavelengths." Proceedings of SPIE **4537**: 325-328.

Chesnin, K. J., S. L. Silverstein and M. P. Besser (2000). "Comparison of an in-shoe pressure measurement device to a force plate: concurrent validity of center of pressure measurements." Gait and Posture **12**: 128-133.

Chung, D (1998). "Neural net based torque sensor using birefringent materials." Sensors and Actuators **70**(3): 243-249.

Dai, X. Q., Y. Li, M. Zhang and J. Cheung (2006). "Effect of sock on biomechanical responses of foot during walking." Clinical Biomechanics **21**: 314-321.

Dario, P, Fermi, D and Vivaldi, F (1987). "Fiber Optic catheter-tip sensor based on photoelastic effect." Sensors and Actuators **12**: 35-47.

Department of Health, National Service Framework for Diabetes: Standards (2003) http://www.nhs.uk/England/AboutTheNHS/Nsf/Diabetes.cmsx.

Dubey, VN and Crowder, R (2006). "A dynamic tactile sensor on photoelastic effect." Sensors and Actuators **128**: 217-224.

Dubey, VN, Grewal, GS and Claremont, DJ (2007). "Load extraction from photoelastic images using neural networks." Experimental Mechanics **47**: 263-270.

Edmund, O (2004). Determining fast axis of quarter wave plate, Edmund Optics. **2004**.

Eghtedari, F and Morgan, C (1988). "A novel tactile sensor for robot applications." Robotica **7**: 289-295.

Eghtedari, F, Hopkins, S and Pham, D (1993). Model a slip sensor. Proceeding International Mechanical Engineers.

Finch, P. M. (1999). "Technology in biomedicine: the EMED Pedar pressure measurement system." The Foot **9**: 1-5.

Freeman, JA and Skapura, DM (1992). Neural Networks: Algorithms, applications and programming techniques, Addison-Wesley.

Gefen, A, Megido-Ravid, M, Azariah, M, Itzchak, Y and Arcan, M (2001). "Integration of plantar soft tissue stiffness measurements in routine MRI of the diabetic foot." Clinical Biomechanics **16**: 921-925.

Gonzalez, RC. Woods, RE, Digital Image Processing (1992). Addison-Wesley.

Gotoh. J, Yoneyama. S, Mawatari. S, Takashi. M (1996). "Photoelastic analysis from a single piece of image with linearly polarized RGB lights". Congress on Experimental Mechanics 160-166.

Govindarajan, R (1997). Development of advanced digital image processing algorithms. Mechanical Engineering. Kanpur, Indian Institute of Technology.

Grewal, GS and Dubey, VN (2007). "Inverse problem of photoelastic fringe mapping using neural networks." Measurement Science and Technology **18**: 1361-1366.

Grewal, GS, Dubey, VN and Claremont, DJ (2006). "Isochromatic demodulation by fringe scanning." Strain **42**: 1-9.

Hagan, M and Menhaj, M (1994). " Training feedforward networks with the Marquardt algorithm." IEEE transactions on Neural Networks 5(6): 989-993.

Hagan, MT, Demuth, HB and Beale, MH (1996). Neural Network Design. Boston, PWS.

Harstell, H., C. Fellner and C. Saltzman (2001). "The repeatability of Total Contact Cast applications: Implications for Clinical trails." Journal of Prosthetics and Orthotics **13**(1): 4-7.

Hayden, S., R. Evans, T. G. McPoil and M. W. Cornwall (2000). "The effect of four prosthetic feet on reducing plantar pressures in diabetic amputees." Journal of Prosthetics and Orthotics **12**(3): 92-96.

Hobbs, J, Patterson, E and Greene, R (2003). "A novel instrument for Transient Photoelasticity." Society for Experimental Mechanics **43**(4): 403-409.

Hopkins, S, Eghtedari, F and Pham, D (1991). "Algorithms for processing data from a photoelastic slip sensor." Mechatronics **2**(1): 15-28.

Hosein, R. and M. Lord (2000a). "A study of in-shoe plantar shear in normals." Clinical Biomechanics **15**: 46-53.

Hosein, R. and M. Lord (2000b). "A study of in-shoe plantar shear in patients with diabetic neuropathy." Clinical Biomechanics **15**: 278-283.

Hosein, R., M. Lord and R. B. Williams (1992). "Method for in-shoe shear stress measurement." Journal of Biomedical Engineering **14**: 181-186.

Hoy, D (1998). "A colour scanner as digital recording polariscope." Experimental Techniques **22**(2): 26-27.

Hu, C-H (1999). "Direct determination of isochromatic fringe order by use of two wavelengths." Applied Optics **38**(25): 5384-5387.

Hughes, R., H. Rowlands and S. McMeekin (2000). "A laser plantar pressure sensor for the diabetic foot." Medical Engineering and Physics. **22**: 149-154.

International Diabetes Federation (2003a). IDF-international diabetes federation-WDD 2004, International Diabetes Federation. **2004.**

International Diabetes Federation (2003b). International Diabetes Federation-Different types of diabetes, International Diabetes Federation. **2004.**

International Diabetes Federation (2003c). International Diabetes Federation-Facts & Figures, International Diabetes Federation. **2006.**

Jones, IA and Wang, P (2003). "Complete fringe order determination in digital Photoelasticity using fringe combination matching." Strain **39**: 121-130.

Kalani, M., G. Jorneskog, N. Naderi, F. Lind and K. Brismar (2002). "Hyperbaric oxygen (HBO) Therapy in treatment of diabetic foot ulcers Long term follow up." Journal of Diabetes and its complications **16**: 153158.

Kihara, T (2003). "An arctangent unwrapping technique of Photoelasticity using linearly polarized light at three wavelengths." Strain **39**: 65-71.

Kumar, V., M. Maru, F. Attar and A. O. Adedapo (2005). "Plantar foot pressure study using tech Fscan Pedobarograph: comparison of normal with hallux rigidus and metatarsalgia." The Journal of Bone & Joint Surgery **88-B**(Supp III): 406.

Lebar, A. M., G. F. Harish, J. J. Wertsch and H. Zhu (1996). "An optoelctronic plantar shear sensing transducer: Design, Validation and Preliminary subject tests." IEEE Transaction Rehabilitation Engineering **4**(4): 310-319.

Lesniak, J, Zhang, SJ and Patterson, EA (2004). "Design and evaluation of the Poleidoscope: A novel digital polariscope." Society for Experimental Mechanics **44**(2).

Lord, M. (1997). "Spatial resolution in plantar pressure measurement." Medical Engineering and Physics. **19**(2): 140-144.

Laing, P and Clwyd, F (1998). "Diabetic foot ulcers." The American Journal of Surgery **176** S(2A): 11S-19S.

Madhu, KR and Ramesh, K (2006). "Noise removal in three-fringe photoelasticity by adaptive colour difference estimation." Optics and Lasers in Engineering **45**(1): 175-182.

Mathworks (2002). MatLAB.

Measurements, G (2004). PhotoStress Method: (Isochromatic fringe characteristics), Vishay Measurement Group.

Merza, Z. and S. Tesfaye (2003). "The risk factors for diabetic foot ulceration." The Foot **13**: 125-129.

Metitur (2004), Parotec System http://www.metitur.fi/english/parotec.html.

Muller, MJ, Diamond, JE and Delitto, A (1989). "Insensitivity, limited joint mobility and plantar ulcers in patients with diabetes mellitus." Physical Therapy. **69**: 453-462.

National Diabetes Information Clearinghouse (2002). Diabetic Neuropathies:The nerve damage of diabetes, National diabetes information clearinghouse (NDIC). **2004**.

Ng, TW, Quek, PK and Lim, KH (2003). "Phase-shifting photoelasticity using flatbed scanner." Optic Engineering **42**(8): 2375-2379.

Nicolopoulos, C. S., E. G. Anderson, S. E. Solomonidis and P. V. Giannoudis (2000). "Evaluation of the gait analysis FSCAN pressure system: clinical tool or toy?" The Foot **10**: 124-130.

Noroozi, S, Amali, R and Vinney, J (2003). "Inverse problem approach using Photoelastic analysis and artificial neural networks in tandem." Strain **40**(2): 73-77.

Novel, De. (2006). EMED System, www.novel.de.

Patterson, DW (1996). Artificial neural networks: Theory and applications, Prentice Hall.

Patterson, DW and Wang, ZF (1991). "Towards full field automated photoelastic analysis of complex components." Strain **27**: 49-56.

Patterson, E and Wang, Z (1998). "Simultaneous observation of Phase-Stepped images for automated Photoelasticity." Journal of Strain **33**(5): 400.

Patterson, E, Ji, W and Wang, Z (1996). "On image analysis for Birefringence measurements in Photoelasticity." Optics and Lasers in Engineering **28**: 17-36.

Patterson, EA (2002). "Digital Photoelasticity: Principles, Practice and Potential." Strain **38**: 27-39.

Payne, C., D. Turner and K. Miller (2001). "Determinants of plantar pressure in the diabetic foot." Journal of Diabetes and its Complications **16**: 277-283.

Perry, J. E., J. O. Hall and B. L. Davis (2002). "Simultaneous measurement of plantar pressure and shear forces in diabetic individuals." Gait and Posture **15**: 101-107.

Pitei, D. L., M. Lord, A. Foster, S. Wilson and M. E. Edmonds (1999). "Plantar pressures are elevated in neuroischemic and the neuropathic diabetic foot." Diabetes Care **22**(12): 1966-1970.

Prechelt, L (1998). "Automatic early stopping using cross validation: quantifying the criteria." Neural Networks **11**: 761-767.

Quaney, B., K. Meyer, ., M. W. Cornwall and T. G. McPoil (1995). "A comparison of tech dynamic pedobarograph and EMED systems for measuring dynamic foot pressures." Foot Ankle International **16**(9): 562-6.

Quiroga, J, Botella, A and Gomez-Pedrero, J (2002a). "Improved method for isochromatic demodulation by RGB calibration." Applied Optics **41**(17): 3461-3468.

Quiroga, J, Servin, M and Marroquin, J (2002b). "Regularization phase tracking technique for demodulation of isochromatics from a single tricolor image." Measurement Science and Technology **13**: 132-140.

Quiroga, JA and Botella, AG (2001). "Demodulation of isochromatic RGB fringe patterns by an improved calibration technique." Proceedings of 4th International Workshop on Automatic Processing of Fringe Patterns.: 126-133.

Ramesh, K (2000). Digital photoelasticity: advance techniques and applications, Springer.

Ramesh, K and Deshmukh, S (1996). "Three fringe photoelasticity -use of colour image processing hardware to automate ordering of isochromatics." Strain **32**(3): 79-86.

Ramesh, K and Deshmukh, S (1997). "Automation of white light Photoelasticity by Phase shifting technique using color image processing hardware." Optics and Lasers in Engineering **28**: 47-60.

Ramesh, K and Ganapathy, V (1996). "Phase-shifting methodologies in photoelastic analysis-The application of Jones calculus." Journal of Strain Analysis **31**(6): 423-432.

Ramesh, K and Mangal, SK (1997). "Data acquisition techniques in digital photoelasticity: a review." Optics and Lasers in Engineering **30**: 53-75.

Ramesh, K. and Tamrakar, D. (2000). "Improved determination of retardation in digital photoelasticity by load stepping." Optics and Lasers in Engineering **33**(6): 387-400.

Randolph, A. L., M. Nelson, S. Akkapeddi, A. Levin and R. Alexandescu (2000). "Reliability of measurements of pressure applied on the foot during walking by a computerized insole sensor system." Archives of Physical Medicine and Rehabilitation **81**: 573-578.

Rhodes, A, Sherk, HH, Black, J and Margulies, C (1988). "High resolution analysis of ground foot reaction forces." Foot Ankle **9**: 153-138.

Rosenblaum, D., S. Hautmann, M. Gold and L. Claes (1994). "Effects of walking speed on plantar pressure patterns and hindfoot angular motion." Gait and Posture **2**: 191-7.

Saad, R., Smith, K. and Benhabib, B. (1994). A novel photoelastic tactile transducer for Robotics. Robotics Research: 5th World Conference.

Sabsik (2005). Camera control software cam2com., Sabsik. **2006**.

Schie, C, Whalley, A, Armstrong, D, Vileikyte, L and Boulton, A (2002). "The effect of silicone injections in diabetic foot on peak plantar pressure and plantar tissue thickness: A 2 year follow up." Archives Physical Medicine and Rehabilitation **83**: 919-923.

Stein, H., E. Yaacobi and R. Steinberg (2001). "The diabetic foot: a daily orthopaedic management problem." Current Orthopaedics **15**: 291-295.

Su, X., Asundi, A. and Sajan, M. (1997). Phase unwrapping in photoelasticity. International Conference on Experimental Mechanics: Advances and Applications, SPIE.

Tappin, J. and K. Robertson (1991). "Study of the relative timing of shear forces on the sole of the forefoot during walking." Journal of Biomedical Engineering **13**: 39-42.

Tappin, J. W., J. Pollard and E. Beckeet (1980). "A method of measuring shearing force on the soles of the foot." Clinical Physics and Physiological Measurement. **1**(83-5).

Tekscan (2004), F-Scan http://www.tekscan.com/medical/system_fscan1.html.

Umezaki, E and Kodama, K (2000). Multiplication and extraction of isochromatics in white light photoelasticity. International Congress on Experimental Mechanics. (18-21).

Urry, S. (1999). "Plantar pressure measurement sensors." Measurement science and Technology **10**: R16-R32.

Vazquez, J, Short, B, Findlow, A, Nixon, B, Boulton, A and Armstrong, D (2003). "Outcomes of hyaluronan therapy in diabetic foot wounds." Diabetes Research and Clinical Practice **59**: 123-127.

Villa, J., Quiroga, J. and Pedrero, G. (2004). "Measurement of retardation in digital photoelasticity by load stepping using a sinusoidal least-squares fitting." Optics and Lasers in Engineering **41**: 127-137.

Viswanathan, V, Snehalatha, C, Sivagami, M, Seena, R and Ramachandran, A (2003). "Association of limited joint mobility and high plantar pressure in diabetic foot ulceration in Asian Indians." Diabetes Research and Clinical Practice **60**: 57-61.

Weaver, J. B., M. Doyley, Y. Cheung, F. Kennedy, E. L. Madsen, E. W. Houten and K. Paulsen (2005). "Imaging the shear modulus of the heel pads." Clinical Biomechanics **20**: 312-319.

World Health Organisation (2004). WHO: The diabetes programme, WHO. **2004.**

World Health Organisation (2007), Prevalence of diabetes in the European Region: Facts & Figures, http://www.who.int/diabetes/facts/world_figures/en/index4.html

Yoneyama, S and Takashi, M (1998). "A new method for photoelastic fringe analysis from a singe image using elliptically polarized white light." Optics and Lasers in Engineering **30**: 441-459.

Yoneyama, S, Gotoh, J, Mawatari, S and Takashi, M (1996). "Photoelastic analysis from a single piece of image with linearly polarized RGB lights." Congress on Experimental Mechanics: 160-166.

Yoneyama, S, Shimizu, M, Gotoh, J and Takashi, M (1998). "Photoelastic Analysis with a Single Tricolor Image." Optics and Lasers in Engineering **29**: 423-435.

Zandman, F, Redner, S and Dally, JW (1977). Photoelastic coatings, Society for Experimental Stress Analysis.

Zhang, M., A. R. Turner and V. C. Roberts (1994). "The reaction of skin and soft tissue to shear forces applied externally to the skin surface." Proceedings of Institution of Mechanical Engineers, Part H (Journal of Engineering in Medicine) **208**(H4): 217-222.